

**Complex 2D & 3D Plasmonic Nanostructures:
Fano Resonances, Chirality,
and Nonlinearities**

Von der Fakultät Mathematik und Physik der Universität Stuttgart
zur Erlangung der Würde eines Doktors der
Naturwissenschaften (Dr. rer. nat.) genehmigte Abhandlung

vorgelegt von
Mario Hentschel
aus Meinerzhagen

Hauptberichter: Prof. Dr. H. Giessen
Mitberichter: Prof. Dr. P. Michler & Prof. Dr. S. Linden

Tag der mündlichen Prüfung: 08. März 2013

4. Physikalisches Institut der Universität Stuttgart
2013

*Nach dem großen Sturm
auch am nächsten Morgen: rot
die Pfefferschoten.*

— Matsuo Bashō (*1644, †1694)

Ach was?!

— Herr Blühmel *alias* Lorient
bürgerlich Bernhard-Viktor Christoph Carl von Bülow (*1923, †2011)

Abstract

This thesis covers two topics of the still emergent field of plasmonics. On the one hand we make use of the interaction of particle plasmon resonances to create 2D as well as 3D complex plasmonic structures which show radically different optical properties than the individual building blocks do. On the other hand we utilize the strongly enhanced local electric field associated with plasmonic nanostructures for nonlinear optical processes.

In particular, we study the formation of Fano resonances in complex nanoparticles arrangements. So-called plasmonic oligomers, that are highly symmetric arrangements of metallic nanoparticles, are discussed in detail. These clusters support dark modes which lead to pronounced scattering minima in their otherwise broad dipolar scattering peaks. We demonstrate the amazing tunability of these clusters and the formation of higher order dark modes. Moreover, we discuss the plasmonic analogue of electromagnetically induced transparency (EIT) in 2D as well as 3D arrangements of metallic nano-bars. We show that such 3D particle groupings are capable of encoding their 3D arrangement in well pronounced and unique optical spectra. We thus envision that our structure can serve as a three-dimensional plasmon ruler enabling the optically determination of three-dimensional arrangements on the nanoscale. Taking the concept of plasmonic EIT one step further, we demonstrate that the destructive interference between normal plasmonic modes, which leads to plasmonic EIT and decreased absorbance in the structure, can be switch to constructive interference and thus enhanced absorbance. It can be argued that this phenomenon is the plasmonic analogue of electromagnetically induced absorbance (EIA).

What is more, we discuss the formation of optical chirality in 3D arrangements of metallic nanoparticles which vastly outperform any naturally occurring chiral substances in the strength of their interaction with an external light field. We deduce the prerequisites for this strong response and demonstrate that only configurational chirality, that is a handed arrangement of equally sized particles, leads to a strong plasmonic chiral optical response. Compositional chirality, that is the use of different sized particles in an unhanded arrangement, is not favourable. This finding is in contrast to chemistry and molecular physics where a so-called chiral center, a carbon atom dressed with four different ligands, is the archetype chiral building block. Moreover, we show that it is possible to optically deduce the spatial arrangements of individual particles in these structures, as chirality is an inherently 3D property. Furthermore, we will demonstrate the formation of a strong and broadband chiral optical response upon the formation

of charge transfer modes, that is, due to ohmic contact of the clusters constituents. Finally, we demonstrate the plasmonic analogue of diastereomers, structures possessing several chiral centers. We thus construct plasmonic composite structures consisting of two different handed sub-units. We show that the optical response, in striking contrast to their molecular counterparts, can be described in terms of fundamental building blocks. The chiral optical response of such complex structures can thus be traced back to the optical properties of the constituting elements.

Finally, we investigate nonlinear optical processes in plasmonic and plasmonic-dielectric-hybrid systems. In particular, we investigate third harmonic generation from dimer nanoantennas and show that the nonlinear optical response, in contrast to common belief, is not governed by gap nonlinearities but fully described by the linear optical properties of the antenna. A simple nonlinear harmonic oscillator model is shown to reproduce all experimental features. Moreover, we will discuss the selective filling of bowtie nanoantennas with the $\chi^{(2)}$ active material $LiNbO_3$ and the nonlinear optical response of this hybrid system. As an outlook we discuss the role of symmetries in nonlinear optics and the perceived implications for nonlinear plasmon optics.

Zusammenfassung

Die vorliegende Arbeit befasst sich mit zwei Aspekten der Plasmonik. Zum einen machen wir uns die starke Wechselwirkung zwischen Partikel Plasmon Resonanzen in benachbarten Metall Nanopartikeln für die Konstruktion von komplexen zwei- und dreidimensionalen Nanostrukturen zunutze. Diese plasmonischen Moleküle weisen kollektive Eigenschaften auf, die sich massiv von den Eigenschaften ihrer Bestandteile unterscheiden. Zum anderen nutzen wir die mit den Resonanzen verbundenen stark überhöhten Nahfelder für nicht-linear optische Prozesse.

Wir untersuchen die Entstehung von Fano-Resonanzen in den Spektren so genannter Plasmonischer Oligomere. Diese Strukturen bestehen aus hoch symmetrischen dicht gepackten Anordnungen einzelner Nanopartikel. Die entstehenden Partikelgruppierungen unterstützen dunkle Moden, d.h. Moden die nicht direkt an ein externes Lichtfeld ankoppeln. Die Wechselwirkung dieser dunkeln Moden mit den direkt anregbaren Moden der Oligomere führt zu Streu-Minima in den vormals deutlich ausgeprägten dipolaren Streu-Maxima. Des Weiteren demonstrieren wir die Formierung dunkler Moden höherer Ordnung in komplexeren Oligomeren, so wie deren spektrale und strukturelle Manipulation. Darüber hinaus diskutieren wir das plasmonische Analogon zur elektromagnetisch induzierenden Transparenz (EIT) in zwei- und dreidimensionalen Strukturen aus individuellen Metall Nanodrähten. Wir zeigen, dass solche dreidimensionalen Gruppierungen in der Lage sind, ihre genaue räumliche Anordnung in ihre spektrale Antwort einzuschreiben. Diese dreidimensionalen "Plasmonenlineale" erlauben daher das optische Auslesen von dreidimensionale Anordnung auf der Nanoskala. Wir zeigen, dass sich das Konzept der plasmonischen EIT durch gezielte Manipulation der Kopplungsphase erweitern lässt. Im Falle der EIT führt die destruktive Interferenz von Normalmoden zu einer deutlichen Reduzierung der Absorption im System. Durch Manipulation der Phasenlage zwischen diesen Moden lässt sich die destruktive in konstruktive Interferenz verwandeln und man beobachtet eine verstärkte Absorption im System. Diese Struktur kann daher als das plasmonische Analog der elektromagnetisch induzierenden Absorption (EIA) angesehen werden.

Darüber hinaus diskutieren wir die Formation einer ausgeprägten chiral optischen Antwort in dreidimensionalen Anordnungen von Metall Nanopartikeln. Wir zeigen, dass nur eine händige Anordnung gleicher Partikel zu einer chiral optischen Antwort führt. Die Anordnung unterschiedlicher Partikel an einem nicht-händigen Gerüst zeigt im besten Falle eine schwache chiral optische Antwort. Dieses Verhalten ist überraschend, da

dies die vorherrschende Bauvorschrift für molekulare chirale Strukturen ist. In einem so genannten asymmetrischen Zentrum sind an ein zentrales Kohlenstoffatom vier unterschiedliche molekulare Gruppen gebunden. Diese asymmetrischen Zentren bilden das Fundament der Mehrheit aller chiralen Moleküle und deren chirale optische Antwort. Weiterhin zeigen wir, dass sich chirale Partikel-Gruppierungen hervorragend eignen, um die räumliche Position einzelner Bestandteile optisch abzufragen. Die Formation von so genannten Ladungstransfer-Moden in komplexen chiralen Anordnungen führt zu einer breitbandigen und extrem starken chiralen optischen Antwort. Weiterhin diskutieren wir komplexe plasmonische Strukturen mit mehreren chiralen Zentren. Die chirale optische Antwort der Strukturen lässt sich aus elementaren Bausteinen zusammensetzen, d.h., die komplexe Antwort kann auf die Antwort der Bausteine zurückgeführt werden. Dieses Verhalten steht im starken Widerspruch zur Molekülphysik, da die chiralen optischen Eigenschaften der analogen Molekülsysteme, die aus mehreren asymmetrischen Kohlenstoffatomen bestehen, nicht auseinander vorhergesagt werden können.

Der letzte Teil der Arbeit widmet sich nichtlinearer optischer Prozesse in plasmonischen und plasmonisch-dielektrischen Hybridsystemen. Im Speziellen untersuchen wir die Erzeugung der dritten Harmonischen von Dimer Nanoantennen. Da diese Systeme eine starke Feldüberhöhung zwischen den Partikeln zeigen, wird im Allgemeinen erwartet, dass die nichtlineare Antwort von den Feldern zwischen den Partikeln dominiert wird. Im Widerspruch zu dieser Erwartung beschreibt ein einfaches harmonisches Oszillatormodell mit kubischer Störung das dritte Harmonische Signal in spektraler Position, Form und Amplitude einzig aus der Kenntnis der linearen Antwort. Darüber hinaus diskutieren wir das selektive Einfüllen von $LiNbO_3$ Nanokristallen in den Zwischenraum von Dimer Nanoantennen und untersuchen die nichtlineare optische Antwort dieses Hybrid-Systems. Als Ausblick diskutieren wir den Einfluss von Symmetrien auf nichtlineare optische Phänomene und die möglichen Konsequenzen für die nichtlineare Plasmonik-Optik.

Publications

Full list of publication

In scientific journals:

1. N. Liu, M. Mesch, T. Weiss, M. Hentschel, and H. Giessen, *Infrared perfect absorber and its application as plasmonic sensor*, Nano Letters **10**, 2342 (2010)
2. R. Ameling, L. Langguth, M. Hentschel, M. Mesch, P. V. Braun, and H. Giessen, *Cavity-enhanced localized plasmon resonance sensing*, Applied Physics Letters **97**, 253116 (2010)
3. M. Hentschel, M. Saliba, R. Vogelgesang, H. Giessen, A. P. Alivisatos, and N. Liu, *Transition from isolated to collective modes in plasmonic oligomers*, Nano Letters **10**, 2721 (2010).
4. M. Hentschel, D. Dregely, R. Vogelgesang, H. Giessen, and N. Liu, *Plasmonic oligomers: The role of individual particles in collective behaviour*, ACS Nano **5**, 2042 (2011)
5. Th. Schumacher, K. Kratzer, D. Molnar, M. Hentschel, H. Giessen, and M. Lipitz, *Nanoantenna-enhanced ultrafast nonlinear spectroscopy of a single gold nanoparticle*, Nature Communications **2**, 333 (2011)
6. H. Schweizer, L. Fu, M. Hentschel, T. Weiss, C. Bauer, P. Schau, K. Frenner, W. Osten, and H. Giessen, *Resonant multimeander-metasurfaces: A model system for superlenses and communication devices*, Physica Status Solidi (b) **249**, 1415 (2012)
7. N. Liu*, M. L. Tang*, M. Hentschel*, H. Giessen, and A. P. Alivisatos, *Nanoantenna-enhanced gas sensing in a single tailored nanofocus*, Nature Materials **10**, 631 (2011)
8. N. Liu, M. Hentschel, Th. Weiss, A. P. Alivisatos, and H. Giessen, *Three dimensional plasmon rulers*, Science **332**, 1407 (2011)

9. T. Utikal, M. Hentschel, and H. Giessen, *Nonlinear photonics with metallic nanostructures on top of dielectrics and waveguides*, Applied Physics B **105**, 51 (2011)
10. M. Gentile, M. Hentschel, R. Taubert, H. Guo, H. Giessen, and M. Fiebig, *Investigation of nonlinear optical metamaterials using second harmonic generation*, Applied Physics B **105**, 149 (2011)
11. D. Dregely*, M. Hentschel*, and H. Giessen, *Excitation and tuning of higher order Fano resonances in plasmonic oligomers clusters*, ACS Nano **5**, 8202 (2011)
12. T. J. Davis, M. Hentschel, N. Liu, and H. Giessen, *Analysis of the three-dimensional plasmonic ruler*, ACS Nano **6**, 1291 (2012)
13. D. Dregely, K. Lindfors, J. Dorfmueller, M. Hentschel, M. Becker, J. Wrachtrup, M. Lippitz, R. Vogelgesang, and H. Giessen, *Plasmonic antennas, positioning, and coupling of individual quantum systems*, Physica Status Solidi (b) **249**, 666 (2012)
14. R. Taubert*, M. Hentschel*, J. Kästel, and H. Giessen, *Classical Analog of electromagnetically induced absorption in plasmonics*, Nano Letters **12**, 1367 (2012)
15. M. Hentschel, M. Schäferling, Th. Weiss, N. Liu, and H. Giessen, *Three dimensional chiral plasmonic oligomers*, Nano Letters **12**, 2542 (2012)
16. M. Schäferling, D. Dregely, M. Hentschel, and H. Giessen, *Tailoring enhanced optical chirality – Design principles for chiral plasmonic nanostructures*, Physical Review X **2**, 031010 (2012)
17. M. Hentschel, T. Utikal, H. Giessen, and M. Lippitz, *Quantitative Modeling of the third harmonic emission spectrum of plasmonic nanoantennas*, Nano Letters **12**, 3778 (2012)
18. B. Metzger, M. Hentschel, M. Lippitz, and H. Giessen, *Third harmonic spectroscopy and modeling of the nonlinear response of plasmonic nanoantennas*, Optics Letters **37**, 4741 (2012)
19. M. Hentschel, L. Wu, M. Schäferling, P. Bai, E. Li, and H. Giessen, *Optical properties of chiral three-dimensional plasmonic oligomers at the onset of charge-transfer plasmons*, ACS Nano **6**, 10355 (2012)
20. M. Hentschel, J. Dorfmueller, H. Giessen, S. Jäger, A. M. Kern, K. Braun, D. Zhang, and A. J. Meixner, *Plasmonic oligomers in cylindrical vector light beams*, Beilstein Journal of Nanotechnology **4**, 57 (2013)

21. M. Hentschel, M. Schäferling, B. Metzger, and H. Giessen, *Plasmonic diastereomers: Adding up chiral centers*, Nano Letters **13**, 600 (2013)

* denotes equally contributing authors.

Book Chapters:

1. D. Dregely, J. Dorfmueller, M. Hentschel, and H. Giessen, *Fabrication, characterization, and applications of optical antenna arrays*, in: Optical Antennas, edited by A. Alù and M. Agio, Cambridge University Press.
2. M. Hentschel, T. Utikal, B. Metzger, H. Giessen, and M. Lippitz, *Nonlinear plasmon optics*, in: 2nd International Workshop Nonlinear Nanostructures for Ultrafast Laser Applications, edited by Rüdiger Grunwald, Springer.

At international conferences (own contributions):

Invited & Colloquia

1. M. Hentschel, M. Saliba, R. Vogelgesang, H. Giessen, A. P. Alivisatos, and N. Liu, *Plasmonic oligomers*, Invited Talk, Nanometa 2011, Seefeld (Austria)
2. M. Hentschel, N. Liu, D. Dregely, and H. Giessen, *Plasmonic oligomers: The role of individual particles in collective behavior*, Invited Talk QFA5, CLEO/QELS 2011, Baltimore (USA)
3. M. Hentschel, *Complex 2D and 3D plasmonic oligomer nanostructures*, Colloquium of the Department of Applied Physics, Hebrew University of Jerusalem, July 2011, Jerusalem (Israel)
4. M. Hentschel, *Complex 2D and 3D plasmonics*, Colloquium of the Institute of Materials Research and Engineering (IMRE), April 2012, Singapore (Singapore)

Contributed Talks

1. M. Hentschel, T. Utikal, M. Lippitz, and H. Giessen, *Size, gap, shape, and material dependence of third harmonic generation from bowtie antenna arrays*, DPG Spring Meeting 2011, Dresden (Germany)
2. M. Hentschel, N. Liu, and H. Giessen, *Plasmonic oligomers*, DPG Spring Meeting 2011, Dresden (Germany)

3. M. Hentschel, *Plasmonic oligomers: the role of individual particles in collective behavior*, Invited Lecture, ICAM Metamaterial Workshop 2011, Hangzhou (China).
4. M. Hentschel, T. Utikal, M. Lippitz, and H. Giessen, *Towards unraveling the mechanism of third harmonic generation in plasmonic nanoantennas*, Talk QFB2, CLEO/QELS 2011, Baltimore (USA).
5. M. Hentschel, T. Utikal, M. Lippitz, and H. Giessen, *Towards unraveling the mechanism of third harmonic generation in plasmonic nanoantennas*, 2nd Workshop Nonlinear Nanostructures for Ultrafast Laser Applications, 2011, Berlin (Germany)
6. M. Hentschel, M. Schäferling, Th. Weiss, H.-G. Kuball, N. Liu, and H. Giessen, *Three-dimensional chiral plasmonic oligomers*, DPG Spring Meeting 2012, Berlin (Germany)
7. R. Taubert, M. Hentschel, J. Kästel, and H. Giessen, *Classical analog of electromagnetically induced absorption in plasmonics*, PIERS 2012, Kuala Lumpur (Malaysia)
8. H. Giessen, N. Liu, M. Hentschel, A. Tittl, R. Ameling, N. Strohfeldt, M. Mesch, J. Zhao, Th. Weiss, and Carsten Sönnichsen, *Fano resonances in complex plasmonic nanostructures for novel sensors*, PIERS 2012, Kuala Lumpur (Malaysia)
9. M. Hentschel and H. Giessen, *Applications of 2D and 3D plasmonic oligomers, metamaterials, and nanoantennas*, MRS Spring Meeting 2012, San Francisco (USA)
10. M. Hentschel, M. Schäferling, Th. Weiss, H.-G. Kuball, N. Liu, and H. Giessen, *Three-dimensional chiral plasmonic oligomers*, META 12, Paris (France)
11. R. Taubert, M. Hentschel, J. Kästel, and H. Giessen, *Classical analog of electromagnetically induced absorption in plasmonics*, CLEO/QELS 2012, San Jose (USA)
12. M. Hentschel, M. Lippitz, T. Utikal, and H. Giessen, *Quantitative Modeling of the nonlinear ultrafast response in a plasmonic system*, Talk QTh3E.5, CLEO/QELS 2012, San Jose (USA)
13. M. Hentschel, M. Schäferling, Th. Weiss, H. G- Kuball, N. Liu, and H. Giessen, *Three-dimensional chiral plasmonic oligomers*, Talk QTh4F.1, CLEO/QELS 2012, San Jose (USA)
14. M. Hentschel, M. Schäferling, N. Liu, and H. Giessen, *Three-dimensional chiral plasmonic oligomers*, EMRS 2012, Strasbourg (France)

15. M. Hentschel, M. Lippitz, B. Metzger, and H. Giessen, *Ultrafast nonlinear plasmonics*, Stuttgarter Lasertage 2012, Stuttgart (Germany)
16. M. Hentschel, M. Schäferling, Th. Weiss, N. Liu, and H. Giessen, *Three-dimensional chiral plasmonic oligomers*, NFO12, San Sebastian (Spain)
17. M. Hentschel, M. Schäferling, B. Metzger, and H. Giessen, *Plasmonic diastereomers: Adding up chiral centers*, DPG Frühjahrstagung 2013, Regensburg (Germany)
18. M. Hentschel, *Three-dimensional chiral plasmonic oligomers*, APS March Meeting 2013, Baltimore (USA)
19. M. Hentschel, M. Schäferling, B. Metzger, and H. Giessen, *Plasmonic diastereomers: Adding up chiral centers*, Sixth international conference on surface plasmon photonics 2013, Ottawa (Canada)

Poster

1. M. Hentschel, N. Liu, and H. Giessen, *Optical properties of plasmonic planar septamer nanostructures*, DPG Spring Meeting 2010, Regensburg (Germany)
2. M. Hentschel, T. Utikal, Th. Weiss, M. Lippitz, and H. Giessen, *Nonlinear Optics with Ultrashort Laser Pulses in Plasmonic Nanooptical Systems*, German-French Colloquium, "French-German Research: 50 Years In The Light Of The Laser", 2010, Berlin (Germany)
3. M. Hentschel, T. Utikal, M. Lippitz, and H. Giessen, *Size, gap, and material dependence of third harmonic generation from bowtie antennas*, NANOMETA 2011, Seefeld (Austria)

At international conferences (other):

1. M. Gentile, M. Hentschel, H. Guo, H. Giessen, and Manfred Fiebig, *Nonlinear optical spectroscopy of metamaterials*, Talk, DPG Spring Meeting 2009, Dresden (Germany)
2. M. Gentile, R. Taubert, M. Hentschel, H. Giessen, and M. Fiebig, *Nonlinear optical spectroscopy of metamaterials*, Poster, DPG Spring Meeting 2010, Regensburg (Germany)
3. H. Giessen, M. Hentschel, N. Liu, *Plasmonic coupling games*, Invited Talk, Gordon Research Conference, Plasmonics, 2010, Waterville ME (USA)

4. H. Giessen, N. Liu, M. Hentschel, *Plasmonic coupling games*, Invited Talk, Metamaterials 2010, Karlsruhe (Germany)
5. C. Dicken, K. Lindfors, M. Hentschel, and M. Lippitz, *Kerr-microscopy of magnetic nanostructures*, Poster, DPG Spring Meeting 2011, Dresden (Germany)
6. R. Ameling, L. Langguth, M. Hentschel, M. Mesch, and H. Giessen, *Cavity-enhanced localized plasmonic resonance sensing*, Talk, DPG Spring Meeting 2011, Dresden (Germany)
7. Th. Schumacher, D. Ulrich, M. Hentschel, H. Giessen, and M. Lippitz. *Optical nanoantennas for ultrafast spectroscopy of single nanoparticles*, Talk, DPG Spring Meeting 2011, Dresden (Germany)
8. T. Schumacher, K. Kratzer, M. Hentschel, H. Giessen, and M. Lippitz, *Optical nanoantennas enhance ultrafast nonlinear spectroscopy of single nanodiscs*, Talk, Nanometa 2011, Seefeld (Austria)
9. R. Ameling, L. Langguth, M. Hentschel, M. Mesch, and H. Giessen, *Cavity-enhanced localized plasmon resonance sensing*, Talk, Nanometa 2011, Seefeld (Austria)
10. M. L. Tang, N. Liu, M. Hentschel, A. P. Alivisatos, and Harald Giessen, *In-situ LSPR sensing of hydrogen storage in palladium nanocrystals at the single particle level*, MRS Spring Meeting 2011, San Francisco (USA)
11. T. Schumacher, K. Kratzer, D. Ullrich, M. Hentschel, H. Giessen, and M. Lippitz, *Nanoantenna-enhanced ultrafast nonlinear spectroscopy of a single plasmonic nanodisc*, Talk QFB3, CLEO/QELS 2011, Baltimore (USA)
12. N. Liu, M. Hentschel, Th. Weiss, H. Giessen, and A. P. Alivisatos, *Towards 3D plasmon rulers*, CLEO 2011, Baltimore (USA)
13. N. Liu, M. Tang, M. Hentschel, H. Giessen, and A. P. Alivisatos, *Nanoantenna-enhanced gas sensing in a single tailored nanofocus*, Postdeadline paper PDPC11, CLEO 2011, Baltimore (USA)
14. T. Schumacher, K. Kratzer, D. Ullrich, M. Hentschel, H. Giessen, and M. Lippitz, *Nanoantenna-enhanced ultrafast nonlinear spectroscopy of a single plasmonic nanodisc*, CLEO/Europe 2011, Munich (Germany)
15. N. Liu, A. P. Alivisatos, M. Hentschel, Th. Weiss, and H. Giessen, *Towards 3D plasmon rulers*, Talk, Fifth international conference on surface plasmon photonics 2011, Busan (Korea)

16. M. Hentschel, T. Utikal, M. Lippitz, and H. Giessen, *Towards the origin of third harmonic generation from bowtie nanoantenna arrays*, Talk, Fifth international conference on surface plasmon photonics 2011, Busan (Korea)
17. N. Liu, M. Hentschel, Th. Weiss, H. Giessen, A. P. Alivisatos, *Towards 3D plasmon rulers*, ICMAT 2011, Suntec (Singapore)
18. T. Schumacher, K. Kratzer, D. Ullrich, M. Hentschel, H. Giessen, and M. Lippitz, *Nanoantenna-enhanced ultrafast nonlinear spectroscopy of a single plasmonic nanodisc*, 13th International Conference on Transparent Optical Networks, June 2011, Stockholm (Sweden)
19. M. Schäferling, D. Dregely, M. Hentschel, and H. Giessen, *Spatially resolved enhancement of chirality and 3D chiral metamaterials*, Talk, Metamaterials 2011, Barcelona (Spain)
20. N. Liu, M. L. Tang, M. Hentschel, H. Giessen, and A. P. Alivisatos, *Nanoantenna-enhanced gas sensing in a single tailored nanofocus*, Talk, Metamaterials 2011, Barcelona (Spain)
21. N. Liu, M. L. Tang, M. Hentschel, H. Giessen, and A. P. Alivisatos, *Antenna-assisted hydrogen sensing in a single plasmonic nanofocus*, SPIE NanoScience + Engineering 2011, San Diego (USA)
22. H. Giessen, N. Liu, A. Radke, M. Schäferling, Th. Weiss, and M. Hentschel, *Chiral plasmonic and metamaterial 3D nanostructures*, Invited talk, The 13th International Conference on Chiroptical Spectroscopy (CD2011), Oxford (UK)
23. T. Schumacher, D. Ullrich, M. Hentschel, H. Giessen, and M. Lippitz, *Nanoantenna-enhanced ultrafast nonlinear spectroscopy of a single plasmonic nanoparticle*, Talk, SPIE Photonics West 2012, San Francisco (USA)
24. T. J. Davis, M. Hentschel, N. Liu and H. Giessen, *Measuring nanoscale motion of complex macromolecules: an analysis of the 3D plasmonic ruler*, ACMM22, Perth (Australia)
25. H. Giessen, N. Liu, M. L. Tang, M. Hentschel, R. Taubert, A. Radke, D. Dregely, A. Tittl, M. Mesch, and A. P. Alivisatos, *Complex and 3D plasmonics: Coupling, sensing, and chirality*, Plenary Talk, ICONN 2012, Perth (Australia)
26. M. Schäferling, M. Hentschel, D. Dregely, and H. Giessen, *Local enhancement of optical chirality in planar and 3D plasmonic nanostructures*, Talk, DPG Spring Meeting 2012, Berlin (Germany)

27. Th. Schumacher, M. Hentschel, H. Giessen, and M. Lippitz, *A point-dipole model for fast computation of plasmonic structures and nanoantennas*, Poster, DPG Spring Meeting 2012, Berlin (Germany)
28. R. Taubert, M. Hentschel, J. Kästel, and H. Giessen, *Classical analog of electromagnetically induced absorption in plasmonics*, Talk, DPG Spring Meeting 2012, Berlin (Germany)
29. W. Tievesch, M. Gentile, M. Hentschel, H. Giessen, and M. Fiebig, *Enhancement of non-linear effects using nano-wires*, Talk, DPG Spring Meeting 2012, Berlin (Germany)
30. Th. Schumacher, D. Ullrich, M. Hentschel, H. Giessen, and M. Lippitz, *Optical nanoantennas for ultrafast spectroscopy of single nanoobjects*, Talk, DPG Spring Meeting 2012, Berlin (Germany)
31. B. Metzger, A. Steinmann, M. Hentschel, and H. Giessen, *High-power widely tunable sub-20 fs Gaussian laser pulses and their application for nonlinear nano-plasmonic spectroscopy*, Talk, DPG Spring Meeting 2012, Stuttgart (Germany)
32. M. Trassin, J. Heron, M. Hentschel, L. You, Q. He, H. Giessen, Y.-H.Chu, S. Salahuddin, and R. Ramesh, *Transverse electric field driven magnetic switch using multiferroics*, Talk. MRS Spring Meeting 2012, San Francisco (USA)
33. R. Taubert, M. Hentschel, J. Kästel, and H. Giessen, *Classical analog of electromagnetically induced absorption in plasmonics*, Talk, META 12, Paris (France)
34. M. Schäferling, M. Hentschel, D. Dregely, and H. Giessen, *Local enhancement of optical chirality in plasmonic nanostructures*, Talk, 8th Workshop on Numerical Methods for Optical Nano Structures, Zürich (Switzerland)
35. Thorsten Schumacher, Daniela Ullrich, Mario Hentschel, Harald Giessen, and Markus Lippitz, *Optical nanoantennas for nonlinear spectroscopy of a single nanoobject*, Poster, Ultrafast Phenomena 2012, Lausanne (Switzerland)
36. S. Jäger, A. Kern, M. Hentschel, K. Braun, D. Zhang, H. Giessen, and A. J. Meixner, *Visualisation of ringmodes in plasmonic aromatic-molecules*, Poster, NFO12, San Sebastian (Spain)
37. M. Schäferling, D. Dregely, M. Hentschel, X. Yin, J. Dorfmueller, and H. Giessen, *Local enhancement of optical chirality in plasmonic nanostructures*, Poster, NFO12, San Sebastian (Spain)
38. B. Metzger, M. Hentschel, M. Lippitz, and H. Giessen, *Second and third harmonic*

spectroscopy of complex plasmonic nanoantennas, Poster, NFO12, San Sebastian (Spain)

39. S. Jäger, A. Kern, M. Hentschel, K. Braun, D. Zhang, H. Giessen, and A. J. Meixner, *Visualisation of ringmodes in plasmonic aromatic-molecules*, Poster, 11th International Conference on Hole Burning, Single Molecule and Related Spectroscopies: Science and Applications, Tübingen (Germany)
40. M. Schäferling, D. Dregely, M. Hentschel, X. Yin, and H. Giessen, *Design of plasmonic nanostructures for chiral sensing*, Talk, TACONA 2012, Bad Honnef (Germany)
41. B. Metzger, M. Hentschel, Th. Schumacher, and H. Giessen, *Nonlinear optical response of complex plasmonic Fano structures*, Talk, Nanometa 2013, Seefeld (Austria)
42. Th. Schumacher, D. Ullrich, M. Hentschel, H. Giessen, and M. Lippitz, *Optical antennas for ultrafast spectroscopy of single CdSe nanoobjects*, DPG Frühjahrstagung 2013, Regensburg (Germany)
43. B. Metzger, M. Hentschel, Th. Schumacher, and H. Giessen, *Nonlinear optical response of complex plasmonic nanoantennas and Fano structures*, DPG Frühjahrstagung 2013, Regensburg (Germany)
44. B. Metzger, M. Hentschel, Th. Schumacher, and H. Giessen, *Nonlinear optical response of complex plasmonic nanoantennas and Fano structures*, Poster, Sixth international conference on surface plasmon photonics 2013, Ottawa (Canada)

Contents

Abstract	5
Zusammenfassung	7
Publications	9
1. Introduction	21
1.1. A Brief History & Introduction to Plasmonics	21
1.2. Outline	24
2. Fabrication Techniques	27
2.1. Introduction	27
2.2. Single-Layer Fabrication	27
2.3. Multi-Layer Fabrication	29
3. Plasmonic Oligomers	33
3.1. Plasmon Hybridization & Plasmon Coupling in Simple Geometries	33
3.2. Plasmonic Heptamers & Oligomers	44
3.3. Plasmonic Analogue of Electromagnetically Induced Transparency (EIT)	74
3.3.1. EIT in Planar Geometries	74
3.3.2. EIT in Three-Dimensional Arrangements	77
3.3.3. Double EIT as Three-Dimensional Plasmon Ruler	86
3.4. Classical Analogue of Electromagnetically Induced Absorption (EIA)	88
3.5. Temperature-dependent Measurements of the EIT Structure	95
3.6. Conclusions, Summary & Outlook	98
4. Plasmonic Chirality	103
4.1. Introduction	103
4.2. Compositional & Constitutinal Chirality	104
4.3. Three-dimensional Chiral Plasmon Rulers	113
4.4. Charge Transfer in Chiral Plasmonic Oligomers	120
4.5. Plasmonic Diastereomers	137
4.6. Conclusions, Summary & Outlook	151
5. Nonlinear Plasmon Optics	155
5.1. Introduction	155

5.2. Third Harmonic Generation From Dimer Nanoantennas	159
5.3. The Nonlinear Harmonic Oscillator Model	169
5.4. Nonlinear Plasmon Optics in Terms of Resonantly Enhanced Optical Non-linearities	175
5.5. Nanoantenna Enhanced Second and Third Harmonic Generation	178
5.6. The Role of Symmetries in Nonlinear Optics	187
5.6.1. Maxwell's Equations and the Wave Equation	188
5.7. Conclusions, Summary & Outlook	194
A. Appendix	201
Curriculum Vitae	248
Acknowledgments	249

1. Introduction

1.1. A Brief History & Introduction to Plasmonics

If light impinges on a noble metal nanoparticle it will excite harmonic oscillations of the quasi-free conduction electrons with respect to the fixed ionic background. The periodic charge displacement will give rise to local electric fields, see figure 1.1. The main benefit afforded by such a plasmonic nanoparticle is its astonishing ability to confine far-field energy into deep subwavelength volumes, which can not be achieved with dielectrics due the fundamental laws of diffraction. The local electric fields can thus significantly surpass the incoming field strength.

The first detailed study on the optical properties of metal nanoparticles and thin films was performed by Michael Faraday and published in 1857 [1]. An astonishing insight was already gained at the time, yet not all conclusions withstood time & further research. As it makes a fascinating reading experience, here is an excerpt from the abstract of the manuscript:

”Conveiving it very possible that some experimental evidence of value might result from the introduction into a ray of separate particles having great power of action on light, the particles being at the same time very small as compared to the wave-lengths, I sought amongst the metals for such. Gold seemed especially fitted for experiments of this nature, because of its comparative opacity amongst bodies, and yet possession of a real transparency; because of its development of colour both in reflected and transmitted ray; because of the state of tenuity and division which it permitted with the preservation of its integrity as a metallic body; because of its supposed simplicity of character; and because known phenomena appeared to indicate that a mere variation in the size of its particles gave rise to a variety of resulting colours. Besides, the waves of light are so large compared to the dimensions of the particles of gold which in various conditions can be subjected to a ray, that it seemed probable the particles might come into effective relations to the much smaller vibrations of the ether particles; in which case, if reflexion, refraction, absorption, &c. depended upon such relations, there was reason to expect that these functions would change sensibly by the substitution of different-sized particles of this

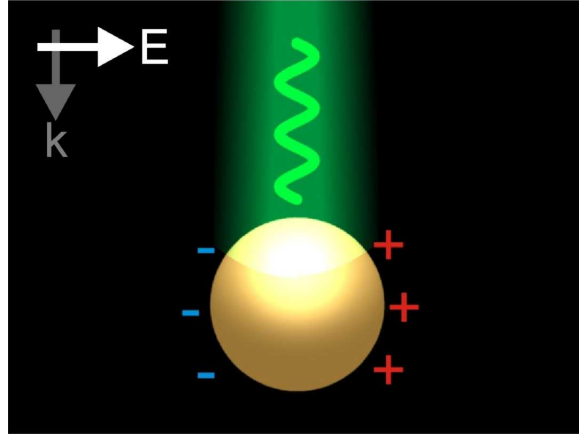


Figure 1.1.: If an external light field with electric field \vec{E} and wavevector \vec{k} is incident on a noble metal particle collective oscillations of the quasi-free conduction electrons can be excited. The periodic displacement of the electron cloud with respect to the fixed ionic background of the particle will cause local electric fields in the vicinity of the particle. This confinement of energy into deep subwavelength volumes leads to a significant local field strength which can, at least potentially, exceed the incoming one by orders of magnitude.

metal for each other. At one time I hoped that I had altered one coloured ray into another by means of gold, which would have been equivalent to a change in the number of undulations; and though I have not confirmed that result as yet, still those I have obtained seem to me to present a useful experimental entrance into a certain physical investigation respecting the nature and action of a ray of light. I do not pretend that they are of great value in their present state, but they are very suggestive, and they may save much trouble to any experimentalists inclined to pursue and extend this line of investigation.”

Robert Wood discovered another intriguing plasmonic phenomenon in 1902 [2]. In studying reflections from metallic gratings he found spectral features he could not explain, later turning out to be surface plasmon resonances excited in the gratings [3]. In 1904 James C. Maxwell Garnett developed a model to describe the colours of metal doped glasses based on the Drude theory of metals [4]. Further pushing the field, Gustav Mie, inspired by Faraday’s earlier work, derived analytical solutions for light scattering from small spherical particles in 1908, a description which is not restricted to metals [5]. R. Gans generalized Mie’s work in 1912 to elliptically shaped particles [6]. The excitation of collective oscillations of conduction electrons, excited by fast electrons passing through a thin metal film, was first discussed by David Pines [7] and Rufus Ritchie [8], being termed a plasmon. In 1970 Uwe Kreibig and Peter Zacharias reported the excitation of particle plasmon resonances in spherical gold and silver nanoparticles, measured by electron energy loss spectroscopy (EELS) [9]. Another important breakthrough was reported by Andreas Otto [10] as well as Erich Kretschmann and Heinz Raether [11] in demonstrating the ability to excite the non-radiative surface plasma waves optically. The

first application, which has by no means diminished in its potential and the fascination it evokes, is surface enhanced Raman scattering driven by plasmon excitations on rough surfaces [12], a process not fully understood to date.

Even so this concept appears to be fairly obvious, the optics of metal nanoparticles, or plasmonics, has proven to be a fascinating field of research. The strong local fields allow for a multitude of applications (each of which could easily fill an entire thesis, thus, only a brief introduction and a number of references are given, original research articles as well as reviews, for further reading):

- One of the first and most intuitive applications is plasmonic sensing. Due to the strong field confinement [13,14], the particle plasmon resonance is very sensitive to the local refractive index of the surrounding medium. A change in the refractive index can be traced by a spectral shift of the resonance position, accompanied by a potential modification of the resonance line shape [15–22]. Obviously, a plasmon sensor is only sensitive to a change in refractive index and is thus "blind" to the actual cause. For specific sensing, e.g. for glucose sensing, it is thus necessary to functionalize the system in order to be only sensitive to the desired analyte. However, this problem has been tackled in numerous publications and amazing progress has been made in terms of sensitivity as well as specificity [23–28], even going towards single particle based sensing strategies [29], and molecular fingerprint vibrational spectroscopy [30–32].
- Another major research area is connected to material design. A plasmonic resonance in a particle can be manipulated by the particles size and shape. It has been demonstrated that, e.g., a U-shaped structure, called a split ring resonator (SRR), can support a plasmonic mode associated with a ring current and thus an induced magnetic dipole moment [33]. This magnetic dipole moment will oscillate at light frequencies, far outperforming any naturally occurring magnetic phenomena which are no longer relevant at these high frequencies [34]. The ability to structure materials at subwavelength scales and create resonances at nearly arbitrary spectral positions has led to the theoretical predication as well as experimental realization of materials with unique properties. Many so called effective media with arbitrarily designable permeability and permittivity have been suggested to create materials with, e.g., negative refractive index [35–45]. Another field within this context is transformation optics [46–48]. Here, one again makes use of designable permeability and permittivity in order to create materials with certain unique functionalities. Instead of creating a lens by changing the shape of a piece of glass, one can structure the refractive index in order to guide the light through the materials as if it would have passed an ordinary lens [49]. This concept allows to nearly arbitrarily guide the flow of light. The most prominent and compelling example, after all, might be optical cloaking [46, 47, 50–63].

- Plasmonics allows to draw compelling analogies to molecular physics. The properties of molecules are determined by their composition as well as their configuration, that is, by the number and kind of atoms as well as by their spatial arrangement. Both determine how the electron wavefunctions mix and hybridize giving rise to new, collective molecular orbitals [64]. In case of plasmonics, the local electric fields take the role of the electron wavefunctions in mediating the coupling between adjacent plasmonic nanoparticles. If two or more plasmonic nanoparticles are brought into close proximity, the modes of the individual particles will mix and hybridize giving rise to new collective modes, thus forming plasmonic molecules. The concept of plasmon hybridization has been introduced by Nordlander and co-workers in 2003 and has stimulated a tremendous amount of research interest [65]. In contrast to molecular physics, the coupling strength can be easily manipulated by the interparticle distance. Similarly, the spatial arrangement of the particles can be chosen at will to create any plasmonic molecule imaginable [66–86], even as metallic strands in photonic crystal fibers [87].

1.2. Outline

This thesis will mainly cover two topics of the still emergent field of plasmonics. On the one hand we will make use of the interaction of particle plasmon resonances to create 2D as well as 3D complex plasmonic structures which show radically different optical properties than the individual building blocks do. In particular, we will study the formation of Fano resonances in complex nanoparticles arrangements as well as plasmonic chirality, which vastly outperforms any naturally occurring chiral substance in the strength of its interaction with an external light field. Moreover, we will make use of the strongly enhanced near-fields for a number of nonlinear optical processes, in particular third harmonic generation from dimer nanoantennas and second and third harmonic generation from composite structures of gold antennas and nonlinear optically active dielectrics.

Due to their rather different nature, each of the three main experimental chapters, which are chapter 3 on Plasmonic Oligomers, chapter 4 on Plasmonic Chirality, and chapter 5 on Nonlinear Plasmon Optics, will feature its own *"Introduction"* as well as *"Conclusions, Summary & Outlook"* sections.

The main outline is as follows:

- Chapter 2 will give a basic introduction to the utilized fabrication techniques, which have been an indispensable prerequisite for the conducted experiments.
- Chapter 3 will introduce the concept of plasmon hybridization and discuss plas-

monic coupling in simple geometries. Subsequently, plasmonic oligomers, that are highly symmetric arrangements of metallic nanoparticles, will be discussed in detail. It will be shown that they support dark modes which lead to pronounced scattering minima in their otherwise broad dipolar scattering peaks. We will demonstrate the amazing tunability of these clusters and the formation of higher order dark modes. Moreover the chapter will discuss the plasmonic analogue of electromagnetically induced transparency (EIT) in 2D as well as 3D arrangements of metallic nano-bars. It will be shown, that such 3D particle groupings are capable of encoding their 3D arrangement in well pronounced and unique optical spectra making them ideal candidates for so-called 3D plasmon rulers. Taking this concept one step further, we will demonstrate that the destructive interference between normal plasmonic modes, which leads to plasmonic EIT and decreased absorbance in the structure, can be switch to constructive interference and thus enhanced absorbance. It can be argued that this phenomenon is the plasmonic analogue of electromagnetically induced absorbance (EIA).

- Chapter 4 will discuss the formation of strong optical chirality in 3D arrangements of metallic nanoparticles and deduce the prerequisites for this strong response. What is more, it is possible to optically deduce the spatial arrangements of individual particles in these structures, as chirality is an inherently 3D property. Furthermore, we will demonstrate the formation of a strong and broadband chiral optical response upon the formation of charge transfer modes, that is, due to ohmic contact of the clusters constituents. Finally, we will draw the plasmonic analogue of the chemical concept of diastereomers, structures possessing several so-called chiral centers. We will thus introduce plasmonic structures with multiple chiral centers and study their optical properties.
- Chapter 5 will discuss in detail nonlinear optical processes in plasmonic nanostructures. In particular, we will investigate third harmonic generation from dimer nanoantennas and show that the nonlinear optical response, in contrast to common belief, is not governed by gap nonlinearities but fully described by the linear optical properties of the antenna. A simple nonlinear harmonic oscillator model is shown to reproduce all experimental features. Moreover, we will discuss the selective filling of bowtie nanoantennas with the $\chi^{(2)}$ active material $LiNbO_3$ and the nonlinear optical response of this hybrid system. As an outlook we will discuss the role of symmetries in nonlinear optics and the perceived implications for nonlinear plasmon optics.

- Chapter 3 is based in part on already published work:

M. Hentschel, M. Saliba, R. Vogelgesang, H. Giessen, A. P. Alivisatos, and N. Liu, *Transition from isolated to collective modes in plasmonic oligomers*, Nano Letters **10**, 2721 (2010)

M. Hentschel, D. Dregely, R. Vogelgesang, H. Giessen, and N. Liu, *Plasmonic oligomers: The role of individual particles in collective behaviour*, ACS Nano **5**, 2042 (2011)

D. Dregely*, M. Hentschel*, and H. Giessen, *Excitation and tuning of higher order Fano resonances in plasmonic oligomers clusters*, ACS Nano **5**, 8202 (2011)

N. Liu, M. Hentschel, Th. Weiss, A. P. Alivisatos, and H. Giessen, *Three dimensional plasmon rulers*, Science **332**, 1407 (2011)

R. Taubert*, M. Hentschel*, J. Kästel, and H. Giessen, *Classical Analog of electromagnetically induced absorption in plasmonics*, Nano Letters **12**, 1367 (2012)

- Chapter 4 is based in part on already published work:

M. Hentschel, M. Schäferling, Th. Weiss, N. Liu, and H. Giessen, *Three dimensional chiral plasmonic oligomers*, Nano Letters **12**, 2542 (2012)

M. Hentschel, L. Wu, M. Schäferling, P. Bai, E. Li, and H. Giessen, *Optical properties of chiral three-dimensional plasmonic oligomers at the onset of charge-transfer plasmons*, ACS Nano **6**, 10355 (2012)

M. Hentschel, M. Schäferling, B. Metzger, and H. Giessen, *Plasmonic Diastereomers: Adding up chiral centers*, Nano Letters **13**, 600 (2013)

- Chapter 5 is based in part on already published work:

M. Hentschel, T. Utikal, H. Giessen, and M. Lippitz, *Quantitative Modeling of the third harmonic emission spectrum of plasmonic nanoantennas*, Nano Letters **12**, 3778 (2012)

M. Hentschel, T. Utikal, B. Metzger, H. Giessen, and M. Lippitz, *Nonlinear plasmon optics*, in: *2nd International Workshop Nonlinear Nanostructures for Ultrafast Laser Applications*, edited by Rüdiger Grunwald, Springer.

* denotes equally contributing authors.

2. Fabrication Techniques

2.1. Introduction

Electron-beam lithography based techniques allow fabrication of nearly arbitrarily shaped structures in two dimensions, utilizing layer-by-layer fabrication techniques it is as well possible to realize quasi-three-dimensional systems. Hence, the technique is highly versatile and has proven to be an indispensable prerequisite for the studies presented in this thesis. The availability of high quality samples with high resolution features and reliable and reproducible parameters has enabled the studies presented here.

Figure 1 depicts a selection of possible geometries fabricated using the techniques described below. The panels (a) to (h) show two-dimensional structures typically made of gold. Panels (i) to (o) show structures fabricated in multi-layer exposures. The Structures of panels (i) and (j) are as well two-dimensional, yet the structures consist of two different materials (gold and aluminium in (i) and gold and palladium in (j)). The structures of panels (k) to (o) are three-dimensional ones, the individual layers being separated by a dielectric spacer. Overall, figure 2.1 shows the nearly limitless structuring capabilities of electron-beam lithography (please note: all scale bars are 100 nm). For more examples please see Appendix A.

The following chapter will give a short overview of electron beam lithography based fabrication techniques. All samples studied in this thesis have been fabricated utilizing the techniques described below.

2.2. Single-Layer Fabrication

The fabrication process is sketched in figure 2.2. After cleaning of the substrate (Suprasil, Heraeus) a double resist layer (PMMA (Poly methyl methacrylate) 250 K, 2,5% & 950 K 1,5%, Allresit) is spin coated (5 s at 3000 rpm, 30 s at 8000 rpm) with intermediate and final backing (5 min at 160°C). In order to ensure conductivity of the substrate we make use of a conductive polymer that can be spin-coated and dissolves in water (Espacer, Showa Denko, spin-coated at 5000 rpm for 1min, no baking). It is as well possible to use

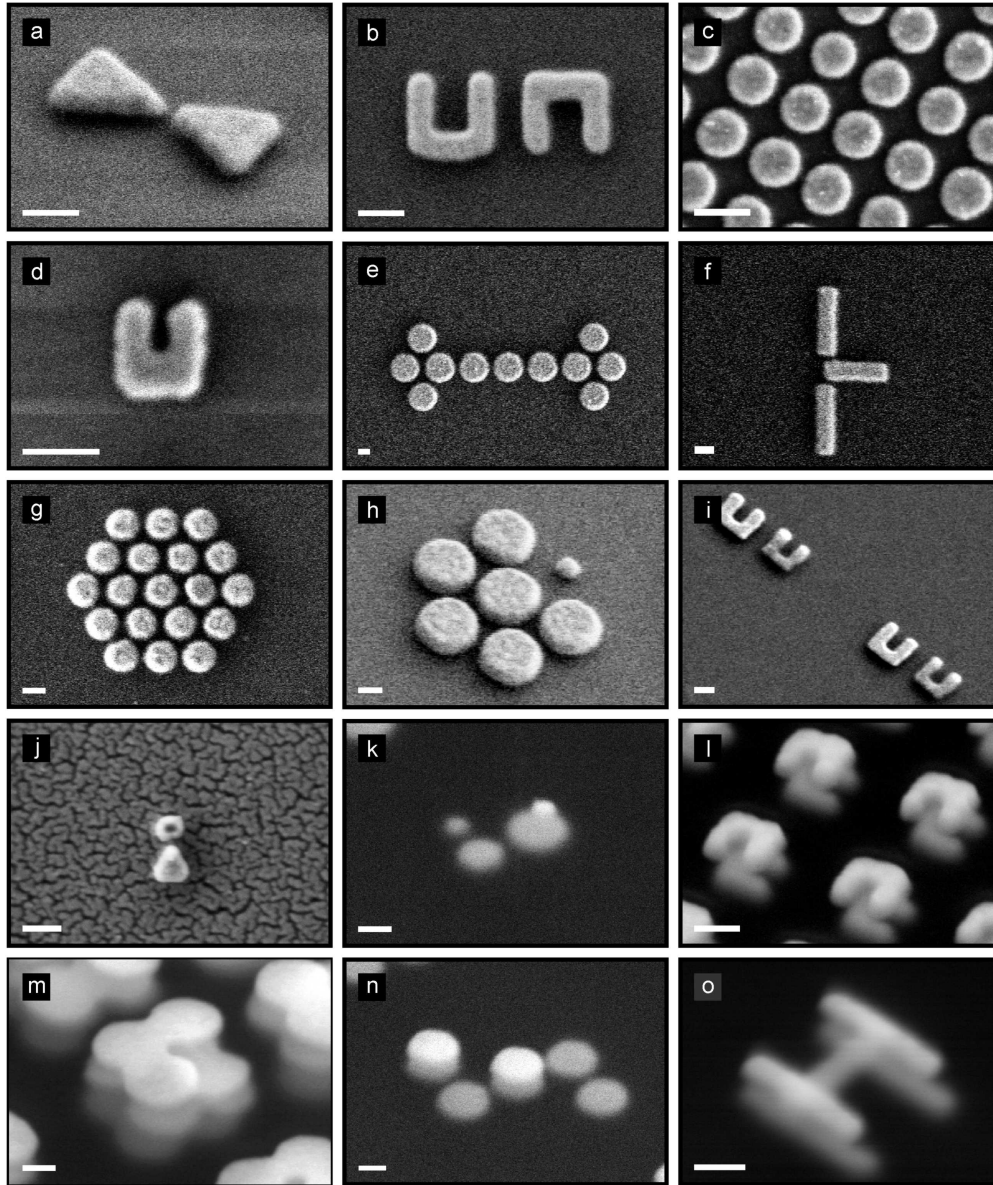


Figure 2.1.: Collection of SEM micrographs of structures fabricated by electron beam lithography. All scale bars are 100 nm. Panels (a) to (j) depict planar structures, panels (k) to (o) are stacked quasi-three dimensional structures. (a) Bowtie nanoantenna [88] (b) Split ring resonator dimer (c) Densely packed array of gold dots (d) Split ring resonator (e) Complex plasmonic oligomer [78] (f) Three coupled plasmonic dipoles (g) Complex plasmonic oligomer (h) Hepatmer with defect [89] (i) Split ring resonator material heterodimer (made from gold and aluminium) (j) Antenna structure for nanoantenna enhanced sensing (material heterodimer of gold and palladium) [29] (k) Chiral structure consisting of four different sized dots [90] (l) Twisted split ring resonators (m) Four-layered structure of twisted L-shapes [91] (n) Complex chiral plasmonic structure (o) Three-layered plasmonic analogue of double electromagnetically induced transparency. [92]

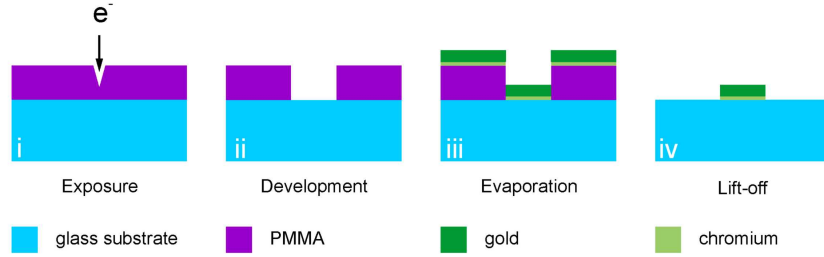


Figure 2.2.: Single layer electron-beam lithography processing. The main fabrication steps involve the actual exposure of a double layered PMMA resist, development, metal evaporation, and lift-off. For details please refer to the main text.

substrate coated with a thin film (~ 10 nm, deposited by the Institut für Bildschirmtechnik) of indium tin oxide (ITO). Judging from experience, the results are overall of higher quality, however, the high refractive index of the ITO (~ 1.76 at 850 nm) is not beneficial for the plasmonic performance of the nanostructures due to the associated resonance red-shift. As a third possibility chromium can be evaporated on top of the resist layer ($\sim 2-5$ nm), yet being rather time consuming. The chromium can be dissolved with commercial chromium etching solutions, making it, however, incompatible with a number of processes. The sample is afterwards exposed (Raith e Line, 20 kV acceleration voltage, $20 \mu\text{m}$ aperture (~ 130 pA current), curved elements step size 6 nm, curved elements dose $325 \mu\text{C}/\text{cm}^2$, area step size 6 nm, area dose $325 \mu\text{C}/\text{cm}^2$, line step size 2 nm, line dose 1500 pC/cm, settling time 1 ms, write field size $100 \times 100 \mu\text{m}^2$; these values are subject to change and are only supposed to give a rough idea). After removal of the conductive layer (either the Spacer or the chromium) the samples are developed for 90 s in a MIBK solution (Methyl isobutyl ketone, diluted 1:5 in isopropanol), the development is stopped by placing the sample for 30 s in isopropanol. Evaporation of typically a chromium adhesion layer and the gold film is performed by thermal evaporation. The remaining resist and metal films are removed in a lift-off process (commercial remover based on NEP (N-Ethyl-2-pyrrolidone), Allresist, 65°C , 2 h).

2.3. Multi-Layer Fabrication

Figure 2.3 depicts the main steps of multi layer processing for the fabrication of quasi three dimensional structures. In order to prevent the structures of different layers to be in ohmic contact and to be able to tailor the vertical distance between these layers, spin-coatable dielectrics are utilized (PC403, JCR or IC1-200, Futurex). The substrate is first coated with a dielectric spacer layer. The reason is twofold: Firstly, the refractive index of the polymers are slightly different than the one of glass ($n_{PC403} = 1.55$, $n_{glass} = 1.5$). Secondly, experience has shown that the exposure parameters slightly vary depending

whether or not the spacer layer is present, which might lead to different results for the first and second layers. After spincoating of the first spacer layer (PC403: 5 s at 2000 rpm, 20 s at 4000 rpm, pre-bake by increase of the baking temperature from 90°C to 130°C, hard-bake 30 min at 180°C) the first layer is exposed. A second spacer layer is applied. In most cases it is crucial to ensure the ideal coupling distance between the individual layers. This distance can be varied by varying the spacer layer thickness. The thickness is mainly determined by two factors, which are the dilution of the polymer in the solvent and the rotation speed during spin-coating. Adjusting both parameters, and cross checking the results using a profilometer, allows for a reproducible tuning. In order for the second layer to be positioned correctly with respect to the first layer, the exact coordinate system of the first layer has to be re-found. However, this requires the alignment of three independent coordinate systems: The system in which the laser interferometer stage is moving, the coordinate system in which the electron beam is deflected, and the sample coordinate system. All these coordinate systems might have shifts in the origin and exhibit angles between the main axes. Additionally, the electron beam needs to be calibrated in magnification with respect to the length on the sample surface. Note that the only reliable coordinate system is the one in which the laser stage moves, thus it is the reference of all others. The procedure is now roughly as follows: The electron beam is adjusted using the stage, ideally rendering both coordinate systems identical. Now, the beam can be used to align the sample coordinate system, which afterwards is ideally identical to the stage coordinate system. However, experience has shown that this procedure is not reliable enough, mainly due to the inability of the systems to reliably align stage and sample coordinate system down the required accuracy of 10 nm. Therefore, we make use of a two-step marker system. Firstly, large markers are used to determine the sample coordinate system, with a maximum error of 500 nm. Figure 2.4 (a) and (b) shows SEM micrographs of these cross-shaped marks and (d) depicts an optical micrograph showing the individual write fields surrounded by the large alignment marks. Each writing field is now equipped with inter-write-field alignment marks, see figure 2.4 (c). The stage moves to the designated write field and is not moved anymore before the exposure. Now, the inter-write-field alignment marks are scanned, aligning the beam coordinate system with the sample coordinate system. Note, there might be a misalignment between stage and sample, however, as the stage does not move anymore before exposure, this is of no concern. Thus, we have eliminated the need of aligning all three systems perfectly. Beam and sample, however, can be aligned nearly perfectly by scanning the inter-write-field alignment marks. The accuracy of the alignment between stage and sample coordinate system only needs to be good enough to find the inter-write-field alignment marks (in the order of a few 100 nm). The second layer is now exposed, developed, evaporated, and lift-off. A final PC403 layer is applied. For additional layers, the procedure is repeated until the desired number of layers is reached.

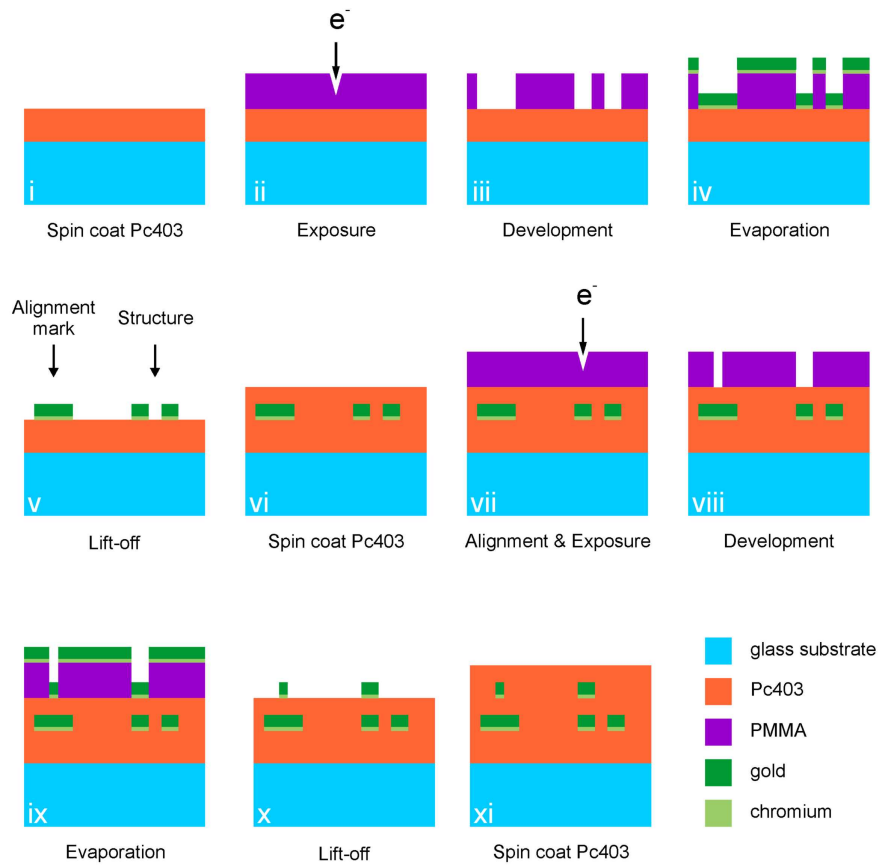


Figure 2.3.: Multi layer electron-beam lithography processing. The main fabrication steps involve the application of a spacer layer (here PC403), exposure of a double layered PMMA resist, development, metal evaporation, and lift-off, application of a spacer layer, repetition of exposure, development, metal evaporation, lift-off, and application of a final spacer layer. For details please refer to the main text.

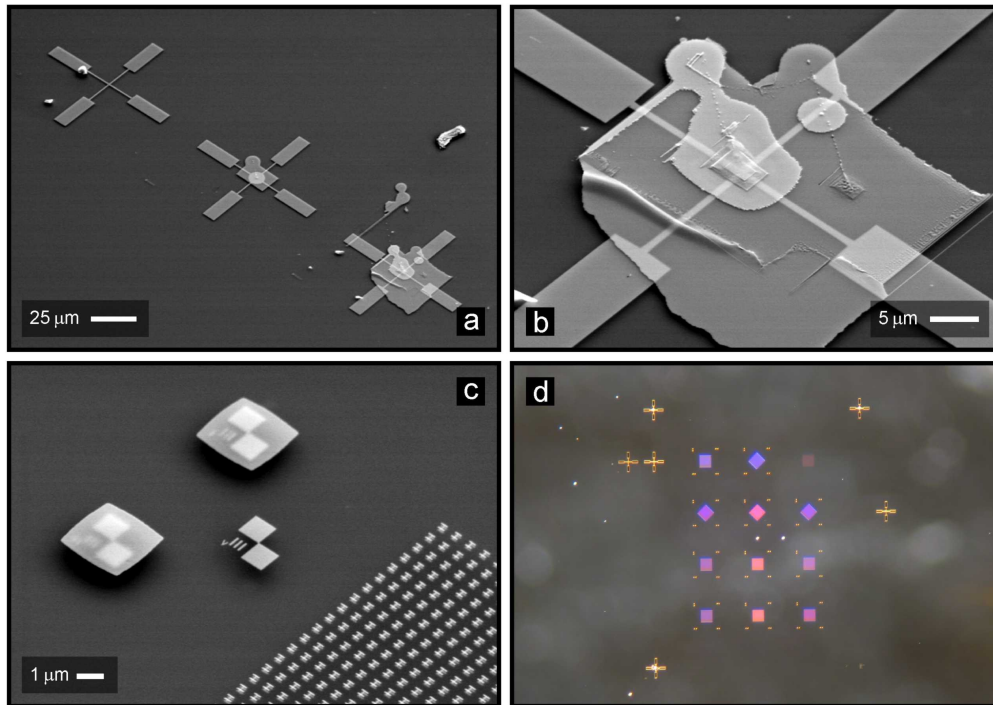


Figure 2.4.: SEM and optical micrographs depicting the alignment marks used for multi layer processing: (a) & (b) Large markers are used to roughly align the stage and sample coordinate systems. (c) Each write-field is equipped with inter-write-field alignment marks enabling the alignment of the electron beam and sample coordinate systems, eliminating the need for a perfect alignment with respect to the stage. Two marks have been used for the exposure of the second and third layer and are therefore covered by a layer of gold. A third one as not been used and shows its double squared shape. The smaller structures on the right hand side are the actual three-layered nanostructures. (d) Optical overview micrograph showing the individual write fields with the inter-write field alignment marks (the small features in the corners) as well as the large markers arranged around the write fields.

3. Plasmonic Oligomers

3.1. Plasmon Hybridization & Plasmon Coupling in Simple Geometries

If two or more metallic nanoparticles are brought into close proximity to one another, the optical spectra of the composite structure can be radically altered. An intuitive and straightforward concept of understanding the optical properties and deriving, at least to first order, the resulting plasmonic modes is plasmon hybridization [65]. Figure 3.1 depicts the plasmon hybridization scheme for a nanoparticle dimer consisting of two equally sized metallic nanorods. When brought into close proximity, the energetically degenerate modes of the two individual nanorods mix and hybridize giving rise to two new hybrid modes. One mode shows a parallel orientation of the dipole moments and is termed the symmetric mode. This mode is lowered in resonance energy due to the attractive interaction between the two induced dipole moments in the nanorods. The other mode displays an antiparallel alignment of the dipole moments, thus being termed the asymmetric mode. As the induced dipole moments repel each other, the mode is raised in resonance energy. If the two particles are identical, only the symmetric mode will be visible in the optical spectrum. In contrast to this mode, the asymmetric one retains no dipole moment and is thus not optically excitable. Such modes are termed dark modes, in contrast to bright modes. Note, however, that dark modes as well do not radiate into the far-field, which significantly increases the life time of the resonance and thus reduces its line width to the contributions of intrinsic damping, such as ohmic losses [93].

Thus, when studying the gap-dependent optical response of such a dimer, as shown in figure 3.2, the spectrum will always, independent of the gap size, exhibit a single resonance (when disregarding higher order modes). In case of well separated particles no coupling takes place and the individual modes are excited and will, as they are energetically degenerate, manifest themselves as a single resonance. When approaching the particles, the coupling strength will increase, increasing the energetical separation between the newly formed hybrid modes. However, still only one mode is visible, being the symmetric one. This mode will red-shift for decreasing gap size, which is particularly obvious for the structures with the smallest gap sizes. In the experiment shown in figure 3.2, already the structure with the largest gap exhibits significant near-field coupling,

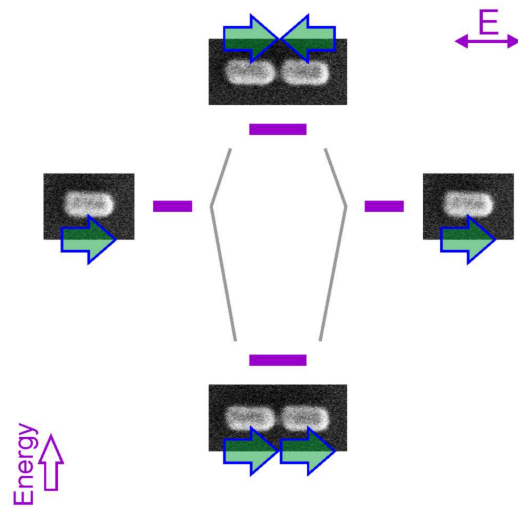


Figure 3.1.: Plasmon hybridization scheme for a nanoparticle dimer. When brought into close proximity, the energetically degenerate modes of the two individual nanorods mix and hybridize giving rise to two new hybrid modes. One mode shows a parallel orientation of the dipole moments, termed the symmetric mode, the other exhibits an antiparallel alignment, thus being termed the asymmetric mode. Due to attractive interaction between the induced dipoles the symmetric mode is lowered in resonance energy, the asymmetric is raised due to repulsive interaction.

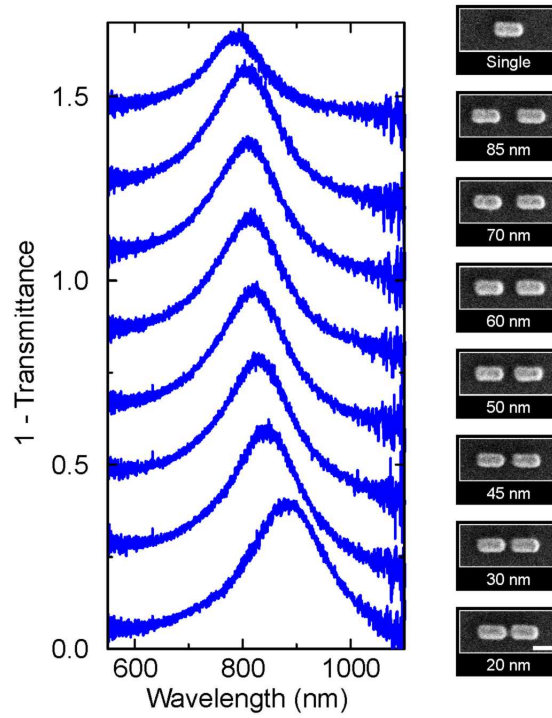


Figure 3.2.: Gap-size dependent experimental 1-transmittance spectra for a arrays of plasmonic nano-rod dimers. When successively decreasing the separation, the coupling strength increases, leading to a significant red-shift of the observed symmetric hybrid plasmon mode. The antisymmetric mode does not manifest itself optically as it retains no resonance dipole-moment. The spectra are shifted upwards for clarity. The scale bar is 100 nm.

which can be seen as the resonance is re-shifted compared to the single rod. Note, that the resonance amplitude has roughly doubled, as two particles are present.

For the experimental observation of the asymmetric mode, one needs to break either the energetical and dipole moment degeneracy of the two initial modes, that is to construct a heterodimer [94], or utilize total internal reflection excitation, similarly to the excitation of dark surface plasmon modes [95].

The plasmon hybridization scheme is not restricted to simple geometries such as plasmonic dimers, but can as well be utilized for more complex structures, where the resulting modes might no longer be as intuitive [80, 85, 96].

Figure 3.3 depicts experimental results for a more complex structure, that is, a chain of individual nanoparticles with increasing length. Each of the particles supports two energetically degenerate plasmon modes within the sample plan. A third mode is supported vertically inside the particle, which is, however, strongly blue-shifted in comparison and can thus be disregarded. When bringing the particles into close proximity collective modes will form, depending on the length of the chain. Again, the symmetric mode is the only one which is optically excitable. Note, that the chains theoretically support a number of modes. Apart from the symmetric one, the dipole moments can alternate along the chain. However, most of these modes are optically inactive as they do not retain a dipole moment. When increasing the length of the particle chain the excitable mode for excitation along the particle chain (right column) will red-shift due to an increased number of attractively interacting dipoles, see mode sketch at the bottom of the Figure. The red-shift is nicely visible in the experimental spectra. However, approximately starting from a chain length of ten particles, the resonance does no longer red-shift by addition of another particle, only the modulation of the resonance increases. This behaviour indicates that the "coupling length" of plasmonic near-field coupling is limited. At one point, the particles at both ends will no longer communicate, adding another particle at one end will not alter the spectral properties anymore, other than increasing the overall dipole moment of the resonance. This behaviour has recently been studied in detail for self-assembled particle chains from monomers to hexamers by another group, indicating the same behaviour [97]. However, the saturation has only been observed in theory and simulation. In the experiment only the onset of saturation is visible as the particle chains reach a maximum length of six particles. When exciting the particle chain perpendicular to its axis (right column of figure 3.3) the spectra show less dependence on the chain length. The mode excited is again a dipolar one, however, now the dipole moments within the particles are aligned in parallel, leading to a repulsive interaction. Thus, the plasmon mode will undergo a blue-shift, which, however, is much less pronounced.

A straightforward idea for a modification of the above experiment is shown in figure 3.4. Here, the chain has been "bend up" to a circle, infinitely continuing the chain. On first sight it is obvious that the spectral behaviour is significantly different for all

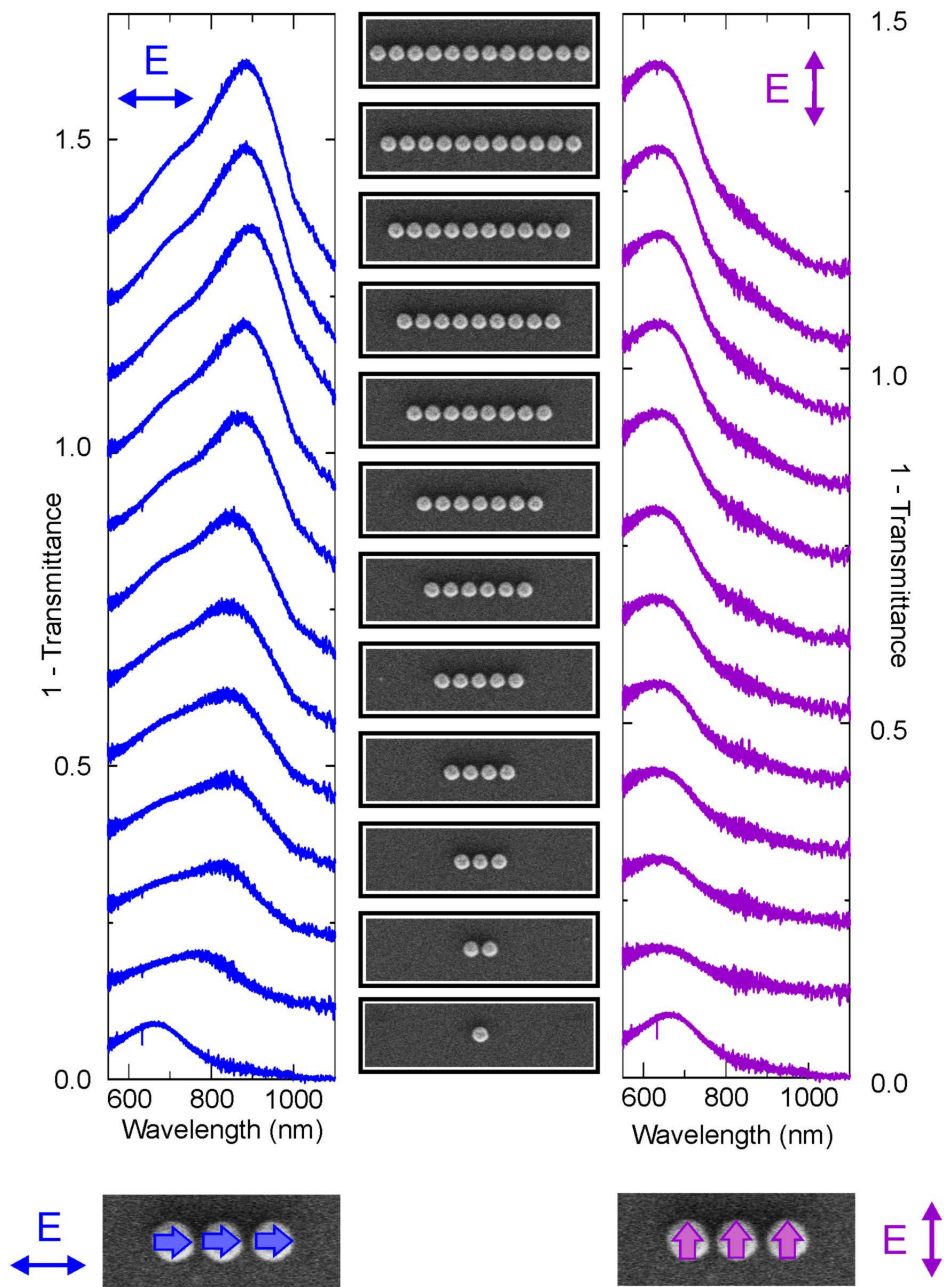


Figure 3.3.: Experimental 1-transmittance spectra for arrays of particle chains of increasing length from one to twelve particles, for excitation along (left column) and perpendicular (right column) to the chain axis. The results demonstrate that plasmonic near-field coupling shows a maximum interaction length as the red-shift of the dipolar modes saturates starting from a chain length of ten particles. Literally speaking, the particles at the two chain ends do no longer communicate with one another, thus it is of no consequence whether or not another particle is added, only the modulation depth increases due to increased dipolemoment.

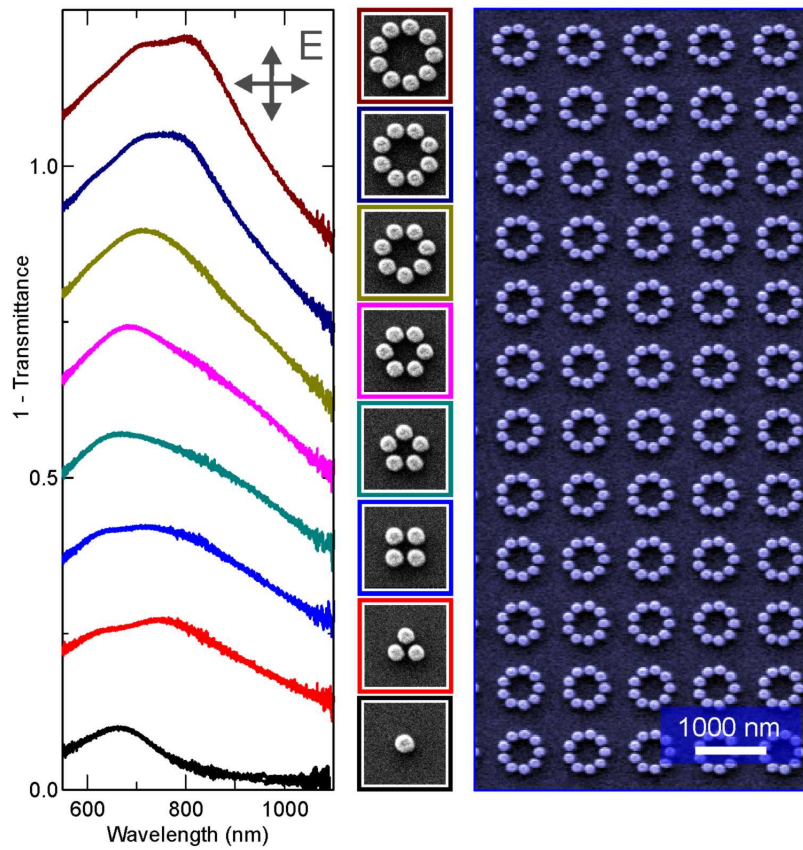


Figure 3.4.: Experimental 1-transmittance spectra for arrays of nanoparticle rings with increasing length (unpolarized excitation). In contrast to the particle chains no saturation effects can be observed. The reason is the poor match of the symmetry of the excitation with the high rotational symmetry of the rings.

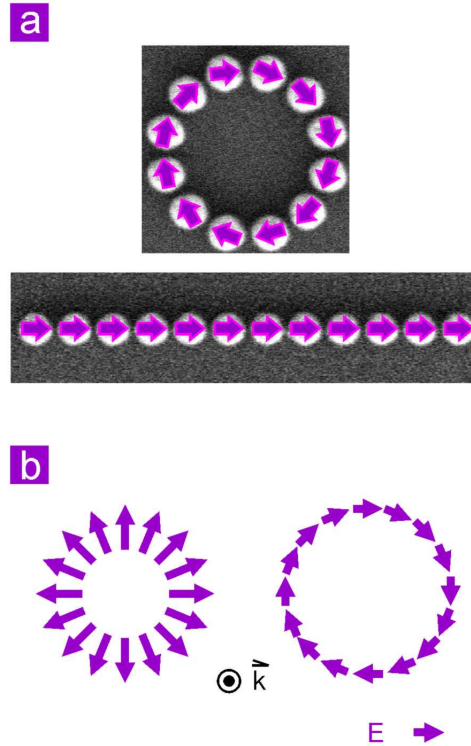


Figure 3.5.: (a) The energetic ground state of the circularly arranged particles and the particle chain is a head-to-tail orientation of the individual dipoles. However, in contrast to the chain mode, the mode of ring structure can not be excited by linearly polarized light. (b) Representation of so-called cylindrical vector beams. One distinguishes two cases: For radially polarized light the electric field is pointing radially outwards (or inwards, respectively). For azimuthally polarized light electric field direction is lying on a circle.

shown structures, no saturation effects can be observed. In principle is not surprising as the modes excited in the structure are defined by the geometrical arrangement of the particles as well as by the symmetry of the exciting light field. In the limit of an infinitely large circle, the circle will appear to consist of four chains of particles and only in this case, saturation is to be expected. For smaller circles the mode will depend on the relative orientation of the "local chain axis" with respect to the external light field. Thus, by increasing the number of particles, the near-field distribution will change. The behaviour of such rings has been studied in a recent publication, with the authors reporting very similar results [98].

The previous experiment shows that the excitation should match the structure in order to observe best coupling. Figure 3.5 (a) depicts such a scenario. The energetical ground state of the particle chain is the symmetric mode in which all dipole moments are aligned in a head-to-tail sequence. Fundamentally, this is the reason for the fast saturation of

the mode under increase of the chain length. For the circular arrangement the energetic ground state is as well the head-to-tail configuration. However, this mode does not retain any dipole moment and will thus not be excited. In order to excite the ground state of the circular arrangement one can make use of so-called cylindrical vector beams [99–103], which were utilized in plasmonics [104,105], and are a key component for STED (stimulated emission and depletion) microscopy [106]. In the focus of such the beam, the state of light polarization is a function of position. One distinguishes two cases, radially and azimuthally polarized light fields, cf. Figure 3.5 (b). In the first case the electric field is pointing radially outwards (or inwards, respectively), in the latter the electric field direction is lying on a circle. The azimuthally polarized light beam will excite the fundamental mode of the ring, whereas the radially polarized light field will excite the energetically highest dipolar mode (all dipole will repel each other, disregarding higher order modes in the individual disks, such as quadrupolar excitations). Therefore, the optical response of the circular structures should saturate much faster under excitation with these light fields, similarly to the excitation of the particle chains with linearly polarized light.

As discussed earlier, the observation of the antisymmetric mode in a plasmonic dimer requires lifting the energetically degeneracy of the two initial mode, and in particular different dipole strength, such that the antisymmetric mode retains dipole strength. Several possibilities can be envisioned. One particular intriguing one is the use of different materials and construct a material heterodimer. In particular in chemical synthesis it is extremely challenging to assembly particles of different materials, and only very recently first results have been reported [107]. However, other fabrication techniques allow to manufacture such structures [108,109], for multi-layer electron beam lithography the usage of different materials is even straightforward. Figure 3.6 depicts the experimental results for split ring resonator (SRR) dimers with various relative orientations made from gold (left column) and made of gold and aluminium (right column). When inspecting the gold-gold structures one only observes a single resonance. In all cases the antisymmetric mode retains no dipole moment and can not be observed optically. The different energetical positions of the resonances are linked to the different coupling strength and mechanisms with sensitively depend on the relative orientation of the SRRs. However, the detailed analysis of this behaviour has been studied in detail earlier and is beyond the scope of this section [96,110,111].

Due to the significantly lower density and atomic number of aluminium its secondary electron emission is drastically lower than for gold. Hence, the tilted and normal view SEM micrographs depicted in figure 3.6 show an excellently visible contrast between the two materials, revealing the structure of the material heterodimers. Note that the structures are nominally of same size, the apparent size difference most likely stems from different penetration depths of the primary electron beam in the SEM. The optical spectra clearly exhibit two resonances, the energetically lower one originates from the symmetric, the higher one from the antisymmetric mode. In using structures of similar size, yet made from materials with different plasma frequencies, the energetically degen-

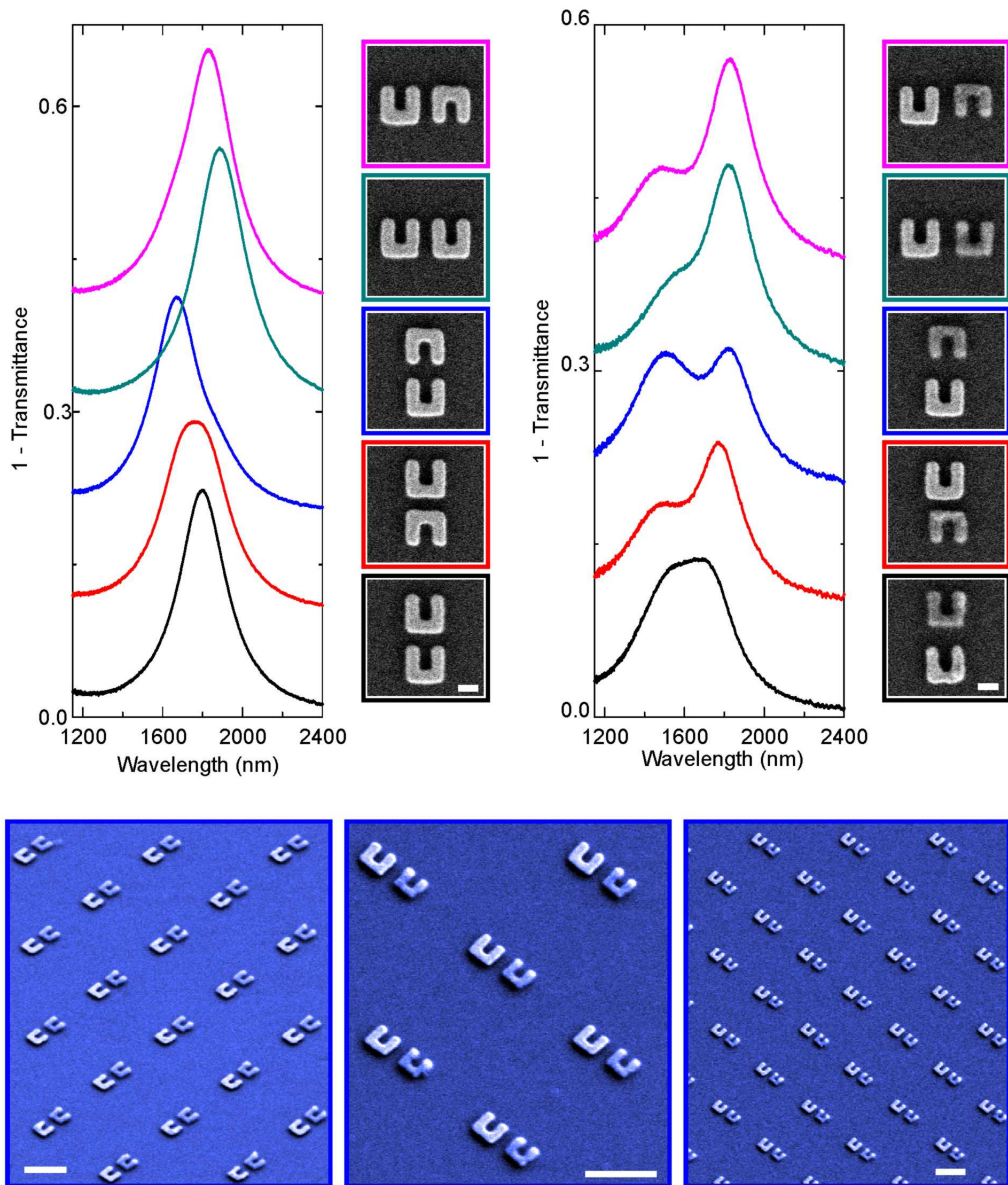


Figure 3.6.: Experimental spectra and SEM micrographs of SRR dimers, made from gold (left column) and made from gold and aluminium (right column). The material heterodimers show excellent material contrast in the SEM micrographs. The spectra of the gold-gold structures only exhibit a single resonance, originating from the symmetric mode. In breaking the energetical degeneracy by using materials with similar size yet made from materials with different plasma frequencies, both modes appear in the far field spectra. The scale bars in the insets are 100 nm, for the overview 500 nm.

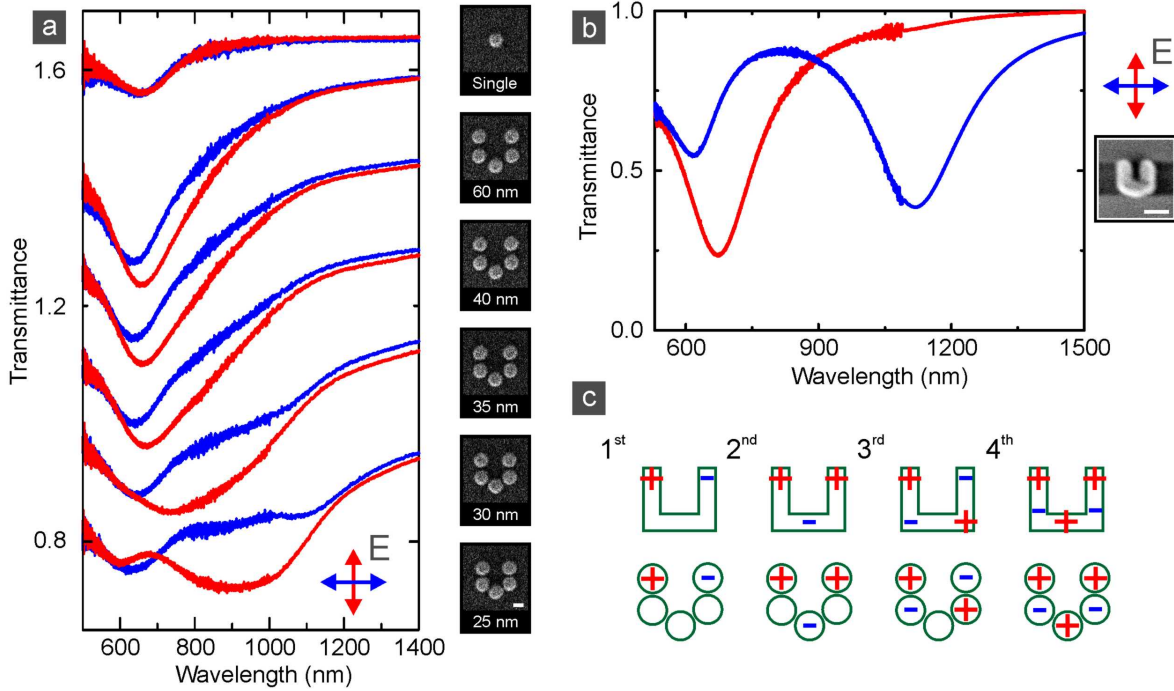


Figure 3.7.: Transmittance spectra for an open ring of nanoparticles with decreasing separation between the particles. The optical response changes dramatically with decreasing separation. For the smallest separation the optical response resembles the response of a split ring resonator, as shown in (b). (c) Sketches of the four fundamental modes of a split ring resonator and the corresponding modes of the open ring structure. The open ring structure does not support the lowest energy mode well, as no conductive coupling between the particles is present. The higher order modes, with increasing number of current nodes, in contrast are better supported. This behaviour explains the poor modulation of the first order mode in the open ring structure. The scale bars are 100 nm.

eracy of the initial modes is lifted allowing for the far-field optical observation of the symmetric and anisymmetric mode.

All so far observed collective modes, that is, modes shared between several nanoparticles, had quite similar character as the initial modes. However, coupling several nanoparticles can lead to significantly modified optical spectra, as is demonstrated in figure 3.7. Five nanoparticles are arranged in an open ring. Only a single dipolar resonance is observable for a particle separation of ~ 60 nm. It is caused by the dipolar plasmon mode of the individual disks. However, the optical response of the cluster is already anisotropic, as the spectra are not identical for horizontally and vertically polarized excitation, indicating that there is already some plasmonic coupling between the disks. When decreasing the distance further, the spectra change dramatically. A strong broadening of the resonances can be observed accompanied by the formation of several additional mode signatures. For the smallest separation of ~ 25 nm one clearly observes four plasmonic modes within

the spectral window shown, two for horizontal and two for vertical excitation. The energetically lowest mode is excited for light polarized along the opening in the ring. The second order mode, however, is excited for light polarized perpendicular to the gap, the third one again for the polarization set along the gap and the highest energy mode for excitation perpendicular to the gap.

The observed mode behaviour, in sequences of the modes and roughly as well for the modulation depth of the resonances, is well known from a split ring resonator. The spectrum and an SEM micrograph of such a split ring resonator are shown in the figure 3.7 (b). Note that only the three lowest order modes can be seen, the fourth is outside of the wavelength range, only the onset of the mode can be seen at the leftmost side. As one can see, the five particles do indeed approximate the shape of a split ring resonator. However, as no conductive connection is present between the individual nanoparticles, the coupling and formation of the split ring resonator like modes is solely enabled by the plasmonic near-fields and the associated displacement currents. This behaviour demonstrates that the optical modes of an object as complex as a split ring resonator can be constructed from individual and simple building blocks. These building blocks arranged in an appropriate fashion, will couple and form collective modes. The nanoparticle arrangement thus has properties which the individual elements do not have, thus showing true collective behaviour.

When expecting the spectra closely, one finds that the lowest energy mode of the particle ring is significantly weaker modulated than in case of the split ring resonator. This mode in a split ring resonator is characterized by a strong magnetic moment which is induced by a current flowing in the ring, see mode sketches in figure 3.7 (c). For the case at hand, this ring current is significantly decreased in magnitude as there is no real current in between the particles but only displacement currents. The higher order modes in contrast are characterized by more complex mode structures. The first order one has no current node, the second order has one, the third order two, and the fourth order mode finally has three nodes, as shown in the mode sketches. These modes are thus better approximated by the coarse geometrical approximation of a split ring resonator by only five particles. One would expect that the modulation of the first order mode will be increased when the "meshing" is increased, that is, if more particles are used to form the split ring resonator.

We would like to note that the results shown in figure 3.7 are the experimental analogue of the so-called discrete dipole approximation [112–114]. Here, one theoretically describes the response of a complex plasmonic object by replacing it with individual dipoles, for which analytical solution for its radiative properties are known. In our case these dipoles are the individual nanoparticles which as well only support dipolar modes, in contrast to the split ring resonator. In both cases, for the experiment as for the theoretical model, the results increase in quality with increasing number of dipoles.

3.2. Plasmonic Heptamers & Oligomers

The above section as demonstrated that groupings of individual metal nanoparticles can have intriguing optical properties which can be extremely different from the response of the individual building blocks. Such structures have thus been termed plasmonic molecules. In molecular physics the constitution as well as the configuration of the molecules determines their properties. In contrast to molecular physics plasmonics allows us to investigate nearly every possible arrangement of nearly arbitrarily shaped particles. One particular arrangement has stimulated a plethora, in the true sense of its meaning, of theoretical and experimental studies, the so-called plasmonic heptamer. It consists of seven particles, one in the center, the other six placed around it in a hexagonal fashion. Such a cluster supports a Fano resonance. Such a Fano resonance in general is caused by the interaction of a continuum of states with a narrow resonance. In the plasmonic case, a spectrally broad dipolar plasmonic resonance serves as the continuum of states, whereas a plasmonic dark mode, that is a mode that does not couple to external light fields, serves as the narrow resonance.

In order to investigate the evolution of the coupling behaviour in such a plasmonic heptamer, the optical response of a series of nanoparticle oligomers with various interparticle gap distances was evaluated. The interparticle gap distance g was decreased from 130 to 20 nm. For excitation of the structures, we used normal incident light with linear polarization as shown in figure 3.8. The experimental spectra of the samples and their corresponding SEM images are displayed in the same figure. The spectrum of the gold monomer is plotted as a green curve in the bottom row. A single dipolar resonance is observed around 700 nm (the curve is magnified by a factor of 5 for better comparability). Turning toward the heptamer with a large interparticle gap distance ($g = 130$ nm), the spectrum shows approximately the same behavior as the isolated nanoparticle due to the well-separated nanoparticle configuration. As the interparticle gap distance is reduced ($g = 60$ nm), a second peak starts to form around 800 nm. The two peaks are separated by a pronounced dip. As the interparticle gap distance is further reduced toward $g = 20$ nm, the spectral features red shift successively. In the ringlike hexamer ($g = 40$ nm), which we display for comparison (see the top black spectrum), the shorter-wavelength peak around 700 nm is also present. In contrast to the heptamers, no pronounced dip is visible in the hexamer. We rather observe a long and unstructured tail toward the long wavelength region.

In order to analyze the underlying physics of the observed resonant coupling transition, simulations were performed using a multiple multipole method, which is a semi-analytical simulation theory based on Mie scattering [115]. The simulated field distribution is described by a sum of distributed expansions, which are analytical solutions of Maxwell's equations, and the coefficients of the expansions are solved at the boundaries. Currently, we cannot calculate truncated cones or consider the glass substrate within our multiple multipole simulation. In the calculations, we therefore used gold nanospheres with a

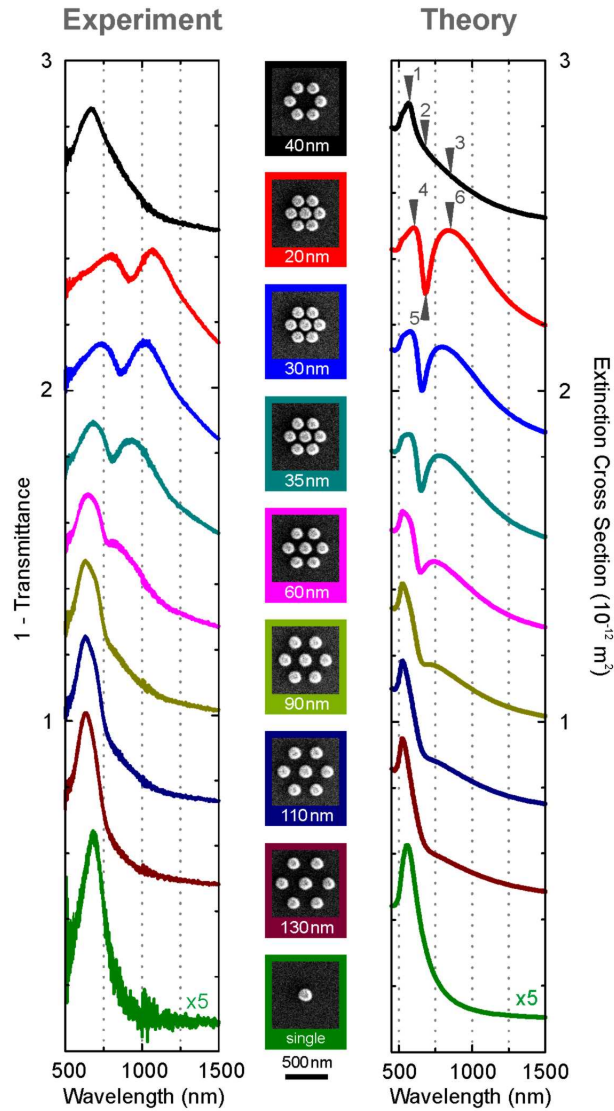


Figure 3.8.: Extinction spectra of a gold monomer, a gold hexamer, and gold heptamers with different interparticle gap separations. Spectra are shifted upward for clarity. (left column) The experimental extinction spectra. (middle column) SEM images of the corresponding samples with indicated interparticle gap distances. The scale bar dimension is 500 nm. (right column) Simulated extinction cross-section spectra using the multiple multipole method. The gold structures are embedded in air. The difference between the experimental and simulated spectra is due to the presence of the glass substrate in the experiment and it is also partially due to the assumption of a nanosphere shape for the trapezoidal nanoparticles in the simulation. In the gold monomer and hexamer, dipolar plasmon resonances are observed. The transition from isolated to collective modes is clearly visible in the different heptamers when decreasing the interparticle gap distance. Specifically, a pronounced Fano resonance is formed as characterized by the distinct resonance dip when the interparticle gap distance is below 60 nm. The presence or absence of the central nanoparticle can switch on or off the formation of the Fano resonance.

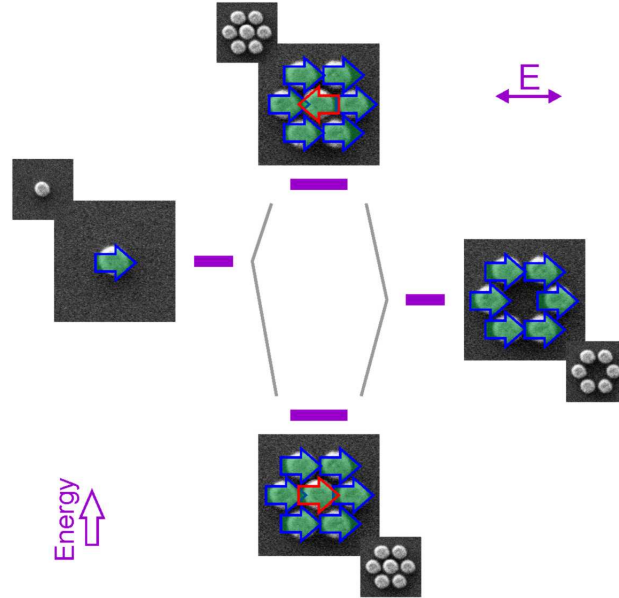


Figure 3.9.: Plasmon hybridization scheme for a heptamer. The structure can be decomposed into two distinct subsystems, namely the center particle and the outer ring. Both support a dipolar resonance each, which will mix and hybridize giving rise to two new collective modes. The symmetric mode is characterized by an extremely large dipole moment due to the in phase oscillation of seven individual dipoles, thus being termed the superradiant mode. The antisymmetric mode possesses only a very small dipole moment, in the ideal case it even vanishes completely, thus being termed the subradiant mode. Due to the huge spectral width of the superradiant mode, both modes spectrally overlap and their mutual interaction leads to the formation of a Fano resonance in the spectrum of the heptamer.

diameter of 160 nm for the central particle and 150 nm for the six satellite particles. The gold nanostructures were surrounded by air. An experimentally measured dielectric function of gold was utilized in the simulations. Figure 3.8 as well presents the simulated extinction spectra for different structures. It is apparent that the experimental results show a good qualitative agreement with the numerical predictions. The overall red shift of the experimental spectra with respect to the simulated spectra is due to the presence of the glass substrate in the experiment. The difference between the experimental and simulated results is also partially due to the assumption of a nanosphere shape for the trapezoidal nanoparticles in the simulation. Nevertheless, all the main spectral features including the distinct resonance dip are clearly predicted.

The plasmon hybridization model can again help us to understand the physics behind the observed phenomenon. From a symmetry point of view the heptamer structure can be decomposed into two separate systems. No symmetry operation allows for an interchange of the middle particle with one of the ring particles, whereas the ring particles are all degenerate as they can be transferred into one another by rotations around an axis pointing out of the surface plane. Thus, for the optical properties the ring and the middle

particle can be viewed as individual subsystems. Both these systems support dipolar type plasmonic resonances (we only need to consider these modes, as higher order modes do not retain a resonance dipole and thus do not couple to the external light field). These modes are sketched as the two initial modes of the composite heptamer in the energy level diagram in figure 3.9. As there is significant attractive interaction between the dipole moments induced in the ring, this mode is lower in resonance energy as compared to the individual particle (please note that the sketch is only schematic. In reality the dipoles will follow the ring shape of the particle arrangement and might even be split in direction in the left- and right-most particles. However, for the fundamental working principle this is of no concern.) If the two subsystems are brought together two new collective modes will form. The net-dipole moment of the ring mode can either be in parallel (that is in phase) or antiparallel (that is out of phase) with the dipole moment of the center dot. The first one is lowered in resonance energy and retains a huge resonance dipole moment as seven individual particles join together in an in phase oscillation. As a consequence, the mode couples extremely well to an external light field and hence it is spectrally very broad. Thus, the mode is termed the superradiant mode. The latter mode is raised in resonance energy and the resonance dipole moment is significantly decreased in the ideal case it the net dipole moment of the ring is even completely cancelled by the dipole moment of the middle particle. This mode is therefore termed the subradiant mode. It is spectrally narrow as its dephasing time is strongly prolonged due to its small resonance dipole moment. The superradiant mode appears as a continuum of states, whereas the subradiant mode is spectrally narrow. The superradiant mode is spectrally so broad that it will overlap with the subradiant mode, causing a Fano resonance due to their mutual interaction. This Fano resonance can be observed in the spectra of the composite heptamer as the pronounced dip in the broad extinction peak caused by the superradiant mode.

In order to gain further insight into the character of the resonances and to substantiate the intuitive picture given above, field distributions at respective spectral positions are shown in figure 3.10. In the hexamer structure, at spectral positions 1, 2, and 3, the currents in the six nanoparticles always oscillate in-phase, manifesting the excitation of the collective dipolar plasmon resonance in the ringlike hexamer. This mode is one of the initial modes and the one sketched in figure 3.9. In inspecting the current distributions (as given by the blue arrows) one sees that the sketch is indeed to schematic. Nevertheless, it catches the essence of the mode. For the heptamer structure, one observes the formation of a bright superradiant collective mode and a dark subradiant collective mode. For the superradiant mode, the oscillating plasmons in the seven nanoparticles are in-phase (see field distributions at spectral positions 4 and 6), exhibiting significant mode broadening due to radiative damping, whereas they are out of phase at spectral position 5. These simulated near-field distributions have recently been experimentally measured by scattering-type near-field optical microscopy [116].

It is worth mentioning that the peak position of the superradiant mode cannot be exactly determined from the spectrum due to the presence of the resonance dip. Nevertheless,

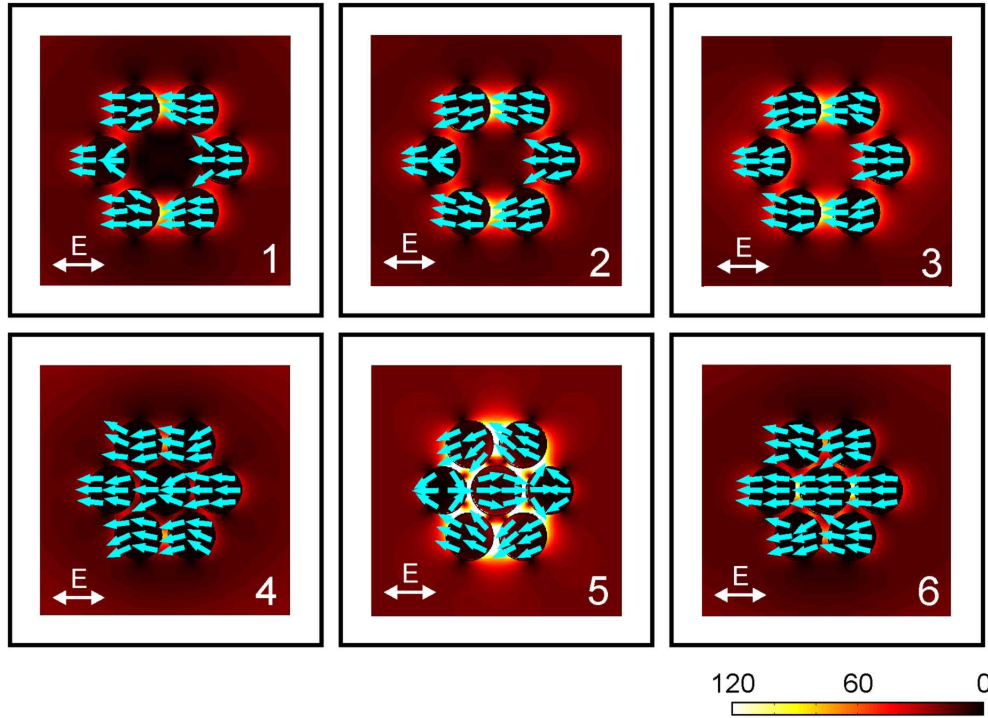


Figure 3.10.: Simulated field distributions for the gold hexamer and heptamer at the respective spectral positions (as indicated by the arrows in figure 3.9) using the multiple multipole method. The blue arrows denote the current density, the colour bar in the background displays the absolute value of the local electric field. It is notable that at spectral position 5 in the heptamer, similar yet opposite oscillating plasmons are excited in the central nanoparticle and the ringlike hexamer, thus leading to a subradiant mode. The destructive interference between the subradiant mode and the broad superradiant mode results in the Fano resonance. In the absence of the central nanoparticle, the nanoparticles in the hexamer always oscillate in phase, leading to a collective dipolar mode.

the resonant behavior at positions 4 and 6 is a good indication for the superradiant mode. For the subradiant mode, the net sum of the plasmon polarizations of the six satellite nanoparticles oscillates oppositely with respect to the plasmon polarization in the central nanoparticle (see field distribution at spectral position 5). The unique symmetry of the heptamer allows for similar yet opposite dipole moments of the central nanoparticle and the ringlike hexamer, thus leading to a narrow mode. The formation of the distinct dip in the spectrum is due to the destructive interference between the narrow subradiant mode and the broad superradiant mode, which is called a Fano resonance. Such a Fano resonance is only observable in the presence of the central nanoparticle. In other words, the central nanoparticle can be utilized to switch on and off the Fano resonance. In the weak coupling region at $g = 110$ nm, the nanoparticles are relatively well separated and the single resonance does not show an obvious spectral shift when decreasing g . At $60 \text{ nm} < g < 110$ nm, the coupling between the nanoparticles becomes stronger and the signature of the Fano resonance comes into existence. The dipolar plasmons of the central nanoparticle start to hybridize with the plasmons of the ringlike hexamer, leading to the formation of the subradiant and superradiant modes. Nevertheless, in this intermediate coupling region, the superradiant mode, which is at a shorter wavelength compared to the subradiant mode, does not have a broad enough line width to substantially overlap with the narrow subradiant mode. As a result, the Fano resonance manifests itself as an asymmetric kink at the right shoulder of the superradiant mode (for example see $g = 90$ nm). At $20 \text{ nm} < g < 60$ nm, the nanoparticles in the heptamer experience strong coupling and form collective plasmonic modes. Due to the strong in-phase plasmon oscillation in the seven nanoparticles, the superradiant mode undergoes a significant broadening and a spectral red shift, while the subradiant mode remains narrow. Consequently, the superradiant mode has a broad enough spectral profile to overlap with the subradiant mode. The conditions of the destructive interference effects are thus sufficiently fulfilled, giving rise to a more pronounced Fano resonance (for example see $g = 20$ nm). In essence, the interparticle gap distance substantially dictates the transition from isolated to collective modes and plays a crucial role for the formation of the Fano resonance in the plasmonic heptamer. It is noteworthy that the line width of the Fano resonance is essentially determined by the intrinsic damping in the metal and the net dipole moment of the subradiant mode. Reducing losses in the metal and optimizing the structural parameters to obtain a reduced net dipole moment are the keys to achieve darker Fano resonances all the way toward electromagnetically induced transparency (EIT)-like resonances. In particular, the field distribution at spectral position 5 (at the Fano dip) reveals significantly enhanced near-fields as compared to spectral positions 4 and 6 [117]. These strongly enhanced near-fields open a number of applications utilizing heptamer and oligomer structures, such as plasmonic sensing [76], SERS [118], or manipulation of the modes with dielectric particles placed inside the regions of enhanced field strength [119].

It is noteworthy, that all of the above discussion has focussed on only a fraction of the modes that are excitable in a heptamer. Each of the seven individual particles supports two energetically degenerate modes in the substrate plane (for our dots the vertical one

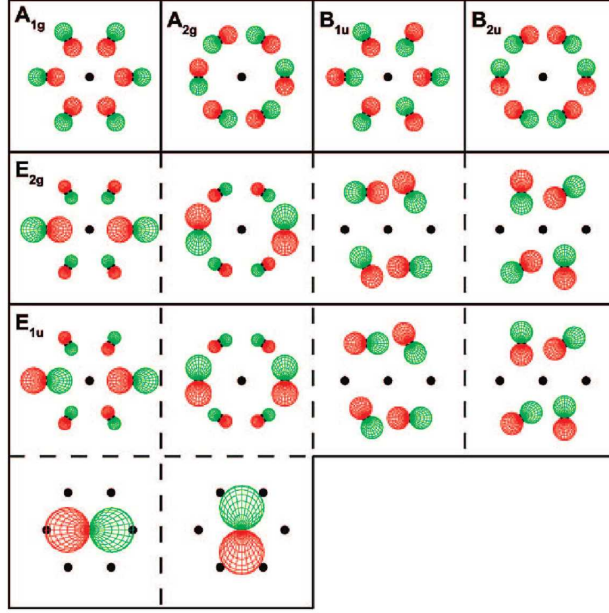


Figure 3.11.: Symmetry adapted basis functions of heptamer planar dipoles generated by using the D_{6h} point group. Only the E_{1u} panels contain modes with finite dipole moments. Adapted from reference [120].

mode is strongly blue-shifted), which should lead to a multitude of modes. However, it is already intuitively clear that quite a number of these modes do not retain dipole moments and are thus optically inactive, rendering them not interesting for experimental studies. From a theoretical standpoint they are extremely interesting and a number of theoretical publications have focused on these modes. The concept of heptamers has been introduced by Nordlander and co-workers in 2009 [120]. Already in this very first publication the modes of the cluster, or rather one of the irreducible representations of the basic mode set [121–123], were given. Figure 3.11 depicts these modes for the ring structure as well as for the central particle. The modes have been deduced considering the symmetries of the cluster (rotations by 60° , 120° , 360° , etc.). For each symmetry operation a mode can be found, as indicated by the symmetry group given in the corners of the mode images. Only a very limited number of these modes have a dipole moment and can hence directly couple to an external light field.

So far we have only considered the fully symmetric heptamer and have found that the heptamer shows truly collective behaviour. However, one can now ask oneself what is the influence of the individual nanoparticle on this collective response.

We first study the contribution of an individual nanoparticle in the outer ring to the collective behavior of a plasmonic heptamer. One of the satellite nanoparticles is successively decreased in size until it diminishes completely. The experimental extinction spectra and corresponding SEM images of the structures are shown in figure 3.12. The

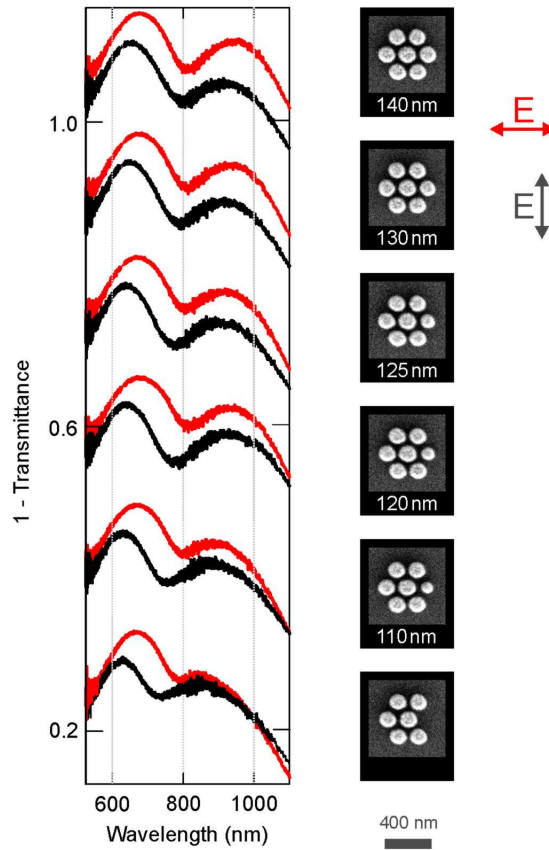


Figure 3.12.: Experimental extinction spectra of the defective heptamer structures in dependence on the defect particle size. The spectra are shifted vertically for clarity. The measured extinction spectra are characterized by red and black curves for the horizontal and vertical polarizations, respectively. Right: Normal-view SEM images of the corresponding structures with indicated defect particle sizes. The scale bar is 400 nm. A successive overall blue-shift of the spectra can be observed for both polarizations. The blue-shift in the vertical polarization is stronger than that in the horizontal polarization.

diameter of the target satellite particle is given below each SEM image. The introduction of the defect nanoparticle gives rise to the drastic reduction of the structural symmetry. The undisturbed heptamer belongs to the symmetry group D_{6h} (C_{6v} if the substrate is considered), whereas the defective heptamer is of $D_{1h} = C_{2v}$ symmetry ($C_{1v} = C_{1h} = C_s$ if considering the substrate). The defective heptamer has only one symmetry axis, which is along the center and the defect particles. The experimental extinction spectra were taken with the electric polarization parallel or perpendicular to this symmetry axis at normal incidence. In the case of the perfect plasmonic heptamer (see the topmost structure in figure 3.12), the extinction spectra for the two orthogonal polarizations are nearly identical, as is expected from the symmetry considerations. The slight deviations between the two spectra are likely due to fabrication tolerances in the experiment. The distinct dip in extinction for each polarization, i.e., the Fano resonance, is due to the destructive interference between the superradiant and subradiant modes in the plasmonic heptamer. More specifically, the dipolar plasmons in the center particle hybridize with the dipolar plasmons in the outer ring nanoparticles, giving rise to a bright superradiant and a dark subradiant mode. In the superradiant mode, all nanoparticles oscillate in phase, leading to significant spectral broadening due to strong radiative damping. In the subradiant mode, the plasmons in the outer ring nanoparticles and the center particle oscillate anti-phase. The unique symmetry of the perfect heptamer allows for similar yet opposite dipole moments in the outer ring and the center particle, hence leading to a spectrally narrow dark subradiant mode. If the super- and subradiant modes spectrally overlap, they can destructively interfere and form a Fano resonance. Its linewidth is determined by the sharpness of the subradiant mode.

By subsequently introducing the defect, i.e., decreasing the size of one satellite nanoparticle, a significant suppression of the superradiant profile linewidth is observable for both polarization directions. This behavior can be related to the reduced dipole moment of the superradiant mode due to the successive reduction of the target ring particle size. This effect is polarization independent and can hence be observed in both spectra. Additionally a blue shift of the Fano resonance can be observed. The shift for vertical polarization is stronger than for the horizontal one. In order to understand the spectral characteristics, the near-field distributions at the respective spectral positions of the structure in which the defect nanoparticle is completely absent are presented in figure 3.13. We use finite integration techniques to calculate the extinction spectra and the near-field distributions at the respective spectral positions (CST Microwave Studio, Darmstadt, Germany). The dielectric function of gold was taken from measured data [124]. In order to account for the quartz substrate in the fabricated structure, the structure is embedded in a homogeneous background material with effective refractive index $n = 1.25$. Since only in-plane modes are studied, the assumption of a homogeneous medium is justified. For vertical modes the symmetry breaking due to the quartz air interface would significantly alter the optical modes, which is not the case for laterally polarized modes. For the excitation polarization along the defect line, the near-field distributions display the horizontal mirror symmetry imposed by the geometry of the structure and closely resemble the field-distributions of the undisturbed heptamer. The removal of the

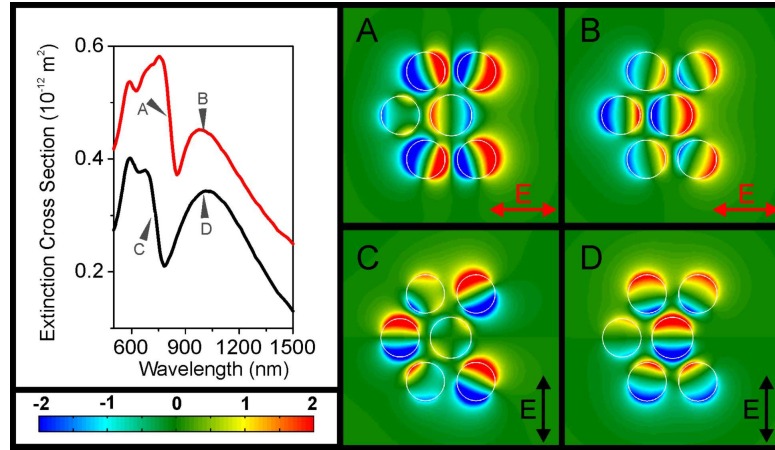


Figure 3.13.: Simulated electric-field distributions (z-component, normalized to the incoming field strength) and extinction cross-section spectra of the structure without the leftmost particle. Horizontal polarization: (A) Anti-phase plasmons are excited in the center particle and the outer particles, in close resemblance to that of the fully symmetric heptamer structure at the Fano resonance. (B) All nanoparticles oscillate in phase. Vertical polarization: (C) Quadrupolar field distributions are observed in the center nanoparticle, effectively reducing the attractive interaction and leading to the blue-shift of the Fano resonance with respect to the symmetric case. (D) All nanoparticles oscillate in phase.

ring particle leads to reduced attractive interaction, explaining the observed blue shift. As the local electric fields associated with the two ring particles along the excitation direction are weak compared to the other five nanoparticles (compare figure 3.13 (A)), the influence of its removal is minor. The observed decreased modulation depth of the Fano resonance is due to the reduced dipole moment of the ring mode upon shrinking of the defect satellite nanoparticle. In essence, removing an outer particle along the symmetry axis at this polarization does not strongly influence the formation of the Fano resonance as long as the net dipole moment of the outer ring can be effectively compensated by the dipole moment of the center nano particle. For the excitation perpendicular to the defect axis, the field distributions do not show any structural symmetry associated with this axis. Interestingly, at spectral position C quadrupolar field distributions are observed in the center nanoparticle as a result of the broken symmetry in the system. This leads to a reduction of the attractive interaction, which effectively raises the resonance energy and explains the observed strong blue-shift of the Fano resonance.

Our experiment shows that the broken symmetry crucially influences the optical response of the plasmonic heptamer. Depending on the position of the defect relative to the light polarization, the optical response of the oligomers strongly differs, validating the different roles of individual particles on the collective behavior of plasmonic aggregates.

Next, we study the influence of the number of nanoparticles in the outer ring on the optical properties of plasmonic oligomers. Figure 3.14 shows the experimental extinction

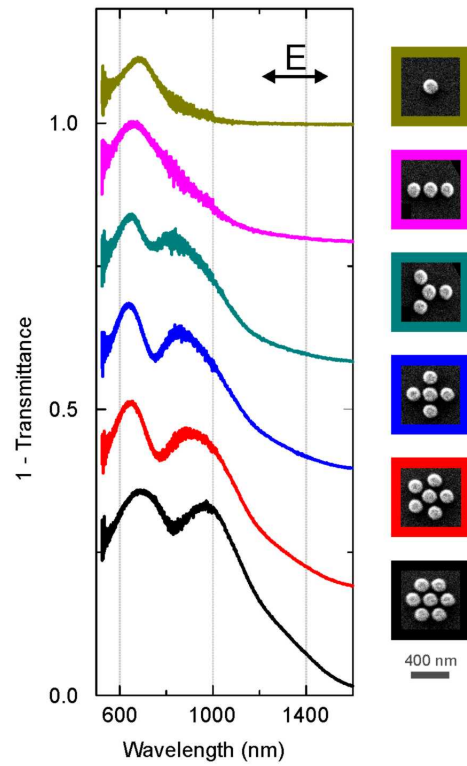


Figure 3.14.: Experimental extinction spectra of the plasmonic oligomers in dependence on the number of particles in the outer ring for horizontal polarization. The spectra are shifted vertically for clarity. Right: Corresponding SEM images. The scale bar is 400 nm. The center and ring particle diameters are 160 nm and 150 nm, respectively. The particle height is 80 nm. A Fano resonance emerges when the number of ring nanoparticles is increased to three. By further adding ring particles, its modulation depth increases and the resonance shape becomes more symmetric.

spectra and the corresponding SEM images of the plasmonic oligomers with different numbers of particles in the outer rings. The ring and center particle diameters are 150 nm and 160 nm, respectively. The number of particles in the outer ring is varied from two to six. The constituting particles are equally spaced for each structure. As a result, the inter-particle distance decreases in the outer ring when more particles are added.

In the case of the single center particle, a dipolar resonance can be excited. When adding two parallel particles to the center particle, there is still a single resonance visible which exhibits a broader linewidth due to a stronger dipole moment. When adding a third particle, the signature of a Fano resonance comes into existence. By further adding particles, the modulation depth of the Fano resonance remarkably increases together with a slight resonance red-shift. In other words, the strength of the Fano resonance can be manipulated by controlling the number of particles in the outer ring. By changing the number of particles in the ring the coupling strength between the particles becomes stronger and the overall number of interacting particles rises. Consequently the dipolar mode of the outer ring is red shifting. As a result the hybridized super- and subradiant modes formed by the red sifted ring mode and the central particle mode are red shifted as well. This readily explains the overall shift of the spectra. The red shift of the superradiant mode is stronger than the one of the subradiant mode, hence decreasing the spectral detuning between the two. This manifests itself in an increasing symmetry of the spectrum. The Fano dip is observed right in the center of the broad superradiant mode when there is no detuning. Additionally the dipole moment of the mode in the outer ring is increasing, making it comparable to the one of the center particle. Matching the dipole moments of the outer ring and the center particle is the key to generate a pronounced Fano resonance in the extinction spectrum. Evidently, by carefully designing the structural symmetry, a Fano resonance can be already established in a simple oligomer consisting of only four particles [75, 125, 126]. behaviour can be ascribed to the interaction of two doubly degenerate E-modes, belonging to the $C_{\infty v}$ symmetry of the center particle and the C_{3v} symmetry of the triangular ring, which ensures both group theoretical and geometrical compatibility.

In order to gain further insight about the formation of a Fano resonance in the quadrumer cluster we fabricated a distance dependent series. The experimental extinction spectra and corresponding SEM images are shown in the left column of figure 3.15. The ring and center particle diameters are 150 nm and 160 nm, respectively. The distance between the center particle and the ring particles is varied between 25 nm and 115 nm. For large gap sizes single-particle-like spectra are observed as the particles are not or only very weakly coupled via the near-field to one another. For a gap size of 55 nm the signature of a Fano resonance comes into existence. Its modulation depth is increasing for decreasing distance. Strikingly, the Fano resonance vanishes completely when removing the center particle from the 25 nm gap structure. The resulting trimer spectrum closely resembles an isolated particle spectrum, indicating that the particles are only very weakly coupled. The formation of a Fano resonance is hence only possible due to the coupling of the three

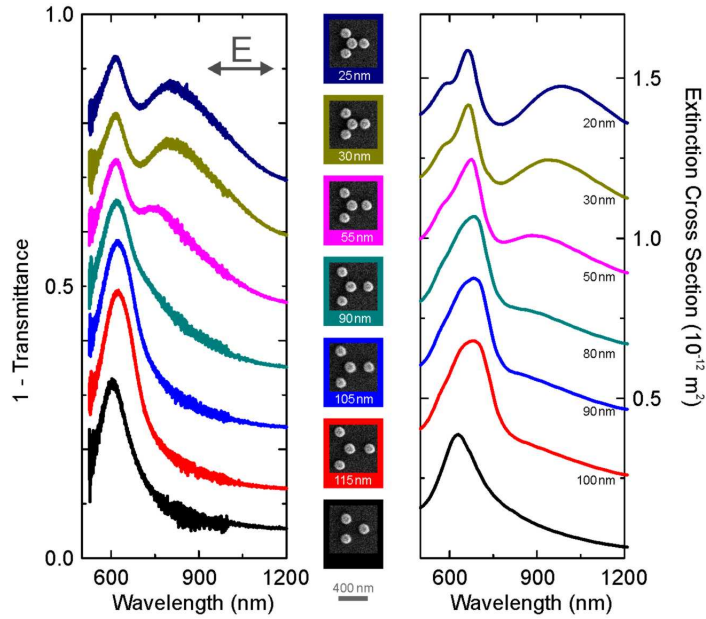


Figure 3.15.: Left column: Experimental extinction spectra of quadrumers in dependence on the interparticle separation and a reference trimer. The spectra are shifted vertically for clarity. Middle column: SEM images of the corresponding structures, the gap between ring and center particle is indicated below. For the largest distances one observes isolated particle-like spectra. Below a gap size of 55 nm (green curve) the signature of a Fano resonance is clearly observable. Its modulation depth increases with decreasing gap size. By removing the center particle the Fano resonance vanishes. Right column: Simulated spectra for the experimentally realized structures.

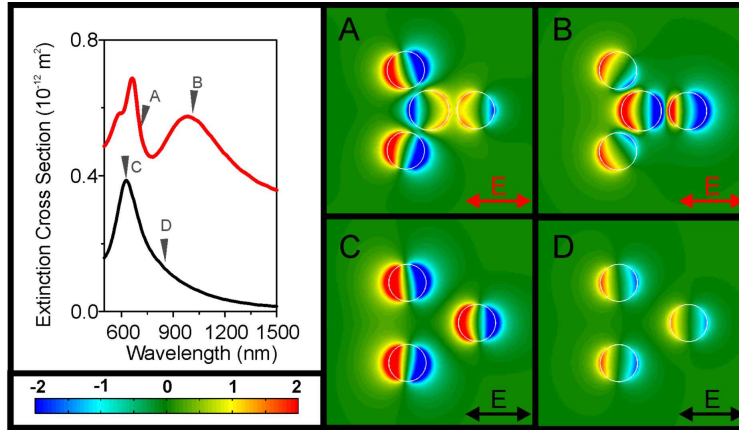


Figure 3.16.: Simulated electric-field distributions (z-component, normalized to the incoming field strength, horizontal polarization) and extinction cross-section spectra of a 20 nm gap quadrumer as well as for the trimer obtained by removing the center particle of the quadrumer. The simulated spectra agree very well with the experimentally obtained spectra of figure 3.15. (A) The field distribution shows an out of phase oscillation of the center particle and the three ring particles which is the signature of the subradiant mode. (B) All plasmons oscillate in phase. Strong coupling between the particles is observed, as is expected for the signature of the superradiant mode. (C) and (D) Only isolated plasmons are visible in the field distribution. All plasmons oscillate in phase with no observable coupling.

ring particles to the center one. The ring particles are too far apart from one another to efficiently interact via their respective near fields. This is in contrast to the heptamer structure where the six ring particles can efficiently couple to one another. Upon removal of the center particle the hexamer spectrum still shows evidence of coupling as it does not resemble a single-particle-like spectrum. The right column of figure 3.15 shows the simulated results of the experimentally realized structures. There is overall excellent agreement between simulation and experiment.

Our interpretation is confirmed by extinction cross section and electric field distribution simulations for a 20 nm gap size quadrumer as well as for a trimer which are shown in figure 3.16. For the strongly coupled quadrumer one observes a well modulated Fano resonance. The near field distribution at spectral position A shows a pronounced anti-phase oscillation of the plasmons in the ring particles with respect to the center one (subradiant mode). At the long wavelength extinction peak (spectral position B) all particles oscillate in phase as is expected for the superradiant mode. In case of the trimer all particles oscillate in phase and show only very weak mutual coupling (spectral positions C and D). These observations confirm our finding that the collective behavior of the quadrumer cluster is indeed mediated by the center particle alone. Removing it leaves isolated particles showing nearly no near field coupling.

The center nanoparticle also plays a key role in determining the resonant behavior of plasmonic oligomers. Figure 3.17 shows the experimental extinction spectra of a series

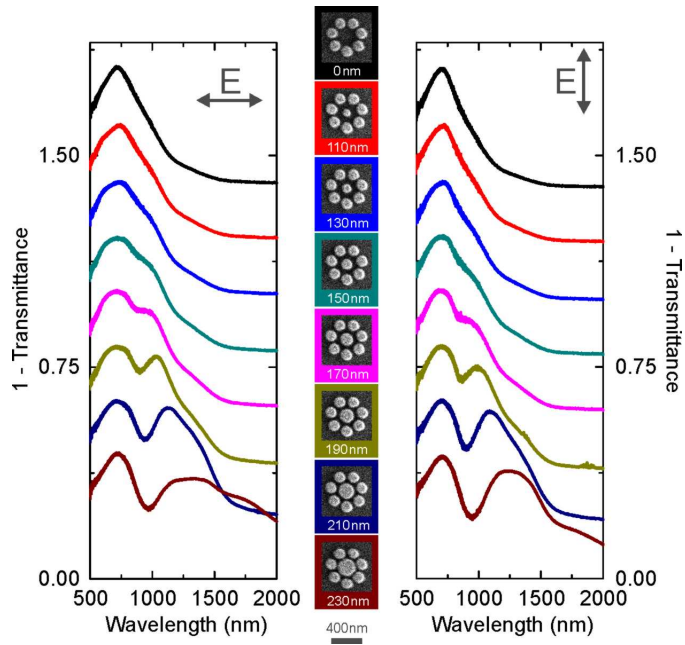


Figure 3.17.: Experimental extinction spectra of the plasmonic octamers in dependence on the center particle diameter for vertical (left column) and horizontal (right column) polarizations. The center particle diameter is indicated in the corresponding SEM images. The scale bar is 400 nm. The signature of the Fano resonance appears when the center particle diameter is increased to 150 nm. The modulation depth is improved with increasing the center particle diameter. The Fano resonance becomes more symmetric and the superradiant mode profile is significantly broadened.

of plasmonic octamers, where seven nanoparticles form the outer ring. The diameter of the center particle is subsequently enlarged from 110 nm to 230 nm as shown in the corresponding SEM images. For the octamer with a missing center particle, one can observe a broad resonance with a long and unstructured tail towards the longer-wavelength side. A Fano resonance emerges as a kink on the right spectral slope when the center particle diameter is increased to 150 nm. By further enlarging the center particle diameter, the modulation strength of the Fano resonance becomes more pronounced, and the Fano resonance gradually shifts to the red. Also, the resonance profile of the superradiant mode is significantly broadened.

In fact, by increasing the center particle diameter, several structural parameters of the octamer are changed simultaneously. First, due to the decrease of the interparticle distance, the coupling strength between the center particle and the ring particles increases, rendering the formation of the super- and subradiant modes possible. For the cases with center particle diameters smaller than 150 nm, the spectra closely resemble that of the structure without the center particle. Starting from a center particle size of about 150 nm the signature of the Fano resonance comes into existence. This behavior shows that the collective super- and subradiant modes have formed. The poor modulation depth of the Fano resonance is hence caused by dipole moment mismatch between center particle and the dipolar ring mode rather than by insufficient near field coupling. Further increasing the center particle diameter and hence its oscillator strength leads to a better match of the dipole moments. This increases the modulation depth of the Fano resonance. In contrast to the heptamer, the dipole moments are no longer matched in the octamer with equally-sized nanoparticles (see the green curve in figure 3.17). Second, the resonance position of the center particle shifts to the red due to the increase of the center nanoparticle diameter. This partially accounts for the overall red-shift of the spectrum. Additionally, the red-shift of the center particle resonance reduces the position detuning between the super- and subradiant modes, leading to a more symmetric Fano resonance in the spectrum. The strong spectral broadening is due to the significantly increased overall dipole moment of the superradiant mode upon growth of the center particle. The spectral differences between the two excitation polarizations can be attributed to fabrication tolerances.

Finally, we show that breaking the symmetry of the heptamer by displacing the center particle from its center position enables intriguing resonant behavior [120, 127, 128]. Essentially, using this scheme, one can study the consequence of symmetry breaking as well as the formation of a true defect by physically bridging the center particle and one ring particle. Figure 3.18 displays the experimental extinction spectra and 30°tilted view SEM images. The nominal displacement d is indicated below each SEM image. When the displacement is enlarged (the center nanoparticle is gradually displaced to the right, see figure 3.18), more and more center particles within an oligomer array ($100 \times 100 \mu\text{m}^2$ size) touch their adjacent ring particles.

For the incident polarization parallel to the displacement axis, a new pronounced reso-

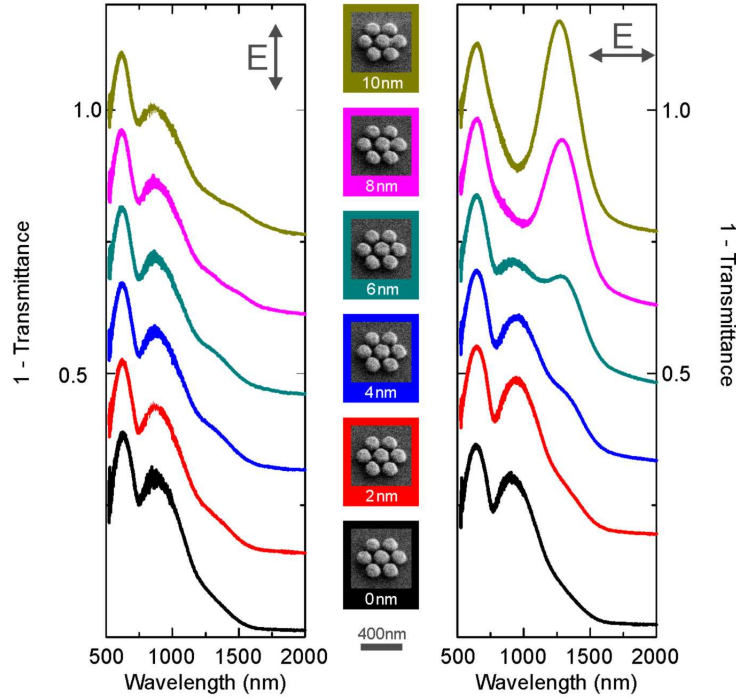


Figure 3.18.: Experimental extinction spectra of the plasmonic heptamer structures in dependence on the lateral displacement of the center nanoparticle to the right for vertical (left column) and horizontal (right column) polarizations. The nominal displacement d of the middle particle from its center position is given below the corresponding SEM images (middle column). The scale bar is 400 nm. For the horizontal polarization, a strong new resonance mode appears at a long wavelength and it gains in strength with increasing displacement. This is due to the formation of a conductive bridge between the center particle and the adjacent rightmost particle, which are clearly visible in the SEM images. The Fano resonance disappears in the process. For the vertical polarization, the overall spectra are nearly unchanged.

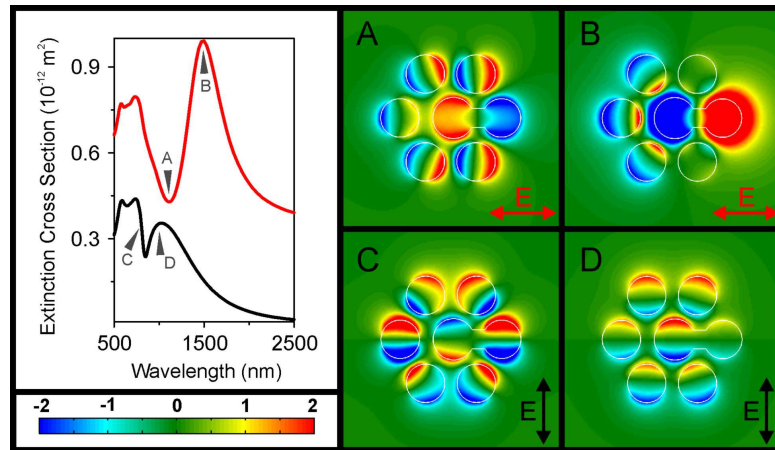


Figure 3.19.: Simulated electric-field distributions (z-component, normalized to the incoming field strength) and extinction cross-section spectra of the heptamer structure, in which the center particle is displaced by 10 nm towards the rightmost particle. Horizontal polarization: (A) Dipolar plasmons excited in the dumbbell-like structure oscillate anti-phase compared to those in the outer ring nanoparticles. Due to the strong mismatch of the resonance positions as well as the dipole moments of the dumbbell-like structures and the outer ring, the Fano resonance cannot be formed. (B) Fields are mostly confined in the dumbbell-like structure and the plasmons oscillate in-phase with those in the outer ring nanoparticles. Vertical polarizations: (C) Similar plasmon oscillations as those in a perfect heptamer at the Fano resonance are observed. (D) All particles oscillate in phase.

nance is visible at a long wavelength around 1250 nm. In order to elucidate the spectral characteristics, field distributions at the respective spectral positions are presented in figure 3.19. It is apparent that at resonance B strong dipolar plasmons are excited in the dumbbell-like structure formed by the two touching particles. The neighboring isolated particles mostly oscillate in phase. At this resonance, the spectral response is dominated by the dipolar plasmons in the dumbbell-like particle, which exhibits strong local electric fields as shown in Figure 3.19 B. The amplitude of resonance B increases with enlarging the displacement due to the fact that more and more dumbbell-like structures are formed in the array. SEM examination of the sample reveals that in the biggest displacement case (see the topmost spectrum in figure 3.18), the dumbbell-like structure is formed in nearly every heptamer in the array. The increasing displacement decreases the effective length of the dumbbell-like structure, thus giving rise to the observed blue-shift of resonance B. The Fano resonance is subsequently smeared out by this long wavelength mode and vanishes completely.

Interestingly, the field distributions at the extinction dip (see spectral position A in figure 3.19) still exhibit an anti-phase plasmon oscillation in the remaining five ring particles and the dumbbell-like defect structure. Nevertheless, due to the strong spectral position detuning and dipole moment mismatch between the defect particle and the ring particles, no Fano resonance is established in this case. In contrast, for the incident polarization perpendicular to the displacement axis, the spectra are mainly unchanged. Even though the center and ring particle touch each other, nearly identical spectral features at the original spectral positions are observed. The corresponding field distributions as shown in figure 3.19 C and D validate that the plasmon configurations are nearly the same as those of an undisturbed heptamer. Dark-field measurements based on single plasmonic heptamers will be greatly helpful to reveal the effects of the conductive bridge [129–132] by measuring individual structures with different touching junctions.

We have demonstrated the amazing tunability offered by the oligomeric design strategy. However, the concept can be further extended. The heptamer is basically the fundamental building block of a hexagonally densely packed array of particles. It is thus straightforward to enlarge the cluster by adding particles according to the hexagonal lattice.

In figure 3.20 we investigate the influence of adding a second outer particle ring to the heptamer configuration. The scanning electron micrographs show the heptamer and the two larger clusters belonging to the same symmetry group D_{6h} . We compare the measured 1-transmittance spectra (left column in figure 3.20) to calculated extinction spectra obtained with Finite Integration Techniques (right column in figure 3.20, for further technical details see Method Section).

The Fano dip in the heptamer spectrum (number of particles $N = 7$) resulting from the interference of the spectrally broad superradiant and the narrow subradiant mode is clearly visible (blue curve). The formation of the two collective modes is mediated via

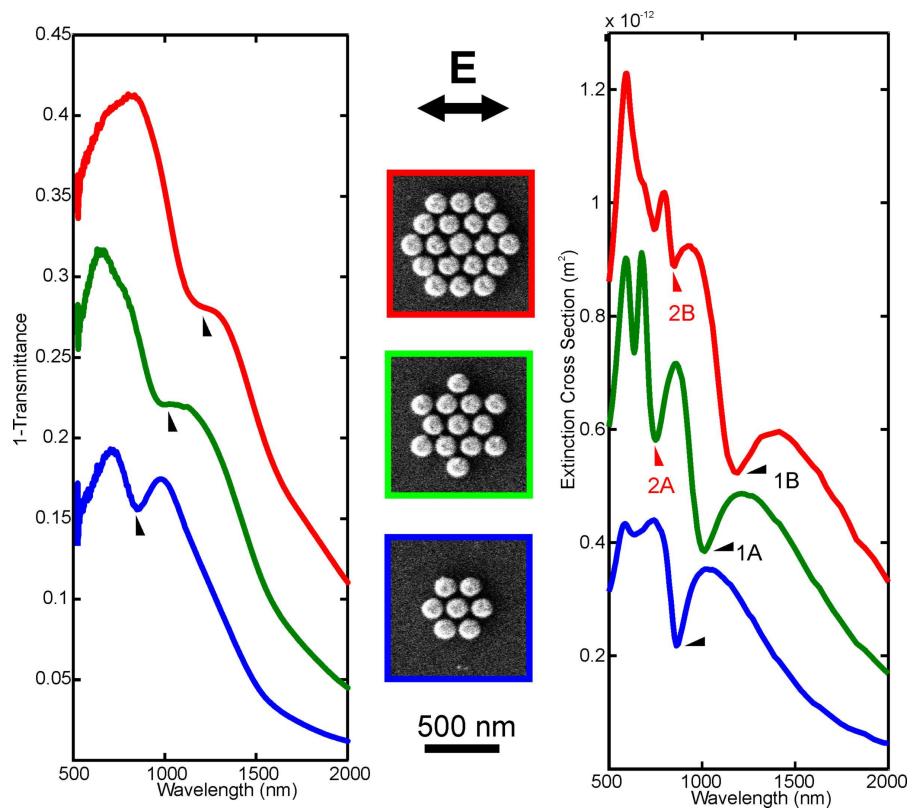


Figure 3.20.: Experimental 1-transmittance spectra (left panel) and simulated extinction spectra (right panel) of the clusters (green and red curves) compared to the spectra of a heptamer (blue curves). By adding a second ring to the heptamer the clusters support a 2nd order Fano resonance (red arrows) as well as the fundamental Fano resonance (black arrows). Only the fundamental dark mode is well modulated in the experimental spectra.

the plasmonic near-fields, leading to in-phase oscillations of the plasmonic nanoparticles (superradiant mode) and out-of-phase oscillation of center particle and ring particles (subradiant mode). With increasing number of particles in the clusters ($N = 13$ and $N = 19$) the overall dipole moment of the superradiant mode increases, resulting in an increased radiative damping and thus a spectral broadening. In the experimental spectra just one Fano dip is observable (indicated by the black arrows) which gradually shifts to lower energies for the larger clusters. This results in a spectral detuning of superradiant and subradiant modes, which is nicely confirmed by simulations.

In simulations, besides the fundamental Fano dip, a second Fano resonance is present for the $N = 13$ and $N = 19$ clusters (red arrows). A second blue-shifted subradiant mode interferes with the broad superradiant mode. The modulation depth of this resonance is low, especially in the case of the $N = 19$ cluster, which makes it impossible to observe it experimentally in our system. Only a slight kink is visible in the experiments. Using single crystalline instead of thermally evaporated gold would decrease the intrinsic damping in the material and lead to a better modulation of the Fano resonances. [133] Furthermore, decreasing the interparticle distance leads to an increased near-field coupling and hence more pronounced resonances. Recent experiments show the realization of sub-10-nm gap sizes employing new fabrication processes. [134]

In order to explain the appearance of higher-order Fano resonances [83, 135–137] in the larger clusters we plot the near-field distributions at the spectral positions of the Fano resonances in figure 3.21. We use plane-wave incidence with linear polarization as indicated by the white arrow. For the $N = 13$ and $N = 19$ clusters two ring modes are supported. Similarly to the heptamer case the particle plasmon mode of the center particle hybridizes with the ring mode of the adjacent six nanoparticles, giving rise to in-phase and out-of-phase collective modes. The outer ring, formed by the added nanoparticles, supports a second ring mode. From the electric near-field distribution at the Fano resonances we infer that hybridization of the outer ring mode with the dark mode of the heptamer configuration leads to a lower energy 1st order and higher energy 2nd order dark mode. This corresponds to in-phase oscillation (top row in figure 3.20) and out-of-phase oscillation of the two ring modes (bottom row in figure 3.21). These two dark modes are shifted to lower and higher energy, respectively, due to attractive and repulsive near-field interaction. Due to its large overall dipole moment the bright mode is spectrally very broad, hence overlapping with both supported dark modes that cause the two Fano dips.

By adding more particles to the outer ring ($N = 19$ versus $N = 13$ cluster) the 1st order and 2nd order Fano resonances shift to lower energies, since the energy of the outer ring mode is lowered due to attractive electric dipole interaction between adjacent nanoparticles. Consequently, the hybridized 1st and 2nd dark modes are lowered in energy which results in a spectral red shift. Also, the linewidth of the 1st order Fano dip increases and the modulation depth decreases for the larger cluster, which can again be understood by inspecting the field-distributions. The net dipole moment in the $N =$

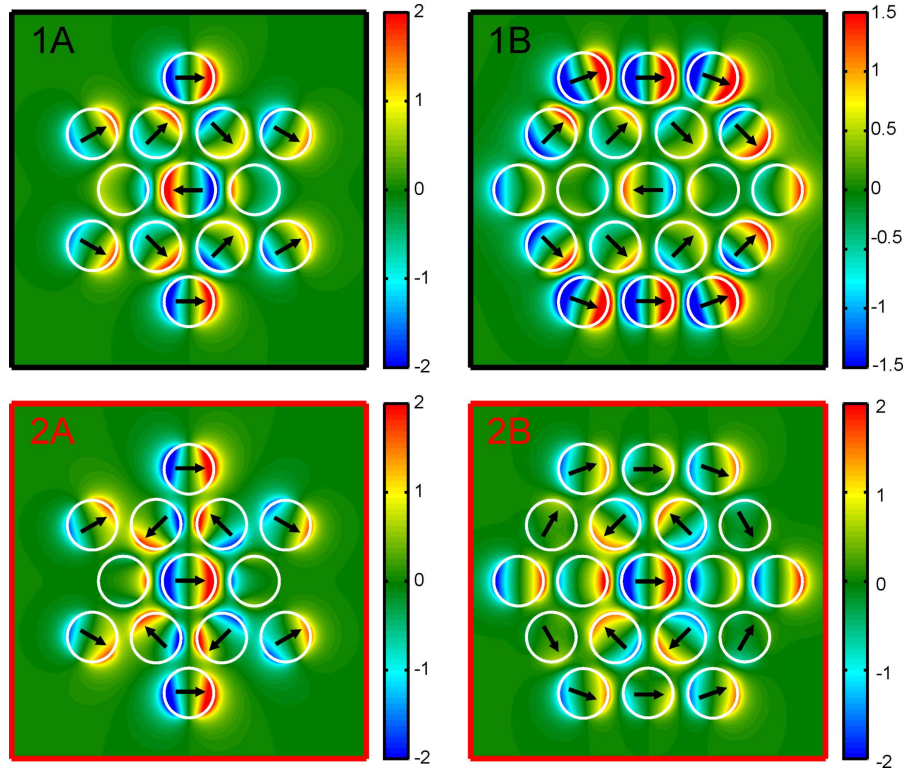


Figure 3.21.: Simulated electric near-field distribution (E-field component perpendicular to the substrate plane normalized to the amplitude of the incident plane wave) of the clusters of the fundamental dark modes (black boxes) and the 2nd order dark modes (red boxes). The spectral positions are indicated by the arrows in figure 3.20. For all cases the center particle oscillates out-of-phase with the adjacent particles building up the inner ring. For the 2nd order dark mode also the outer ring oscillates out-of-phase with respect to the inner ring which is not the case for the fundamental mode where all ring particles oscillate in-phase.

13 cluster at the 1st order Fano resonance is lower than for the $N = 19$ cluster, where the dipole moment of the in-phase oscillating ring particles dominates the out-of-phase dipole moment of the center particle.

On the high energy side of the theory spectra we observe even higher-order excitations. At these energies quadrupolar excitations in the nanoparticles become important. These modes can no longer be easily understood in the dipolar model which we employed so far.

We have seen that the addition of nanoparticles to a heptamer leads to the formation of new collective modes that modify its spectra. Another possibility to enlarge the clusters while keeping a high degree of structural symmetry is to elongate the cluster along one of its axes, or, to phrase it differently, surround a chain of center particles with a ring of outer particles. [138,139] Therefore we add 3, 6, 9, and 12 nanoparticles to the heptamer configuration, hence elongating the cluster gradually in one direction. The structures are depicted in figure 3.22. We calculate the extinction spectra for incident polarization along the two symmetry axes as shown in figure 3.22.

For incident polarization along the long axis of the cluster (blue curves), no additional Fano dip arises with increasing chain length. Surprisingly, the Fano resonance only shows minor shifts in its spectral position by elongating the cluster. Hybridization of the ring mode and the center particle chain mode leads to the formation of a superradiant mode where all particle plasmons are in-phase and a subradiant mode where the center particle plasmons are out-of-phase with respect to the ring particle plasmons (see figure 3.23). Interference of these modes leads to the asymmetric dip in the blue spectra. For the superradiant mode two spectral changes are observed for larger clusters. First, the width of the superradiant mode is significantly broadened since the sum of the dipole moments of all in-phase oscillating particle plasmons is increasing. Second, the mode shifts to lower energies as the attractive electric dipole forces increase with adding particles to the cluster.

When the incident light is polarized along the short axes of the clusters (green curves), higher-order Fano resonances are observed. In figure 3.22 we label them with arrows and denote them as 1st (black arrows), 2nd (red arrows), and 3rd (blue arrows) order. The spectral position of the same-order Fano dips is shifted to lower energies for increasing number of center particles. Compared to the perpendicular polarization the superradiant mode is not significantly broadened and no energy shift is observed, indicating that radiation damping and coupling forces in the collective bright mode are not largely altered for incident polarization along the short axes of the plasmonic oligomer clusters. It is noteworthy that an additional Fano resonance is only observed if the number of center particles is uneven. In the case of the heptamer and the cluster with 2 center particles, only one Fano dip is present, whereas for the clusters with 3 center particles a second Fano dip is formed and for 5 center particles even a third Fano dip is observed. The 1st and 2nd order dark modes are increasingly detuned from the bright mode in

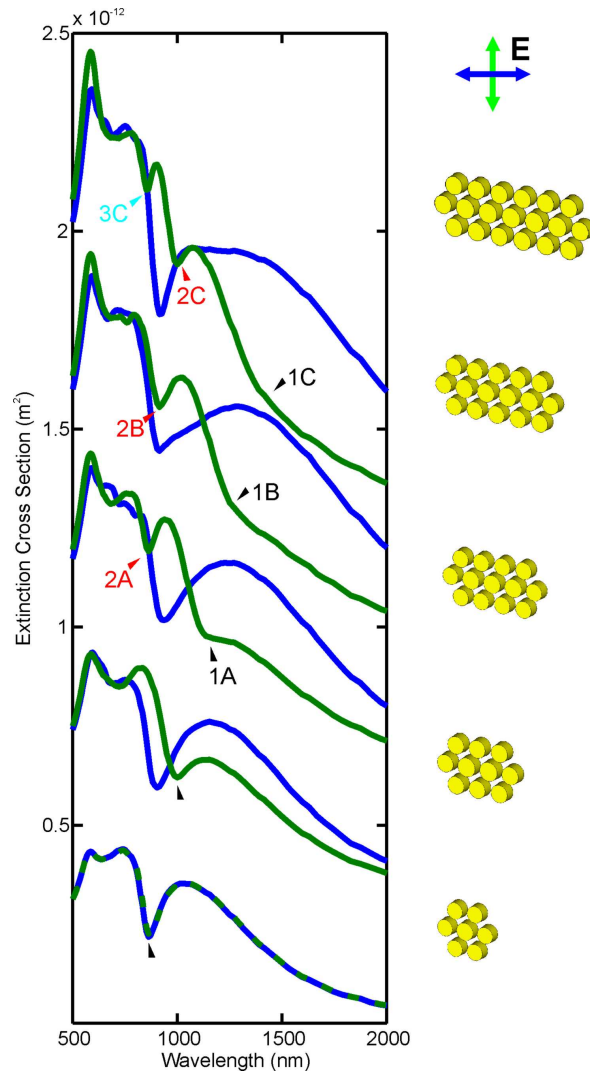


Figure 3.22.: Simulated extinction spectra of the elongated oligomers for horizontal (blue curves) and vertical (green curves) incident polarization. The spectra are shifted for clarity by an offset. For vertical polarization, with increasing number of particles the elongated oligomers support besides the fundamental dark mode (black arrows) higher-order dark modes (2^{nd} and 3^{rd} order dark modes indicated by red arrows and blue arrow respectively). Changing the polarization can switch on or off and tune the spectral position of the narrow Fano resonances. For horizontal polarization higher-order subradiant modes are not observed.

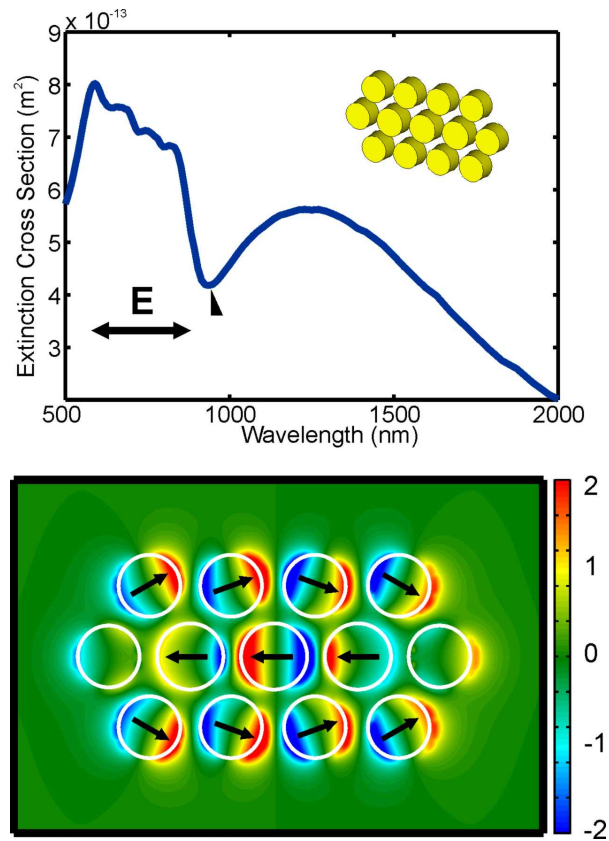


Figure 3.23.: Simulated extinction spectrum of the elongated oligomer with 3 center particles for horizontal incident polarization. The black arrow indicates the spectral position of the calculated near-field distribution at the Fano resonance. The center particle plasmons are out-of-phase with respect to the ring particle plasmons. Only the fundamental dark mode is supported for horizontal polarization. Similar field distributions are obtained at the Fano resonance for the oligomers with 2, 4, and 5 center particles.

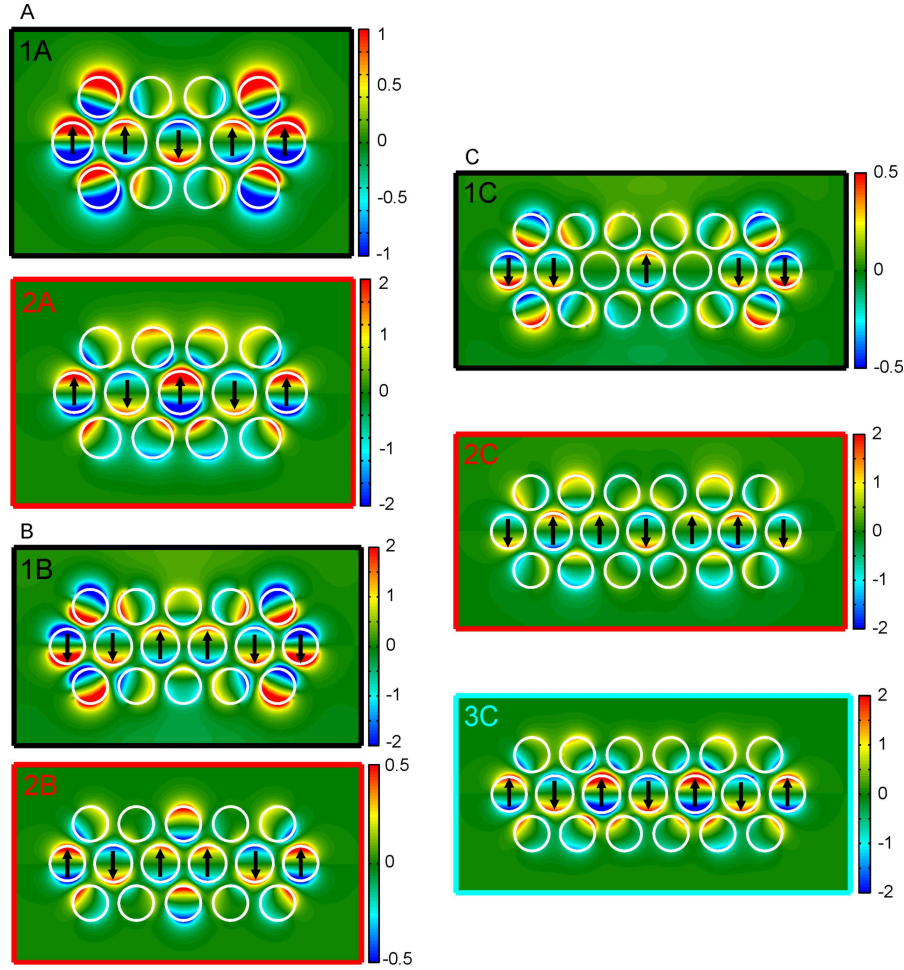


Figure 3.24.: Simulated near-field distributions of the elongated oligomers for vertical polarization at the spectral positions labeled in figure 3.22. Oligomers with A) three center particles and B) four center particles supporting fundamental (1A and 1B) and 2nd order (2A and 2B) subradiant modes. C) Oligomer with five center particles exhibits three subradiant modes.

larger clusters which makes the fundamental Fano dip barely visible in this case.

The difference in geometry of the clusters along their two symmetry axes causes a pronounced anisotropy in the spectral response. Depending on the polarization direction it is possible to switch Fano resonances on and off within the spectrum of the same plasmonic system. In the case of the cluster with three center particles at the spectral position of the Fano resonances (figure 3.24 A) the three center particles oscillate out-of-phase with respect to each other. The low energy fundamental dark mode is an in-phase oscillation of this mode supported by the center particles with the ring mode, whereas the ring mode oscillates out-of-phase for the high energy 2nd dark mode. The higher attractive forces in the case of the in-phase oscillation of the ring mode and the mode supported by the center particles (1st dark mode) leads to a lowering of energy

when compared to the out-of-phase oscillation in the case of the 2nd dark mode. The situation is similar for the cluster with four center particles (figure 3.24 B). There, due to mirror symmetry, the two innermost center particles form a synchronous pair which oscillates out-of-phase with respect to the next left and right middle row particle. Again, hybridization of this mode with the outer ring mode results in the formation of a fundamental and a 2^{nd} order dark mode. The situation changes by adding a fifth center particle. In figure 3.24 C, the field distributions of the three dark modes are depicted. In the 1^{st} and 2^{nd} order mode the two left and two right middle row particles pair and oscillate out-of-phase with respect to the center particle. This mode hybridizes with the outer ring mode and results in the two collective dark modes shifted to lower and higher energy due to attractive and repulsive near-field interaction. At the spectral position of the 3^{rd} order mode, the mode supported by the center particles is an out-of-phase oscillation of all particles with respect to each other. It is remarkable that an antisymmetric oscillation in the laterally aligned center particle chain can be excited without breaking the symmetry and introducing any retardation into the system.

In the electric near-field distribution we observe that the contribution to the overall ring dipole moment is dominated by the three left- and three rightmost ring particles. The residual ring particles are only weakly contributing to the formation of the collective dark modes. Therefore, in the following we consider plasmonic oligomers where we leave out the residual ring particles. This strategy opens up the possibility to increase the modulation depth and to shift the spectral position of the narrow Fano resonances. In figure 3.25 we compare the spectra of the elongated chain oligomers (green curves) with the oligomer clusters where we remove the upper and lower ring particles (red curves). The modulation depth of the low-energy Fano resonance is very poor. It shifts to the red upon increasing number of center particles and vanishes completely for the large cluster with four central nanoparticles. Strikingly, the 2nd Fano resonance that first appears for the cluster with 3 center particles is strongly modulated compared to the oligomer chain cluster. Good cancellation of the net dipole moment and spectral overlap of dark and bright mode is achieved in this case. Furthermore the Fano dip is shifted to higher energies by removing ring particles compared to the Fano feature in the plasmonic chain oligomer. This behavior is also observed for the cluster with 4 center particles, though the 2^{nd} order Fano resonance is broadened compared to the 3 center particle cluster.

In figure 3.26 we plot the simulated spectrum and near-field distributions of the cluster with three center particles. The spectral positions of the first lower-energy and second higher-energy dark modes are indicated with a black and red arrow, respectively. The excited modes are similar to the two dark modes of the elongated chain cluster with all ring particles (see figure 3.24 A), resulting from hybridization of the ring particle mode with the center particles mode. Energetically, the two modes are shifted to higher energies by removing ring particles. This is due to less attractive interaction via near-field coupling between the plasmonic nanoparticles. The spectral feature of the 1^{st} order dark mode is nearly absent in the spectrum. The 8 in-phase oscillating particles create a dipole moment which is only very weakly reduced by the out-of-phase oscillation of

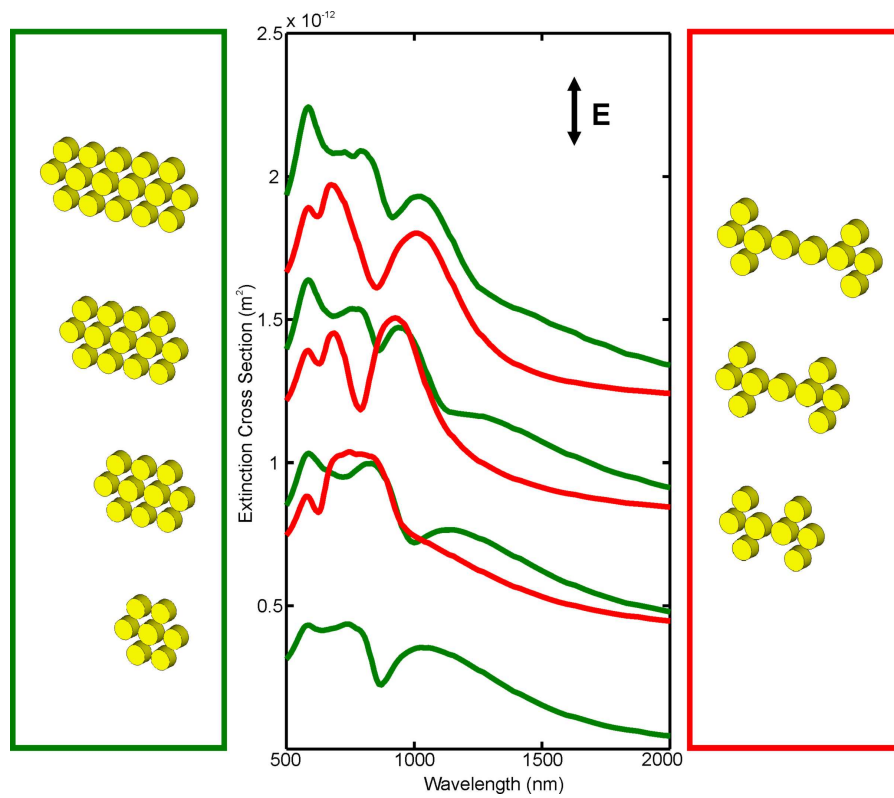


Figure 3.25.: Simulated extinction spectra for elongated oligomers with removed ring particles compared to extinction spectra of the chain oligomers. Leaving out certain ring particles leads to higher modulation depth of the Fano resonance in the extinction spectra (red curves) than for the elongated oligomers (green curves). Also, the spectral position is shifted to shorter wavelengths.

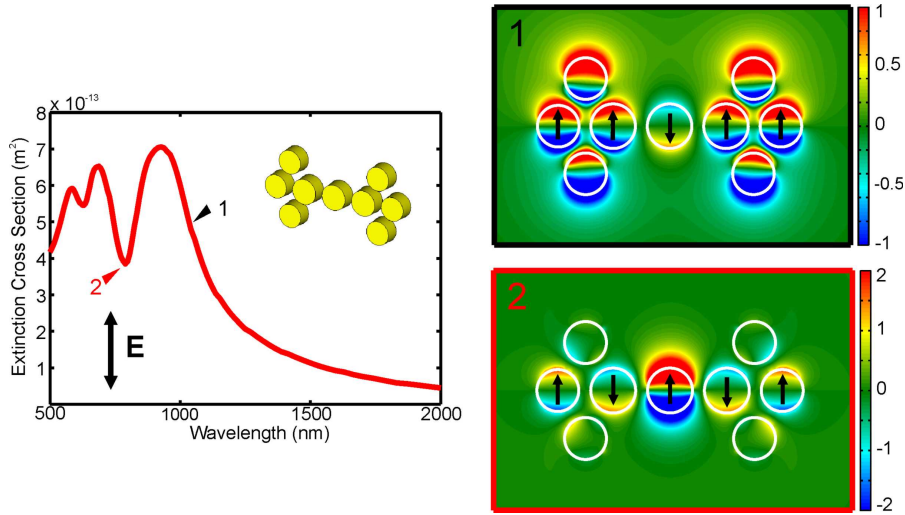


Figure 3.26.: Electric near-field distribution of the oligomer with three center particles and missing ring particles. The spectral positions are labeled in the extinction spectrum. The 2^{nd} order subradiant mode is very pronounced since the overall dipole moment of the in-phase and the overall dipole moment of the out-of-phase oscillating particles are matched. Contrarily, the first order dark mode is barely visible in the spectrum since the absolute dipole moment of the outer particles is overdominating the out-of-phase dipole moment of the center particle.

the center particle which makes the dipole moment comparable to the dipole moment of the bright mode. Therefore, an asymmetric dip in the spectrum is barely visible at this energy. In case of the unchanged chain oligomers the additional particles in the ring further reduce the dipole moment (cf. the field distribution of figure 3.24 A) leading to the Fano dip in the green spectrum. Yet, a very pronounced modulation of the 2^{nd} order Fano resonance is achieved by removing these upper and lower ring particles. This is due to a very efficient reduction of the net dipole moment in this particle configuration at this energy. Comparing the electric near-fields of the 2^{nd} order dark mode in figure 3.26 with the field distribution in figure 3.24 A we deduce that the additional ring particles tend to increase the overall dipole moment, which explains the lower modulation depth of the Fano dip in the green curve compared to the Fano dip in the red curve of figure 3.25. Hence, leaving out certain ring particles leads to a shift in energy of the Fano resonances and a tremendous increase of the modulation depth of the 2^{nd} order Fano resonance. We also would like to point out that by adding one particle to the two-center particle cluster a narrow extinction dip at 800 nm opens up in the previously broad extinction peak.

We have fabricated a series of clusters and compare them to the oligomer spectrum with the polarization set along the short axes of the clusters. The experimental results are shown in figure 3.27. The fundamental dark mode is only observed in the heptamer spectrum (blue curve) due to dipole moment mismatch of in-phase and out-of-phase oscillating nanoparticles and energy detuning of bright and dark mode in the case of the

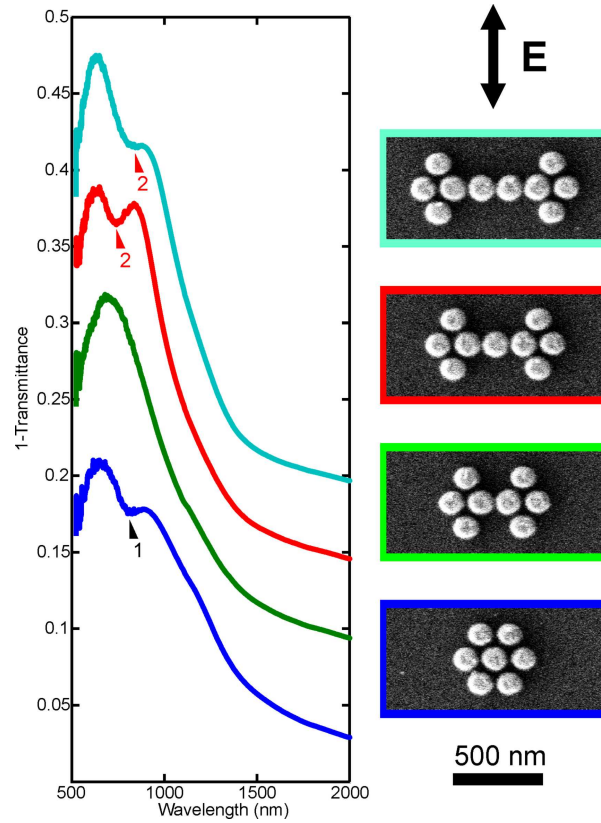


Figure 3.27.: Experimental 1-transmittance spectra of the elongated oligomers with missing ring particles. Only the 1st order subradiant mode is existent in the heptamer (blue curve) and the oligomer with two center particles (green curve). Adding one or two more particle leads to a formation of a 2nd order Fano resonance (red arrows in the red and cyan spectrum). The fundamental dark modes are not observable in the spectra due to dipole moments mismatch.

bigger clusters. Symmetry forbids the existence of a 2nd dark mode for the cluster with two center particles. In the case of three center particles we identify the Fano lineshape as the 2nd order dark mode since it is clearly shifted to higher energies, when compared with the Fano resonance in the heptamer. Adding a further center particle shifts the 2nd dark mode to lower energies and decreases the modulation depth just as predicted by simulations (see figure 3.25). Due to the reduction of the net dipole moment of the 2nd dark mode in this cluster configuration we can now clearly observe experimentally the higher-order Fano resonance in our oligomer cluster.

3.3. Plasmonic Analogue of Electromagnetically Induced Transparency (EIT)

3.3.1. EIT in Planar Geometries

The coupling of bright and dark modes and the formation of a Fano resonance can be viewed in the framework of a plasmonic analogue of electromagnetically induced transparency (EIT). EIT [82, 140, 141] is an effect which originates from the interference of two different excitation pathways. [142] The coupling of a bright and a dark resonance can lead to destructive interference of the excitation pathways giving rise to a sharp peak of nearly perfect transmission within a broad transmittance dip. Even though EIT is an inherently quantum mechanical effect, it is possible to observe EIT-like effects in systems of classical oscillators [143–145] and particularly for optical oscillators such as high-Q microresonators [146–149] as well as metamaterial [150–152] and plasmonic structures [83, 92, 135, 153, 154], where it emerges from the interference of the normal modes rather than from quantum interference of excitation probabilities. EIT is very useful to enhance nonlinear interaction in optical media [155]. It can be harnessed for dispersion engineering, in particular the realization of slow light [146, 148, 156] or delay lines [152], reduction of losses [151], or plasmonic sensing with narrow linewidths [25, 26, 76].

Figure 3.28 (a) depicts a planar structure which can be viewed as a plasmonic analogue of EIT, often referred to as a dolmen type or π shaped structure. The structure consists of three individual nano wires. When suggestively decreasing the distance between the wire pair and the single center wire, the dipolar resonance feature observed in the spectra starts to broaden. Starting from a separation of ~ 60 nm, a small kink forms within the broad dipolar resonance feature. Further decreasing the distance the kink increases in strength until a window of increased transmittance has formed within the former broad transmittance dip.

This behavior can be understood when examine the schematic energy level diagram in figure 3.28 (b). The energy level $|1\rangle$ is coupled to the ground state $|0\rangle$ by a bright dipole-allowed transition with resonance frequency ω_0 . This dipolar plasmonic resonance is supported by the single wire. At the same time, it is coupled to a dark state $|2\rangle$ which might be detuned by a shift δ . This dark, or in this case quadrupolar, mode is supported by the combined modes of the wire pair. The direct excitation $|0\rangle \rightarrow |2\rangle$ is dipole-forbidden, therefore its decay rate γ_2 is smaller than the bright transition rate γ_1 . However, the coupling of the levels $|1\rangle$ and $|2\rangle$, described by the coupling constant κ , allows for a population of state $|2\rangle$ which will cause a back action and an excitation of level $|1\rangle$. Overall this level scheme allows for two different excitation pathways leading to an occupation of the dipole allowed state $|1\rangle$: the direct transition

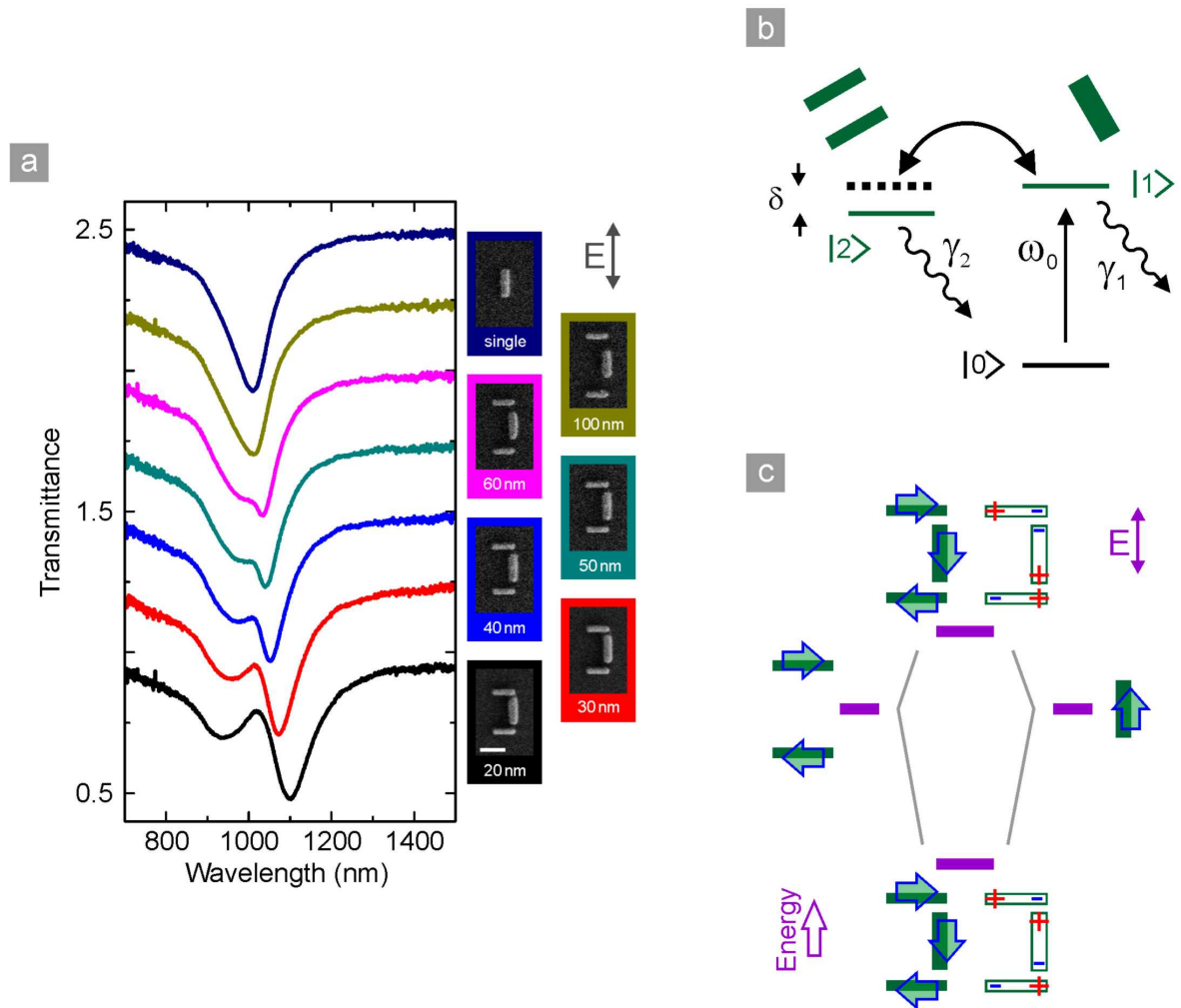


Figure 3.28.: (a) Experimental transmittance spectra for a set of a dolmen type plasmonic EIT structure with decreasing particle separation. (b) Due to destructive interference between a bright and a dark mode a window of enhanced transmittance forms at the position of the former transmittance dip. (c) The spectra can as well be understood in terms of plasmon hybridization between a dipolar mode in the nanorod and a quadrupolar mode supported by the wire pair, leading to a hybridization induced mode splitting between the symmetric and antisymmetric hybrid modes around their common resonance frequency. The figure as well shows sketches of the hybrid modes. As the modes spectrally overlap, the normal modes will interfere and at the spectral position of the transparency window only the signature of the dark quadrupolar mode will be visible in the nearfield.

$|0\rangle \rightarrow |0\rangle$ and the indirect one $|0\rangle \rightarrow |1\rangle \rightarrow |2\rangle \rightarrow |1\rangle$. The two excitation pathways will interfere, modifying the actual population of level $|1\rangle$. This coupling will lead to destructive interference and is called EIT and causes a vanishing excitation probability of level $|1\rangle$. This vanishing excitation probability of level $|1\rangle$ will lead to significantly reduced interaction of the dipolar mode with an external light field causing a window of transparency within the former broad dipolar transmittance dip.

One can as well view the phenomenon in terms of plasmon hybridization, as shown in figure 3.28 (c). The dipolar resonance can be excited from far field radiation polarized along the axis of the single nanowire. The charge distribution of the dipole will induce charge distributions of opposite sign in the wire pair. The combination of two dipolar charge distributions, however with opposite sign, will give rise to a quadrupolar field distribution. Thus, one effectively couples a dipolar to a quadrupolar mode, as indicated by the initial modes. (Note that indeed the dipoles of the wire pair cannot oscillate in phase due to their arrangement next to the dipolar wire, only out of phase oscillations are possible.) According to plasmon hybridization one will obtain the symmetric and the antisymmetric combination of these two initial modes. Due to attractive interaction, one is raised in resonance energy, the other is lowered due to repulsive interaction. When closely examining these modes, one realizes that their superposition will lead to vanishing field strength at the dipole. This is exactly what takes place at the transmittance peak: The two new modes spectrally overlap, and the field at the dipolar oscillator vanishes, leading to vanishing oscillation amplitude. Therefore, one can term this behavior interference of normal modes. The new hybrid modes can as well be seen as two polariton branches in the interplay of the dipolar and quadrupolar modes. For vanishing coupling only the dipolar mode is observable, the quadrupolar mode is truly dark. Therefore, the linewidth of the two modes are extremely different, the dipolar one I dominated by radiative losses, whereas the spectral width of the dark mode is given by the intrinsic losses, mainly losses in the metal. As soon as the modes couple, the hybrid modes will inherit properties of both modes. Interestingly, one of the modes will be more quadrupolar like whereas the other is more dipole like. Therefore, one often observes different linewidth for the two modes visible in the spectra. In particular in the case shown in figure 3.28 the lower energy mode exhibits a significantly smaller linewidth. When examining the sketches of the modes in figure 3.28 (c) one clearly sees that the higher energy mode has an overall much stronger dipolar character as compared to the lower energy mode. This behaviour has already been discussed in plasmon-waveguide hybrid systems where one can track the two initial and the hybrid modes when tuning coupling strength and relative spectral position of the plasmon and waveguide mode [157–160]. The plasmon serves as the bright and spectrally broad mode, the waveguide is, due to its extremely small intrinsic losses, spectrally narrow. In this case, one of the polariton branches is as well more "plasmon mode like", the other more "waveguide mode like". Note that this is of course only a manner of speaking as the polariton branches are hybrid states of both initial modes, as in the case of the purely plasmonic system. For the energetically degenerate case, the mode mixing is "total" and a linewidth difference can indeed no longer be found, both modes have equal contributions of the bright and dark modes. This is as well the

reason why in the experiment of Liu et al. [141] the two mode branches show identical linewidth, as compared to the in figure 3.28 discussed case of the planar EIT.

Interestingly, the very same behavior can be observed with two coupled classical harmonic oscillators of which only one is externally driven [144]. One will observe a splitting of the modes around the common resonance frequency, in particular the externally driven oscillator will be at rest at its former peak oscillation amplitude. This phenomenon is utilized in a dashpot. Note that effectively it is just a reshuffling of the overall oscillation amplitude. Instead of a single strong resonance one will obtain two new modes, yet with decreased peak amplitude, which is beneficial for the systems mechanical life time.

Both discussed pictures are equally valid. However, the first quantum mechanically inspired picture is somewhat more intuitive. One is compelled to immediately agree on the concept of a vanishing exaction amplitude. The notion of a driven mechanical oscillator, being at complete rest due to the coupling to a non-driven oscillator, which will oscillate, is somewhat harder to except.

3.3.2. EIT in Three-Dimensional Arrangements

Lateral plasmonic coupling is weak. The reason is fairly obvious when considering a simple dipole-dipole interaction scheme: When two metallic nanoparticles, e.g., two disks, are placed next to each other their mutual interaction can, to first order, be approximated by two dipoles residing in the center of mass of the two particles. The lateral distance is then given by the particles diameter and the surface to surface distance. If these same two disks are stacked on top of each other, the vertical coupling distance is only given by the thickness of the particle plus the vertical gap. Thus, the same two disks will show significantly increased interaction strength when stacked on top than for side by side arrangement. Obviously, this is not true for two spheres, as thickness and diameter are identical here. However, it is still beneficial to stack them on top, as it allows for the observation of the antisymmetric mode. Due to retardation effects, that is the finite speed of light, the two particles are not excited simultaneously, therefore the resulting antisymmetric mode will show a slight phase lack between the two dipoles leading to an non-vanishing overall dipolemoment, hence making the mode observable in the spectra.

Overall, it therefore seems beneficial to study EIT in a three-dimensional system where the dipole is stacked on top of the quadrupolar wire pair. An additional benefit afforded by a three-dimensional geometry is an increased geometrical tunability of the system.

Figure 3.29 depicts the geometry of a double electromagnetically induced transparency coupling scheme where two quadrupolar resonances are coupled to one dipolar one. The middle nanorod (in red) is perpendicularly stacked between two parallel rod-pairs (in

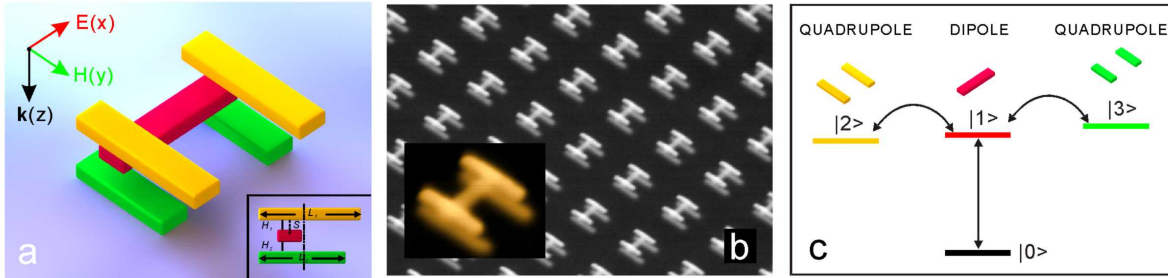


Figure 3.29.: (A) Schematic diagram double EIT system. The arrows denote the displacement of the central red bar which is to be measured with respect to the upper and lower bars. Inset: definitions of the geometrical parameters. The red rod is displaced from the symmetry axis of the bottom green rod-pair by S . The lengths of the top yellow and bottom green rods are L_1 and L_2 , respectively. The vertical distance between the red rod and the yellow (green) rod-pair is H_1 (H_2). (B) SEM image of a typical sample fabricated by electron beam lithography. The structure is on a glass substrate. The gold rods are embedded in a photopolymer (PC403), which serves as a dielectric spacer. All the gold rods have the same thickness and width, which are 40 nm and 80 nm, respectively. $S = 40$ nm, $H_1 = H_2 = 30$ nm, $L_1 = 340$ nm, and $L_2 = 270$ nm. The length of the middle rod is 260 nm. The periods in both the x and y directions are 700 nm. The in-plane distance between the two rods in each rod-pair is 150 nm. (C) Level scheme for two quadrupolar resonances that are coupled to a dipole in a four-level system. Resonance I results from destructive interference between pathways $|0\rangle \rightarrow |1\rangle$ and $|0\rangle \rightarrow |1\rangle \rightarrow |2\rangle \rightarrow |1\rangle$. Resonance II results from destructive interference between pathways $|0\rangle \rightarrow |0\rangle$ and $|0\rangle \rightarrow |1\rangle \rightarrow |3\rangle \rightarrow |1\rangle$.

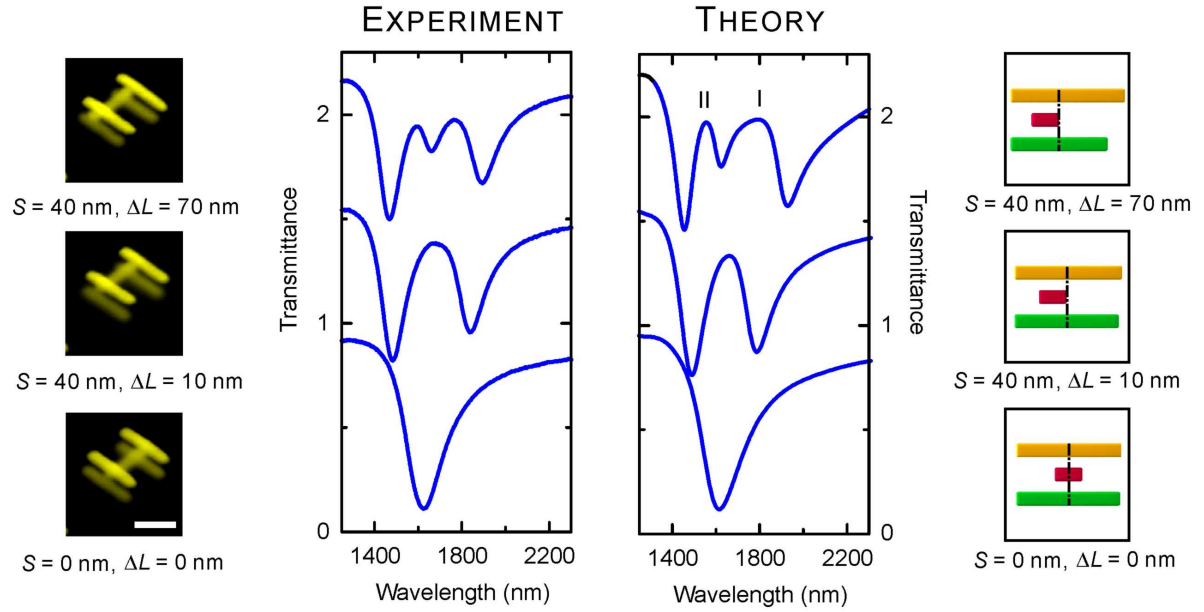


Figure 3.30.: Experimental and calculated transmittance spectra of the double EIT system in dependence on structural tuning. Spectra are shifted upwards for clarity. Bottom curves: $S = 0$ nm, $L_1 = 310$ nm, and $L_2 = 310$ nm ($\Delta L = L_1 - L_2 = 0$ nm). Middle curves: $S = 40$ nm, $L_1 = 310$ nm, and $L_2 = 300$ nm ($\Delta L = 10$ nm). Top curves: $S = 40$ nm, $L_1 = 340$ nm, and $L_2 = 270$ nm ($\Delta L = 70$ nm). One and two transmittance peaks develop inside the broad dipolar absorption dip, depending on the degree of structural symmetry breaking.

yellow and green). The lengths of the top yellow and bottom green rod-pairs are L_1 and L_2 , respectively. The middle rod is displaced from the symmetry axis of the bottom green rod-pair by S . The vertical distance between the red rod and the yellow (green) rod-pair is H_1 (H_2). An overview of one typical sample is shown in figure 3.29 (b). The near-infrared transmittance, reflectance, and absorbance spectra of the samples at normal incidence were measured by a Fourier-transform infrared spectrometer with electric field polarization parallel to the middle red rod, as illustrated in figure 3.29 (a).

The optical properties of this complex structure can be understood by first starting with the highest symmetry configuration (the bottom curve in Figure 3.30 (a)), in which the yellow and green rod-pairs are of equal length ($\Delta L = L_1 - L_2 = 0$ nm), and the central dipole-coupled red rod sits along the symmetry axis of the two quadrupole-coupled rod-pairs ($S = 0$ nm). In this case, there is only a single broad resonance visible from the excitation of the dipolar plasmons in the single nanorod. Excitation of the quadrupolar modes can occur only when the system symmetry is reduced, giving rise to near-field coupling between the dipolar and quadrupolar resonances. For example, when a displacement of the middle rod is introduced ($S = 40$ nm), a transparency window appears inside the broad outer resonance profile as characterized by the middle curve

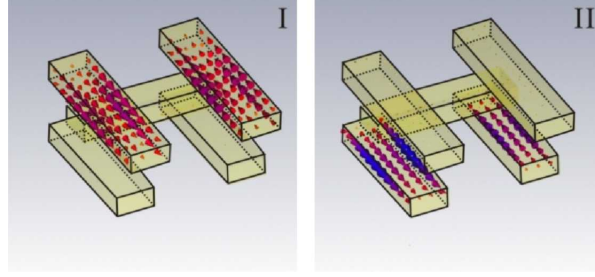


Figure 3.31.: Calculated current distributions at resonances I and II, as indicated in figure 3.30. At resonance I (II), antisymmetric charge oscillations are excited in the top (bottom) rod-pair while the middle rod contains nearly no current.

in Figure 31. Furthermore, by introducing a length difference between the two rod-pairs ($\Delta L = L_1 - L_2 = 70$ nm) while keeping the displacement $S = 40$ nm, a dip in the transmittance emerges in the middle of the transparency window, giving rise to two transmittance peaks as shown by the top curve in figure 3.30. The corresponding SEM images of the structures are shown in figure 3.30 to the left of the spectra. Simulations for the optical spectra were performed based on a Finite Integration Time Domain algorithm as well as the Fourier modal method. The permittivity of the gold is described by the Drude model with plasma frequency $\omega_{pl} = 1.37 \times 10^{16} s^{-1}$ and damping constant $\omega_c = 1.22 \times 10^{14} s^{-1}$. The refractive indices of the glass substrate and PC403 are taken as 1.5 and 1.55, respectively. Figure 3.30 presents the calculated transmittance spectra of the samples based on the Fourier modal method. The experimental results show an excellent overall agreement with the numerical predictions.

Calculated current distributions at the respective spectral positions I and II as indicated in figure 3.30 are presented below the spectra in figure 3.31. In particular, a quadrupolar current distribution in the longer top rod-pair is observed at the spectral position of transmittance peak I, and likewise a quadrupolar current distribution in the bottom shorter rod-pair is visible at the spectral position of transmittance peak II.

Figure 3.29 (c) shows a prototype four-level system, which can be used to interpret the above phenomena. In our structure, the red middle rod is strongly coupled to light, giving rise to a broad dipolar (bright) resonance due to significant radiative losses. This can be correlated with the dipole-allowed transition from $|0\rangle \rightarrow |1\rangle$ in figure 3.30 (c). The green and yellow rod-pairs can support quadrupolar modes, which are subradiant (dark). They can be correlated with the two dipole-forbidden transitions from $|0\rangle \rightarrow |2\rangle$ and $|0\rangle \rightarrow |3\rangle$, respectively. The two quadrupolar modes are associated with very narrow resonances, whose linewidths are solely determined by the nonradiative damping in the metal. In the presence of a nonzero displacement S , the two dark quadrupoles can be strongly coupled to the middle dipole due to near-field coupling. As a result, destructive interference of two excitation pathways, namely the direct excitation of the dipolar mode in the red rod ($|0\rangle \rightarrow |1\rangle$) and the indirect excitation due to its interactions

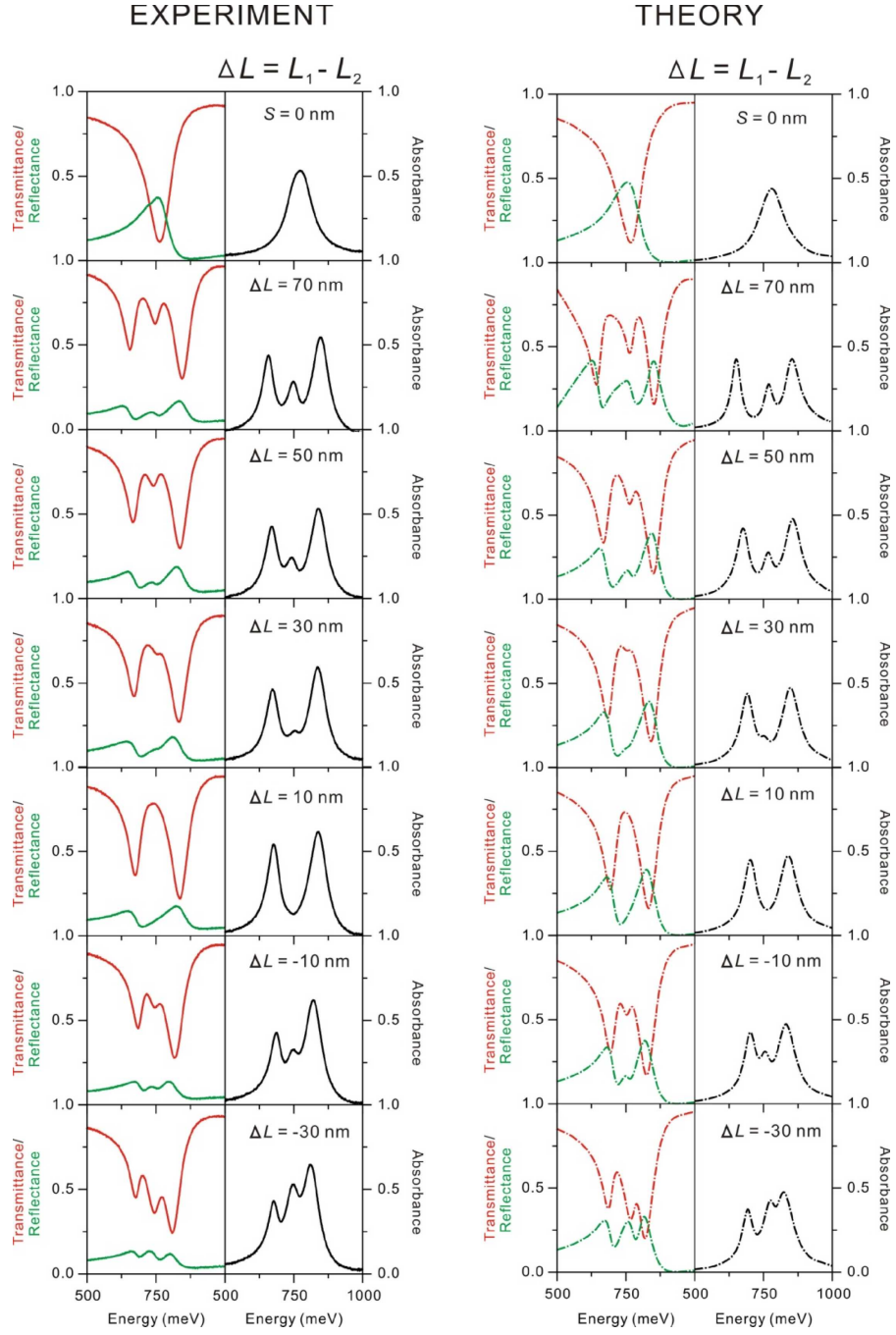


Figure 3.32.: Structural optimization for spatial tuning. Experimental and calculated spectra of the 3D plasmonic structure in dependence on length difference $\Delta L = L_1 - L_2$. S is 40 nm. The sum of the lengths of the two rod-pairs is kept constant as $L_1 + L_2 = 610$ nm.

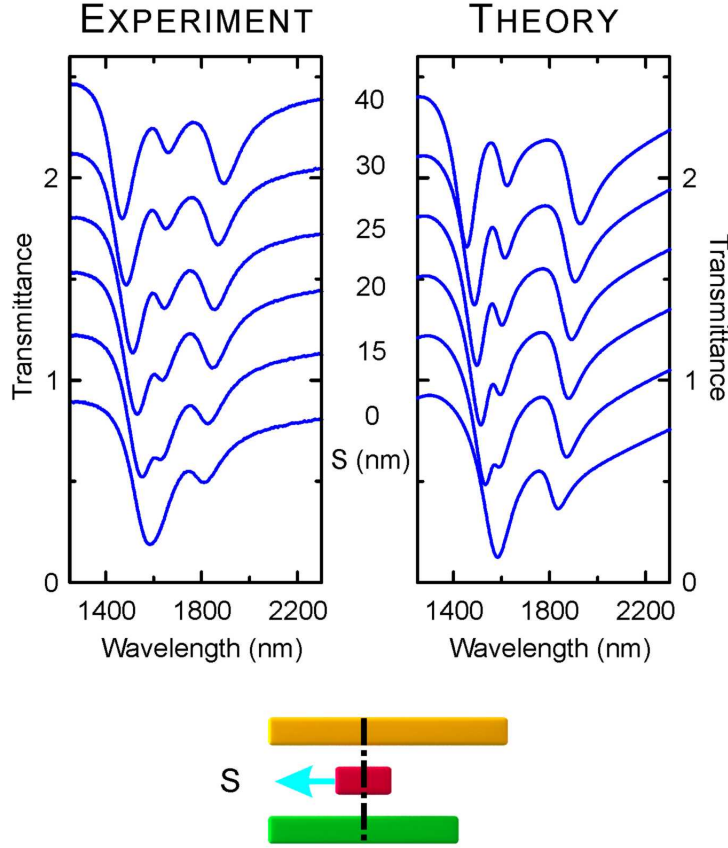


Figure 3.33.: Experimental (left) and calculated (right) transmittance spectra of the double EIT system in dependence on lateral displacement S . Spectra are shifted upwards for clarity. The geometrical parameters: $L_1 = 340$ nm and $L_2 = 270$ nm. The length of the middle rod is 260 nm. The weight of the two quadrupolar transmittance peaks is strongly dependent on the lateral displacement of the dipolar rod.

with the quadrupolar modes in the yellow ($|0\rangle \rightarrow |1\rangle \rightarrow |2\rangle \rightarrow |1\rangle$) and green ($|0\rangle \rightarrow |1\rangle \rightarrow |3\rangle \rightarrow |1\rangle$) rod-pairs, results in transmittance peaks at resonances I and II, respectively. Consequently, due to this destructive interference, currents are nearly absent in the middle rod at these two resonances. This is evident from the current distributions in Figure 3.31. It is worth mentioning that the middle curve in figure 3.30 is correlated with the degenerate case, where the two quadrupoles have approximately identical resonance energies. A more complete structural tuning to optimize the double quadrupolar resonances is shown in figure 3.32. Please note the excellent agreement between simulation and experiments for all shown geometries.

Next, we study the response of the optical to a minute lateral displacement change within the 3D plasmonic structure and show that they can give rise to a significant variation of the transmittance spectra. We start with the structural configuration ($\Delta L = L_1 - L_2 = 70$ nm) of figure 3.30. Figure 3.33 shows the experimental spectra, in which the lateral

displacement S is successively decreased from 40 nm to 0 nm. The calculated spectra in figure 3.33 show an excellent agreement with the experimental results. Examining the intensities of the resonances. It is evident that as S decreases, the two quadrupolar resonances are both suppressed due to the reduced structural asymmetry. The higher-energy quadrupolar resonance (resonance II) subsides much faster than the lower-energy one (resonance I). This is due to the fact that resonance II is associated with the bottom shorter rod-pair. A slight lateral detuning of the middle rod has a larger influence on this shorter rod-pair than on the top longer rod-pair due to the asymmetric structural configuration. Subsequently, resonance II vanishes when the single middle rod is placed overlapping with the symmetry axis of the bottom shorter rod-pair, i.e., $S = 0$ nm. In this case, resonance I is still visible since the middle rod has a finite displacement with respect to the symmetry axis of the longer rod-pair. In essence, a minute spatial change within the 3D plasmonic structure can give rise to distinct shape and intensity variations in the spectra. These effects might be exploitable for developing sensitive 3D plasmon rulers, which are not solely based on the colorimetric detection scheme but rather on the full high resolution plasmonic spectral behavior. In principle, using differential spectroscopy, even smaller displacements should be detectable.

Figure 3.34 depicts a set of experimental spectra for another geometrical variation of the double EIT system. All dimensions are kept fixed and only the upper quadrupole wire pair is sifted relatively to the two lower layers, from large negative to large positive displacements. The spectra number three and four do thus only display the signature of the lower layer quadrupole as the upper quadrupole is not displacement relative to the dipole (as can be seen in the SEM images), hence the upper layer quadrupole does not couple to the dipolar resonance. In all other cases coupling takes places between both quadrupolar wire pairs and the dipole, thus the corresponding spectra show the signature of both quadrupoles, the lower energy mode corresponds to the upper layer quadrupole, the higher energy mode to the lower layer quadrupole. Note that the coupling to the lower layer quadrupole is weak due to a small offset of dipole and quadrupole, thus the spectral feature, being a transparency window, is weak as well. For the upper layer quadrupole the coupling becomes strong for the largest displacements and a more pronounced transparency window and be observed. It is interesting that all spectra are distinctively different with respect to the strength of the lower energy quadrupole resonance strength, making it possible to conclude on its position solely from the optical spectra. Note that there are slight deviations in the strength of the resonance associated with the lower layer quadrupole. However, from design the offset of this quadrupole wire relative to the dipole is kept fixed and thus the strength of the resonance should stay fixed as well. The spectral changes are thus caused by unintentional shifts which are within the experimental tolerances; these deviations are in the order of 10 nm and yet show noticeable spectral changes as well. This high sensitivity is as well caused by the overall weak coupling strength of the lower layer quadrupole to the dipole, its displacement is small, thus already a small relative shift will significantly alter the coupling strength.

Intuitively, one would expect the spectra to diminish significantly in quality and spectral

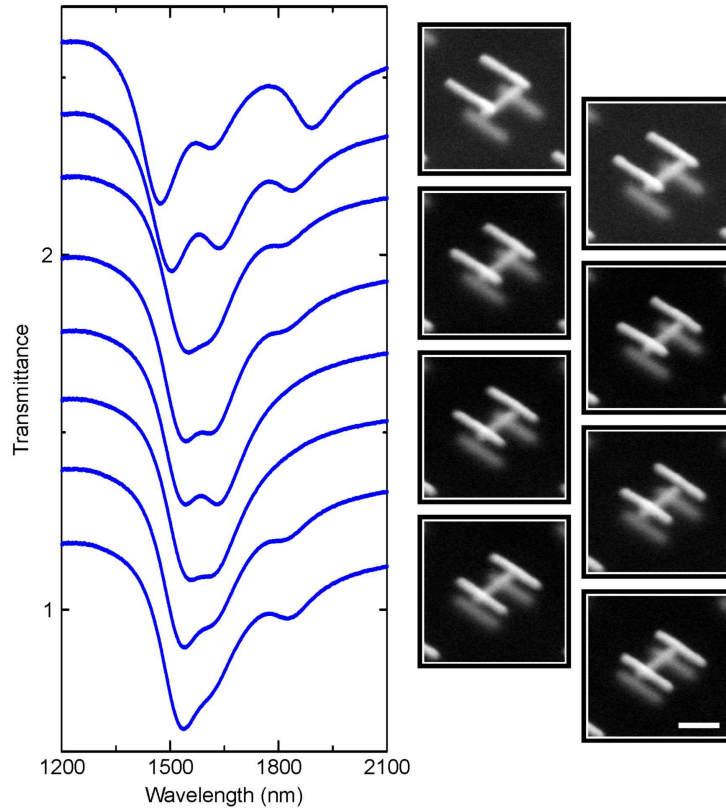


Figure 3.34.: Keeping the lower layer quadrupole wire pair and the dipole wire fixed in their respective positions, the relative displacement of the upper layer quadrupole has been varied. For large positive and negative displacement the signatures of both quadrupolar modes are visible. For displacements in between these extremes, the relative displacement of the upper layer quadrupole to the dipole is zero, thus the coupling vanishes and only a single resonance is transparency window is visible, origination form the coupling to the lower layer quadrupole. The scale bar is 200 nm.

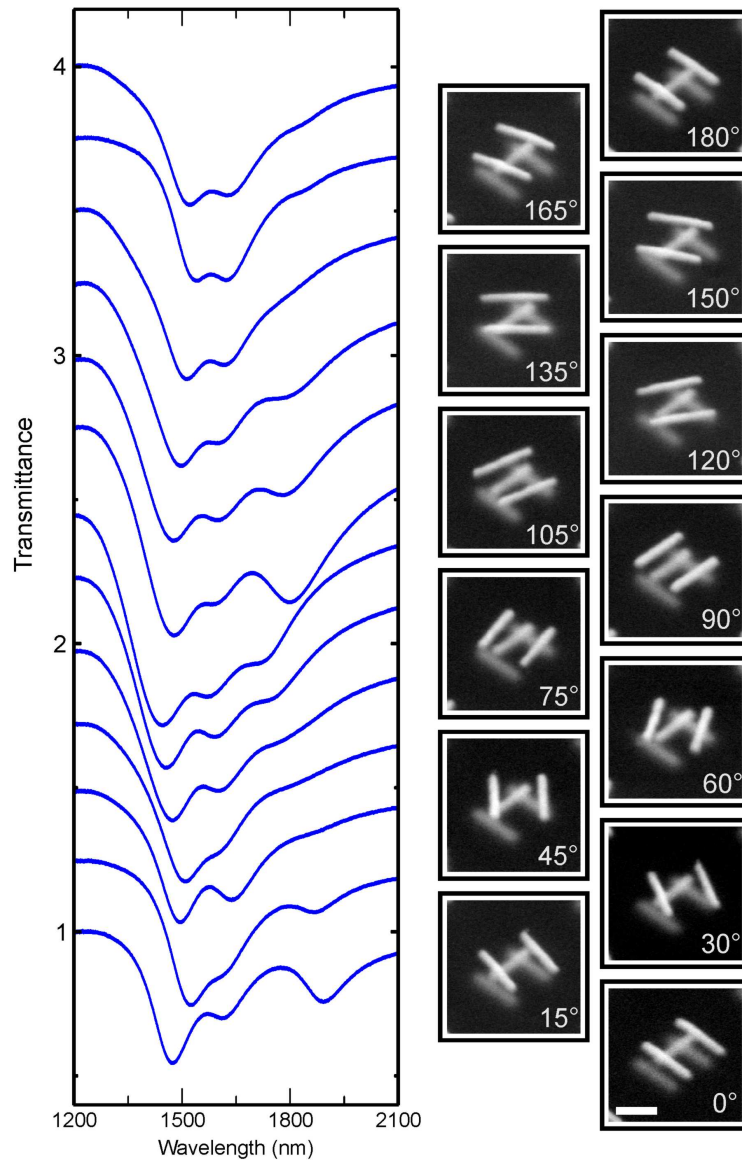


Figure 3.35.: Experimental spectra for a set of rotations of the upper layer quadrupole. Rotating the quadrupole leads to a successive vanishing of the quadrupolar mode and leads to the formation of two energetically degenerate dipolar modes for a rotation angle of 90° . Thus, one loses one of the spectrally narrow features in the optical spectra. Nevertheless, all spectra show distinct differences, making it possible to deduce the rotation angle of the quadrupole from the spectra. As the rotation axis is around the dipole which is displaced from the quadrupole, 0° and 180° rotation angle are not equivalent. The scale bar is 200 nm.

sharpness of the features as soon as the spectrally narrow quadrupole resonances are lost. If one would rotate one of the quadrupole wire pairs the quadrupolar modes successively vanishes and transforms into two bright energetically degenerate dipolar modes as soon as they are aligned parallel to the dipole. Figure 3.35 depicts such an experimental series where the upper layer quadrupole has been rotated in steps of 15° from 0° to 180° . The rotation axis is centred on the dipole, therefore, as the quadrupole is offset from the dipole, 0° and 180° are geometrical not equivalent. Despite the complex geometrical tuning the spectra still exhibit significant modulation and narrow and well pronounced spectral features. All 14 spectra show distinct differences, making it feasible to deduce the rotation angle of the upper layer quadrupole solely from the optical response.

3.3.3. Double EIT as Three-Dimensional Plasmon Ruler

In the last paragraph we have demonstrated that the double EIT nanoparticle arrangement is capable of encoding its three-dimensional arrangement in well modulated spectra with sharp and well pronounced features. Moreover, we have shown that the spectra are not only very robust against three-dimensional variations and distortions, but show distinct differences in changing the arrangement. We thus envision that our structure can serve as a three-dimensional plasmon ruler enabling the optical determination of three-dimensional arrangements on the nanoscale.

It has already been demonstrated that the coupling between two metallic nanoparticles generates a light-scattering spectrum that depends strongly on the interparticle distance. This effect has been used to create plasmon rulers which can be used to measure nanoscale distances in one dimension [161]. Plasmon rulers based on sensitive colorimetric schemes have been developed for monitoring DNA hybridization [162] and biological activities in living cells [163, 164]. Compared to molecular rulers based on dye-pair fluorescence resonance energy transfer [165], plasmon rulers offer exceptional photostability and brightness because of the use of noble metal nanoparticles. Beyond dimers, multiple nanoparticles can be placed in proximity to each other. In the resulting assemblies, plasmonic coupling would lead to lightscattering spectra that are sensitive to a complete set of three-dimensional (3D) motions. Such a 3D ruler would have great impact in many fields of biology and soft materials science by providing a complete picture of time-dependent nanoscale motions and rearrangements. However, typical dipolar plasmon resonances are broad because of radiative damping [166], and as a result the simple coupling between multiple particles produces indistinct spectra that are not readily converted into distances.

We propose to use high resolution plasmon spectroscopy in combination with plasmon induced transparency and higher order resonances to overcome these limitations, and we demonstrated a 3D plasmon ruler. This offers a blueprint to optically determine the structural dynamics of single 3D entities. Commonly, techniques such as nuclear mag-

netic resonance and x-ray diffraction are used to determine 3D structural information. These techniques generally require a large amount of analyte to obtain good signals, hampering applications at the single entity level. Additionally, x-ray diffraction does not work in situ or in vivo and involves complicated sample crystallization processes.

The key development reported here is thus the ability to create sharp spectral features in the otherwise broad resonance profile of plasmon-coupled nanostructures by using interactions between quadrupolar and dipolar modes. The key elements of the use of our structure as a 3D plasmon ruler are the sharp spectral features of the quadrupolar resonances and their extremely high sensitivity to any spatial or structural changes. The dipolar resonance profile, which is generally used for detecting spectral shifts in plasmon rulers, is divided by two quadrupolar resonances that lead to significantly reduced linewidths and therefore increased figures of merit. This is a fundamental criterion for the implementation of sensitive plasmon rulers. In the near-field regime, dipole-quadrupole coupling is more distance-dependent than dipole-dipole coupling. The use of the 3D plasmonic structure allows us to retrieve 3D structural changes that occur owing to the transition from one configuration to another by reading out spectral changes of the well-modulated plasmon spectra.

To demonstrate the fundamental concepts of 3D plasmon rulers, we used in our study a complex sequence of nanolithography steps. The resulting optical response of the 3D plasmon ruler has been correlated with the particle plasmon resonances of the individual nanostructure assembly. The same concepts can be applied to single metallic nanocrystals joined together by oligonucleotides or peptides [167–170], giving rise to a new generation of plasmon rulers with unprecedented ability to monitor the sequence of events that occur during a wide variety of macromolecular transformations in three dimensions. Metallic nanoparticles of different lengths or sizes could be attached at different positions of the DNA or protein [171, 172], and each metallic element may move individually or collectively in three dimensions. Dark-field microspectroscopy of the scattering or the extinction spectrum would offer a useful tool to identify the 3D arrangement of the different constituents in real time, as it is unambiguously correlated to very distinct and rich spectral features. As in the case of nuclear magnetic resonance, 3D plasmon rulers could use a lookup database where the optical spectra corresponding to all possible structural configurations are stored. Spectral features can then be associated with certain distortions. Novel methods of data mining and inference would facilitate this task. This concept can be further extended by using polarization sensitivity as well as tomography-like spectroscopy from different directions. The realization of 3D plasmon rulers using nanoparticles and biochemical linkers is challenging, but 3D nanoparticle assemblies with desired symmetries and configurations have been successfully demonstrated very recently [171–176]. These exciting experimental achievements will pave the road toward the realization of 3D plasmon rulers in biological and soft-matter systems.

3.4. Classical Analogue of Electromagnetically Induced Absorption (EIA)

In the last paragraphs we have seen a number of intriguing coupling phenomena which relay on the interaction of bright and dark modes. We have found that the resulting spectra can be understood in terms of destructive interference of excitation pathways. However, there is one obvious question: Why is the interference destructive? As well as the even more exciting question: Can one switch from destructive to constructive interference?

Such a process, being termed electromagnetically induced absorption (EIA) has been investigated in atomic physics [177–179]. Instead of observing enhanced transmission as in the case of EIT, the coherent coupling to the dark state results in a narrow peak of enhanced absorbance on top of the broad dipolar absorbance feature.

Here, starting from the atomic physics concept of EIA, we introduce a plasmonic system which can be regarded as its classical analog. Figure 3.36 (a) depicts the coupling scheme. Overall, it is very similar to the one shown for the EIT case in figure 3.28. The energy level $|1\rangle$ is coupled to the ground state $|0\rangle$ by a bright dipole-allowed transition with resonance frequency ω_0 . At the same time, it is coupled to a dark state $|2\rangle$ which might be detuned by a shift δ . The direct excitation $|0\rangle \rightarrow |2\rangle$ is dipole-forbidden, therefore its decay rate γ_2 is smaller than the bright transition rate γ_1 . However, the coupling of the levels $|1\rangle$ and $|2\rangle$, described by the coupling constant $\kappa \cdot e^{i\varphi}$, allows for a population of state $|2\rangle$ which will cause a back action and an excitation of level $|1\rangle$. Overall this level scheme allows for two different excitation pathways leading to an occupation of the dipole allowed state $|1\rangle$: the direct transition $|0\rangle \rightarrow |1\rangle$ and the indirect one $|0\rangle \rightarrow |1\rangle \rightarrow |2\rangle \rightarrow |1\rangle$. The two excitation pathways will interfere, modifying the actual population of level $|1\rangle$. In contrast to the conventional EIT coupling scheme, we introduce a complex coupling coefficient which allows us to manipulate the coupling phase between dipolar and quadrupolar oscillator. Depending on the coupling phase φ , destructive as well as constructive interference can be achieved. The first one is called EIT and causes a vanishing excitation probability of level $|1\rangle$, the latter yields an increased excitation probability of level $|1\rangle$ and hence enhanced absorption, resembling the characteristic behavior of EIA in atomic physics. We would like to point out that our system considers two resonant oscillators that are coupled with additional phase lag in between them. Previous works demonstrated coupling of different, detuned oscillators which exhibited a phase lag [180–182].

In our plasmonic system, bright and dark transitions are realized by metallic nano-cut-wires: a dipole wire for the bright transition which is stacked on top of a quadrupole wire pair representing the dark transition. Incoming light is polarized along the dipolar wire. A schematic of the system is depicted in figure 3.36 (b). By increasing the lateral

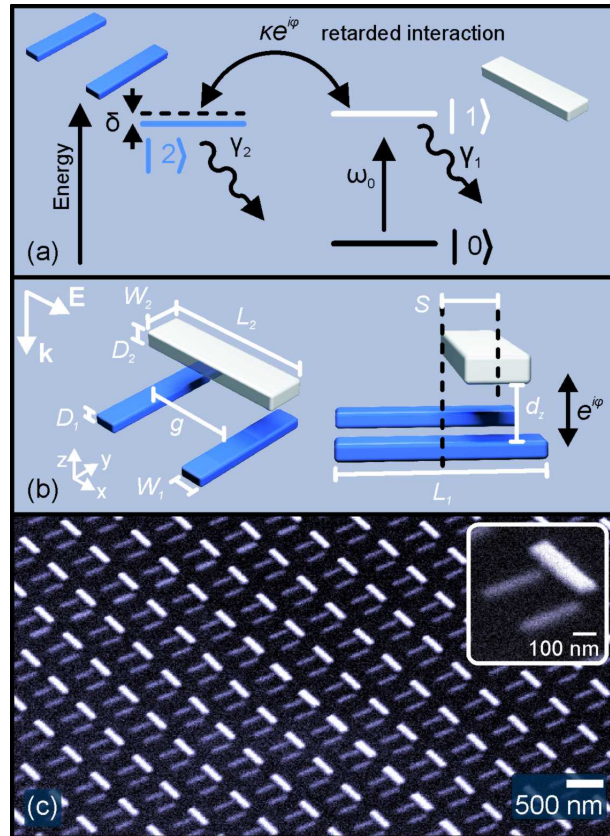


Figure 3.36.: (a) Three-level model scheme for the system. The energy level $|1\rangle$ can be excited from the ground level $|0\rangle$ by a bright transition with a large dipole moment and is simultaneously coupled to a dark state $|2\rangle$. This coupling mechanism is retarded by a phase factor $e^{i\varphi}$. By changing φ , a phase delay can be introduced into the coupling between bright and dark mode. (b) Geometric parameters of the structure. The phase difference between dipolar and quadrupolar oscillator can be tuned by changing the vertical spacing d_z . (c) SEM micrograph of the structure with maximum offset S .

displacement S of the dipole, electromagnetic coupling between dipole and quadrupole is possible. This system is similar to the one that has been used to obtain the plasmonic analog of EIT, however, in that case the coupling between dipole and quadrupole was accomplished solely by near-field coupling.

In contrast, the coupling between dipolar and quadrupolar oscillator in our structure is neither near-field coupling nor far-field coupling. In case of near-field coupling, the interaction would be mediated by the evanescent fields of the plasmonic oscillators. The quasistatic approximation would be valid and hence no retardation would be possible. On the other hand, for far-field coupling the dipole field would be purely wave-like and coupling to a quadrupolar mode would not be possible. Therefore, our coupling scheme relies on an intermediate coupling regime, where near-field effects still play a role, so that coupling to the quadrupolar oscillator is still possible, but simultaneously retardation effects, which are characteristic for a travelling wave, are already relevant. Hence, the most important structural parameter is d_z . We note, that a change in d_z will not only change the phase φ but also the coupling strength κ .

In order to increase the observability of the effect, it is desirable to reduce the absorbance of the bare dipolar resonance compared to the absorbance of the quadrupolar mode. This is accomplished by changing the wire geometry: compared to the quadrupole wire dimensions, we increase the width W_2 and height D_2 of the dipole wire, preserving the spectral position by tuning the length L_2 . Doing so leads to an increase of scattering while the absorption is reduced.

Additionally, a detuning δ of the spectral positions of dipolar and quadrupolar mode is desirable. As plasmonic resonances are inherently broader than typical atomic resonances, the difference in linewidths γ_1 and γ_2 is not as pronounced as in the case of atoms. Thus, the double-peaked structure of the absorbance spectrum is much clearer with slight detuning than it would be for a degenerate system.

It is noteworthy that the realization of EIA in a classical system, just as the plasmonic analog of EIT is tightly connected to Fano resonances in plasmonic structures and both represent limiting cases of those [79, 80, 183].

We fabricated several structures by a two-step electron beam lithography process. The first layer is defined in a first exposure step. Then an adhesion layer of 2 nm Cr and a 40 nm gold layer are thermally evaporated. After lift-off of the residual resist, the spacer layer is applied. We use a spin-on-dielectric (Futurrex IC1-200) which also serves as a planarization layer. The thickness of this layer is crucial as the coupling in our case strongly depends on a correct spacing.

The dipole wire layer is defined in a second aligned exposure step, followed by thermal evaporation of 2 nm Cr and 60 nm gold, lift-off, and planarization. Scanning electron micrographs of the fabricated structures are shown in figure 3.36 (c). The large vertical

spacing of $d_z \approx 100$ nm is clearly observable in these images. Structures with different offsets S are fabricated in order to examine different coupling strengths. The quadrupole wire pair dimensions for the experimentally realized samples are $L_1 \times W_1 \times D_1 = 375 \times 65 \times 40$ nm³ with a spacing of $g = 220$ nm. The dipole wire dimensions are $L_2 \times W_2 \times D_2 = 420 \times 120 \times 60$ nm³. The periodicity is 700 nm in both directions, the sample area is 90×90 μ m². The experimentally acquired offsets S in the fabricated structures were $S=30, 45, 60,$ and 150 nm.

Reflectance and transmittance measurements for the different structures were performed using a Fourier transform infrared spectrometer microscope with a 15x Cassegrain objective (NA=0.4) and a liquid nitrogen cooled MCT detector. The experimental transmittance and reflectance spectra are shown in the top left panel of figure 3.37. Finite integration technique calculations performed with the commercial software package CST Microwave Studio are displayed on the right panel for comparison. For increasing offset S , a dip in reflectance as well as a peak in transmittance emerge at the quadrupole resonance frequency. The appearance of a peak in transmittance seems to indicate a badly tuned EIT effect. However, the modulation depth of this spectral feature is stronger in reflectance than it is in transmittance, thus indicating that the absorbance of the structure changes.

The absorbance can be calculated using $A=1-T-R$, and the resulting spectra are displayed in the bottom panel of figure 3.37. In these graphs the double-Lorentzian spectral shape is well pronounced. For maximum offset S the experimentally observed peak absorbance is 38% compared to 28% in the uncoupled case which corresponds to an enhancement factor of 1.35. In the calculations, this difference is even more pronounced with a peak absorbance of 44% versus 20% (enhancement factor 2.2). It has to be noted, that the absorption is confined to a narrow, sub-dipolar-linewidth spectral region due to the coupling to the quadrupolar resonance. This is qualitatively very different from a simple absolute enhancement of the dipolar absorption by introducing additional losses. Differences between experimental and simulated results can be attributed to inhomogeneous broadening in the ensemble originating from fabrication tolerances, to the averaging over a range of angles of incidence in the measurement, and to a deviation of the gold material properties from the theoretical values due to grain boundaries and impurities in the evaporated gold.

In order to further elucidate the physical processes involved, we model our system by two harmonic oscillators with a complex coupling coefficient $\tilde{\kappa} = \kappa \cdot e^{i\varphi}$, where φ represents the phase retardation due to the coupling distance in propagation direction. As only the dipole wire is excited directly, only one of the oscillators couples to the light field. This yields the absorbance:

$$A(\omega) = \text{Im} \frac{f\Omega_q}{\tilde{\kappa}^2 - \Omega_d\Omega_q} \quad (3.1)$$

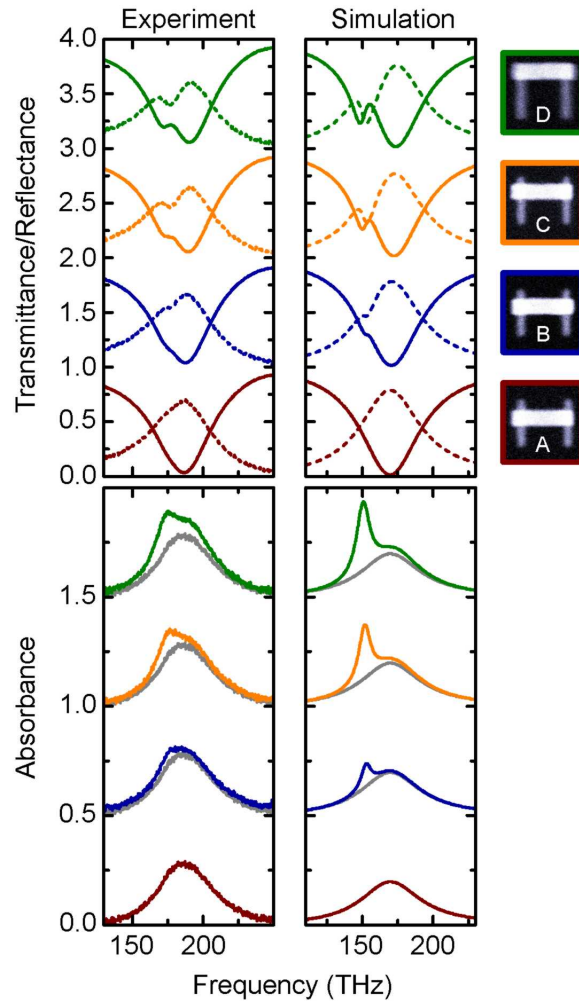


Figure 3.37.: Top row: Measured (left) and calculated (right) transmittance spectra (solid) and reflectance spectra (dashed) for different offsets S . Bottom row: Corresponding measured (left) and calculated (right) absorbance extracted from the transmittance and reflectance data using $A=1-T-R$. For increased offset S and therefore increased coupling strength between dipolar and quadrupolar oscillator, a narrow absorbance dip originating from the excitation of the quadrupole appears. The minimum offset absorbance curve is shown in every graph in light gray for comparison. Simulated spectra using a finite integration technique are shown for offsets of $S=0, 40, 80,$ and 120 nm. The insets on the right side show top view SEM micrographs of the corresponding samples ($S=30, 45, 60,$ and 150 nm).

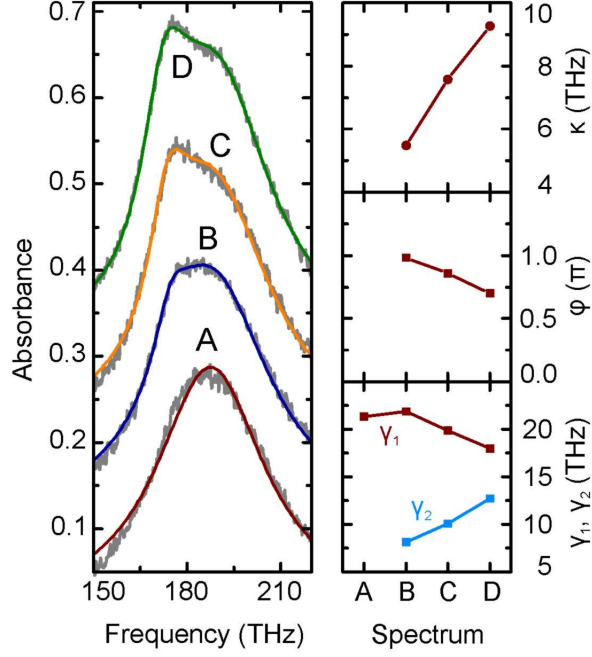


Figure 3.38.: Fit curves of equation 3.1 to the experimental spectra. The fit parameters κ , φ , γ_1 , and γ_2 are obtained from the experimental spectra and shown in the right panels.

where $\Omega_d = \omega - \omega_0 + (i\gamma_1/2)$ and $\Omega_q = \omega - \omega_0 + \delta + (i\gamma_2/2)$ have been used, and f is an amplitude coefficient. $A(\omega)$ represents the imaginary part of the solution of the coupled differential equations of two oscillators, which gives the dissipated energy. Fits to the experimental absorbance spectra using equation 3.1 are shown in figure ???. As expected, the linewidth of the quadrupolar oscillator is smaller than that of the dipolar oscillator. For increasing offset, the coupling amplitude κ increases, at the same time, the phase φ changes to a final value of $\varphi = 0.7\pi$ for maximum offset.

To further investigate the phase behavior we performed electromagnetic field calculations, which are displayed in figure 3.39 (a). The fields were evaluated for a vertical spacing of $d_z = 100$ nm and an offset of $S = 120$ nm at $f_q = 152$ THz. As we deal with a plasmonic system that intrinsically relies on retardation effects, it is important to evaluate the fields in different planes perpendicular to the light propagation axis. Therefore the field cross sections in a plane slightly above the dipole and the quadrupole are displayed. Likewise, the fields are shown for different times $\omega_q t$, with $\omega_q = 2\pi f_q$. The field amplitude at the dipole wire is maximum for $\omega_q t = 1.24\pi$, and at the quadrupole wire pair for $\omega_q t = 1.74\pi$. For both maxima the field at the respective other oscillator is very low, indicating an out-of phase oscillation of dipole and quadrupole. This can be observed in more detail in figure 3.39 (b): here the field intensity at two distinct points, as indicated by circles in figure 3.39 (a), at the tip of one quadrupole wire (light blue) and the dipole wire (gray) are shown as a function of time.

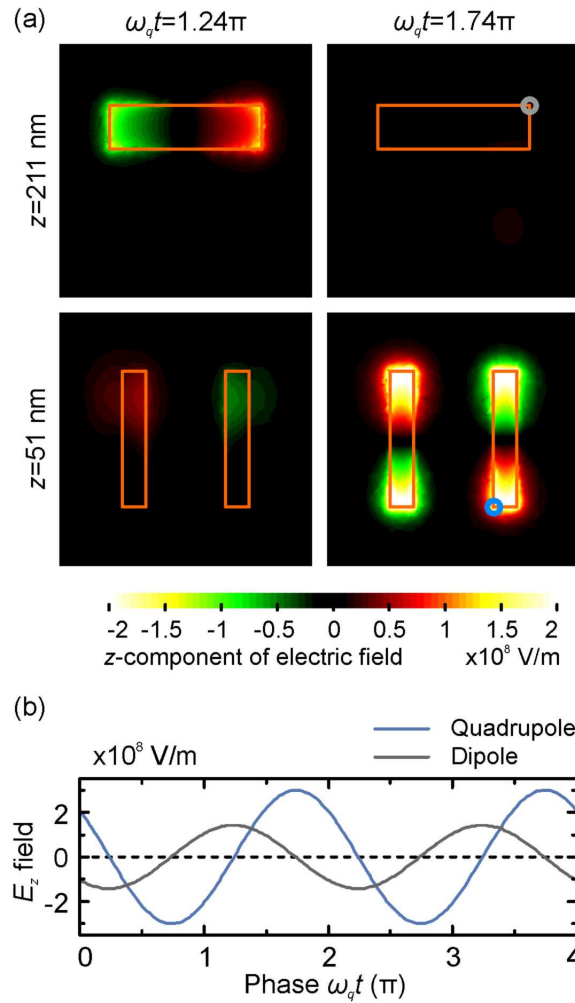


Figure 3.39.: (a) Calculated z -component of the electric field in a plane slightly above the dipole wire (top row) and the quadrupole wire pair (bottom row). Obviously, maximum field strength at the dipole and quadrupole wires are observed at different times. z denotes the vertical position of the cross section. The field at the former is maximum for $\omega_q t = 1.24\pi$ (left column) while the field at the latter reaches its maximum for $\omega_q t = 1.74\pi$ (right column). (b) Calculated time evolution of the electric field strength at the dipole and quadrupole wire tip (position indicated by a blue and gray circle in (a)). The phase difference between both oscillators is 0.5π .

In conclusion, we have demonstrated an analog system to electromagnetically induced absorption for classical oscillators by coupling a plasmonic dipole nanowire to a plasmonic quadrupole wire pair. The coupling was realized such that excitation of the quadrupolar resonance is still possible, but phase retardation due to enlarged spacing between the oscillators is already significant, hence operating in an intermediate coupling regime. Therefore we were able to manipulate the coupling phase of the oscillators and obtain constructive interference of the two excitations, leading to enhanced absorption. This intermediate coupling regime offers new fascinating possibilities such as phase control for plasmonic coupling [184].

It is noteworthy that, unlike the plasmonic analog of EIT, it is not possible to realize our system mechanically by oscillators and springs [144], as the coupling force is not instantaneous but inherently relying on retardation.

3.5. Temperature-dependent Measurements of the EIT Structure

One of the main benefits afforded by plasmonics is simultaneously one of its biggest drawbacks: Plasmonic resonances couple extremely well to an external light field. On the one hand this allows funnelling energy from the farfield into the near-field of the particle with an astonishing efficiency. Due to reciprocity this as well works the other way round: Processes occurring in the nearfield of a plasmonic resonance can communicate with the outside world by radiating energy into the farfield, such as emitters coupled to an plasmonic antenna or changes in the dielectric environment sensed by a plasmonic particle. On the other hand this efficient coupling leads to an extremely small lifetime in the order of 10 fs for a plasmonic excitation [93, 185]. In terms of resonators, plasmon resonances have very poor quality factors as they store energy only for a very limited time. As a consequence, a plasmonic resonance has a huge spectral width. For quite some applications this is bothersome. If, e.g., the shift of a resonance is to be detected, the overall linewidth should be small and thus the steepness of the change large. Additionally, small dephasing times lead to small field enhancements. Intuitively, this behaviour is obvious: The longer energy can be stored by the resonator, the higher the field concentration will be.

Hence, it is highly desirable to reduce the linewidth of plasmonic resonances. The decay of a plasmon occurs due to the loss of coherence in the system. On the one hand energy can be lost due to radiative decay. On the other hand inelastic scattering processes between electrons and electrons and electrons and phonons occur in the nanoparticle. An additional channel of coherence loss is given by elastic scattering processes, where no energy is dissipated but rather phase relations are lost. All above mentioned processes

occur for a single particle. If one studies an ensemble of particles one has to consider inhomogeneous dephasing, that is, different resonance frequencies of the individual particles [185,186]. Due to these differences, the overall phase relation between the individual resonators is lost, leading to an additional resonance broadening of the ensemble.

Plasmonic systems are radiation damped systems. The main dephasing channel is radiative loss. In order to decrease the resonance linewidth one should therefore make use of plasmonic dark modes. These modes do not couple directly to the external light field and can thus not decay radiatively. Their linewidth is therefore solely limited by the intrinsic scattering processes (and, to be accurate, by inhomogeneous broadening in an ensemble). This concept has been utilized in a plethora of systems and studies. The most prominent one is a dolmen type electromagnetically induced transparency (EIT) structure. Here, a dipolar resonance supported by a single wire, is coupled to a pair of wires which support a quadrupolar resonance. This quadrupolar resonance can not radiate its energy, the coherence is solely lost nonradiatively. The plasmonic coupling of the two resonances leads to the formation of two new collective modes which manifest themselves as scattering peaks in the spectrum. Both modes in part inherit the linewidths of the initial modes as they are the bonding and anti-bonding combinations of these. As a consequence, the overall spectral response of the systems exhibits spectral features with sub-dipole linewidths.

A further reduction of the spectral linewidth is only possible by reducing the nonradiative losses in the system. One straightforward idea is thus to study the temperature dependence [187, 188] of such a plasmonic EIT system. By cooling the system, more and more phonon modes are frozen, hence severely reducing the electron phonon interaction [187].

The experimental setup consists of a FTIR spectrometer connected to an IR microscope attached to a cold finger cryostat. Liquid helium circulating in the cold finger allows to cool down the sample to about 10K. Due to the presence of the cold finger, only reflectance spectra can be measured. The setup is been operated by the group of Prof. Dressel in the 1st Physics Institute and the measurements have been performed by Rebecca Beyer.

Figure 3.40 depicts the measured reflectance spectra of a stacked dolmen type EIT structure [141] for temperatures between 300 K (room temperature) and 10 K. The black spectrum represents the measurement at room temperature and serves as comparison. The spectra clearly show that the overall change in the spectral response is very small. Starting from about 200 K one observes slight changes in the spectral response, in particular the scattering maxima of the two modes is increased. This trend continues for decreasing temperature, yet the overall changes remain small. However, the response indeed indicates a reduction of the resonances linewidth. Figure 3.41 depicts the measurements for 300 K, 50 K, and 20 K for better visibility of the changes. The measurements clearly show the expected trend, however the effect is extremely small.

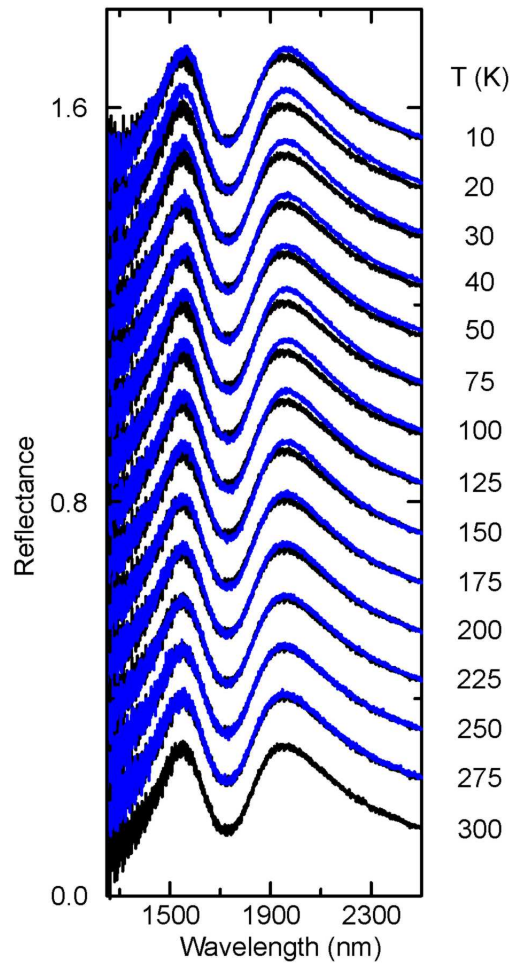


Figure 3.40.: Temperature depended measurements of the reflectance of a dolmen type stacked EIT structure. Starting from a temperature of about 200 K the optical response changes slightly, this trend continues for further reduced temperatures. However, the overall changes are marginal. The intrinsic losses of gold are dominated by electron-electron interactions which are temperature independent. The strongly temperature dependent electron-phonon interaction plays a minor role.

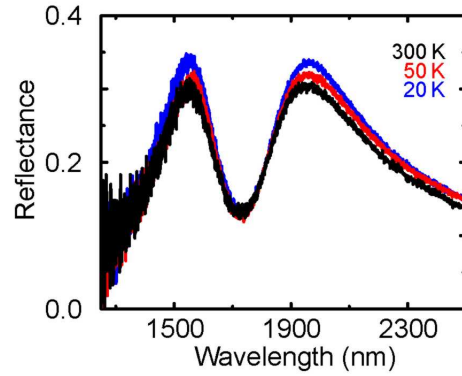


Figure 3.41.: Temperature depended measurements of the reflectance of a dolmen type stacked EIT structure, for 300 K, 50 K and 20 K, for better comparability.

Overall, the observed behaviour is not surprising as the contribution of electron-phonon scattering to the intrinsic losses is small, it is dominated by electron-electron interactions which are, to good approximation, independent of the temperature [187, 189].

In order to gain quantitative values one would need to model the optical response of the system. In previous publication a simple coupled harmonic oscillator model has been used [141, 144, 190]. In particular, it allows extracting the damping constants of the bright and dark modes, which are given by the radiative and nonradiative losses. From the temperature dependence of these values one can conclude on the actual contribution of electron-phonon interaction. However, the model provides an expression for energy dissipation, which would correspond to the absorbance in our system. Yet, due to the measurement geometry we can only measure the reflectance R . However, only when measuring the transmittance T as well one can calculate the absorbance A by assuming $A=1-R-T$ holds.

3.6. Conclusions, Summary & Outlook

The first part of this chapter studied the optical properties of simple nanoparticle geometries. Their response is mainly covered by dipolar and thus spectrally broad resonances, leading to rather dull optical spectra. Nevertheless, we have found that nanoparticle arrangements can support collective modes and can thus possess optical properties that are radically different than the properties of the individual building blocks.

However, as soon as a plasmonic mode does not retain a dipole moment it will not directly couple to an external light field, hence being termed a dark mode. Such a dark mode can not decay radiatively, therefore its linewidth is solely determined by intrinsic losses, e.g., in the metal itself. Utilizing such dark modes allows creating narrow spectral

features in the otherwise broad dipolar response of plasmonic nanostructures. We have demonstrated this phenomenon in different systems, in particular in plasmonic oligomers and 2D and 3D arrangements of nanorods.

We theoretically and experimentally studied the transition from isolated to collective modes in plasmonic oligomers. The inter-particle distance plays a key role for the formation of collective modes. We have shown how the plasmon hybridization method can be applied to analyze the optical properties of plasmonic oligomers. The interference between a subradiant mode and a superradiant mode leads to a pronounced Fano resonance, which is governed by the presence of the central nanoparticle in the plasmonic heptamer. The experiment agrees very well with our simulation using the multiple multipole method. We have demonstrated that experimental observations of distinct spectral features are possible in high-quality nanolithographic ensemble structures. So far, bottom-up synthesis methods have been deficient in manipulating the inter-particle distance in a controlled fashion, therefore lacking the possibility to study the transition behavior in plasmonic oligomers.

Moreover, we studied the influence of individual particles on the collective behavior of plasmonic oligomers. We found that the defect position within the plasmonic oligomer plays a major role for the optical response. This indicates that particles at different spatial positions contribute unequally. The spectral overlap of the super- and subradiant modes can be tuned by the coupling strength, the center particle size, the outer ring particle size, and the number of ring particles. It is noteworthy that already a three-particle ring around a center particle can closely resemble the spectrum of an undisturbed heptamer. Upon shifting of the center particle towards the outer ring until touching, a pronounced long-wavelength mode appears for the incident polarization along the touching bridge. The Fano resonance diminishes due to the occurrence of the new mode. On the other hand, for the incident polarization perpendicular to the bridge, the Fano resonance is very robust against the defect introduced by physically connecting the two particles.

Furthermore, we studied theoretically and experimentally the appearance and properties of higher-order Fano resonances in large oligomer clusters. Calculating the near-field distribution allowed us to observe the hybridization of a second ring mode with the dark mode in a plasmonic heptamer, leading to the occurrence of a higher-order Fano resonance. Furthermore, we investigated plasmonic structures where we elongated the heptamers in one direction by adding additional center particles. When the incident polarization was set along the short axes of the clusters, higher-order Fano resonances up to a 3rd order dark mode were observed. In that case, due to the structural symmetry, an additional dark mode was only observed if the number of center particles is uneven. It is noteworthy that by changing the incident polarization by 90° only the fundamental dark mode could be excited for all elongated plasmonic oligomers. This can be used in future applications to turn on and off spectrally narrow resonances. By leaving out certain ring particles we could tune the 2nd order Fano resonance in energy and likewise

increase the modulation depth tremendously.

In utilizing the coupling between individual nanorods we have shown the classical analogue of electromagnetically induced transparency (EIT). Here, a pair of wires supports a dark quadrupolar resonance which is nearfield coupled to a bright dipolar resonance of a single nanorod. The interaction of these two modes leads to the formation of a narrow window of enhanced transmittance within former transmittance dip associated with the dipolar resonance. We have shown that such structures can be utilized as 3D plasmon rulers, which are capable of encoding their 3D arrangement in well modulated spectra with a number of pronounced spectral features.

What is more, we have demonstrated an analog system to electromagnetically induced absorption (EIA) for classical oscillators by coupling a plasmonic dipole nanowire to a plasmonic quadrupole wire pair. The coupling was realized such that the excitation of the quadrupolar resonance is still possible, but phase retardation due to enlarged spacing between the oscillators is already significant, hence operating in an intermediate coupling regime. Therefore we were able to manipulate the coupling phase of the oscillators and obtain constructive interference of the two excitations, leading to enhanced absorption. This intermediate coupling regime offers new fascinating possibilities such as phase control for plasmonic coupling.

We envision for the future plasmonic oligomers and complex nanostructures of different hierarchies, including three-dimensional oligomers, oligomers with defects or extremely high symmetry, oligomers that show aromatization effects, and oligomers functionalized with other materials, such as quantum emitters. Soon, bottom-up methods such as DNA scaffolding could also establish the framework for arranging high-quality plasmonic oligomers with different degrees of freedom in large quantities. [171, 191, 192]

In molecular physics, atoms join together in different combinations and configurations to form molecules. Analogically, this can be accomplished by using particles with different sizes and even different materials. [108] Metals with different plasma frequencies, for example gold and aluminium disks of an identical size, can lead to different spectral positions of their particle plasmon resonances. This offers an additional degree of freedom to vary the particle resonance position while conserving the structural symmetry of the system. As we have shown, it is possible to design structures of particular symmetries to generate independent spectral features at different polarizations. This might be useful in differential diagnostics applications. Introducing vertical coupling between the oligomer constituents is possible by building three-dimensional artificial plasmonic molecules using a layer-by-layer technique. The resulting interaction can be much stronger than lateral coupling. Additionally, the excitation of antisymmetric modes is facilitated by retardation effects. It is also remarkable that the electric fields at the Fano resonance are extremely localized in the gaps between the oligomer constituents. [117] This might make our geometry highly useful for practical applications, such as surface-enhanced Raman scattering, [193] plasmonic sensing, [26, 76] higher-order harmonics generation, [194, 195]

etc. Moreover, we have demonstrated that such artificial plasmonic molecules provide high tuning possibilities on multiple sharp spectral features. This makes them very suitable for low-loss nanoscale waveguiding in plasmonic nano-circuits, [196,197] high-Q applications, such as nanolasers, or strong coupling of quantum systems to nanocavities.

We believe the bridging of chemistry and plasmonics will initiate many novel phenomena and will bring about numerous useful electromagnetic analogues of chemical molecules in plasmonics.

4. Plasmonic Chirality

4.1. Introduction

Chirality has gathered significant interest in different fields of research due to its fundamental importance in nature and living matter. Chirality has two distinctive meanings. On the one hand it refers to a simple geometrical property: A chiral object cannot be superimposed with its mirror image. The original structure and the mirror image are called the two enantiomers of a chiral compound. On the other hand, chirality can manifest itself optically, namely in a different response of a chiral structure to left- or right-handed circularly polarized light. The interaction of chiral molecules or structures with circularly polarized light in turn causes a multitude of intriguing phenomena, such as circular dichroism or optical rotatory dispersion [198].

Life itself is about chirality. Starting from the essential amino-acids, via carbohydrates, all the way to the nucleic acids and proteins: A huge number of biomolecules are chiral. In fact, many molecules exist in only one possible handedness, e.g., all essential amino-acids are L-enantiomers, indicating that the associated physiological processes show 100% stereoselectivity [199, 200]. Accordingly, chirality and its origin has been the subject of intense research on the route to unravel the basic foundation of life itself [201–205].

Most naturally occurring chiral optical phenomena are intrinsically weak. Chiral molecules have small dipole moments and hence couple only weakly to an external light field. Sugar solution for example is known to cause comparably strong optical polarization rotation, nevertheless centimeters of solution at molar concentrations are needed for efficient rotation of linear polarization. Similarly, it is challenging to study chiral molecules or even to optically discriminate enantiomers.

Recently, it has been proposed that plasmonics, i.e., the optics of metal nanoparticles, might help in overcoming some of these fundamental limitations. Such nanoparticles are known for their highly efficient interaction with an external light field. This property is caused by the large dipole moments of the plasmonic resonances which fundamentally stem from the collective oscillation of the quasi-free conduction electrons. In particular, the interaction strength with an external light field surpasses the one for molecules

by orders of magnitude. Accordingly, it has been recently demonstrated that the chiral optical response of three-dimensional plasmonic nanostructures is significantly enhanced [206–219]. Moreover, it has been demonstrated that even handed planar plasmonic structures show huge chiral interaction with circularly polarized light despite the fact that they are not truly chiral [220–225].

In contrast to molecules, complex plasmonic oligomers composed of noble metal nanoparticles allow for a nearly arbitrary manipulation of their constitution and configuration [80]. This amazing potential enables us to design and tailor the optical response of plasmonic structures nearly at will [83, 84, 97, 121, 122, 135, 226]. We can thus optimize the property of a given structure in order to meet the needs of the intended application [23, 31, 227, 228].

What is more, it has been recently demonstrated that in the vicinity of chiral plasmonic structures electromagnetic fields with strong optical chirality are formed [229–233], which strongly interact with chiral molecules. It has been proposed that these fields might ultimately enable the detection of individual chiral molecules and their discrimination due to a significantly enhanced interaction of the molecules with the external light field mediated by the plasmonic nanostructure [234–236]. Nevertheless, these experimental studies are at the very beginning and yet need to be fully understood. In any case, for applications of chiral optical phenomena in plasmonic nanostructures, it is highly desirable to maximize the chiral optical response of a given structure while simultaneously allowing for a spectral tunability or possibly for broadband operation.

Combining chiral plasmonics and stereochemistry will hence open up an entirely new field of plasmonically enhanced chiral optical response in hybrid systems for the detection of chiral molecules, for the design of chiral optical modulators and devices [206], and applications in medicine and drug development [237, 238].

4.2. Compositional & Constitutinal Chirality

First studies have been undertaken to create three-dimensional and thus true chiral structures. Yet, the fabrication of three-dimensional chiral plasmonic structures that exhibit a strong chiral optical response remains an experimental challenge. Direct laser writing and subsequent metallization [206, 208], multilayer electron-beam lithography [209–212, 239], self-assembly [213, 240, 241], as well as DNA-enabled self-assembly techniques [171, 172, 215, 242–245] have been utilized so far. Here, we use the most flexible concept of three-dimensional chiral plasmonic oligomers that consist of individual metal nanoparticles with nearly arbitrarily selectable properties in order to create artificial plasmonic molecules by means of multi-layer electron-beam lithography.

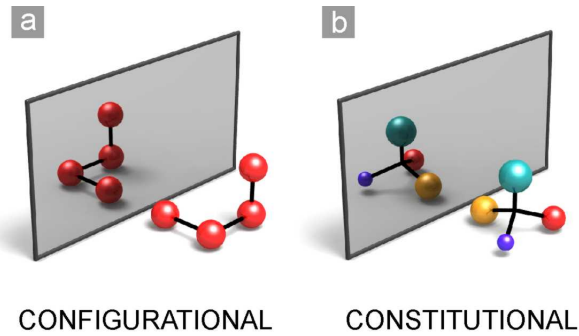


Figure 4.1.: From a geometrical point of view two basic possibilities can be envisioned how to render an arrangement of particles chiral: (a) Identical particles are arranged in a handed fashion, termed configurational chirality. (b) Different particles are arranged in an unhanded geometry, e.g. at the corners of a tetrahedron, termed constitutional chirality.

Figure 4.1 depicts a simplified sketch of the two basic and most straightforward geometrical possibilities to introduce handedness and hence to create chirality in an arrangement of particles. The first possibility is to arrange identical constituents into a handed structure, which we term configurational chirality. The second one uses a non-handed structure, in this case a tetrahedron, dressed with different particles at its corners, termed constitutional chirality. In chemistry the latter is referred to as a molecule with stereogenic center and constitutes a very prominent and hence an archetype structure. In contrast, inducing handedness due to configuration is less common [246]. The premiere reason for this is its mechanical instability without adding an additional scaffold.

Conceptually, both design strategies can be transferred to plasmonic molecules [171,214,215,247–249]. Here the coupling is mediated by the plasmonic near-fields. It is crucial to note that the constituents of the plasmonic molecules do not necessarily couple despite the fact that they are in close proximity. Efficient coupling is only possible if the individual plasmonic atoms have similar resonance frequencies, as plasmonic coupling is resonant coupling. Indeed, we show that in plasmonic chiral molecules only configurational chirality will manifest itself in a strong chiral optical signal and that compositional plasmonic chirality is not favorable.

In order for particle assemblies to be chiral they need to be truly three-dimensional. Such clusters can be fabricated using the very versatile top-down technique of electron-beam lithography combined with layer-by-layer stacking [250]. Figure 4.2 depicts exemplary tilted view scanning electron microscope (SEM) images of fabricated two-layered quadrumer structures. The first layer consists of three particles arranged in an L-shape. The fourth particle is stacked on-top of the first layer and determines the handedness of the structure. The individual clusters are arranged in a C_4 symmetric lattice in order to prevent biaxiality of the super-structure and hence to suppress contributions of polarization conversion [251].

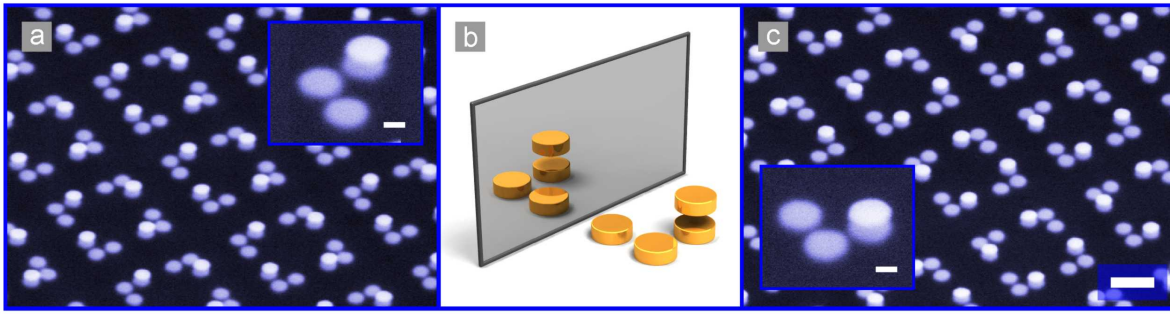


Figure 4.2.: (a) and (c) Tilted overview SEM images of chiral plasmonic molecules. b) Schematic sketch. The quadrimeric structures consist of two layers fabricated by electron-beam lithography. The first layer consists of three particles arranged in an L-shape, the second layer contains a single dot. The position of the dot in the second layer determines the handedness of the structure. The individual clusters are arranged in a C_4 symmetric lattice, which prevents the super-structure from being biaxial and thus suppressing polarisation conversion. The scale bar of the overview is 500 nm, for the insets 100 nm.

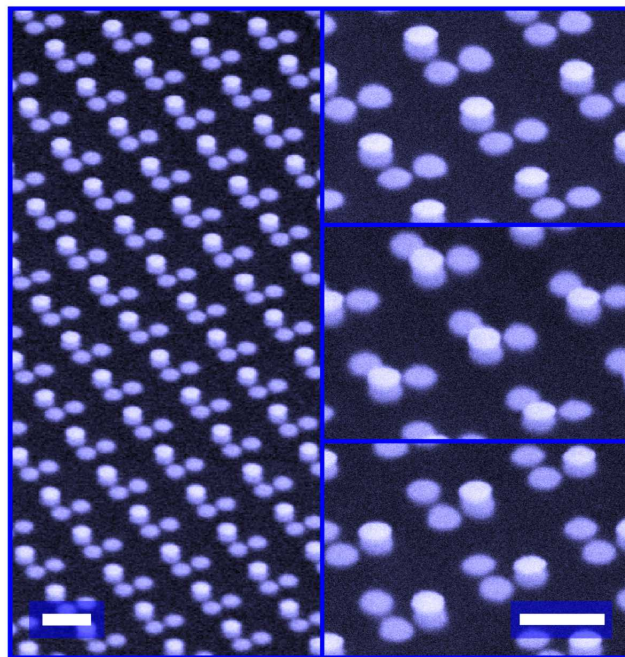


Figure 4.3.: Left side: Exemplary tilted view SEM image of chiral quadrumer clusters arranged in a regular square lattice. Right side: Left- and right-handed as well as achiral clusters. All scale bars are 500 nm.

Figure 4.3 depicts SEM images of clusters which are arranged in a regular square lattice. We have fabricated the structures in order to demonstrate the importance of uniaxiality for the optical properties. Figure 4.4 therefore shows the optical response of these clusters under circularly polarized excitation. Figure 4.4 (a) depicts ΔT spectra for forward and backward illumination of only the first layer. A strong signal is present which is nearly perfectly mirrored at the zero line for change of the illumination direction. This signal stems from the fact that the superstructure consisting of the individual clusters is biaxial. Due to different refractive indices for light polarized along the two main axis of the lattice polarization conversion occurs. If the illumination direction changes, this contribution must indeed change its sign, which is observed in the experiment. Figure 4.4 (b) shows the ΔT spectra for forward and backward illumination of a left-handed cluster, as shown in the inset. For a true chiral signal one expects identical spectra. However, strong differences can be observed. Judging from the conclusions drawn from Figure 4.4 (a) this behaviour is again caused by polarization conversion. The optical response is a combination of the chiral optical one and polarization conversion. That the spectra look different is immediately clear, as the chiral optical signal does not change sign for change of the illumination direction, the signal stemming from polarization conversion however does. Therefore, in the one case the two spectral responses are added in the other they are subtracted. To first order approximation one can take this into account by assuming the following to hold true

$$\Delta T_{measured}^{up} = \Delta T + \Delta T_{planar}^{up} \quad (4.1)$$

$$\Delta T_{measured}^{down} = \Delta T + \Delta T_{planar}^{down} \quad (4.2)$$

and

$$\Delta T_{planar} = \Delta T_{planar}^{up} = -\Delta T_{planar}^{down} \quad (4.3)$$

then

$$\Delta T_{planar} = 1/2 \left(\Delta T_{measured}^{up} - \Delta T_{measured}^{down} \right) \quad (4.4)$$

where up and down denote the two illumination directions, ΔT the "true" chiral signal which does not change upon illumination direction change, and ΔT_{planar} the contribution from polarization conversion. These relations then allow to calculate the ΔT spectra from the two measurements in forward and backwards illumination direction. [252]

It is important to note that this technique might not be entirely correct as it assumes the chiral signal to stay perfectly the same upon change of direction. Additionally, we assume that the chiral signal and the polarization conversion are purely additive and can be disentangled which is not necessarily true for strong signals [253, 254]. Nevertheless, Figure 4.4 (c) depicts the calculated ΔT spectra using the above relation. Overall, we find a good agreement with the expected behavior. The chiral optical response of the two enantiomers changes sign for interchanged handedness and the achiral structures exhibits significantly reduced signal strength. However, there is still significant signal

left despite the fact the structure should be achiral. The cause of this behavior is not clear at the moment as it might be connected to calculation or to fabrication tolerances, yet it will be discussed in detail below.

In order to characterize chiral structures one normally examines the circular dichroism (CD) spectra. CD is defined as the difference in absorbance for left and right circularly polarized light. In contrast to transmittance, our setup does only allow measuring the reflectance R_{RCP} and R_{LCP} for circularly polarized light in a very limited wavelength range. Outside this range the footprint of the sample, its reflectance, the intensity of incoming radiation, as well as the detector sensitivity are not large enough to perform reasonable measurements. Thus we define the quantity ΔT as the difference in transmittance T_{RCP} and T_{LCP} for right and left circularly polarized light, respectively. As we ensured the uniaxiality of the superstructure we can assume any contribution of polarization conversion to be negligible, hence the transmittance difference ΔT is directly correlated to CD . [251] In order to experimentally confirm this assumption we have performed reflectance and transmittance measurements with circularly polarized light in the wavelength range between ~ 1000 nm and 1600 nm. The resulting $\Delta T = T_{RCP} - T_{LCP}$ spectra and $CD = A_{LCP} - A_{RCP}$ spectra are shown in Figure 4.5. Note, that the order of RCP and LCP changes as $A = 1 - T - R$ holds. We find excellent agreement between the two sets of spectra, confirming that no contribution of polarization conversion is present and the entire optical response is dominated by the difference in absorbance for left- and right-handed circularly polarized light. In the following it is thus sufficient to examine the $\Delta T = T_{RCP} - T_{LCP}$ spectra which can be measured over the required broad spectral range. From now on, all structures will be arranged in a C_4 symmetric lattice.

Figure 4.6 depicts the transmittance spectra for circularly polarized excitation for the left-handed configurationally chiral cluster. The spectra show a number of resonances and pronounced differences, indicating strong chiral optical activity. Accordingly, the transmittance differences, as shown in the upper row of Figure 4.6, exhibit values as high as 7%. The complicated structure of the spectra makes a clear assignment of modes difficult. In fact, as four particles, each exhibiting two energetically degenerate modes laying in plane of the disks are interacting a significant number of collective modes is to be expected.

Figure 4.7 depicts spectroscopic results for configurationally chiral clusters. The transmittance difference reaches values up to 7%. Changing the handedness of the structures is expected to flip the ΔT spectrum, which is convincingly demonstrated by the excellent mirror symmetry of the two spectra with respect to the zero line. The achiral structure shows a small remaining signal which most likely stems from fabrication tolerances, e.g., the relative positions of the upper dots of the left- and right-handed structures. The remarkable sensitivity of the structure to these minute deviations will be discussed in detail below. As an imported control experiment Figure 4.7 (b) shows the ΔT spectra for the left and right handed enantiomers for opposite illumination directions. For a

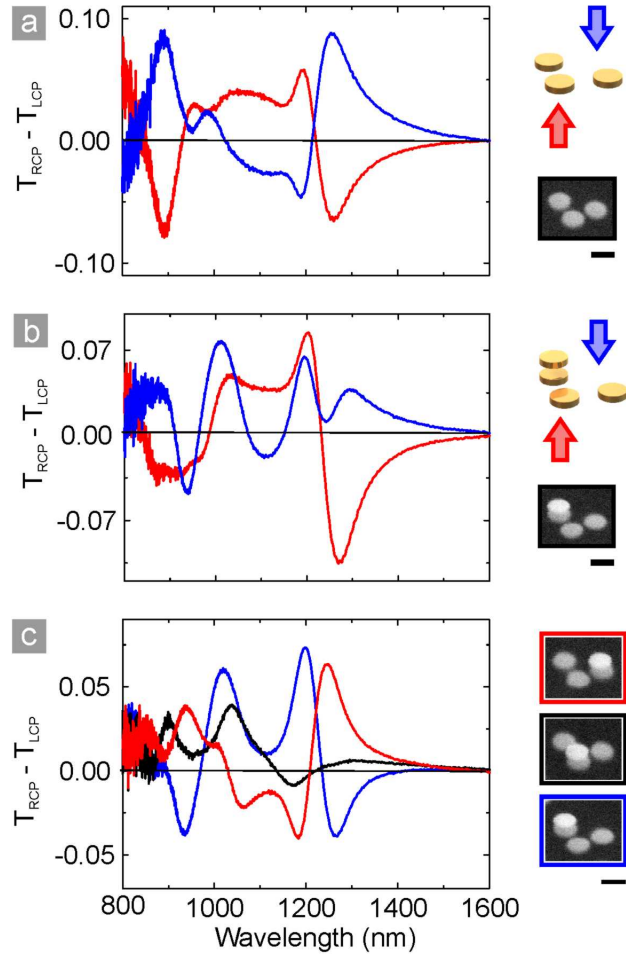


Figure 4.4.: Chiral optical response of the clusters arranged in a regular square lattice (with no C_4 superstructure symmetry). (a) Spectra for forward (blue) and backward (red) illumination of only the first layer. (b) Spectra for forward and backward illumination of the left-handed structure shown in the inset. (c) Calculated chiral optical response of the clusters, for details please refer to the text. All scale bars are 200 nm.

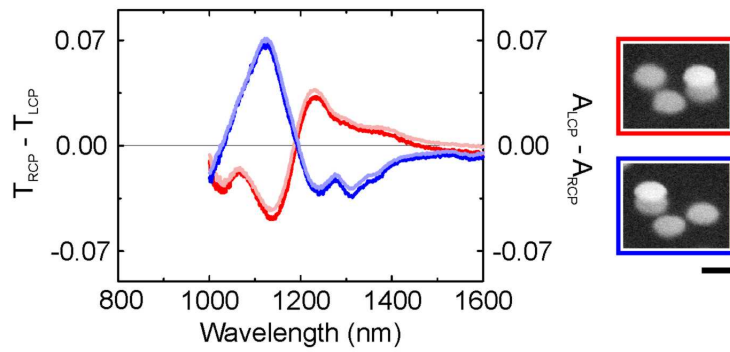


Figure 4.5.: Comparison of the ΔT spectra (dark blue and red) and the difference spectra of the absorbance (light blue and light red). Due to limitations of the used spectrometer, reflectance spectra for circularly polarized light are only measurable in the depicted wavelength regime. The spectra show that indeed all signals are caused by circular dichroism and the $\Delta T = T_{RCP} - T_{LCP}$ spectra yield the same information as the absorbance spectra. The scale bar is 200 nm.

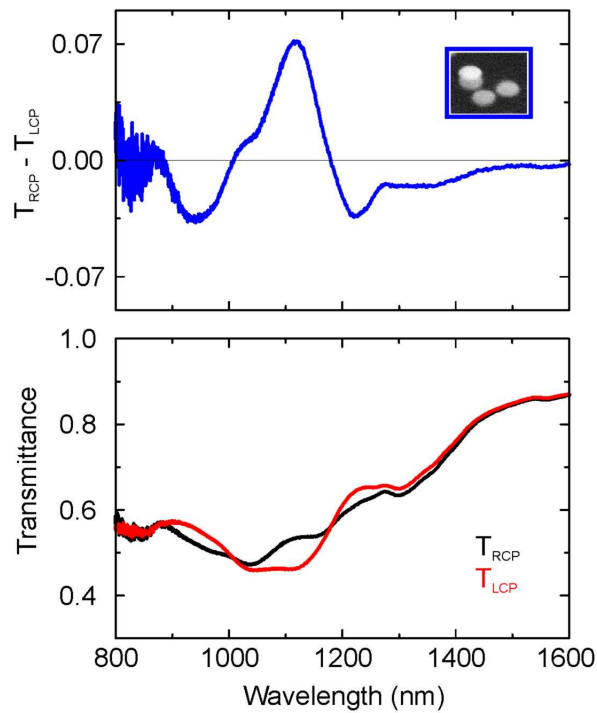


Figure 4.6.: Transmittance spectra for right- and left-handed circularly polarized light for the left-handed configurationally chiral cluster shown in the inset (lower row) and calculated transmittance difference (upper row).

true chiral structure (as warranted by the C_4 symmetry of our superstructure arrangement) the handedness does not depend on the direction of light propagation. Indeed, we find nearly perfectly identical spectra for both structures under forward and backward illumination. This finding additionally underlines that we do not observe polarization conversion as this contribution would change sign for different illumination directions (cf. Figure 4.4).

Naturally occurring chiral optical materials show weak CD, showing values of the dissymmetry factor g of about $\sim 10^{-7}$ to $\sim 10^{-5}$. Our structures, being about 100 nm in thickness, show enormously high values of around 7% transmittance difference for left and right hand circularly polarized light, which roughly corresponds to a maximum dissymmetry factor $g \sim 0.14$ for the structures of Figure 4.7 (a). This behavior can be explained as follows: If circularly polarized light interacts for example with a chiral molecule, it displaces the electron clouds of the molecule from their equilibrium position forcing them to move on helical paths. The helical movement of these displacement currents (as generally no real current can flow) gives rise to an induced magnetic moment component parallel to the usual electric dipole moment and in the direction of propagation of the light, resulting in a unique interaction of the molecule with circularly polarized light. In our system, however, we can excite real currents flowing in the disks together with displacement currents between the elements. Overall, these real currents and the displacement currents in the plasmonic molecule are much stronger compared to a molecule, as the gold particles possess a large number of free electrons. Basically, this huge interaction strength is the basis of all plasmonic phenomena. Hence, once more, one benefits from the resonant excitation and generation of localized plasmons associated with huge dipole moments and flowing currents, explaining the strong circular optical response of our clusters.

Figure 4.8 depicts the optical response of clusters arranged in a constitutional fashion, comprising of particles of different size (200 nm, 150 nm, 90 nm, and 60 nm, respectively). In contrast to the configurational case shown in Figure 4.7 we only observe a very weak chiral optical response. The reason for this behavior is an insufficient resonant plasmonic coupling between the particles. From a coupling point of view the structure consist of four nearly or completely uncoupled plasmonic particles and hence does not possess a strong chiral optical response. The remaining response most likely stems from a weakly resonant coupling of the second biggest particle in the upper layer to the biggest particle of the lower layer. For comparison, the transmittance spectra for left- and right-handed circularly polarized light (for the structure shown in the inset), are depict in figure 4.8 (c). One still observes strong plasmonic modes within the measurement region, thus the absence of plasmonic activity is clearly not the reason for the vanished chiral optical response.

Figure 4.9 depicts spectra and SEM images of structures showing a combination of compositional and constitutional chirality, exhibiting no chiral optical response at all, despite the fact that these structures possess a geometrical handedness. Overall we can

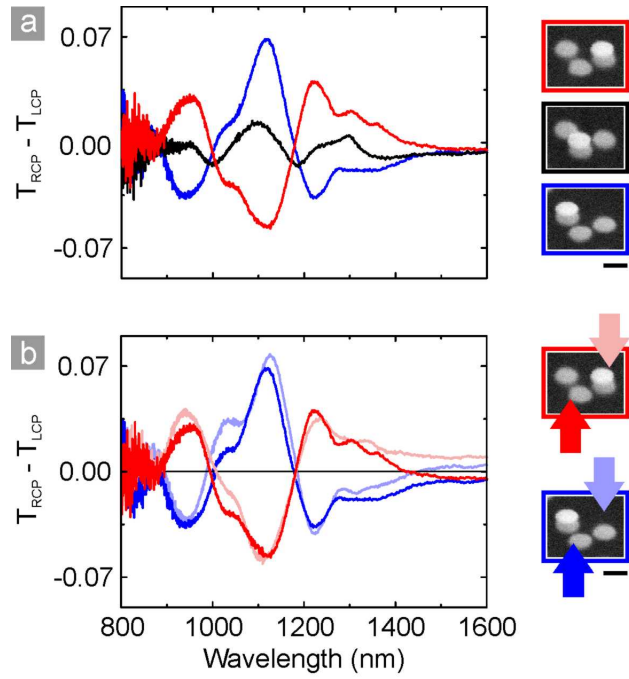


Figure 4.7.: (a) Experimental $\Delta T = T_{RCP} - T_{LCP}$ spectra calculated as the difference in the transmittance of right and left hand circularly polarized light. Two dispersive features can be observed with a maximum ΔT of $\sim 7\%$. The spectra are nicely vertically mirrored at the zero line for interchanged handedness. The achiral structure shows small differences in the transmittances which can be explained by deviations in the relative position of the upper layer dot. (b) As expected for a true chiral structure (warranted by our C_4 symmetry) the ΔT spectra do not significantly change for forward and backward illumination. The scale bars are 200 nm.

thus deduce that resonant plasmonic coupling between the clusters constituents is of utmost importance and an indispensable prerequisite for a pronounced chiral optical response.

The major importance of resonant coupling of the cluster particles is even more strikingly visible in figure 4.10 depicting the experimental proof of vanishing chiral optical response upon decreasing resonant coupling. The quadrumer structure becomes truly three-dimensional and thus chiral due to the coupling of the L-shaped nanoparticle arrangement to the single dot in the upper layer. Reducing this coupling should render a chiral optical response impossible. In order to prove this behavior we successively decrease the size of the dot in the upper layer. Both enantiomers with four equally sized particles in figure 4.10 (a) show strong chiral optical response. Reducing the diameter of the upper dot in figure 4.10 (b) from 200 nm to 140 nm significantly weakens the coupling strength of the upper dot to the lower layer. Yet, there is still a chiral optical response observable, although strongly reduced in magnitude. The chiral optical response vanishes completely for an upper dot diameter of 80 nm (cf. figure refFigure10c (c)). The resonance energies of the upper and lower layer dots are too different to still facilitate an efficient coupling. Despite the fact that the structure still shows a structural handedness it effectively collapses into a two dimensional system which cannot exhibit chirality. In order for the system to be "plasmonically" three-dimensional all the particles need to couple efficiently. In a plasmonic system a mere structural handedness does not suffice for a chiral optical response.

For comparison and completeness, figure 4.11 depicts the transmittance spectra for left- and right-handed circularly polarized light for one of each of the enantiomers shown in figure 4.10.

4.3. Three-dimensional Chiral Plasmon Rulers

The non-vanishing chiral optical response of the achiral structure in figure 4.7 is an intriguing phenomenon which has to be studied in greater detail. Inspection of the SEM images of these structures suggests small deviations of the position of the upper dot from its symmetric position. Yet, these small deviations cause a significant change in chiral transmittance ΔT . In biology and chemistry circular dichroism is a powerful tool for structural investigations. Likewise, we can expect that structural changes will have a significant impact on the chiral optical spectra of the plasmonic cluster hence rendering them ideal candidates for a three-dimensional plasmon ruler. [92, 161, 171, 255].

In order to test the capabilities of the chiral plasmonic clusters as three-dimensional plasmon ruler we fabricated a series of clusters deliberately displacing the upper dot from the symmetric position of the achiral structure. Figure 4.12 depicts a selection of

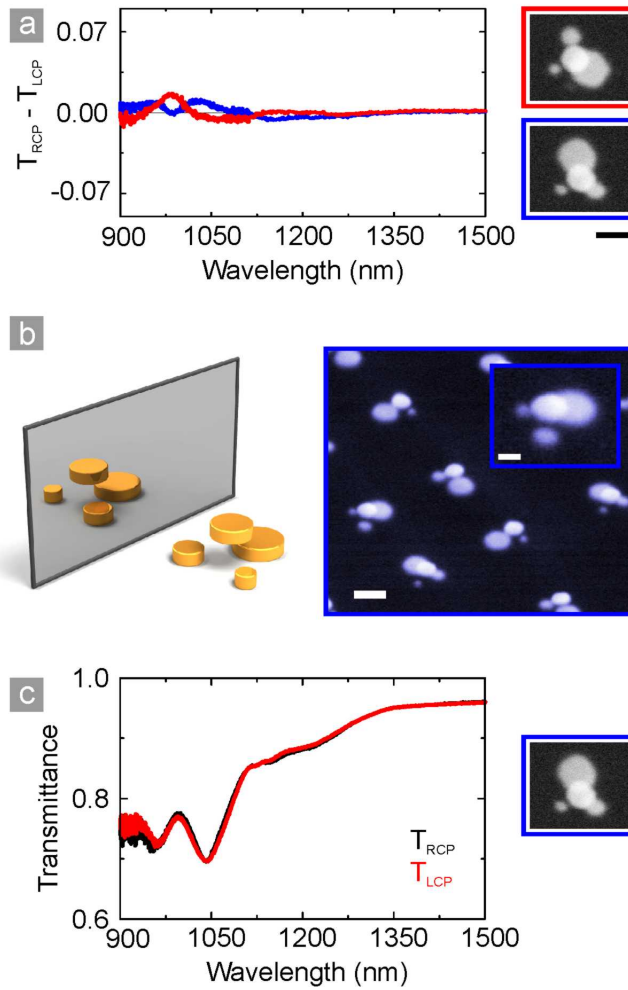


Figure 4.8.: (a) Spectra and SEM close-up micrographs of compositionally chiral clusters. The constituting dots in the tetrahedral structure are of different size (200 nm, 150 nm, 90 nm, and 60 nm, respectively) and consequently do not couple efficiently via their plasmonic near-fields to one another. The clusters hence comprise four nearly uncoupled and thus individual particles and therefore only show a very weak chiral optical response. Hence, compositional plasmonic chirality with different sized nanoparticles is at best very weak. The scale bar is 200 nm. (b) Artist's impression of the compositionally chiral clusters and tilted view SEM micrographs of the clusters. The scale bar is 100 nm for the close-up images and 200 nm for the overview. (c) Transmittance spectra for left- and right-handed circularly polarized light for the structure shown in the inset.

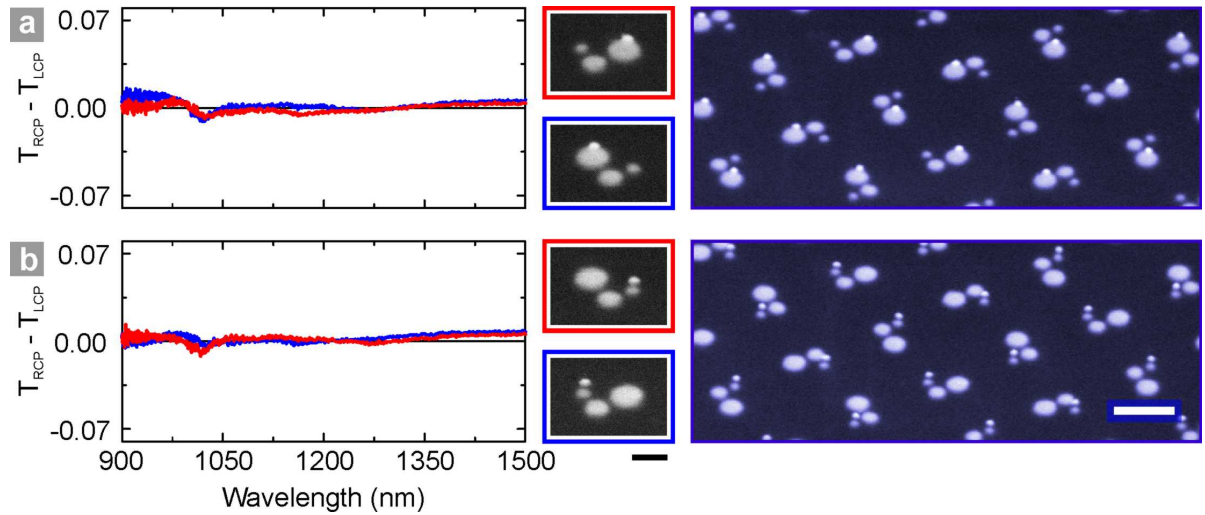


Figure 4.9.: Compositional chirality only leads to vanishing optical chirality in a plasmonic system. The constituting dots in the structures are of different size (200 nm, 150 nm, 90 nm, and 60 nm, respectively) and consequentially do not couple via their plasmonic near-fields to one another. The clusters hence comprise of four nearly uncoupled and thus individual particles and therefore do not show a chiral optical response. The scale bar for the insets is 200 nm, for the overview images 500 nm.

ΔT spectra (in blue) for five different displacements and the corresponding normal view SEM images, the complete series with displacements in 10 nm is depicted in figure 4.13. One observes huge changes in the ΔT spectra for comparably small relative sifts. This is particularly obvious when comparing the spectra before and after an additional shift. The grey spectra correspond to the spectra of the preceding displacement. For each step changes in the spectral shape as well as in the magnitude are clearly observable. Strikingly, this behavior will be visible for the analogous shift in the other direction as well, accompanied by a sign flip of the ΔT spectra. Hence, the position of the upper dot can be traced in 2D above the structure. Figure 4.14 demonstrates that this is still feasible when the dot is no longer on-top of the L-shape. It is noteworthy that even the position of the dot in the vertical direction can be traced. An increased (decreased) distance will lead to a decreased (increased) coupling strength of the upper dot to the L-shape. Overall, we hence have experimentally demonstrated that the three-dimensional chiral quadrumer cluster is capable to encode its arrangement in unique $\Delta T = T_{RCP} - T_{LCP}$ spectra, rendering the retrieval of the 3D structural information possible. 3D chiral plasmon rulers could utilize a lookup database, as in the case of nuclear magnetic resonance (NMR), where the optical spectra corresponding to all possible structural configurations are documented. Spectral features could then be associated uniquely to certain distortions.

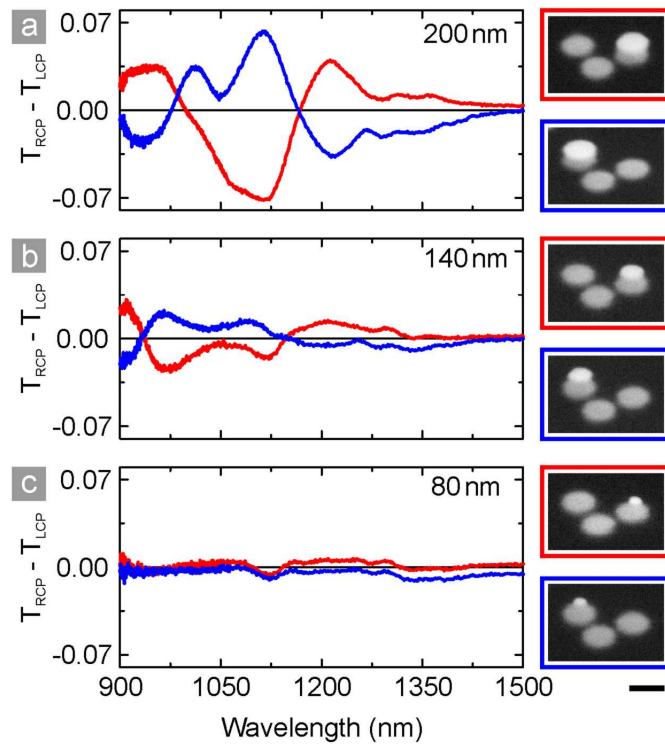


Figure 4.10.: Spectra and SEM micrographs of chiral oligomer clusters with different sized upper layer dots. When decreasing the size of the dot in the upper layer the plasmonic coupling between the lower layer and the upper layer vanishes. From a plasmonic coupling point of view this effectively collapses the system to a two-dimensional one which is not capable of supporting chiral optical properties. The scale bar is 200 nm.

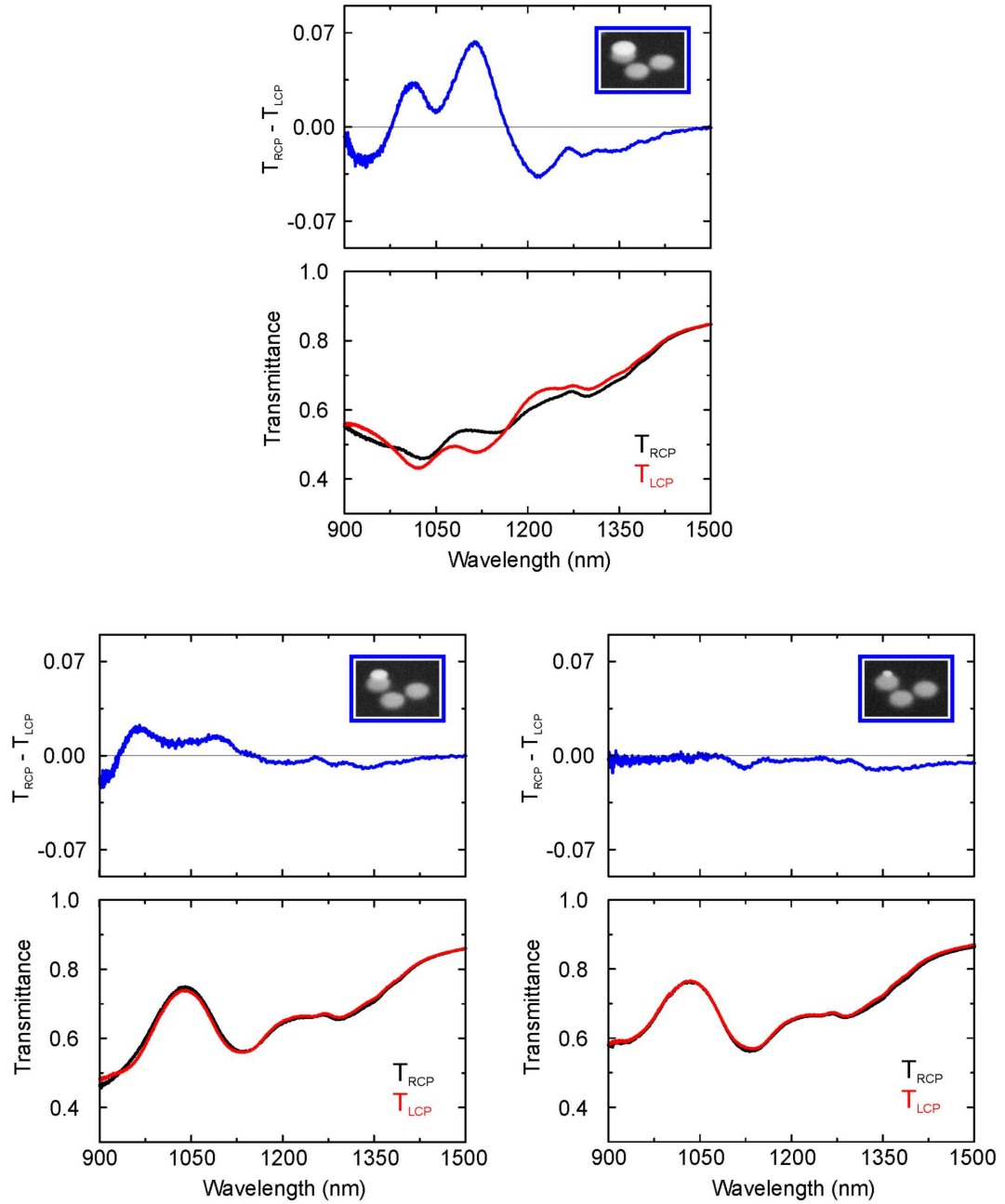


Figure 4.11.: T_{RCP} and T_{LCP} spectra as well as the difference spectra for the depicted enantiomers. All spectra show signatures of strong plasmonic modes. Under decreasing upper particle diameter, the coupling between the two layers vanishes, rendering the clusters two-dimensional in a plasmonic sense. Consequently, the chiral optical response vanishes and the T_{RCP} and T_{LCP} spectra become almost identical.

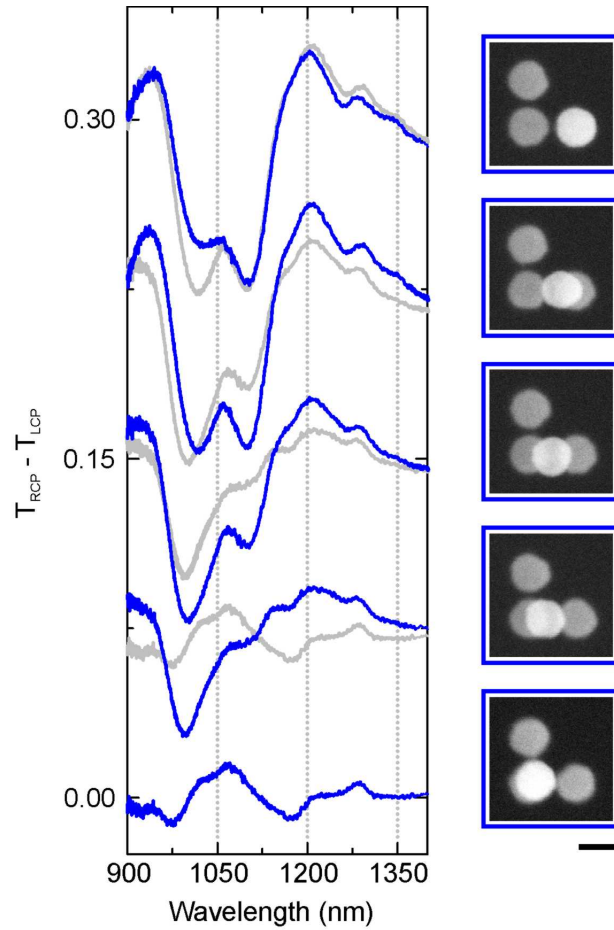


Figure 4.12.: Chiral plasmonic nanoparticle clusters can serve as a three-dimensional chiral plasmon ruler. $\Delta T = T_{RCP} - T_{LCP}$ spectra for a set of deliberate shifts of the upper dot from the symmetric achiral position (blue) and their corresponding SEM images. The spectra are shifted upwards for clarity. The grey spectra depict the response of the preceding structure to facilitate comparison of the spectra. The spectra show significant changes of the spectral features as well as in the magnitude of the signal. The scale bar is 200 nm.

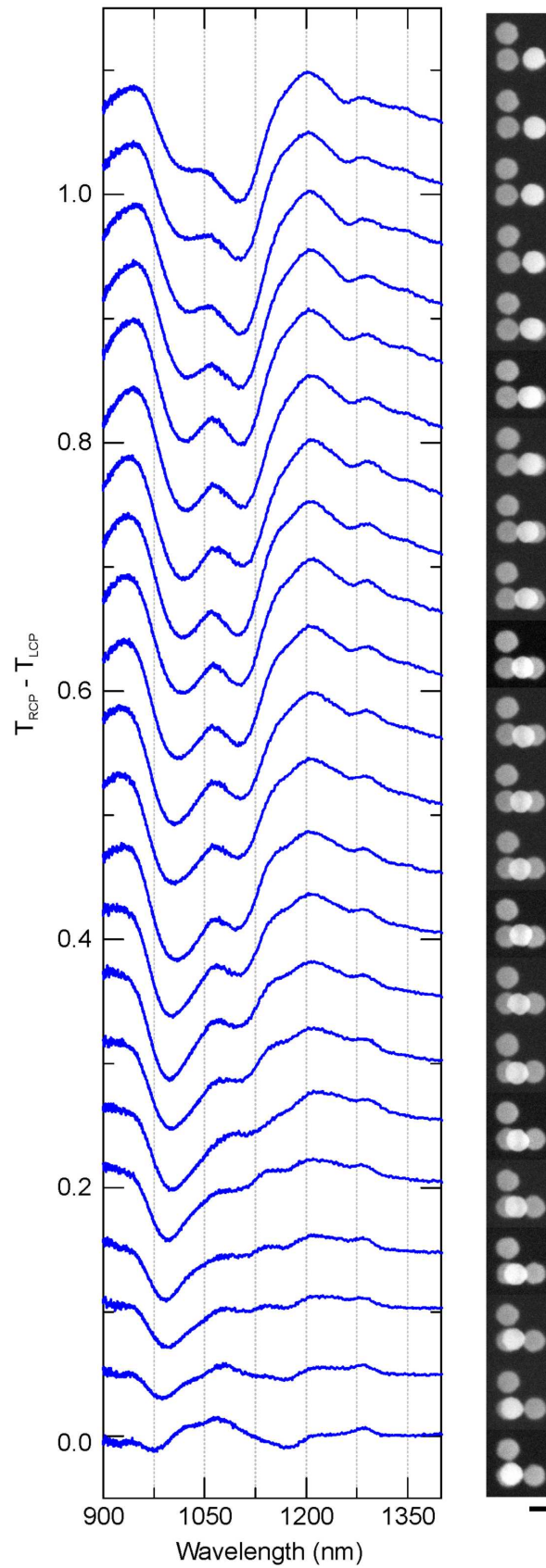


Figure 4.13.: Demonstration of the three-dimensional chiral plasmon ruler. The upper dot is successively displaced in nominal steps of 10 nm. Despite the rather small relative displacements one can observe clear and pronounced changes in the spectral shape as well as in the magnitude. The spectra are shifted upwards for clarity. The scale bar is 200 nm

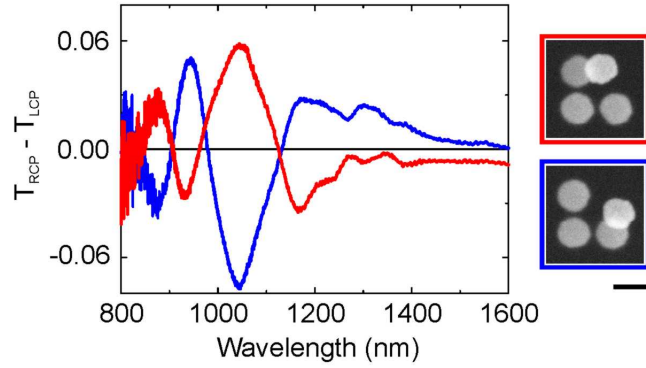


Figure 4.14.: Demonstration of the three-dimensional chiral plasmon ruler for displacements which are not along the arms of the lower layer L-shape. It is still possible to observe strong and well modulated $\Delta T = T_{RCP} - T_{LCP}$ spectra. The scale bar is 200 nm.

4.4. Charge Transfer in Chiral Plasmonic Oligomers

The most prominent example of a chiral structure is a spiral, cf. figure 4.15 (a). Yet, the fabrication of such structures remains challenging. Impressive work has been done utilizing direct laser writing and subsequent gold plating to obtain solid metal structures [206, 207] or electroless plating of a dielectric chiral matrix [208]. However, the miniaturization of these spirals in order to obtain a chiral optical response in the near infrared or even visible wavelength regime has not yet been demonstrated. A straightforward idea, however, is to replace the spiral with individual nanoparticles arranged in a handed fashion, as sketched in figure 4.15 (a). The depicted arrangement of six particles can be viewed as the first winding of a spiral. The benefit afforded by this strategy is threefold. Firstly, the fabrication of such structures is possible by self-assembly techniques [171, 243–245, 256], as well as multi-layer electron beam lithography [90, 209, 251]. Secondly, the fundamental plasmonic modes of the structure are significantly blue-shifted due to reduced coupling. Instead of conductive coupling, as in the case of a solid spiral, the particles interact via their respective near-fields. Thirdly, the spectral regime in which the chiral optical response occurs can be nearly arbitrarily shifted by changing the particle size and by choice of the appropriate metal [108, 257, 258].

A spiral is better approximated if more particles and more layers are utilized. In practice, both quantities are limited by experimental feasibility. Figure 4.15 (b) depicts artist's impressions as well as tilted view scanning electron microscope (SEM) images of our fabricated structures. The structures consist of two layers fabricated by electron beam lithography. Both layers contain three particles arranged in an L-shape. The layers are twisted with respect to one another, which determines the handedness of the resulting structure. Changing the size of the individual particles allows tuning of the coupling strength within each layer. An increase in particle diameter will increase the coupling due to closing of the interparticle gap. As soon as the particles touch the coupling mechanism

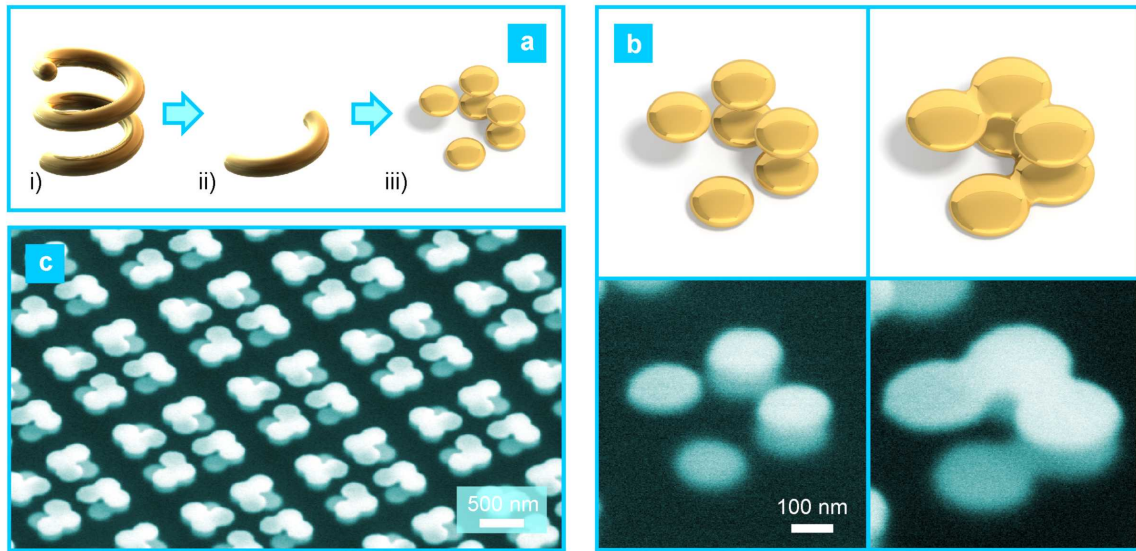


Figure 4.15.: (a) A 3D spiral is a prototype chiral structure. In order to experimentally realize such a configurationally chiral structure one can approximate the first winding of the spiral by a handed arrangement of individual nanoparticles. (b) Our fabricated structures consist of two twisted layers, each containing three particles arranged in an L-shape (artist's impression in the upper row, SEM micrographs of the fabricated structures in the lower row). This design furthermore allows merging the particles into one another, increasing the coupling strength. (c) Tilted overview SEM image of a fabricated array. The structures are arranged in a C_4 symmetric and thus uniaxial lattice in order to suppress contributions of polarization conversion.

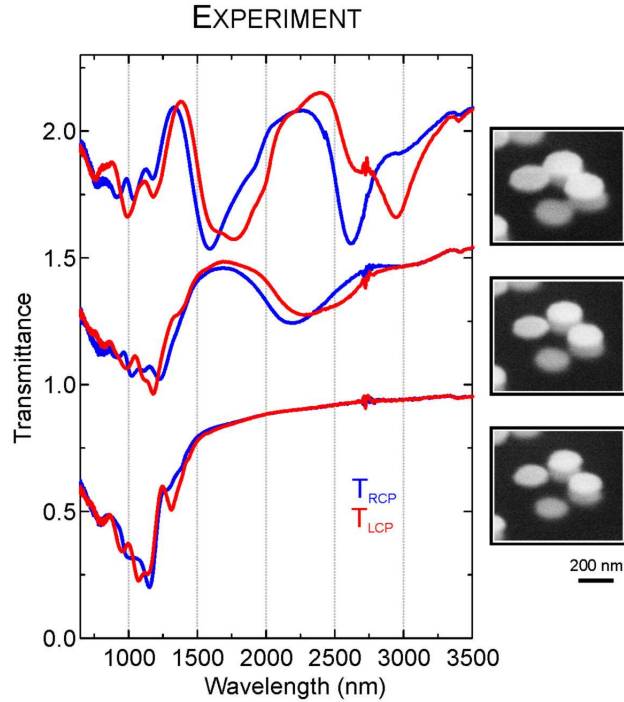


Figure 4.16.: Transmittance spectra for right- and left-hand circularly polarized light for oligomers with different diameter of the constituting particles as well as tilted view SEM images of the corresponding structures. The lowest row depicts the case of well separated particles, the middle row just touching particles, and the upper row the case of completely fused particles. The spectra are shifted upwards for clarity.

within the layers changes from capacitive, i.e., near-field coupling, to conductive coupling which leads to the formation of a charge transfer mode [129–131,259,260]. Thus, one can laterally merge the dots of each layer which significantly increases the coupling strength and the dipole moment of the resulting resonances. Moreover, it further improves the approximation of a three-dimensional spiral. Figure 4.15 (c) shows a tilted overview SEM image of our fabricated oligomer. The four elements of the unit cell are arranged in a C_4 symmetric fashion and thus form a uniaxial lattice which suppresses contributions of polarisation conversion.

In order to study the chiral optical response of our oligomers we have successively increased the size of the individual particles. Figure 4.16 depicts the transmittance spectra for right- and left-handed circularly polarized light for three different particle sizes. The lowest spectra show the response of an oligomer with well separated particles. The response is thus described in terms of capacitive coupling, i.e., near-field coupling. We observe strongly modulated spectra in the visible and near-infrared part of the spectrum with a number of different modes and a pronounced difference for the two different circular polarizations. This already indicates strong chiral optical interaction. The uppermost spectra illustrate the case of fully touching particles and are thus characterized

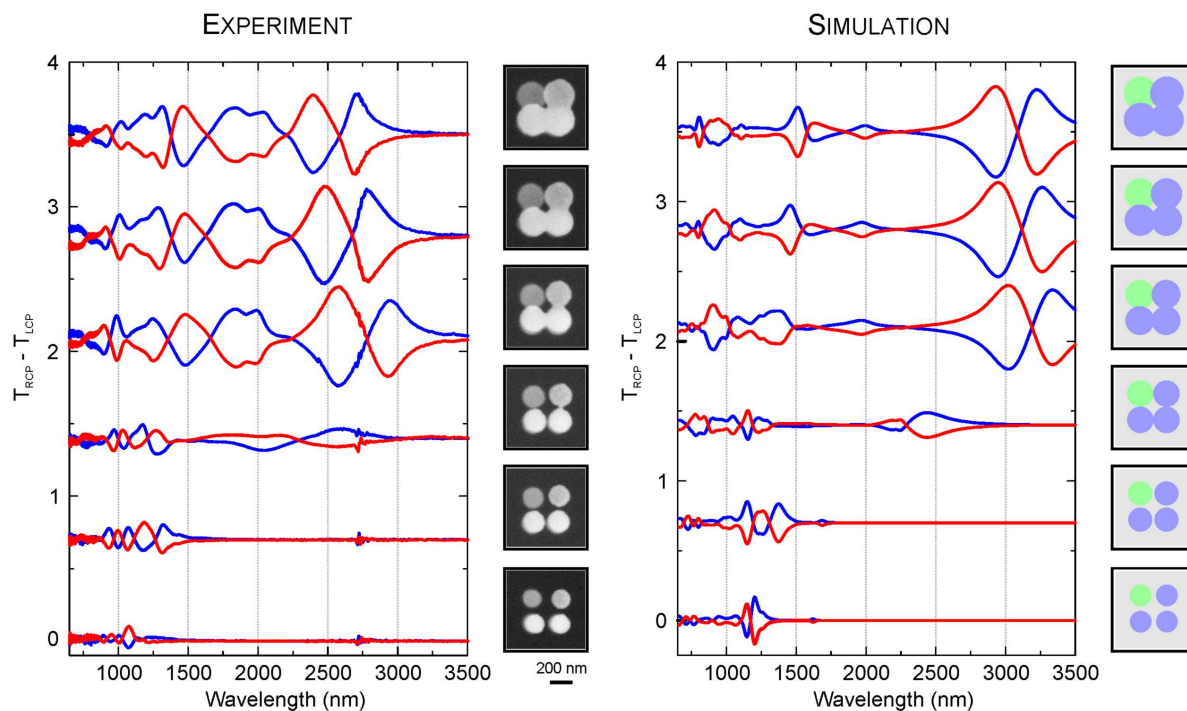


Figure 4.17.: Experimental (left) and simulated (right) ΔT spectra, defined as the difference in the transmittance of right- and left-handed circularly polarized light. The red and blue spectra correspond to the left- and right-handed enantiomers, respectively. In experiment and simulation one observes the appearance of a new fundamental and a number of higher order modes upon the increase of the size of the constituting particles (cf. the normal view SEM images and sketches). The reason is the transition from capacitive to conductive coupling and thus the appearance of a charge transfer mode. The difference in the transmittance of right- and left-handed circularly polarized light reaches values as high as 35%. The spectra are shifted upwards for clarity.

by conductive coupling and the appearance of the charge transfer plasmon. First of all we notice a significant red-shift of the fundamental plasmon mode from about 1200 nm to 3000 nm. This behavior is expected due to the increased length of the merged particles upon charge transfer. However, we as well observe a number of additional resonances in the visible and near-infrared wavelength range. Even in the visible these resonances show strong modulation which is comparable to the response of the oligomer with well separated particles. Overall, the differences for the two polarizations are even stronger in the conductively coupled case. The middle spectra depict the case for just touching particles. Due to fabrication tolerances not all particles are actually touching which allows us to observe the transition from the capacitively coupled to the conductively coupled case. Consequently, the spectra show the formation of the new lowest energy modes while the modes of the separated oligomer are still partially visible.

In order to directly compare the chiral optical response of the oligomers upon increasing

particle size we plot the experimental $\Delta T = T_{RCP} - T_{LCP}$ spectra for both enantiomers in the left column of 4.17. Compared to figure 4.15 we show additional oligomers with intermediate particles sizes which allows for a better understanding and visualisation of the transition behavior. The red and blue spectra correspond to the left- and right-handed enantiomers of each oligomer. For all cases we observe excellent mirror symmetry of the ΔT spectra which is expected for interchanged handedness. The two lowest oligomers correspond to the case of fully separated particles and thus to the near-field coupled regime. The coupling strength increases with increasing diameter as the spectral features are red-shifting. Yet, the overall mode structure remains unchanged. The next set of spectra shows the transition regime between capacitive and conductive coupling. Inspection of normal view SEM micrographs indicates that not all particles but only about $\sim 50\%$ are actually touching. Despite this uncertainty the mirror symmetry between the spectra of the two enantiomers is still excellent, indicating that the fraction of touching particles is about equal. When further increasing the size of the individual particles they start to fully merge. We observe the formation of an extremely strong and broadband chiral optical response between roughly 700 nm and 3500 nm, which corresponds to a bandwidth of more than 2 octaves. The transmittance difference reaches values up to nearly 35% which roughly corresponds to an ellipticity of 20° . The reason for the strong chiral optical response is most likely connected to the strongly increased dipole moment of the plasmonic resonances. The L-shaped particle which forms due to the merging of the individual particles possesses a significantly larger volume and thus a larger number of quasi-free conduction electrons and consequently a larger dipole moment of its plasmonic modes. Further increasing the size of the particles leads to a spectral shift of the resonances but no longer to a significant change in the mode structure, as the overall geometrical shape of the structure no longer changes. We expect that the mode structure will only significantly change again when the dotted L-shaped particle approaches a perfect undistorted L-shape. Additionally, one observes a blue-shift of the plasmonic resonances in the spectra, which is particularly obvious for the lowest energy modes. Intuitively one would have expected a red-shift due to the increased size of the merged particle. Yet, this red-shift is overcompensated by the blue-shift of the plasmon modes upon increase of the width of the structures which is accompanied by the size increase of the individual particles.

All our experimental findings are confirmed by numerical calculations (cf. figure 4.17, right column). The three-dimensional Maxwell's equations are solved using the finite element method (COMSOL Multiphysics Finite Element Analysis Simulation Software). The dielectric function of gold is taken from the Palik handbook [261]. A unit cell consisting four elements arranged in the C_4 symmetric fashion was simulated, which is the same as the fabricated structure shown in figure 4.15 (c). At the sides of the unit cell, periodic boundary condition is assumed in order to obtain the optical response of the whole oligomer array. A normal incident circularly polarized light source (500 to 3500 nm) is used. As the incident light wave strikes the structure, it will be absorbed, reflected or transmitted through the structure. The absorbed power is computed through the volume integration of the resistive heating in the gold nanoparticles. The reflected

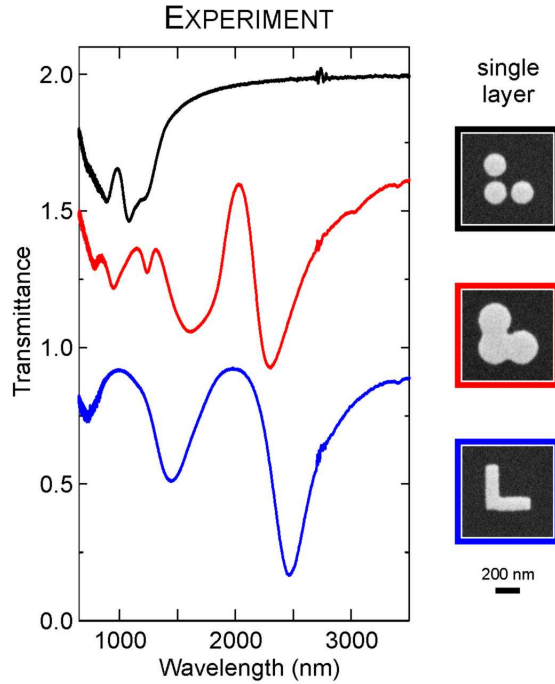


Figure 4.18.: Transmittance spectra under linear polarized excitation for single layered reference structures, which are isolated particles, merged particles, and a perfect L-shape. The dotted L-shape combines the benefits from the isolated dots and the perfect L-shape: A large number of resonances can be observed. The spectra are shifted upwards for clarity.

or transmitted power is calculated through the surface integration of the power flow over the surfaces far away from the nanoparticle layers. The sum of calculated power of absorption, reflection and transmission is checked against the incident power to ensure the accuracy of simulation. In addition, the near field information at the resonant wavelengths in which we are interested can be directly obtained from the simulations as well.

The transmittances to the right- or left-handed circularly polarized light are simulated for each oligomer, and the differences ΔT are obtained accordingly. The initial red-shift of the resonances as well as the later blue-shift are well reproduced. Overall, we observe a few small deviations. In particular, the simulation predicts a significantly larger spectral separation between the fundamental resonance and the higher order modes. Yet, the overall mode profiles are very well reproduced. We attribute the differences to the highly complex shape of the nanoparticles and the complex structure and arrangements. Small deviations between the simulated and measured structural geometry, which are well within the tolerances of the fabrication techniques, might cause already significant deviations.

So far, the appearance of the higher order modes remains unclear. Intuitively, one would

expect an overall red-shift of all modes and therefore the disappearance of a chiral optical response in the visible and near-infrared. The experimental spectra in figure 4.18 are capable to explain the observed phenomenon. As a reference we fabricated single layered structures, which are separated particles, merged particles, and a perfect L-shape. The spectra have been obtained under excitation with linear polarized light, polarized under 45° with respect to the lattice. Note that the structures are still arranged in a C_4 symmetric lattice, despite that fact that only one structure is depicted in the corresponding SEM micrograph for clarity. For the isolated particles (black) we observe a number of resonances which are all well below 1500 nm in resonance wavelength. The perfect L-shape (blue) exhibits three pronounced resonances. These resonances correspond to the three fundamental split ring resonator (SRR) modes as the L-shape resembles a SRR [262]. When turning to the case of the merged particle depicted in the middle row, we observe a combination of the two previously mentioned extreme cases. The L-shape is distorted by the waists of the individual merged particles. Indeed, the corresponding spectrum exhibits a multitude of additional higher order modes. This fact explains the presence of the higher order modes in the visible and near-infrared region in the chiral optical response of the two-layered oligomers. All observed modes are caused by the hybridization of the modes of the individual building blocks. An increased number of modes supported by the building blocks will lead to a larger number of hybridized collective modes of the oligomer. The true benefit afforded by the distorted L-shape is thus the ability to support a large number of different modes which retain significant resonance dipole moment and thus couple efficiently to an external light field.

In order to further elucidate this experimental finding we simulated the optical response of the individual building blocks of our chiral plasmonic oligomers. Figure 4.19 depicts the transmittance spectra as well as near-field intensity maps of the isolated particles and the perfect L-shape under circularly polarized excitation. The far-field optical response of the structures is identical for left- and right-handed circularly polarized incident light. This behavior is expected as the structures are achiral and the arrangement uniaxial. Thus, one does neither observe circular dichroism nor polarisation conversion. Both spectra exhibit two main and well modulated resonances. The lowest energy mode A of the isolated particle structure is a combination of dipolar excitations in the individual particles, leading to a mode that can be characterized as a bonding dipole mode. The higher energy mode B in contrast is characterized by strong quadrupolar excitations, leading to a bonding quadrupole type mode. The perfect L-shape on the other hand shows much simpler mode behavior. As expected, we observe a $\lambda/2$ (C) and a λ mode (D) as the two fundamental standing wave type modes of a wire. Higher order standing wave modes are most likely present, yet their modulation is weak. The excitation of these modes depends strongly on the resonance dipole moment associated with it, which is expected to drop significantly for increasing mode order [262].

In order to understand the complex yet intriguing behavior of the three dimensional oligomers, we now turn our attention to the case of the merged three-particle structure. Figure 4.18 depicts the simulated transmittance spectra as well as the calculated near-

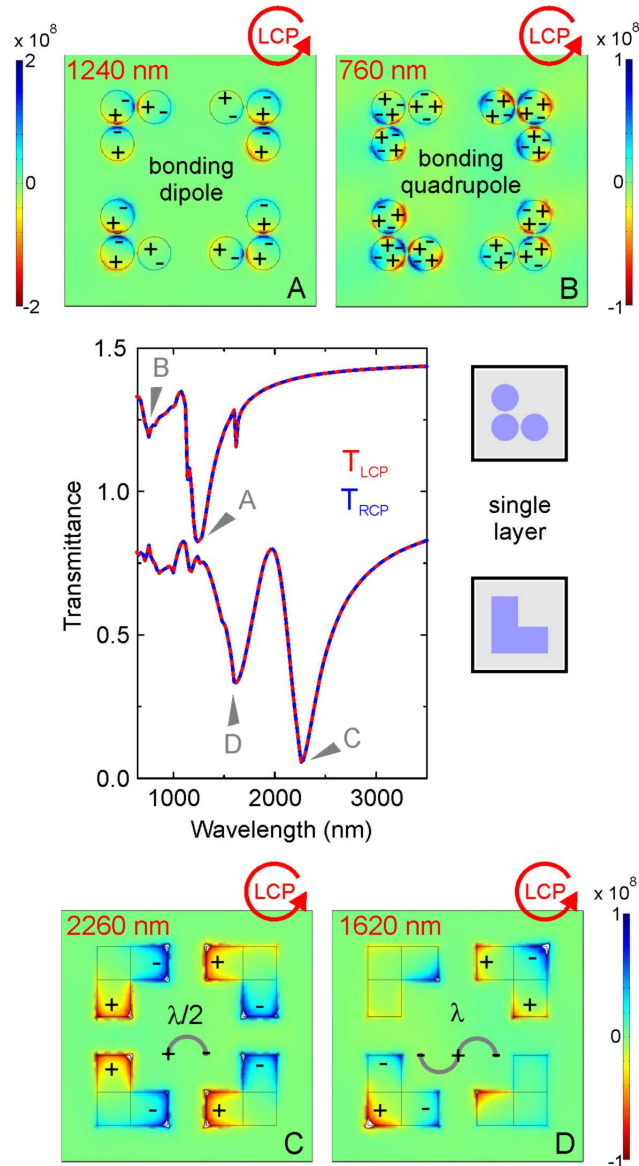


Figure 4.19.: Simulated far- and near-field optical response of single layer isolated particles and perfect L-shape structures under circularly polarized excitation. The transmittance spectra for left- and right-handed circularly polarized incident light are identical, as to be expected for an achiral and uniaxial structure. The near-field plots reveal bonding dipole and quadrupole type modes for the three particle structure and standing wave type modes for the perfect L-shape. The near-field plots are depicted for left-handed circularly polarized excitation, as indicated by the red arrow. The spectra are shifted upwards for clarity.

field intensity maps. Again, we observe an identical far-field optical response for left- and right-handed circularly polarized excitation. However, in contrast to the previous case we observe a multitude of well modulated resonances, in good agreement with our experimental results shown in figure 4.18. Interestingly, the mode structure of the distorted L-shape is a combination of the modes found in the structures of Figure 4.19. The two lowest energy modes at spectral positions A and B are $\lambda/2$ and λ modes. In contrast to the perfect L-shape we as well observe a well modulated $3\lambda/2$ mode at spectral position C. The waists of the structure perfectly match the profile of this $3\lambda/2$ mode. Thus, the mode retains a significantly stronger resonances dipole moment facilitating its excitation. Additionally, we observe bonding dipole and bonding quadrupole type modes at spectral positions D and E which are, again, enabled by the distortions induced by fusing the three individual particles into the L-shape. Thus, we can deduce from the calculations that the distorted L-shape combines the benefits from both the isolated three particle structure and the perfect L-shape, underlining the experimental findings of figure 4.18.

As we now have a clear understanding of the mode structure of the individual layers we can attempt to unravel the mode structure of the double layered chiral structures. Firstly, we will examine the case of the fully fused distorted L-shape in figure 4.21. The upper part depicts the calculated transmittance spectra for left- and right-handed circularly polarized excitation as well as the calculated $\Delta T = T_{RCP} - T_{LCP}$ spectrum. The lower part shows near-field distributions at four selected spectral positions. The color of the surrounding frame and arrow indicates the polarization of the excitation (blue = RCP, red = LCP). Intuitively, we expect the modes of the structure to be combinations of the modes of the individual building blocks. In order to elucidate this behavior, we first turn our attention to the fundamental mode of the structure. We clearly see that this mode strongly splits in resonance energy depending on the polarization of the incoming light. If we examine the field plots at spectral positions A and B we see that the modes are of similar character, yet show different phase behavior. Both modes are combinations of the fundamental $\lambda/2$ mode of the merged L-shape. Under right-handed circularly polarized excitation the modes of the individual layers are in phase whereas they are in antiphase for left-handed circularly polarized excitation. We can associate each mode with an induced ring current that is flowing along the particle shape. In order to understand the energy splitting it is most intuitive to consider the magnetic moments induced by these ring currents, which are sketched as purple and black arrows next to the corresponding field distribution. For the lowest energy mode we see that the magnetic moments are aligned in parallel. This alignment is energetically favourable and reduces the resonance energy of the mode. In contrast, the magnetic moments for the higher energy mode at spectral position B are antiparallel which raises the resonance energy [96,209]. The comparably large energy splitting between the two modes is thus due to the strong induced magnetic moments and their interaction. Importantly, when changing the handedness of the structure, the lowest energy mode will be the one under left-handed circularly polarized excitation, thus LCP and RCP switch their respective roles when changing the handedness of the structures. As it is not feasible to discuss all modes

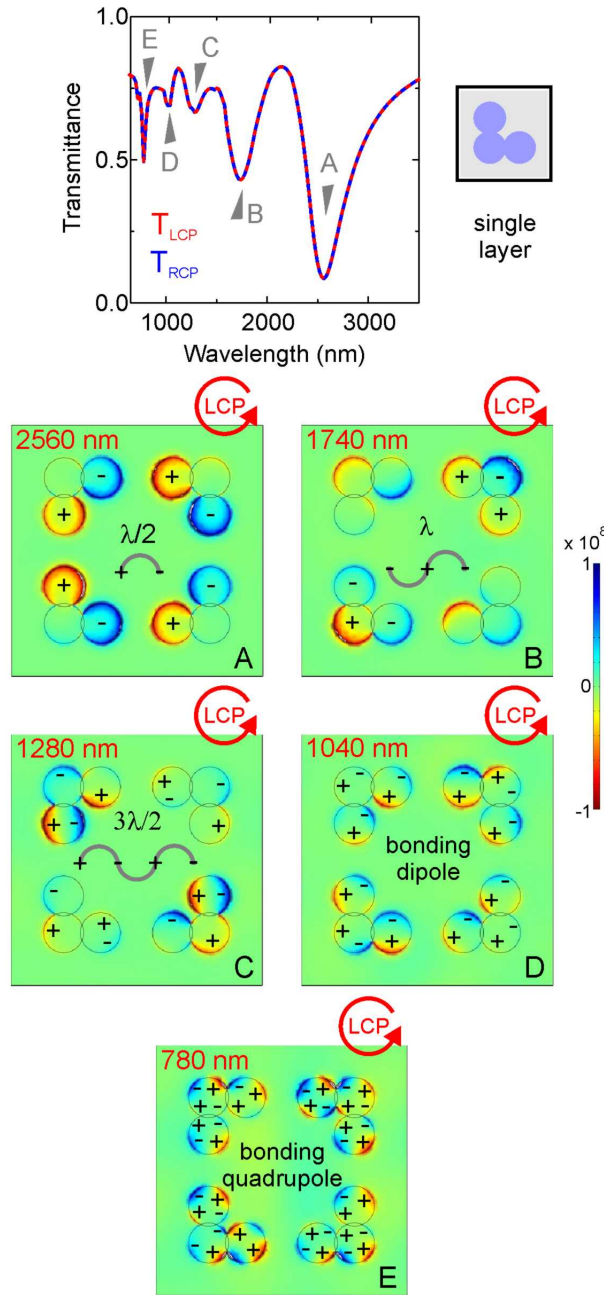


Figure 4.20.: Simulated far- and near-field optical response of a single layer merged L-shape structure under circularly polarized excitation. The transmittance spectra for left- and right-handed circularly polarized incident light are identical, as to be expected for an achiral and uniaxial structure. We observe a multitude of well modulated resonances. The corresponding modes are a combination of the isolated three-particle and the perfect L-shape cases. We observe $\lambda/2$, λ , and $3\lambda/2$ standing wave type modes and simultaneously bonding dipole and bonding quadrupole type modes.

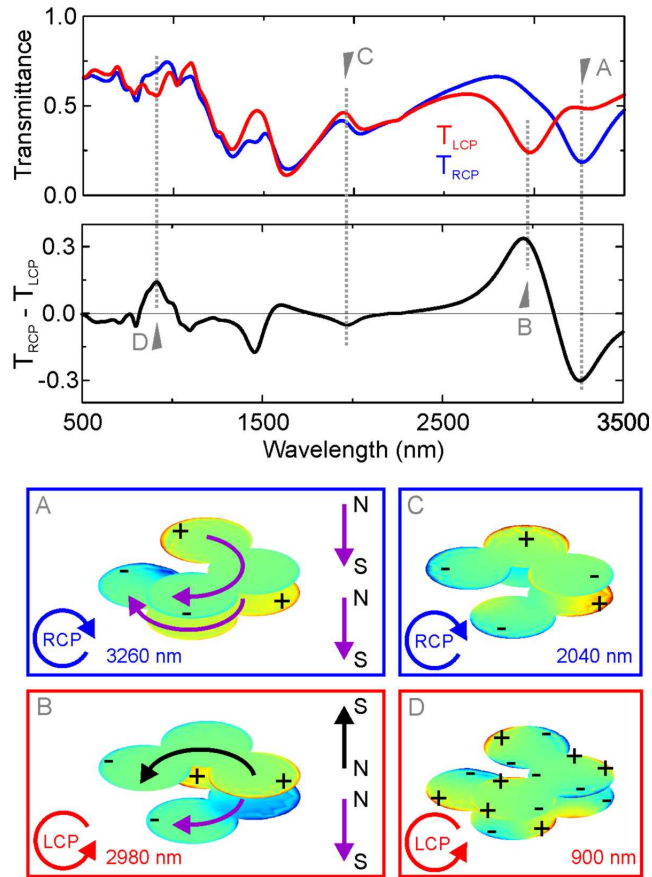


Figure 4.21.: Calculated near- and far-field optical response of a two layered chiral plasmonic oligomer, consisting of molten together L-shapes. The two lowest energy modes at spectral positions A and B correspond to the combination of the fundamental $\lambda/2$ modes of the individual layers. The lowest energy mode is characterized by a parallel arrangement of the magnetic moments induced by the ring currents in the particles, the higher energy mode shows a antiparallel arrangement. The modes at spectral positions C and D are combination of the λ modes and the bonding quadrupole modes, respectively.

of the structure we only show two additional representative cases. At spectral position C we observe a bonding combination of two λ modes. At spectral position D we observe a rather complicated mode profile which is the combination of two bonding quadrupole type modes. The shown near-field distributions thus underline that all observed modes are basically combinations of the fundamental modes of the individual building blocks, which are shown in figure 4.20.

In figure 4.22 we depict the calculations for the isolated particle structure. The calculated transmittance spectra for left- and right-handed circularly polarized excitation as well as the calculated ΔT spectrum are shown in the upper part, the lower part shows near-field distributions at four selected spectral positions. When examining the two energetically lowest modes A and B one again finds a combination of the energetically lowest mode of the individual layer. The overall behavior is very similar to the previously discussed case of the merged L-shape. Despite the fact that there is no conductive coupling between the particles we can again define ring currents in the individual layers. Even without a conductive bridge between the particles, the near-field coupling gives rise to displacement currents. The lowest energy mode is again characterized by parallel alignment of the induced magnetic moments whereas the mode at slightly higher energy shows antiparallel alignment. In contrast to the merged L-shape we only observe a weak splitting in resonance energy. The reason is the much smaller induced magnetic moment, as the ring currents in the individual layers are significantly smaller due to the absence of conductive coupling. Additionally, we plot the field distributions for two higher order modes at spectral positions C and D. We again basically observe combinations of the fundamental modes of the individual layers. Yet, there is one pronounced difference which is important to note. As there is no conductive coupling between the individual particles of each layer, the particles are comparably weakly coupled as lateral plasmonic near-field coupling is weak. In contrast, the coupling between the particles stacked on top each other is significantly stronger. Therefore, the overall mode profiles are slightly distorted from the pure combinations of the modes of the individual layers as the coupling between the stacked particles of the two layers is more efficient.

A somewhat intuitive and straightforward question concerns the evolution of the chiral optical response upon adding of additional layers. Figure 4.23 depicts tilted view SEM micrographs of chiral structures with up to four layers. The fabricated structures are composed of the molten together L-shapes. The close-up images show, for one handedness, one, two, three, and four layered structures. The overview image shows the four layered structure. Note, that all structures are fabricated simultaneously on the same substrate. With each finished layer, a certain set of structures is completed and only the fields which are supposed to have more layers are processed further. This guaranties identical spacer layer and gold layer thicknesses for the different structures, making it possible to compare the spectra. The close-up images underline this fact: The closer a gold structure is to the surface of the top-most PC403 layer, the better it is visible in the SEM micrographs. The two-layered structure looks rather blurry as it is covered by three layers of ~ 70 nm thick PC403. The structuring of this field has stopped after

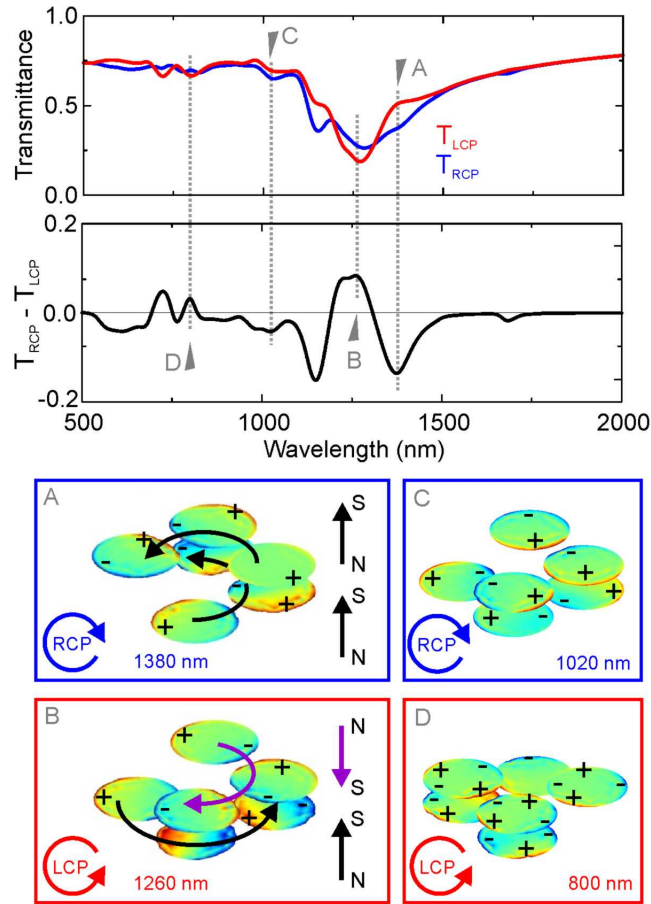


Figure 4.22.: Calculated near- and far-field optical response of a two layered chiral plasmonic oligomer, consisting of isolated particles. The two lowest energy modes at spectral positions A and B are combination of the bonding dipole modes of the individual layers. Together with the displacement currents in between the particles we can define effective currents in each layer, giving rise to magnetic moments, similar to the case in figure 4.21. The relative orientation of the magnetic moments determines the resonance energy of the modes. The higher energy modes at spectral positions C and D are as well basically combinations of higher order modes of the individual layers.

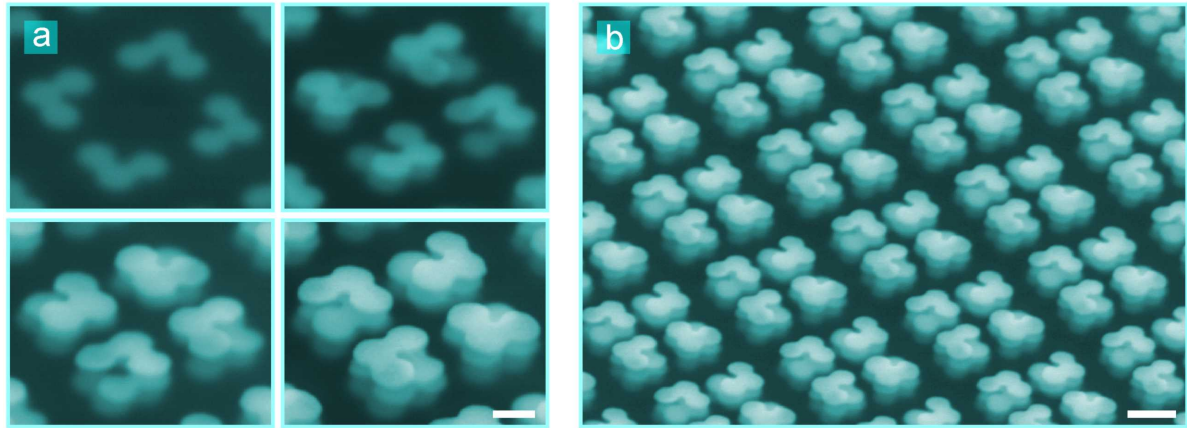


Figure 4.23.: SEM micrographs of multi-layered chiral structures comprised of the molten together L-shape. (a) The Close-up images show the evolution from the single layered to the quadruple layered structure. The scale bar is 200 nm. (b) Overview image of the four layer structure. The scale bar is 500 nm.

two exposure steps and processing only continued for the fields supposed to become three and four layered. The three layer structure therefore appears much clearer, as its top-most layer is only covered by two layers of PC403. Accordingly, the top-most layer of the four layered structure is only buried below a single layer of PC403 and therefore appears very clear.

Intuitively, one would expect the chiral optical response to increase with the number of layers. First of all, the increase of layers leads to a better approximation of a spiral. Secondly, the dipole moment of all plasmonic resonances will significantly increase due to the increase in gold filling fraction.

The left column of figure 4.24 depicts the transmittance spectra for circularly polarized light for the structures shown in the SEM micrographs in the middle column. For the first layer the transmittance spectra are nearly perfectly identical, as expected for an achiral structure. For the two layered structure one observes significant mode splitting and the appearance of additional plasmonic modes. This behaviour continues for the three and four layered structures. In the latter case, one observes a multitude of plasmonic modes which make it nearly impossible to assign these modes to certain combinations of the fundamental modes of the L-shape, as shown in figure 4.20. However, again in accordance with the expectation, the modulation depth increases significantly with increasing number of layers. For the four layered structure the transmittance drops on resonance to values as low as $\sim 3\%$. This behaviour is connected to the huge dipole strength of the plasmonic modes formed in the composite structure. Basically, the whole unit cell is filled with metal (cf. figure 4.23). Additionally, one observes a successive red-shift of the resonances with increasing number of layers, which is in particularly visible for the fundamental one. This behaviour is expected as more and more layers

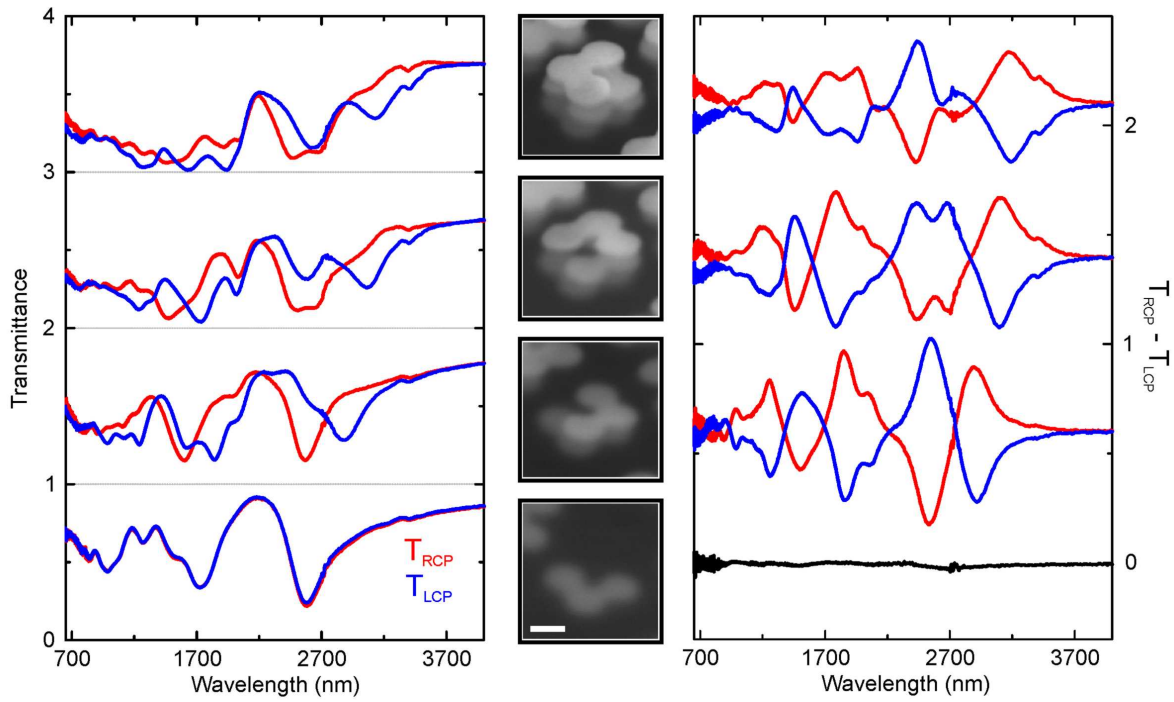


Figure 4.24.: Left column: Transmittance spectra for right- and left-handed circularly polarized light for the structures shown in the SEM images in the middle column (scale bar 200 nm), with increasing number of layers. The right column depicts the $\Delta T = T_{RCP} - T_{LCP}$ spectra for both enantiomers each. The difference in transmittance reaches the maximum value for the two layered structure with about $\sim 42\%$. Afterwards, the chiral optical response surprisingly diminishes. However, note that the modulation depth of the transmittance spectra monotonically increases.

are coupled together, lowering the resonance energy of the fundamental mode due to attractive interaction (cf. figure 4.20).

To a surprise, the chiral optical response does not follow this trend. The right column of figure 4.24 depicts the chiral optical response for both enantiomers each, exhibiting the expected excellent mirror symmetry. The maximum transmittance difference is reached for the two layered structure, with values as high as $\sim 42\%$. For three layers the difference is already smaller and continues to diminish for the four layered structure. As in the case of the transmittance spectra it is very difficult to assign certain modes or to track the evolution of individual modes. Only rarely one is tempted to interpret an additional mode splitting: When increasing the number of layers from two to three the ΔT resonance around 2500 nm seems to split, which as well seems to be the case for the transmittance spectra. However, it is important to note that the CD features might spectrally overlap, as might the modes in transmission, which makes it most likely impossible to draw any conclusion without reliable simulations and simulated field distributions. Each individual layer supports five strong modes, as shown in figure 4.20. All of these modes will mix and hybridize when the four particles are brought into close proximity leading to a huge number of collective modes.

However, one might wonder whether the difference in absorbance is actually the best quantity to look at. One can clearly see that the modulation depth of the resonances in transmittance is strongly increasing, as one would expect for an increased number of layers. Hence, it is surprising that the CD seems to drop. When examining the SEM overview image in figure 4.23 (b) one realizes that a significant fraction of unit cell is actually filled with gold due to the dense packing within the array but as well due to the presence of four layers. This huge amount of gold will give rise to significant absorbance with might not be related to a chiral optical response but rather due to ohmic losses in the metal. If the overall absorbance increases, the relative transmittance T_{RCP}/T_{LCP} might be the better quantity to look at. In the end the chiral structure is supposed to suppress the transmittance of the "wrong" handed light while still transmitting a high fraction of the "right" handed light, even in the presence of ohmic losses, which are insensitive to the polarization state of the incoming light.

Figure 4.25 depicts the relative transmittance T_{RCP}/T_{LCP} for the structures shown in figure 4.24. Let us first consider the spectra shown in solid lines, which correspond to the structures shown in the inset, and thus as well correspond to the transmittance spectra shown in the left column of figure 4.24. The spectra seem to indicate that the relative transmittance, that is the relative suppression of the "wrong" handed over the "right" handed light, is significantly increasing with increasing number of layers. For the four layered structure the relative transmittance reaches values as high as ~ 13 , meaning that 13 times as much "correctly" polarized light is transmitted as compared to the undesired one. The dotted lines show the same relative transmittances for the enantiomers. As expected, the spectra change sign for exchanged handedness. However, the relative suppression is significantly weaker and does not increase with increasing number of

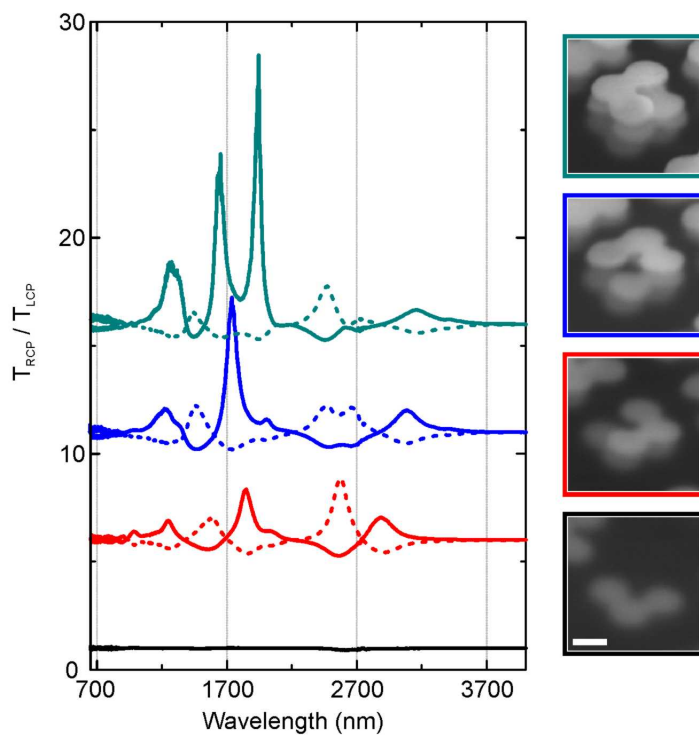


Figure 4.25.: Relative transmittance T_{RCP}/T_{LCP} for the structures with increasing number of layers. Solid: Spectra for the structures shown in the inset. Dotted: Spectra of the corresponding enantiomers. The solid lines seem to suggest a significant increase of the relative transmittance with increasing number of layers, reaching values as high as 13. However, the spectra of the enantiomers, while confirming the spectral shape, do not show this trend. The reason is connected to the inability of the FTIR spectrometer to deliver absolute values for the transmittance, the error is in the order of $\sim 5\%$. For very small remaining transmittance, as it is the case here (cf. figure 4.24, left column) this is of major influence. Hence, one cannot draw any solid conclusions from the experiment.

layers. The reason for these discrepancies is connected to the limited ability of the FTIR spectrometer to measure absolute values. The error on these values can be around 5%, which is of no consequence for relative values, such as the $\Delta T = T_{RCP} - T_{LCP}$ spectra. However, as soon as relative transmittance T_{RCP}/T_{LCP} is studied, it is of significant difference whether the transmittance drops down to 3% or 8%. As there is no way of "normalizing" the spectra, there is no way of knowing whether or not the relative transmittance is indeed increasing with increasing number of layers, or not. Simulations could again help in unraveling the processes, yet they are extremely demanding due to the large unit cell and the multi-layered nature of the structures.

4.5. Plasmonic Diastereomers

In 2003 Nordlander and co-workers introduced the concept of plasmon hybridization [65] for the description of complex plasmonic nanostructures, bridging the established field of molecular physics with the emergent field of plasmonics. Since then, researchers have drawn inspiration from Chemistry, as well as molecular and atomic physics, transferring well-known and intriguing phenomena to the realm of plasmonics. This strategy created a plethora of fascinating plasmonic systems [80,83,120,138], such as plasmonic molecules and polymers [84,263], plasmonic hierarchical systems [264], or the classical analogue of electromagnetically induced transparency [79,82,140,265].

Chirality is a particular exciting chemical concept as it is nearly omnipresent in nature [203,204,237]. A large number of bio-molecules are chiral, such as sugars, the essential amino acids, or nucleic acids, to name a few. The chemical construction kit offers several possibilities to create chiral molecules. The most prominent one, however, is the so-called chiral center [199,266]. In such a center four different molecular groups or atoms are bond to a tetravalent carbon atom, thus being termed an asymmetric carbon atom. Such a carbon atom dressed with hydrogen, fluorine, chlorine, and bromine atoms, is an archetype chiral system. Depending on the sequence of the atoms the center can be either left- or right-handed.

Quite a number of chiral molecules are even more complex as they contain several chiral centers. If a molecule possesses n chiral centers a large number of potential three-dimensional arrangements, so-called stereoisomers, exist because these centers can be either left- or right-handed. Such a molecule can form a maximum of 2^n so-called chiral diastereomers, which do not differ in chemical composition but rather in their three-dimensional arrangement. If two such molecules differ in the handedness of all n chiral centers they are called enantiomers, meaning they are true mirror images of each other. Such enantiomers have identical chemical and physical properties, unless they interact with chiral molecules or circularly polarized light. In particular, the chiral optical responses of enantiomers are intimately correlated, as the circular dichroism (CD) spec-

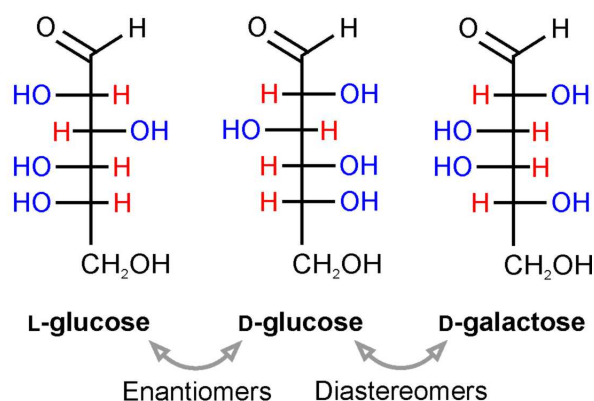


Figure 4.26.: A large number of bio-molecules are chiral due to the presence of a chiral center or asymmetric carbon atom. However, a number of molecules contain several chiral centers. One example is D-glucose containing five centers, as can be seen in the Fisher projection depicted in the center of the figure. In general, one can change the handedness of each chiral center individually, leading to $2^4 = 16$ different molecules, or so-called diastereomers. These molecules have identical chemical composition, yet their 3D arrangement is different. The left hand side depicts L-glucose, where all chiral centers are changed in handedness, making it the enantiomer of D-glucose. If only one specific chiral center is changed, the resulting molecule is D-galactose, a diastereomer of D-glucose.

trum flips sign for changed handedness. If two such molecules differ in the handedness of exactly one center they are termed epimers. Interestingly, epimers or diastereomers have different physical and chemical properties, in particular the CD response of these molecules can be very different and there is in general no correlation or dependence of the spectral response of the one molecule on the response of the other molecule. The only exceptions to this rule are so-called meso compounds. Despite the fact that they consist of two or more chiral centers they are achiral due to the presence of a symmetry plane within the molecule and hence do not show any CD [266].

An example of such a system is shown in figure 4.26. It depicts the Fisher projection of D-glucose consisting of 5 chiral centers. Thus, this system in principle possesses a maximum of $2^4 = 16$ diastereomers. The mirror image of D-glucose, i.e., its enantiomer, is shown on the left hand side, being L-Glucose. If one changes the handedness of one specific center, one obtains D-galactose, thus being a diastereomer (in principle even an epimer) of D-glucose. The example of D-Glucose demonstrates that the chemical concept of multiple chiral centers allows for construction of a large number of complex chiral molecules from basic building blocks. The physical and chemical properties, in particular the CD response, of the resulting composite molecules are not necessarily connected to one another in a simple or straightforward way or might even be completely independent of each other. This class of diastereomers is an exciting field of research, as molecules with the same chemical composition have different properties owing to their different three-dimensional arrangement. Importantly, the chiroptical response of a molecule can

in general not be determined from the chiroptical response of a diastereomer. The physical properties of diastereomers are unrelated [199].

Recently, it has been proposed and demonstrated that the concept of a chiral center can be transferred to plasmonics [171,243,267]. The four different atoms or molecular groups at the corners of the symmetric tetrahedron which is fixed by the central carbon atom are replaced by four different metallic nanoparticles. However, it was found that the chiral optical response of this system is comparably weak, as the four different particles are only weakly coupled due to resonance energy and dipole moment mismatch [90]. Nevertheless, one can construct the plasmonic analogue of a chiral center by employing four equally sized particles arranged in an asymmetric, that is, handed fashion [247,268,269]. In this Letter, we demonstrate that we can construct composite molecules which comprise two or more chiral centers. We find that the CD response of our composite plasmonic molecules can be approximated as the sum of the CD response of the fundamental building blocks. What is more, we demonstrate that the additivity of the CD response is caused by weak near-field interaction between the individual chiral centers. As soon as the centers are coupled to one another, this additivity vanishes.

Figure 4.27 (a) depicts the fundamental building blocks of our chiral composite molecules. The first layer of the structures contains an L-shaped arrangement of three particles. A fourth particle in the second layer determines the handedness of the resulting center. In contrast to an asymmetric carbon it is straightforward to have a right- (R) and left-handed (L) as well as an achiral (A) center due to the configurational asymmetry in three dimensions. In order to form a composite molecule two of these centers are combined such that they share one "plasmonic atom". Conceptually, there are several possibilities to join the individual centers. In our case the first layer takes an S-shape, as indicated in Figure 4.27 (b). This geometry is particularly interesting as the first layer exhibits so-called 2D chirality [220,221,270,271]. As a consequence, all combinations of two chiral centers, independent of their respective handedness, will result in a truly 3D chiral structure. For instance, the combination of a left- and right-handed center (which we term (L+R)) as well as two achiral centers (A+A) will result in a chiral molecule. From a geometrical point of view, this observation is not surprising, yet intuitively one would have expected an (L+R) molecule to be achiral, as one would expect the combination of achiral centers to be achiral. Figure 4.27 (c) depicts tilted and normal view SEM images of our molecules. The position of the upper layer dot is excellently visible in the normal view SEM micrographs. Firstly, two particles are directly on top of each other and secondly the particle in the upper layer is much closer to the sample surface. Both factors cause the secondary electron emission to be significantly stronger, such that the particle appears brighter in the micrographs. We will thus use these SEM micrographs in the following Figures for illustration purposes.

Our construction rules, as laid out in figure 4.27, allow for 6 different composite molecules and their respective enantiomers, as depicted by SEM micrographs in figure 4.28. A number of combinations result in the same geometry, so is the (R+L) molecule identical

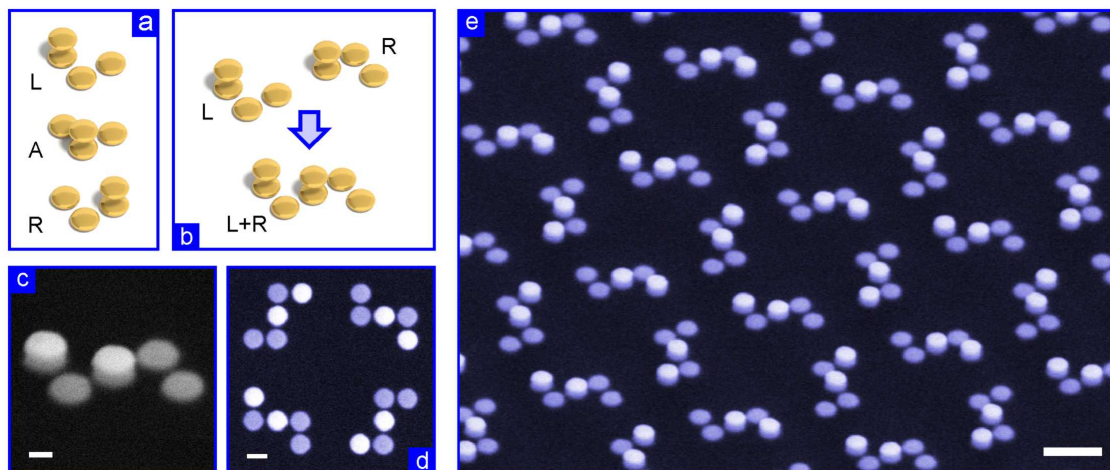


Figure 4.27.: (a) Construction scheme of our plasmonic diastereomers. The chiral centers consist of four equally sized particles arranged in an asymmetric fashion. Three particles are arranged in an L-shape in a first layer, the fourth is stacked above the others determining the handedness of the resulting structure. In contrast to asymmetric carbon atoms the plasmonic chiral center can be either left- (L) or right-handed (R), as well as achiral (A). (b) In order to form composite molecules we combine two chiral centers such that they share one common "plasmonic atom". The resulting first layer assumes an S-shape, hence being "2D chiral". As a consequence, each combination of chiral centers will result in a chiral composite molecule. The panel depicts the case of an (L+R) molecule consisting of an L and an R chiral center. (c) Tilted and (d) normal view SEM micrographs of (L+R) molecules, fabricated in a two-step electron beam exposure process. The close-up as well as the normal view micrographs demonstrate the excellent alignment between the two fabricated layers. (e) The overview images reveal the C_4 symmetric arrangement of the individual clusters, suppressing lattice-induced contributions of polarization conversion. The scale bars in the close-ups are 200 nm and 500 nm for the overview image.

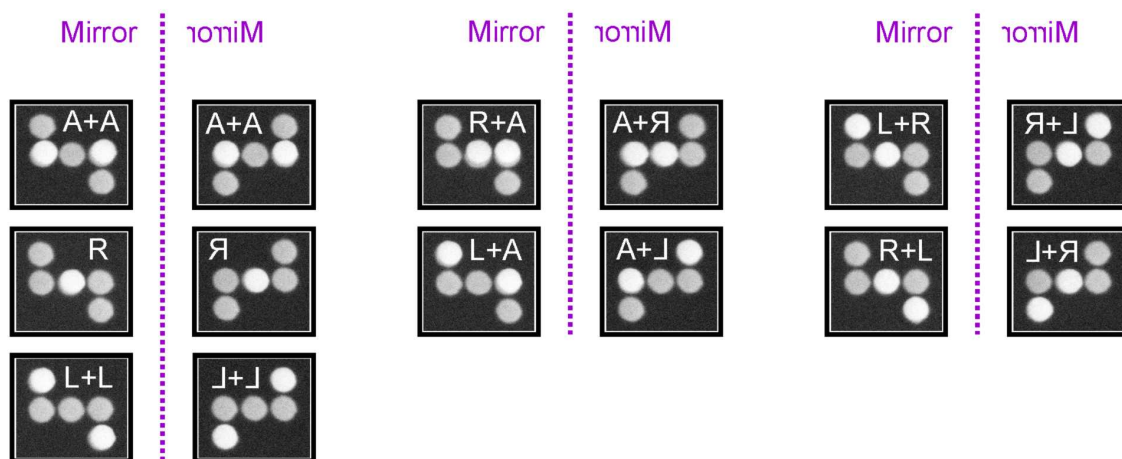


Figure 4.28.: The construction rule laid out in figure 4.27 allows for a number of composite chiral structures (note, that the upper layer particles appear brighter). However, a number of combinations results in the same molecule, such as the (L+R) and the (R+L) molecules (right-most column). In total, one obtains six independent molecules as well as their respective enantiomers.

to the (L+R) one as a rotation by 180° transfers the structures into one another, cf. the right-most column of figure 4.28. Similarly, all combinations are symmetric with regard to the handedness of the two centers. It is important to note that the (R+R) cluster contains only one particle in the upper layer, as the corresponding first layer atoms are shared in order to form the composite molecule. The six resulting molecules are thus (A+A), (A+R), (A+L), (R+R) = (R), (L+L), and (L+R). It is important to note that all the molecules are chiral and all of them are apparently independent 3D structures.

In order to study the chiral optical response of our molecules, the left column of figure 4.29 depicts the transmittance spectra for right- and left-handed circularly polarized incident light for the structures shown in the corresponding SEM micrographs. Already the transmittance spectra show the strong difference in the response of the structures upon the two different circular polarizations. The right column of figure 4.29 depicts the $\Delta T = T_{RCP} - T_{LCP}$ spectra for the displayed structures as well as their corresponding enantiomers. For all the structures we observe excellent mirror symmetry for the ΔT spectra of the two enantiomers as expected. The overall CD response reached values as high as $\sim 12\%$.

On first sight, the spectra appear to be very different. For example, the ΔT spectra of the (R) composite molecule seem to have unique mode signatures. However, when closely examining the spectra, we find striking similarities among them, despite the fact that from a geometrical standpoint all the molecules are different. For example, all clusters containing at least one R chiral center show the same spectral feature in the CD

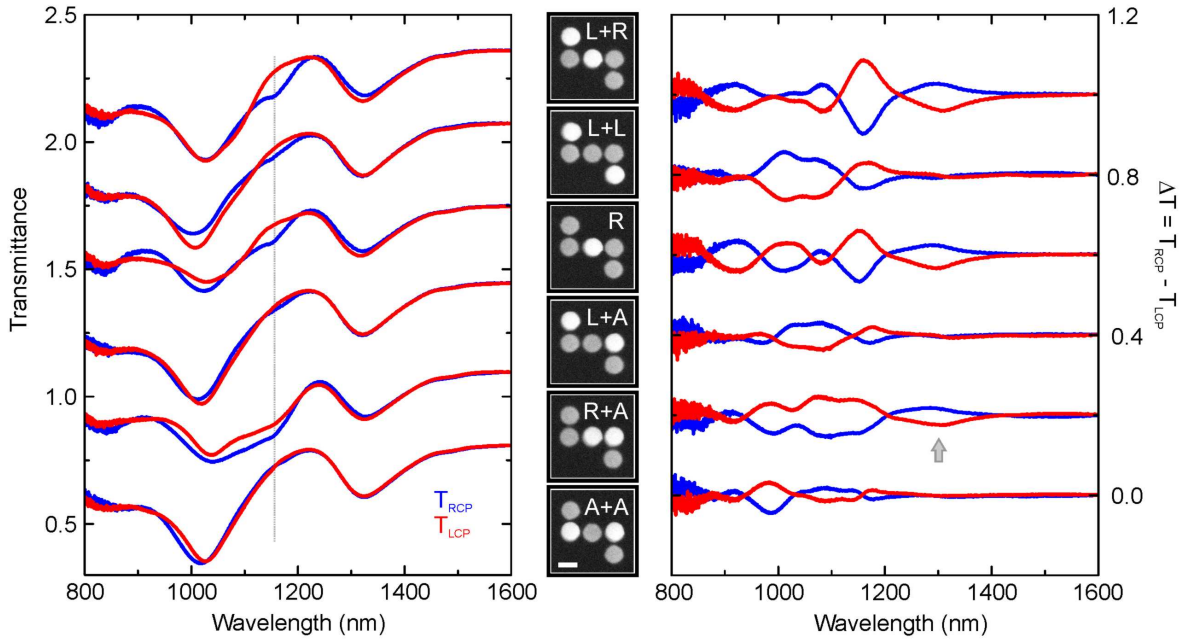


Figure 4.29.: Experimental realization of the six independent composite molecules and their respective enantiomers as laid out by the construction rules shown in figure 4.27. The left column depicts the experimental transmittance spectra for right- (blue) and left-handed (red) circularly polarized light for the structures shown in the normal view SEM micrographs in the middle column. Note, that the particles of the upper layer appear significantly brighter in the SEM micrographs, additionally the SEM micrographs are labelled. All molecules show significant chiral optical response, manifesting itself in the pronounced differences in the transmittance spectra. The right column depicts the $\Delta T = T_{RCP} - T_{LCP}$ spectra for both enantiomers, respectively. The spectra show excellent mirror symmetry for interchanged handedness, as expected. The chiral optical response reaches values as high as $\sim 12\%$. Overall, the spectra show remarkable similarities, indicating that the chiral optical response might be generated by a limited basis set. The spectra are shifted upward for clarity (transmittance by 0.5, ΔT by 0.2). The scale bar is 200 nm.

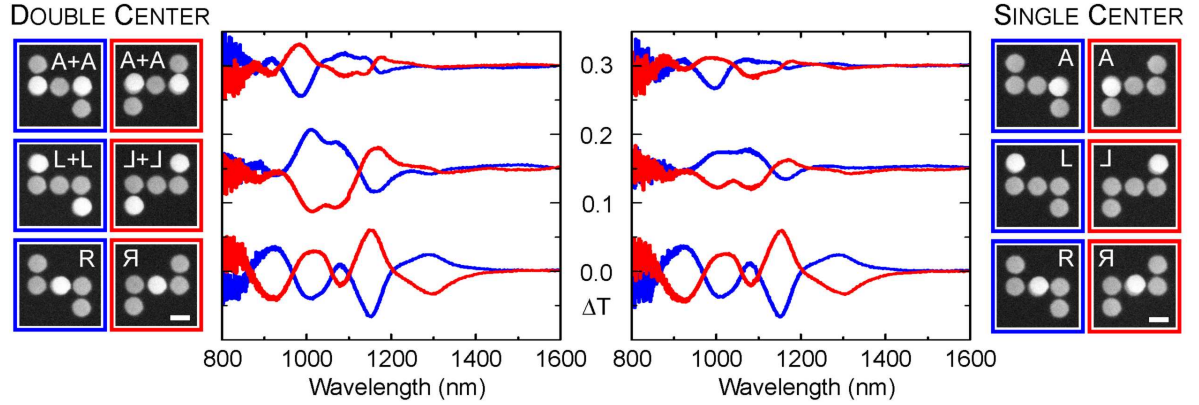


Figure 4.30.: Experimental $\Delta T = T_{RCP} - T_{LCP}$ spectra for the "pure" composite molecules consisting of two same handed chiral centers, that are the (A+A), (L+L), and (R+R) = (R) molecules, are shown in the left column. The right column depicts the response of the corresponding single center structures with only a single particle in the second layer. Note that the (R) molecule in any case consist of only a single particle in the second layer as the corresponding first layer plasmonic atom is shared in order to form the molecule. The lowest row depicts spectra of two fabricated sets of (R) molecules, demonstrating the excellent reproducibility of our fabrication method. When comparing the double and single center structures one clearly sees that the overall mode structure is identical. Thus, adding a second same handed center doubles the CD response but does no longer change the mode structure. The two chiral centers therefore appear to be decoupled. The spectra are shifted upward by 0.15 for clarity. The scale bars are 200 nm.

response centered on 1300 nm (see arrow), whereas all other molecules do not. Similarly, a distinctive dent in the transmittance spectra at 1150 nm for RCP light can be observed in the response of these molecules (compare the line in the left column). What is more, all composite molecules containing at least one L chiral center are characterized by a broad and featureless peak in the transmittance spectra for RCP and LCP light in the spectral region between ~ 1000 nm and 1300 nm. The remarkable similarities indicate that the chiral optical response of the composite molecules might be generated by a limited spectral basis set. Thus, an intriguing question arises: Can we construct the chiral optical response of the composite molecules from a basis set of fundamental chiral spectra, in the same manner we construct the molecules themselves from a geometrical basis set of fundamental chiral centers? For example, closely examining the ΔT response of the (L+R) molecule, one gets the impression that it might actually be the combination of the responses of the (L+L) and (R) composite molecules, as it is as well geometrically composed from these.

As a first step in order to answer this intriguing question, we examine the chiral optical response of the "pure" composite molecules (A+A), (L+L), and (R+R) = (R) in figure 4.30. The left column shows the response of the molecules with two identical chiral centers, the right column shows the response for molecules with only one center each,

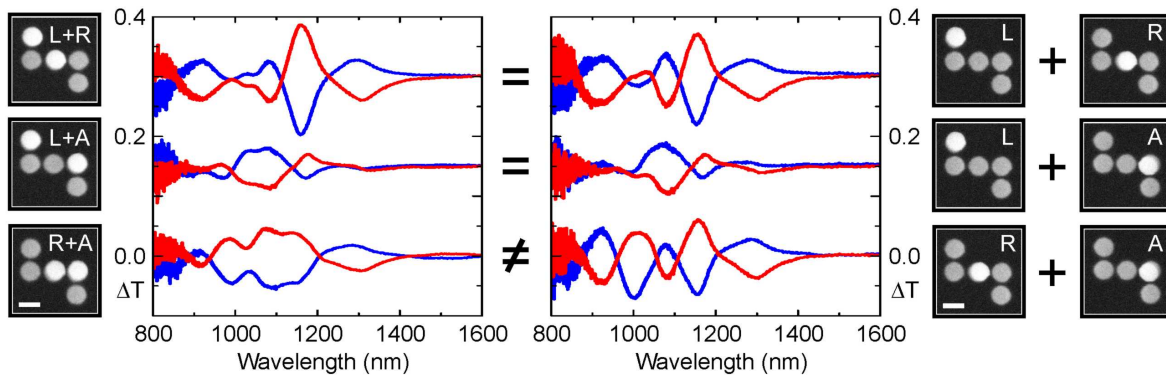


Figure 4.31.: Experimental verification of the approximate additivity of the CD response of the composite molecules. The left column depicts the $\Delta T = T_{RCP} - T_{LCP}$ spectra of the composite molecules (L+R), (L+A), and (R+A). Geometrically, the (L+R) cluster is composed of the single centered molecules (R) and (L). The right column thus depicts the sum of the CD response of these two molecules. One finds an excellent agreement between the measured and calculated spectra. The same holds for the (L+A) molecule composed of the single centered (R) and (A) molecules. For the (R+A) molecule on the other hand the spectra show significant differences, thus indicating that the additivity of the CD response has vanished for this molecule. The spectra are shifted upward by 0.15 for clarity. The scale bars are 200 nm.

yet with the full first layer. Let us first examine the (A+A) and (L+L) molecules. The overall mode profile and the spectral features observed in the ΔT spectra remain unchanged. However, the absolute amplitude of the CD response is roughly cut in half. The handedness of the structure is not changed when adding a second same handed center, as expected. However, it is surprising that the overall mode structure appears to be unchanged, in spite that the structures are different from a purely geometrical point of view. We can thus conclude that the two chiral centers are decoupled and their response adds up and increase the magnitude of the CD response. The lowest spectra in figure 4.30 depict the response of the (R+R) molecule. Note that this molecule always contains only a single particle in the second layer and thus one chiral center as the lower layer particle is the shared atom of the composite molecule. For this molecule the figure contains the spectra of two sets of "plasmonic molecules" fabricated independently of each other. The spectra are more or less perfectly identical with each other, underlining the extremely high reproducibility of our fabrication method, which will be important for the considerations below. Overall, in contrast to the findings shown in figure 4.29, the mode profile of the structures depicted in figure 4.30 appear to be very different and no similarities between the spectra can be observed. Thus, these plasmonic molecules might constitute the basis set generating the CD space of the composite molecules, as stated above.

In figure 4.31 we examine the capabilities of this potential chiroptical basis set. The left

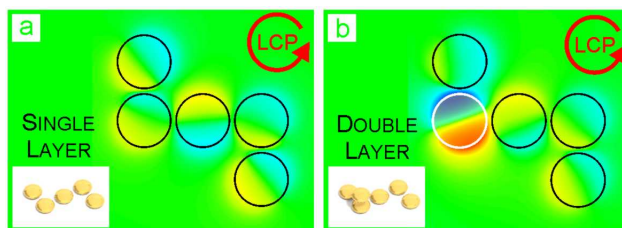


Figure 4.32.: Simulated electric near-field distributions on resonance upon circularly polarized excitation for (a) a single first layer and (b) the (A) composite molecule. The presence of a particle in the second layer modifies the field distribution of the first layer. However, by closely examining the field distribution one realizes that only the next-nearest particles are strongly influenced. In particular, the field distributions around the two right-most particles are basically unchanged. This indicates that for an additional particle placed on-top of one of these particles the first layer will appear unchanged no matter whether or not another particle is already present. The two chiral centers are therefore decoupled and the chiral optical response will be approximately additive.

column depicts the chiral optical response of the composite molecules (L+R), (L+A), and (R+A). If the structures shown in figure 4.30 are indeed the basis set of the composite molecules, one should be able to calculate the chiral optical response of all other molecules from the chiral optical response of these building blocks. Geometrically, the (L+R) molecule is composed of an (L) and an (R) building block. The right column of figure 4.31 thus depicts the sum of the CD response of an individual (L) and (R) molecular building block, as indicated by the SEM micrographs. The agreement between the measured response and the calculated one is excellent, not only with respect to the spectral features and the mode structure, but as well regarding the amplitude of the CD response. The same conclusion holds true for the case of the (L+A) molecule. Again, not only the geometry but as well the optical response is generated by the fundamental building blocks L and A. Please note that eight experimental transmittance spectra are needed in order calculate each of the ΔT spectra pairs in the right column, imposing high demands on the reliability and reproducibility of structure fabrication. In contrast to the former cases, the suggested procedure fails to predict the CD response of the (R+A) molecule. The calculated CD spectra are strongly deviating from the measured ones. Conceptually, both findings are equally puzzling: *Why is the chiral optical response in the one case determined by the response of the building blocks and in the other case not?* The finding is in particular unexpected, as the composite molecules are different geometrical structures and one would thus expect a different plasmonic mode structure and CD response.

Calculated electric near-field distributions, as shown in figure 4.32, are capable to explain both findings. figure 4.32 (a) depicts the near-field distribution on resonance of the first layer when being excited by circularly polarized light. When adding a particle in the second layer, as shown for an (A) building block in figure 4.31 (b), the near field distribution in the first layer is modified. However, when comparing this distribution

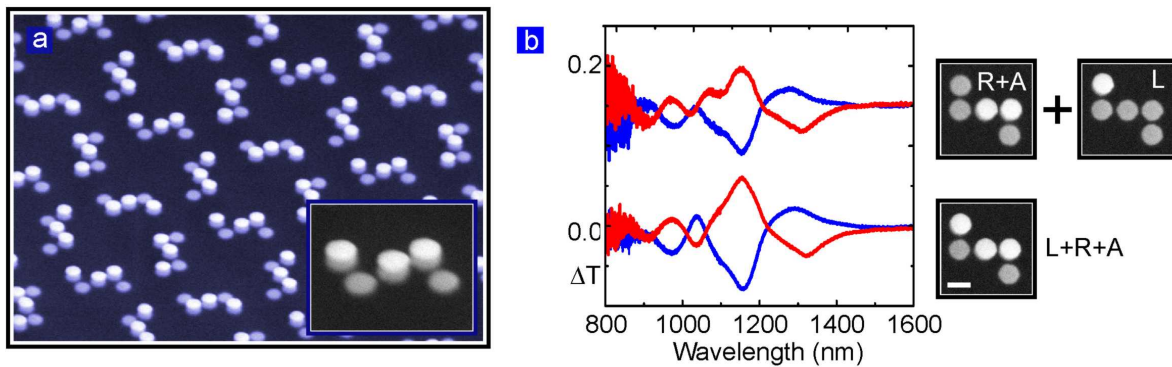


Figure 4.33.: (a) Tilted overview SEM images of the composite (L+R+A) molecules. (b) Due to near-field coupling between the particles of the upper layer the (R+A) composite molecule is a building block of its own and the CD response cannot be calculated from simple addition of the response of the (R) and (A) building blocks. However, the $\Delta T = T_{RCP} - T_{LCP}$ spectra of the even more complex (L+R+A) molecule can again be approximated by adding up the responses of the (R+A) molecule and the (L) building block, proving that the (R+A) composite molecule is indeed a fundamental building block as well.

to the one in figure 4.31 (a) a significant influence of the second layer particle can only be seen for the next-nearest neighbours. In particular, the two rightmost particles are basically unaffected by the presence of the second layer particle. This finding can be explained by the comparably weak lateral coupling between adjacent nanoparticles. To first order approximation the coupling can be described in terms of the interaction of two point dipoles located in the center of mass of the disks. However, the distance between these dipoles is given by the diameter of the disk plus the gap between the disks. In contrast, the distance between the dipoles for the stacked arrangement is only given by the thickness of the disks plus the vertical stacking distance. Therefore, the upper layer particle will not influence the near-field distributions of the two rightmost particles. In turn, this implies that for a second particle being placed in the upper layer, it is of no consequence whether or not there is already another particle present. No near-field coupling between these two chiral centers takes place, they do not influence each other and their chiral optical response will be decoupled and thus be additive. This behaviour will obviously change dramatically as soon as near-field coupling between the centers starts to be important. In fact, for the (R+A) molecule the additivity of the CD response is destroyed as the particles of the second layer are coupled. The two particles are next-neighbours, thus they are strongly near-field coupled. This coupling gives rise to modified electromagnetic modes within the plasmonic structure and thus the CD response can no longer be calculated from the buildings blocks (R) and (A). The (R+A) molecule is therefore actually a building block of its own. The additivity of the CD response, as shown in figure 4.31, is thus caused by the decoupling of the chiral centers within the molecules due to vanishing near-field coupling between them. As soon as there is electromagnetic near-field interaction or cross-talk, this additivity vanishes.

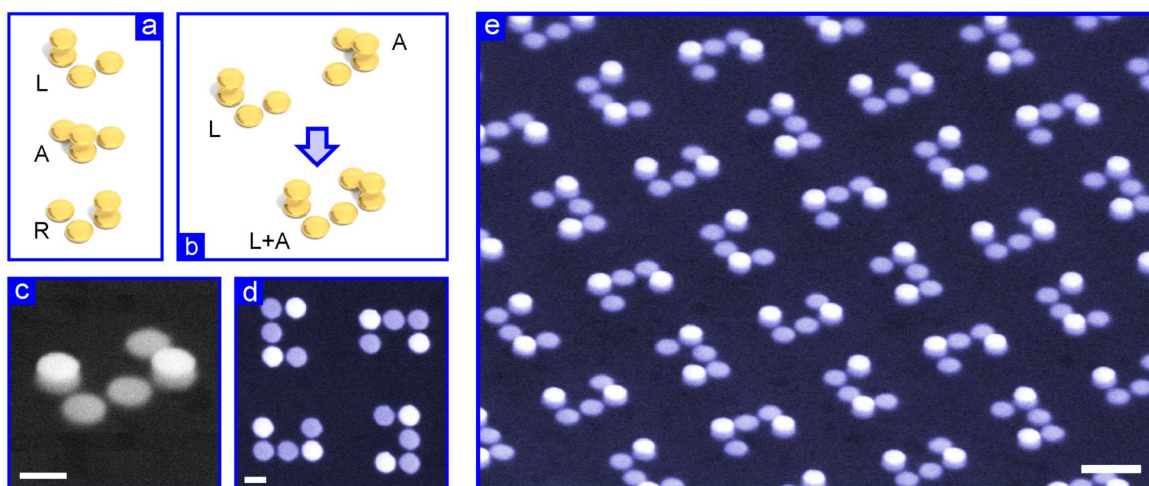


Figure 4.34.: Construction rules for a different set of plasmonic diastereomers. The individual chiral centers, shown in (a), are connected so that the first layer takes a U-shape, as shown in (b). (c) and (d) Tilted and normal view SEM micrographs of the fabricated structures, demonstrating excellent overlay accuracy. The scale bars are 200 nm. (e) Tilted overview SEM micrograph. The scale bar is 500 nm.

In order to further substantiate our findings, we investigate the properties of an even more complex composite molecule in figure 4.33. Figure 4.33 (a) depicts tilted view SEM images of a composite (L+R+A) molecule. If indeed the (R+A) molecule is a building block as suggested by the above results, the chiral optical response of the complex (R+A+L) molecule should be constructable from the response of the (L) and (R+A) building blocks. Figure 4.33 (b) thus depicts the chiral optical response of the composite molecule as well as the calculated spectra from the (L) and (R+A) building blocks. The calculated and the measured CD response again agree excellently in mode profile, spectral features, and amplitude, substantiating the role of the (R+A) molecule as separate building block in its own right.

So far we have studied composite molecules where all combinations result in a chiral compound. This fact is connected to the shape of the first layer. As it took an S-shape, which is 2D chiral, all possible positions of the upper layer dot will render the structure 3D chiral. In order to obtain achiral composite molecule one has to change the construction rules. Figure 4.34 depicts such a different set of rules. The individual centers, shown in figure 4.34 (a), are now joined such, that the first layer takes a U-shape, which is not 2D chiral. As a consequence, a number of composite molecules will be achiral. Figure 4.34 (c) depicts SEM micrographs of fabricated structures, again demonstrating excellent overall accuracy.

Figure 4.35 depicts the composite molecules which can be obtained by the construction rule as laid out in figure 4.34. In contrast to the previously discussed case one can construct six independent molecules of which three are achiral. A number of facts

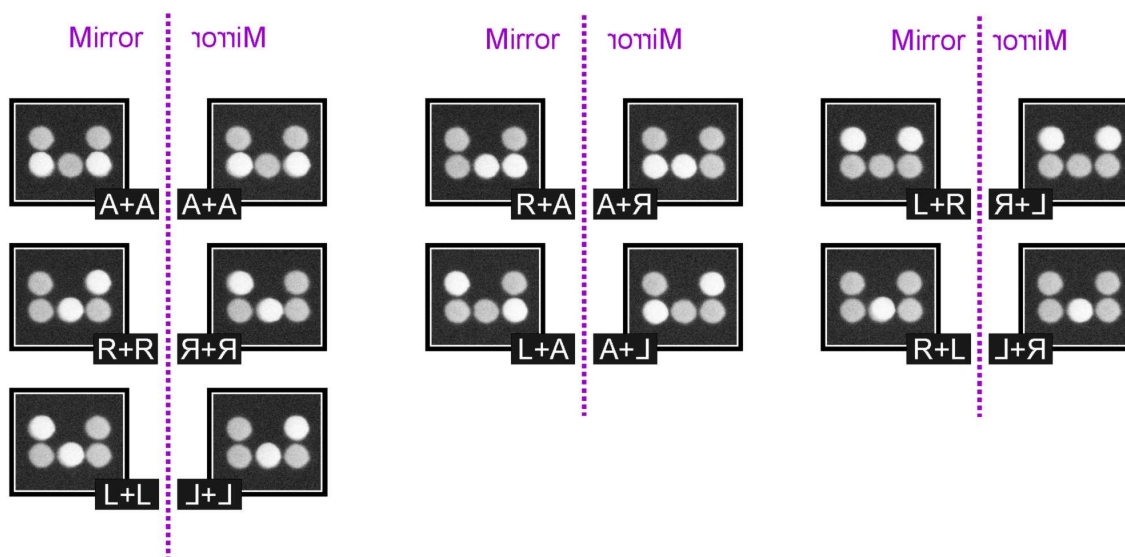


Figure 4.35.: The construction rule laid out in figure 4.34 allows for a number of composite chiral structures (note, that the upper layer particles appear brighter). In contrast to the earlier case, the composite molecules (A+A), (L+R) and (R+L) are achiral due to the presence of a mirror plane within the molecules. Note, that the (R+R) molecule is the enantiomer of the (L+L) one. Overall, one obtains three independent chiral molecules and their respective enantiomers as well as three independent achiral molecules.

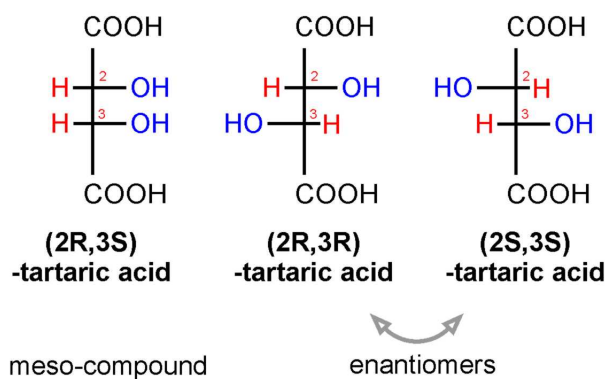


Figure 4.36.: Fisher projections of the stereoisomers of tartaric acid. Tartaric acid consists of two chiral centers, nevertheless it only possesses three stereoisomers, two of which are chiral and one is achiral. The achiral (2R,3S)-tartaric acid is called a meso-compound. The meso-compound is achiral due to the presence of a mirror plane within the molecule. (Note: the numbers 2, 3 denote the respective carbon atom, R, S denote their handedness).

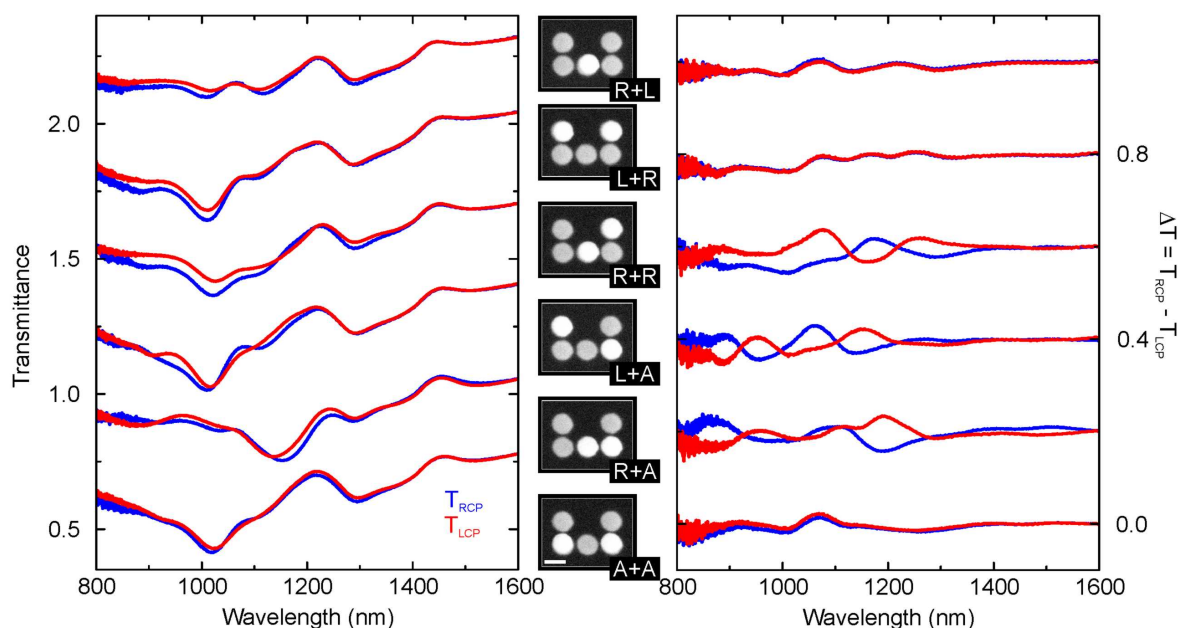


Figure 4.37.: Experimental realization of the three independent chiral composite molecules and their respective enantiomers, as well as the three achiral structures (fabricated twice). The left column depicts the experimental transmittance spectra for right- (blue) and left-handed (red) circularly polarized light for the structures shown in the normal view SEM micrographs in the middle column. The right column depicts the $\Delta T = T_{RCP} - T_{LCP}$ spectra for both enantiomers, respectively. The spectra show excellent mirror symmetry for interchanged handedness, as expected. The chiral optical response reaches values as high as $\sim 12\%$. Overall, the spectra show remarkable similarities, indicating that the chiral optical response might be generated by a limited basis set. The spectra are shifted upward for clarity (transmittance by 0.5, ΔT by 0.2). The scale bar is 200 nm.

appear interesting: The (R+R) molecule is the enantiomer of the (L+L) molecule. The achiral structures are achiral due to the presence of a mirror plane within the molecule. The (L+R) and (R+L) molecules are composed of two chiral building blocks and are nevertheless achiral. Such a phenomenon is as well known in chemistry. Here, a molecule composed of two or more chiral centers can as well be achiral due to the presence of a mirror plane. One terms such a molecule a meso-compound. The potential existence of a meso-compound is the reason why a molecule with n chiral centers can have a maximum of 2^n diastereomers. A number of three dimensional arrangements can in fact lead to a meso-compound which is not termed a diastereomer. An example is tartaric acid which comprises of two chiral centers, shown in figure 4.36. However only (2R,3R)-tartaric acid and its enantiomer (2S,3S)-tartaric acid are chiral. (2R,3S)-tartaric acid is a meso-compound due to the presence of a mirror plane, such that (2R,3S)-tartaric acid is the same as (2S,3R)-tartaric acid [199] (Note: the numbers 2, 3 denote the respective carbon atom, R, S denote their handedness, see also figure 4.36).

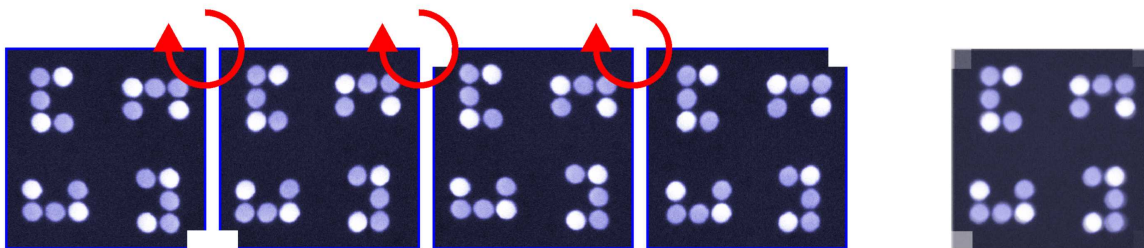


Figure 4.38.: On first sight the arrangement of the U-shaped clusters appears to be not C_4 symmetric. However, when successively rotating the same SEM micrograph clockwise by 90° (left part of the figure) and overlaying the semitransparent images (right-most image) one can hardly see any deviation, thus the arrangement is indeed C_4 symmetric.

The left column of figure 4.37 depicts the transmittance spectra for left- and right-handed circularly polarized light for the structures shown in the insets in the middle column. The right column depicts the $\Delta T = T_{RCP} - T_{LCP}$ spectra for both enantiomers of each structure. For achiral structures two arrays of molecules have been fabricated to check experimental consistency and reproducibility, hence even for the achiral (A+A), (L+R) and (R+L) molecules two ΔT spectra are shown. In contrast to the conclusions drawn from figure 4.29 for the diastereomers with 2D chiral first layer, all spectra for the structures at hand do show very different behaviour. Only the feature around 1500 nm appears in the spectra for all molecules. Even more confusing, the achiral structures seem to show significant chiral optical response. Moreover, for the chiral molecules one does not observe the expected mirror symmetry of the CD response, significant dissimilarities are present. Both findings point to the presence of another contribution to the optical response of the molecules. The first idea coming to mind is polarization conversion. However, the C_4 symmetric lattice should suppress this contribution effectively, as we have seen earlier. Figure 4.38 demonstrates that the lattice is indeed C_4 symmetric. Inspecting the SEM micrographs in figure 4.34 one might be tempted to assume otherwise; this false impression is caused by the U-shape of the particle and the fact that the rotation axis is not in the center of the particle, as it is the case for the S-shaped molecules. Figure 4.38 demonstrates that the lattice is indeed C_4 symmetric, as intended. Moreover, if the spectral features would indeed be caused by polarization conversion they should be identical for all achiral structures as the effect is caused by the lattice and not by the objects placed at the individual lattice sides.

Another potential source for the deviations are fabrication tolerances. It might be possible that the differences are caused by misalignment between the two layers, which changes in magnitude and direction from field to field. Figure 4.39 convincingly shows that this is not the case. As already stated above the (R+R) molecule is the enantiomer of the (L+L) molecule. Nevertheless, both molecules and their respective enantiomers have been fabricated. Two of the resulting CD spectra should thus be identical (yet, they change from red to blue and vice versa), if not disturbed by fabrication errors. The

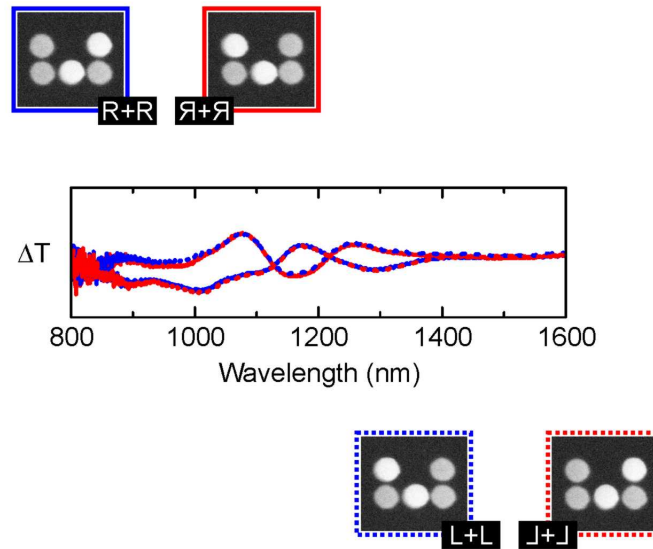


Figure 4.39.: Overlaid ΔT spectra for the (R+R) and (L+L) molecules and their respective enantiomers. The enantiomer of the (R+R) cluster is the (L+L) one, thus two spectra of different colour should be identical. Indeed, only minute differences can be observed, showing that fabrication does not limit the experiment.

overlaid spectra in figure 4.39 are nearly perfectly identical, only minute differences can be observed. Hence, fabrication does not limit the experiment.

The source of the additional signal hence remains unclear at the moment. Maybe it is caused by a slight conical shape of the individual dots, which would already render the first layer 3D chiral. Such effects have already been observed for comparably high planar swastika shaped structures [225]. However, if that would be the case, it should as well have been observed in all previously discussed cases.

4.6. Conclusions, Summary & Outlook

In conclusion, we have shown that three-dimensional plasmonic oligomers can form artificial "plasmonic molecules" with a strong chiral optical response. Being composed of individual metallic nanoparticles whose properties can be nearly arbitrarily changed these clusters are spectrally highly tunable. We have shown that resonant plasmonic near-field coupling is an indispensable prerequisite for the emergence of a chiral optical response. Hence, only configurational chirality is possible in a plasmonic molecule. Inducing a handedness by different particle sizes in a symmetric configuration causes no chiral optical response as the particles are not resonantly coupled. Moreover, we have shown that a chiral particle cluster can serve as a three-dimensional chiral plasmon ruler

with the capability to encode its three-dimensional arrangement in strongly modulated optical spectra.

In studying charge transfer in complex chiral plasmonic oligomers we have demonstrated in experiment and simulation a strong and broadband chiral optical response with a bandwidth extending from 700 nm to 3500 nm. We have shown that the broadband response occurs at the onset of charge transfer between the individual particles. On the one hand this causes a strong red-shift of the fundamental mode, shifting the chiral optical response to longer wavelength. On the other hand, due to the geometrical distortions of the particle, higher order modes of the structure can be excited with high efficiency and are hence responsible for the observed chiral optical response at higher energies. We have shown that the modes supported by the stacked structures are combinations of the modes of the individual layers. The lowest energy modes are associated with strong magnetic moments induced by ring currents inside the particles and displacement currents between them. The parallel or antiparallel alignment of these moments determines the energetic position of the respective modes and depends on the handedness of the structure and of the incident circularly polarized light. We believe that the concept of three-dimensional chiral plasmonic oligomers together with the excitation of charge transfer plasmon modes is a promising route for strong and broadband chiral optical systems.

Our proof-of-concept studies on structures fabricated by electron-beam lithography as a top-down technique should be realizable in larger quantities using self assembly strategies [272] with progressing advances in DNA enabled self assembly [170, 173–175, 273–276]. Charge transfer in such clusters can be achieved by subsequent metal-overgrowth [256]. These clusters will pave the road for new devices possessing unprecedented strong chiral optical responses. Being three-dimensional and hence showing true chirality these clusters are expected to show an even higher response and coupling to chiral bio-molecules for enantiomer sensors with single molecule sensitivity for applications in medicine, biology, drug development, and biosensing [28, 277–279].

In case of the plasmonic diastereomers we have shown that the chiral optical response of such complex structures can be traced back to the optical properties of the constituting elements. We can thus unravel the optical response of our molecules in a straightforward way offering simple and intuitive design rules for complex composite chiral molecules. The individual building blocks of our composite molecules can be left- or right-handed, as well as achiral, offering a large parameter space. We have shown that the CD response of the composite molecules can be constructed from the CD response of a limited basis set, just as the molecules themselves are constructed from a basis set of chiral centers. As long as there is no near-field coupling between the chiral centers, the CD can be obtained by adding up the CD response of the individual building blocks. As soon as there is cross-talk, i.e., near-field coupling between the chiral centers, the additivity vanishes and the behaviour becomes more complex.

Our study underlines the nearly unlimited potential of artificial plasmonic molecules. By drawing inspiration from Nature and Chemistry we have proposed and demonstrated another intriguing phenomenon on the route to tailor the optical response of complex plasmonic nanostructures at will.

5. Nonlinear Plasmon Optics

5.1. Introduction

Plasmonics is the optics of metal nanoparticles. If an external light field impinges on a metal nanoparticle, collective oscillations of the quasi-free conduction electron are excited. The charge cloud is displaced with respect to the fixed ionic background and thus causes local electric fields. The main benefit afforded by plasmonics is its ability to concentrate incoming electromagnetic energy into deep subwavelength volumes. On the one hand the metal particles themselves are in general smaller or at least comparable to the wavelength of light. Additionally, the so-called hot spots at which the field enhancement occurs are significantly smaller than the particle itself. The local electric field strength can thus surpass the incoming field strength by orders of magnitude. The process is moreover surprisingly efficient as the plasmonic resonances couple extremely well to an external light field due to the large resonances dipole moment which is fundamentally connected to the large number of free conduction electrons.

Due to this strong confinement, highly efficient nonlinear optics utilizing plasmonic structures were in the focus of interest from the beginning of plasmonics. The intensity of, e.g., second harmonic generation (SHG) scales with the fourth power of the fundamental field strength, third harmonic generation (THG) even scales with the sixth power. Keeping in mind that the local electric fields associated with a plasmonic resonance can, at least in theory, exceed the incoming field strength by orders of magnitude, extremely efficient nonlinear conversion efficiencies are to be expected.

The first nonlinear optical experiments on plasmonic systems date back to the early 1980. Wokaun and co-workers studied second harmonic generation from metal-island films and microstructured silver films and interpreted the enhanced response in terms of localized surface plasma oscillations [280]. Ricard and co-workers demonstrated optical phase conjugation from a composite material of gold or silver spheres immersed in water. The value of the optical Kerr coefficient on resonance was found to be about three orders of magnitude larger than off-resonantly [281]. Enhanced second-harmonic generation from rough metallic films was as well investigated in detail [282,283]. Early on it was realized that plasmon resonances on the surface play an integral role in all the processes, being second harmonic generation or surface enhanced Raman scattering [284–286]. In fact,

in the beginning mostly composite materials with small metal inclusions were studied. Their nonlinear optical properties could be modelled by nonlinear extensions of Maxwell-Garnett [4,287] and effective-medium theories [288,289]. Apart from phase conjugation, difference frequency mixing, four wave mixing [290], second harmonic generation, and other nonlinear optical processes were reported.

Conceptually, a number of mechanisms could be responsible for the nonlinear optical response of a metal nanoparticle residing in a dielectric environment:

- **Surface nonlinearities:** When the particle is excited close to its plasmon resonances the quasi free conduction will perform harmonic oscillations. Yet, due to the finite size of the particles and the presence of the surface, anharmonicities will start to play a major role. It has been shown that for very small nanoparticles this anharmonicity can lead to a significant source of third harmonic radiation, showing a fourth order dependence of the TH intensity on the diameter of the particle. In this model the third harmonic contribution can be seen as induced by the surface of the sphere and thus the induced dipole is proportional to the surface area of the sphere. Note that this contribution vanishes as soon as the anharmonicity in the potential vanishes, that is, as soon as the particle becomes too large for the oscillating electrons to see the surface.
- **Bulk or volume nonlinearities:** Another mechanism is linked to the bound electrons of the material itself. The signal could stem from the contribution of the individual constituents of the cluster rather than from its overall properties, thus being a molecular, size-independent property. This contribution would depend on the volume of the nanoparticle as the signal increases linearly with the number of individual "molecules" in the cluster. The nonlinear signal would hence increase with the sixth power of the particle radius. This term is thus considered as the volume contribution to the nonlinear signal.
- **Field enhancement:** The last contribution originates from the enhanced local electric fields associated with the plasmonic resonance. If the particle is surrounded by a dielectric, the strong near-fields can enhance the nonlinear response from this dielectric. Additionally, the near-fields close to the nanoparticle surface can enhance the signal from the bulk nonlinearity of gold itself.

Obviously, the origin of the nonlinearity might vary when changing the studied systems. Additionally, two or more processes might occur simultaneously.

In 2005 Lippitz et al. for the first time studied third harmonic generation from single gold nanoparticles [291]. They attempted to unravel the mechanism responsible for the signals observed, yet, a clear differentiation between surface and bulk contributions was not possible.

In spite of the remaining open questions regarding the nonlinear processes in these comparably simple systems, a multitude of research has been devoted to much more complicated systems. With the advent of well controllable fabrication and synthesis methods, such as electron beam lithography or wet chemical growth methods, complex plasmonic materials became available. One of the first examples is the work by Klein et al., studying second harmonic generation from arrays of split ring resonators [292]. Split ring resonators are U-shaped nanostructures which basically constitute a nano-scale version of an LC-circuit. Their most intriguing property is the presence of a strong plasmonic resonance which is associated with the excitation of a ring current in the U-shape and thus a magnetic moment at optical frequencies. As such a material property is not present in any naturally occurring material, these composite systems are termed metamaterials. The authors explained the strong second harmonic response in this system by including a nonlinear source term based on the magnetic component of the Lorentz force. For the first time it had been suggested that the tailoring of an artificial material would allow for the tailoring of the nonlinear optical properties beyond the capabilities of naturally occurring materials.

Fuelled by these early experiments nonlinear effects were studied in a plethora of systems, such as - to name a few - SHG on L- and T-shaped nanoparticles [185, 293–295], on chiral [296] and planar chiral systems [297–299], SHG from 3D nanocups [300] and nano-apertures in metal films [301, 302], SHG from silver triangle arrays [303], THG from individual dimer nanoantennas [304, 305], and from arrays of nanoantennas [88, 306], THG on disk arrays [307], frequency mixing at coupled gold nanoparticles [308, 309], SHG and THG from arrays of split ring resonators [310, 311] and inverse split ring resonators [312]. Moreover, the systems became more complex by incorporating elliptical particles into glasses [313], combination with crystalline substrates [314, 315], coupled systems of plasmonic resonances and waveguide modes [186, 316–318], gaseous media in the vicinity of the nanostructures for enhanced higher harmonics generation [194, 195, 319], metallic shells around highly nonlinear cores [320], and loaded nanoantennas [321, 322]. Another degree of complexity was recently introduced by multi-resonant plasmonic systems in the hopes of enhancing the fundamental as well as higher harmonic fields which are involved in the conversion processes [323–325].

However, despite the experiments made, a surprisingly large number of open questions remains. One of the main drawbacks of the conducted experiments, to a surprise, appears to be the complexity of the structures. The motivation behind the complex structures is multifold: Firstly, the structures allow for a nearly arbitrary manipulation of their linear optical properties. Secondly, the structural geometry of the systems can be manipulated which is believed to be particularly important due to the strong symmetry dependence of nonlinear optical processes. Thirdly, researchers are driven by the dream of disentangling linear and nonlinear optical properties, that is, strongly different nonlinear optical responses of two systems despite identical linear optical ones.

As already much simpler structures are not yet fully understood the entanglement of

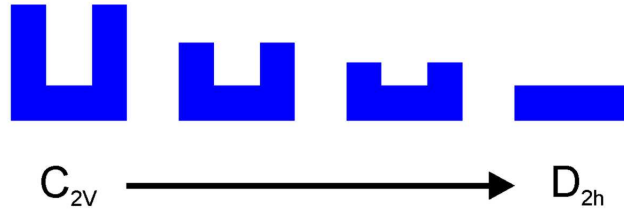


Figure 5.1.: A split ring resonator (SRR) belongs to the C_{2v} symmetry group. As it breaks inversion symmetry the structure allows for second harmonic generation in electric dipole approximation. A single bar, being if D_{2h} symmetry, does not allow for SH in electric dipole approximation. Successively reducing the arm length of the SRR should thus allow for the direct observation of the influence of symmetry on the nonlinear optical conversion process.

a multitude of different factors, such as linear properties, spatial symmetries, changing near-field distributions, the presence of different materials and multiple resonances, makes it nearly impossible to deduce the origin of the nonlinear response and the true influence of the individual subsystems. Figure 5.1 illustrates an example of such a seemingly straightforward experiment. It has been demonstrated that split ring resonators are comparably efficient sources of second harmonic radiation. As in electric dipole approximation SHG is symmetry forbidden in inversion symmetric systems it is widely believed that symmetry breaking is a key ingredient in this process. Thus, it appears to be straightforward to test this hypothesis by making use of the nearly unlimited structural tunability of plasmonic nanostructures. In reducing the length of the split ring resonator arms the structures can successively been transformed into a bar. In doing so, the symmetry of the system is increased from C_{2v} to D_{2h} [326]. Most importantly, the bar is inversion symmetric and is thus expected to not show any second harmonic response under normal incidence illumination. To first sight, one would thus expect the second harmonic response of the structures to successively decrease from the maximum signal of the "full" split ring resonator to none for the bar, depending on the "degree" of symmetry breaking in the system. Even so there is no real "degree" of asymmetry in geometrical systems such as this, there still needs to be a continuous transition from the one into the other system, i.e., from symmetry allowed SHG to symmetry forbidden SHG (in electric dipole approximation). This experiment should therefore be a convincing test of the symmetry dependence of the second harmonic response.

However, it is imperative to note that the symmetry is not the only property that is changing in the system. Firstly, the linear optical properties will undergo significant changes. The spectral position of the fundamental plasmonic mode basically depends on the overall length of structure. This length decreases as the length of the split ring resonator arms decreases, causing a blue shift of the plasmonic mode. As it is physically meaningless to compare the response of resonant and off-resonant systems, this spectral shift needs be compensated. This can be done either by increasing the overall size of the structure or by using a tunable laser source to excite the structures. Note that in

both cases the amount of gold, which is typically used to fabricate the structures, will significantly change as well. Therefore, if the gold itself is involved in the conversion process, this change in material filling fraction might have a significant influence. Furthermore, the overall plasmonic mode will change drastically. The fundamental split ring resonator mode is associated with a magnetic moment, whereas the bar just supports a simple dipolar mode. Thus, the near-field distributions will be dramatically different. Simultaneously, the dipole moment of the resonances will change as well. On the one hand due to the change in mode character but on the other hand as well due to the change in structure volume and thus due to the change of the number of free electrons participating in the collective oscillations. As a consequence, the spectral linewidth and thus the dephasing time of the different modes in the structures will be strongly different. Yet, already basic nonlinear optical textbooks show us the close connection of a resonance linewidth or damping on the nonlinear optical response [327, 328]. As a further direct consequence of the different gold volume, the overall scattering amplitude of the resonance will change, changing the interaction strength of the laser field with the structure. Additionally, when changing the laser wavelength one might probe the spectral dependency of the $\chi^{(2)}$ active material from which the signal is fundamentally stemming, which could be the gold or the substrate.

Overall, a change in the second harmonic signal could thus be caused by: the changing structural symmetry, the different material filling fractions, the change in resonance linewidth, the change of the scattering amplitude, the change in mode character (disappearance of the magnetic mode), the change in the near-field distribution or by a spectral dependency of the molecular χ^2 of the substrate or gold. Thus, we have to conclude that this experiment, despite the fact that it appeared perfectly reasonable in the beginning, is futile as no conclusions can be drawn whatsoever.

In the following, we thus perform third harmonic generation experiments on a simple prototype system comprising of two individual metallic bars or triangles, forming nanoscale antennas. The distance between the elements as well as their basic size allows to controllably change the linear optical properties of the system. Additionally, the strong confinement of the local electric fields within the gap of the antennas is expected to cause a strong nonlinear optical response, rendering this system highly interesting.

5.2. Third Harmonic Generation From Dimer Nanoantennas

As already discussed, plasmonic structures, such as plasmonic nanoantennas, concentrate energy in subwavelength volumes [329–332]. The field enhancement can exceed values of 10^3 [333]. The strongly enhanced local electric fields boost the nonlinear optical re-

sponse of nanoantennas and other metallic nanostructures. Similar to the case of metal-dielectric photonic crystals [317], both the optical nonlinearity of the metal [334, 335] and the nonlinearity of the dielectric material in the antenna hot spot can contribute to the signal [314, 320, 321]. Hence, in the case of gap nanonantennas we expect THG from the bare antenna and the THG originating from the gap region. The notion of a hot spot suggests that the gap signal exceeds the antenna signal. Yet, it is a priori not possible to disentangle these two contributions without modelling the systems and its response. A full numerical simulation of the local optical field and its interaction with the local nonlinear polarizability is able to differentiate between these contributions [317]. However, a more intuitive understanding is desirable for a rational design of antennas for nonlinear applications [336]. Many aspects of harmonics generation in nanoantennas are still unclear and not well understood, e.g., the role of resonance strength and width, field enhancement in the hot spot, and the influence of antenna geometries on the overall conversion efficiency. While the nonlinear response of metal nanostructures was optimized in recent publications [291, 304–306, 308, 337], only little attention was paid to the simultaneously changing linear response. However, already nonlinear optics textbooks show the close connection between linear and nonlinear properties of matter [327].

In order to investigate some of the mentioned aspects, we study dimer nanoantennas which consist of two equally sized plasmonic nanoparticles separated by a gap. In close proximity to one another the plasmonic resonances in the particles mix and hybridize, giving rise to two new collective modes, as shown in the plasmon hybridization scheme [65] depicted in figure 5.2 (a). For light polarized along the long axis of the antenna, the symmetric dipole allowed mode is decreased in resonance energy, whereas the antisymmetric mode is increased in energy. The latter mode cannot be excited for normal light incidence because of its zero net dipole moment. Hence, the gap size as well as the size of the triangles will determine the spectral position of the dipole allowed mode. This behavior is visible in the experimental linear extinction spectra of a series of bowtie nanoantennas, shown in figure 5.2 (b). For decreasing gap size we observe a strong resonance red-shift. Upon ohmic contact the resonance shifts outside the observable wavelength region. [130, 131, 338] Thus, we have a system at hand that allows for an independent spectral tunability either by the size of the individual element or by the gap distance. Furthermore, a change of the particle size and thus its volume will allow to tailor the dipole moment or oscillator strength of the plasmonic resonance. Note that we perform all experiments on arrays ($100 \times 100 \mu\text{m}^2$) of nominally identical, non interacting antennas (see figure 5.2 (c)) so that a loosely focused laser beam can be used.

The structures are defined in double layer PMMA using electron beam lithography (Raith e Line) on a bare Suprasil quartz glass substrate (Heraeus) followed by thermal evaporation of a 2 nm Cr adhesion and a 40 nm Au layer and a subsequent lift-off procedure. Scanning electron microscope images are obtained using a Hitachi S-4800 electron microscope. For the excitation of the nanostructures 8 fs laser pulses centered around 817 nm with a spectral bandwidth extending from 690 nm to 930 nm are utilized

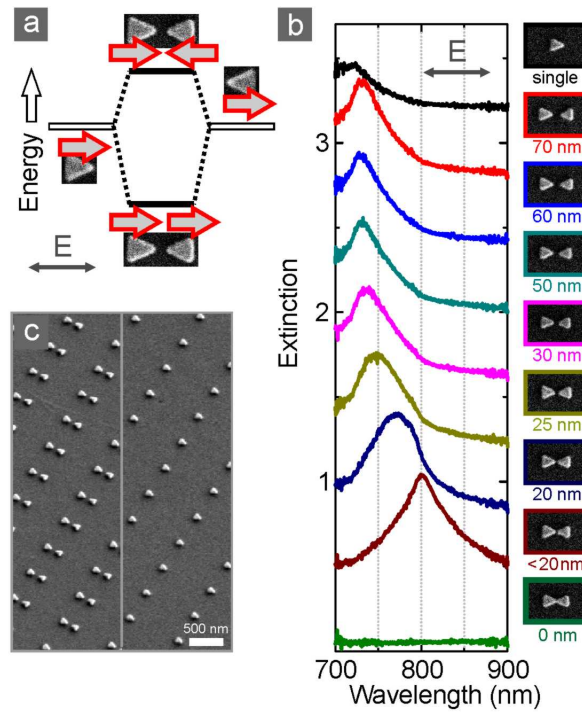


Figure 5.2.: (a) A bowtie nanoantenna constitutes a plasmonic dimer which can be described within the framework of plasmon hybridization. Two collective modes are formed, namely a symmetric dipole-allowed one with a lower resonance energy and an antisymmetric dark mode with higher resonance energy. The dipole-allowed mode can be tuned in resonance energy by the size of the triangles and the gap size. (b) Experimental linear extinction spectra for a series of equally sized triangles but decreasing gap size. The spectra have been offset vertically for clarity. One observes the predicted resonance red-shift upon closing of the gap. (c) Exemplary tilted overview SEM images of the studied antenna arrays.

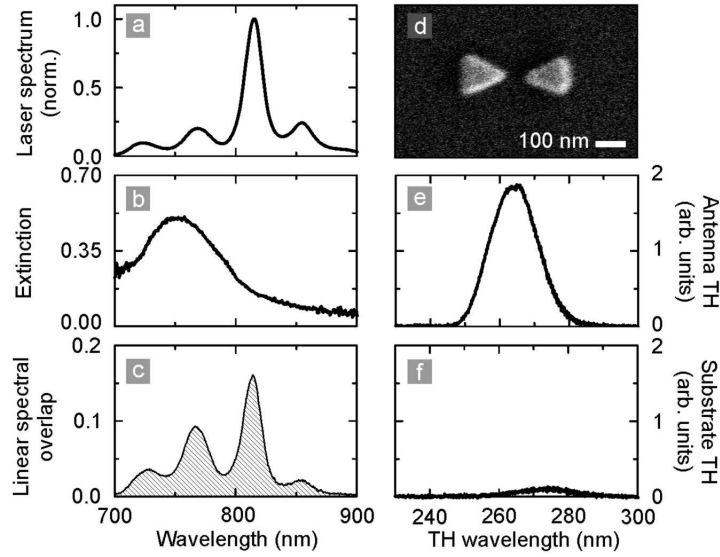


Figure 5.3.: Linear and nonlinear optical properties of a bowtie antenna array, basic triangle size $(135 \times 160) \text{ nm}^2$, gap size 70 nm. (a) Spectrum of the laser source. (b) Linear extinction spectrum of the antenna array. (c) Linear spectral overlap spectrum defined as the product spectrum of the laser and extinction spectra. (d) SEM micrograph of one antenna from the array, periodicity 800 nm x 500 nm. (e) Third harmonic spectrum of the antenna array. (f) Third harmonic spectrum of the bare substrate.

(VENTEON, pumped by a Coherent Verdi V10). The incoming radiation is focused onto the sample and recollimated using spherical mirrors ($f = 100 \text{ mm}$). For TH measurements a quartz glass prism sequence is used to filter out the fundamental light. The spectrally resolved detection is performed by a grating monochromator and an attached LN_2 cooled UV-enhanced CCD camera sensitive to the fundamental as well as the TH light in the UV region at around 270 nm (Roper Scientific).

Our setup allows measuring the third-harmonic (TH) spectrum radiated by the antennas and simultaneously their linear optical properties using the broadband laser as white light source. This in situ measurement ensures identical excitation conditions of the plasmonic resonances as in the nonlinear optical measurements.

Figure 5.3 depicts the performed linear and nonlinear measurements for an exemplary bowtie antenna array. The left column shows the linear optical properties: Panel (a) shows the spectrum of the driving laser source. The linear spectral response of the antenna array is depicted in panel (b). The interaction strength of the laser source and the nanostructure is basically determined by two quantities: Firstly, by the spectral detuning between the peak intensity of the laser and the resonance maximum of the plasmonic resonance. In order to excite the plasmonic resonance efficiently it is important to drive it resonantly. Secondly, it is determined by the overall interaction strength of the resonance with an external light field. This interaction strength is given by the

resonance dipole moment which is linked to the number of free electrons participating in the collective plasmonic oscillation and thus to the volume of the nanostructure. The resonance dipole moment manifests itself as the area content of the extinction peak. In order to quantify the interaction strength between the laser source and the nanostructure we define the so-called linear spectral overlap spectrum, which inherently includes both quantities. It is obtained as the product spectrum of the laser and extinction spectra, as shown in panel (c). It is important to note that the laser spectrum together with the linear extinction spectrum of the nanostructure determines the spectral position of highest interaction. It is hence crucial to measure the linear response carefully.

The right column of figure 5.3 depicts the nonlinear optical response of the array: In panel (e) the third harmonic (TH) spectrum of the array and in (f) the third harmonic spectrum of the bare glass substrate. Two observations are immediately apparent: The TH signal originating from the antenna array is significantly stronger than the substrate TH. Additionally, the two spectra exhibit their maxima at different spectral positions. The signal from the bare substrate is roughly centred on 272 nm, 1/3 of the wavelength of the peak intensity of the fundamental laser spectrum whereas the other peaks at ~ 264 nm. Not only does the presence of the plasmonic resonance seem to boost the TH signal, it is as well spectrally shifting the TH emission maximum.

It is commonly expected that the TH response of a gap nanoantenna is dominated by the contribution arising from the strongly enhanced fields inside the nanoscale gap. If the TH from the hot spot would indeed dominate the TH from the antenna itself, then the nonlinear conversion efficiency of a dimer nanoantenna should drastically increase when the gap size decreases as the near-field localization is particularly strong for small gap sizes. In order to check this intuitive picture, figure 3 depicts the TH spectra for two different sized bowties under decreasing gap size. The left column depicts the TH spectra for triangles of $(125 \times 150) \text{ nm}^2$ basic size, the right column for a size of $(170 \times 190) \text{ nm}^2$. In both cases the gap sizes are varied, starting from single triangles over gap sizes of 70 nm, 60 nm, and 50 nm (from top to bottom). For the smaller antennas we observe a significant increase in the TH signal strength under decreasing gap size, seemingly consistent with our intuitive expectation. In striking contrast, we observe a strong decrease in TH signal strength under decreasing gap size for the larger antennas. Furthermore, the larger antennas produce significantly stronger signals for all gap sizes. Additionally, we observe for all antennas a small red-shift of the TH emission maximum under closing gap. For the smaller antennas the emission maximum is below 272 nm (indicated by the grey arrow) and approaches this value, whereas the emission maximum is at longer wavelength for the bigger antennas and shifts even further away from it when decreasing the gap size.

These findings are a strong indication that the depicted experiments are dominated by the linear optical response of the antennas and not by gap nonlinearity. We have already shown in figure 5.2 that the linear extinction spectrum undergoes a significant red-shift when decreasing the gap size. Additionally, figure 5.4 illustrates that the TH emission

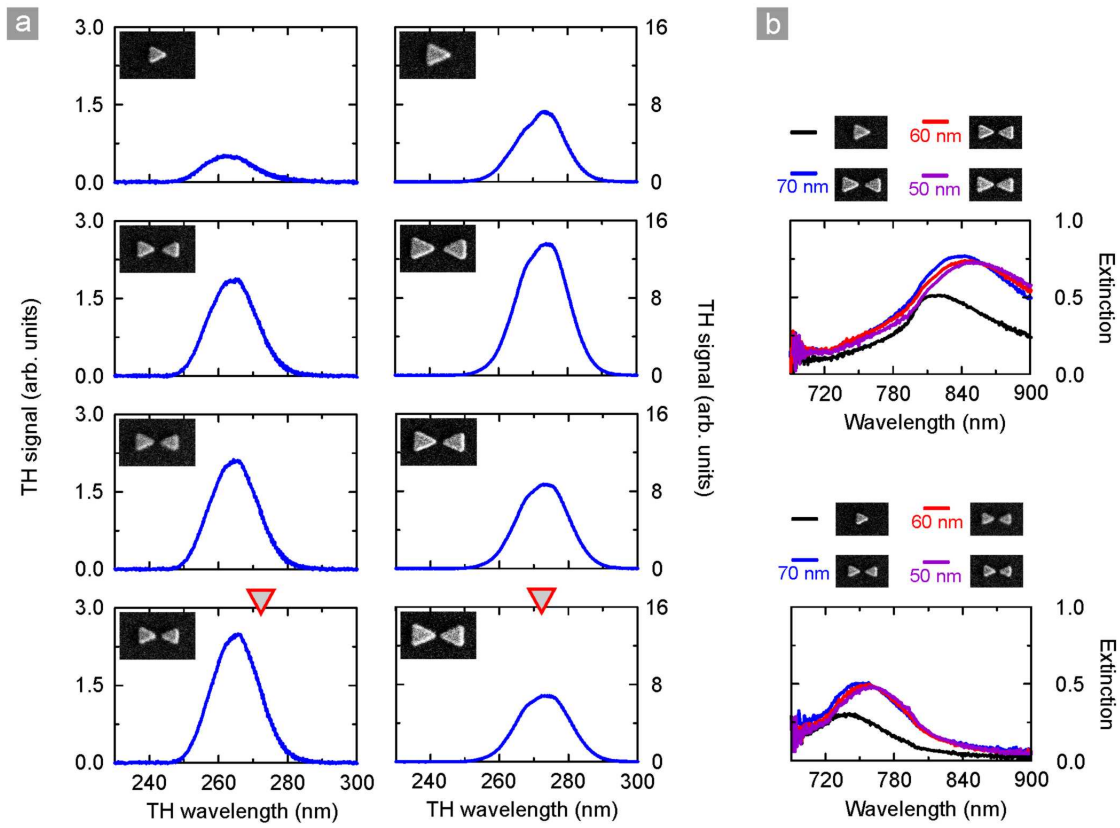


Figure 5.4.: (a) Third harmonic spectra of antenna arrays as a function of decreasing gap size. The left column depicts the TH spectra for triangles of $(125 \times 150) \text{ nm}^2$ basic size, the right column for a size of $(170 \times 190) \text{ nm}^2$. The gap sizes are varied in both cases from single triangles, 70 nm, 60 nm, and 50 nm gap size (from top to bottom). (b) Linear extinction spectra of the structures in (a).

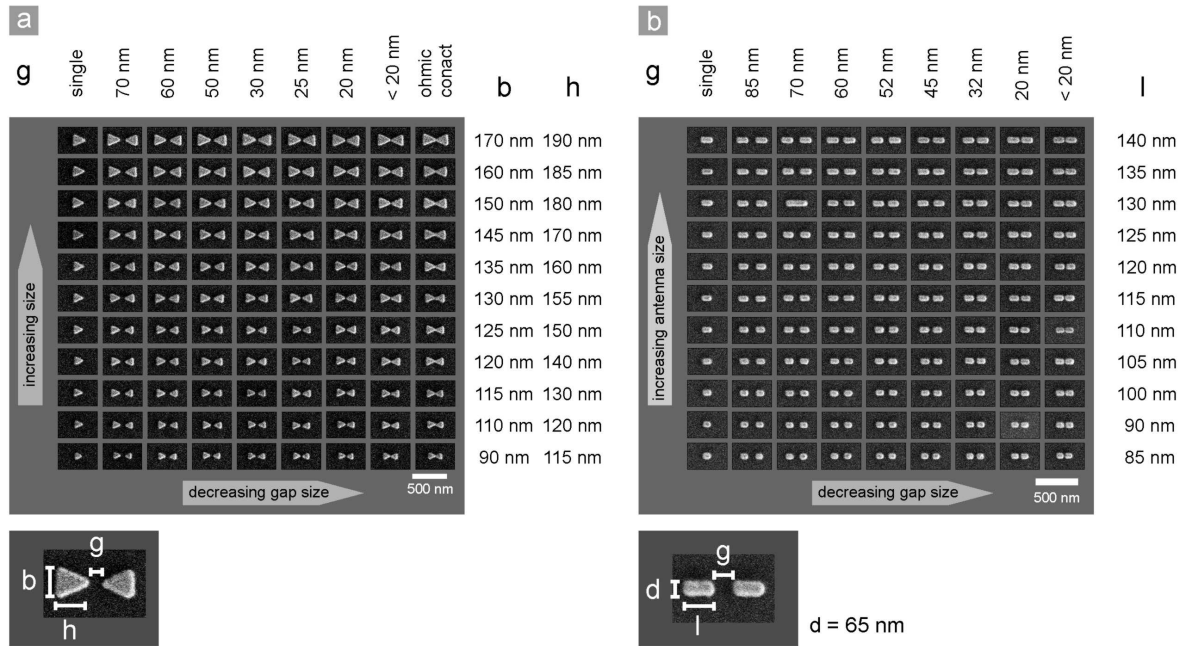


Figure 5.5.: Geometric parameters of the fabricated antenna arrays. (a) Bowtie nanoantennas, each antenna represents an entire $100 \times 100 \mu\text{m}^2$ array, periodicity $800 \text{ nm} \times 500 \text{ nm}$, gold thickness 40 nm . An identical sample of 99 arrays has been covered with 100 nm SiO_2 . (b) Gap nanoantennas consisting of two rod shaped nanoparticles. As before, each antenna represents an entire $100 \times 100 \mu\text{m}^2$ array, periodicity $800 \text{ nm} \times 500 \text{ nm}$, gold thickness 40 nm .

maximum is below 272 nm for a plasmonic resonance below the maximum laser intensity as the spectral position of maximum interaction strength, as given by the linear overlap spectrum, is below the laser center wavelength. This proves that the plasmon resonance is significantly shifting the maximum TH signal from the intuitively expected $1/3$ of the maximum laser intensity. Thus, already alone from the nonlinear optical behaviour we can deduce that the smaller antennas are blue-detuned from the laser center wavelength, whereas the bigger ones are red-detuned. This as well explains the direction of the shift for the two antenna geometries: For decreasing gap size the plasmon resonance red-shifts, as does the spectral position of maximum interaction strength. Therefore, the TH center wavelength is shifting towards the laser center wavelength for the smaller antennas and shifting away from it for the bigger antennas. The measured linear optical spectra which are shown in figure 5.4 (b) confirm our interpretation.

To further substantiate this explanation and to deepen our understanding of the underlying processes, we have fabricated a series of samples and studied their TH response. We varied the triangle size and gap size of the bowtie antennas, resulting in 99 different combinations. To modify the field distribution even further, we changed the index of refraction of the environment by covering an identical sample with 100 nm SiO_2 . Thirdly, we changed the shape of the antennas from a bowtie antenna (consisting of triangles)

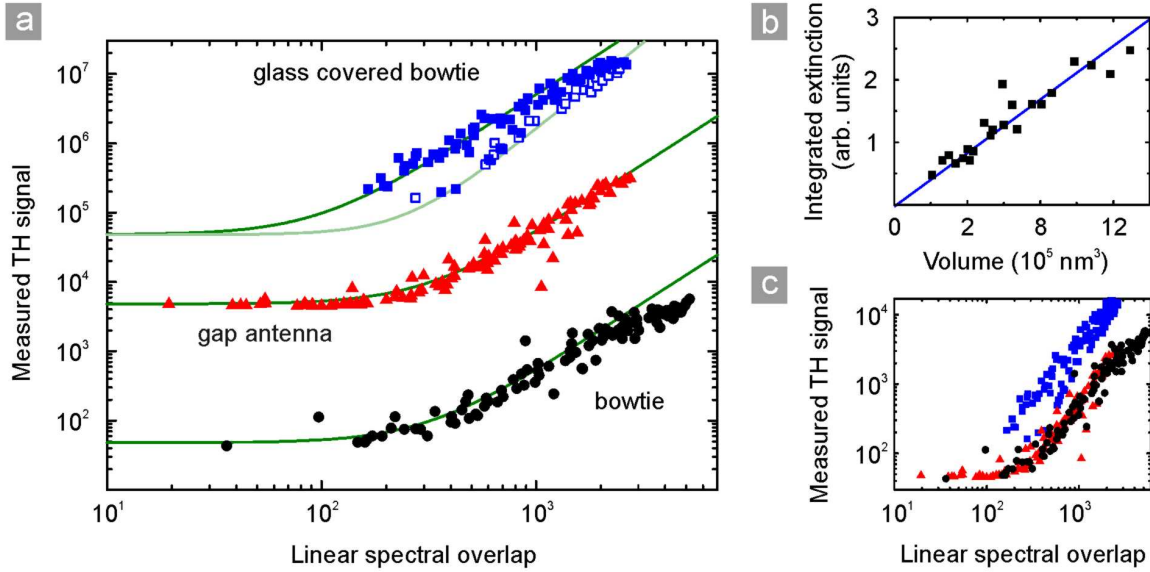


Figure 5.6.: (a) Integrated measured third harmonic signal versus the integrated linear spectral overlap spectrum for the bowtie antenna, gap antenna, and glass covered bowtie antenna arrays. The data points are shifted upwards for clarity. (b) Integrated linear extinction versus the nominal volume for a selection of antenna arrays. (c) Comparison of the conversion efficiencies for the different antenna geometries. The data of (a) is plotted without the vertical shift for direct comparability.

to a gap antenna (consisting of rectangles), again varying size of the rectangle and the gap between the rectangles. In total we thus examined 297 antenna fields. Figure 5.5 depicts exemplary SEM micrographs as well as the geometrical dimensions of the structures. The obtained results have shown us the crucial importance of the linear optical properties for the nonlinear optical ones. Hence, it is imperative to know and quantify the linear optical response as only this will render a comparison of the TH conversion efficiencies possible. So far we are not capable to disentangle the influence of the changing linear optical properties under manipulation of the geometrical parameters from any possible influence of gap nonlinearities or possible further unknown contributions.

In figure 5.3 we have already introduced the linear spectral overlap spectrum. This spectrum describes how efficient the laser source interacts with the plasmonic nanoantennas. If one integrates this spectrum one obtains a scalar value quantifying the interaction strength between the external light source and the nanoantenna. In figure 5.6 (a) we plot the integrated measured TH signal against the linear spectral overlap for all 297 antenna arrays. Remarkably, we find a distinct correlation between the two quantities. It is important to note that in this plot we can not distinguish the different antenna arrays. Independent of gap size or basic size all antenna arrays obey the same correlation between the spectral overlap and the TH signal strength. This is a clear indication that not the actual gap size itself is the key parameter determining the TH signal strength,

but rather the linear optical properties, which are the spectral detuning of the plasmonic resonance from the laser source, the amplitude of the resonance, as well as its linewidth being a measure of the quality factor of the resonance. All these parameters determine the value of the linear spectral overlap.

To further underline this strong correlation we have fitted the data points using a function of the form $I_0 + A \cdot x^n$. For off-resonant antenna arrays, meaning antenna arrays with a vanishing spectral overlap, the TH signal approaches a constant value. This behaviour is particularly visible for the gap antenna arrays. Quite a number of gap antenna arrays are in fact significantly blue-shifted as compared to the laser spectrum. Interestingly, the TH signal strength for the off-resonant case is very similar for the bowtie antennas, gap antennas, and glass covered bowtie antennas. This finding already points to the origin of the signal: The constant background I_0 basically describes the TH signal originating from the bare substrate in the absence of any resonant plasmonic object.

The data points for the bowtie and gap antennas follow a quadratic ($n = 2$) dependence in the linear spectral overlap and no subgroups seem to form here. In contrast, the glass covered bowtie antenna arrays form two distinct subgroups: One follows the same quadratic behaviour, the other one is nearly perfectly parameterised by $n = 2.5$. As the glass covered bowties have the same geometrical dimensions as the uncovered bowties, yet reside in a higher effective refractive index environment due to the SiO_2 overcoating, the resonances are significantly red-shifted. Hence, one possible explanation for the observed deviations is linked to the spectral position of the plasmonic resonance, meaning whether it is blue- or red-detuned from the laser center wavelength. Therefore, in figure 5.6 (a) the red-detuned covered bowtie antenna arrays are depicted with open symbols, the blue-detuned with closed ones. It can be seen that most of the data points of the second subgroup are actually red-detuned structures. Such strongly red-detuned arrays are not present in the bowtie and gap antennas arrays sets. This is why we only observe the first subgroup. We can thus deduce that the positive or negative detuning between the resonance and the laser source seems to be of crucial influence. Yet, the reason for this behaviour remains unclear at this point.

Overall, the question arises why the TH signal strength appears to be quadratic in the spectral overlap and whether or not there is causation. To further elucidate this point, we plot for a selection of arrays in figure 5.6 (b) the integrated linear extinction against the nominal volumes of the nanostructures. The integrated extinction depends linearly on the volume of the nanostructure. This behaviour is actually not surprising as the overall oscillator strength depends on the number of free electrons and thus on the gold volume. As the extinction enters linearly in the spectral overlap we can thus deduce that the TH signal actually scales quadratically with the volume of the nanostructure. Figure 5.6 (c) depicts the same data points as figure 5.6 (a), yet without the vertical displacement. In this plot it is apparent that the different antenna geometries do not exhibit the same conversion efficiencies. The bowtie and gap antennas show very similar TH signal strength for the same spectral overlap. In contrast, the glass covered bowtie

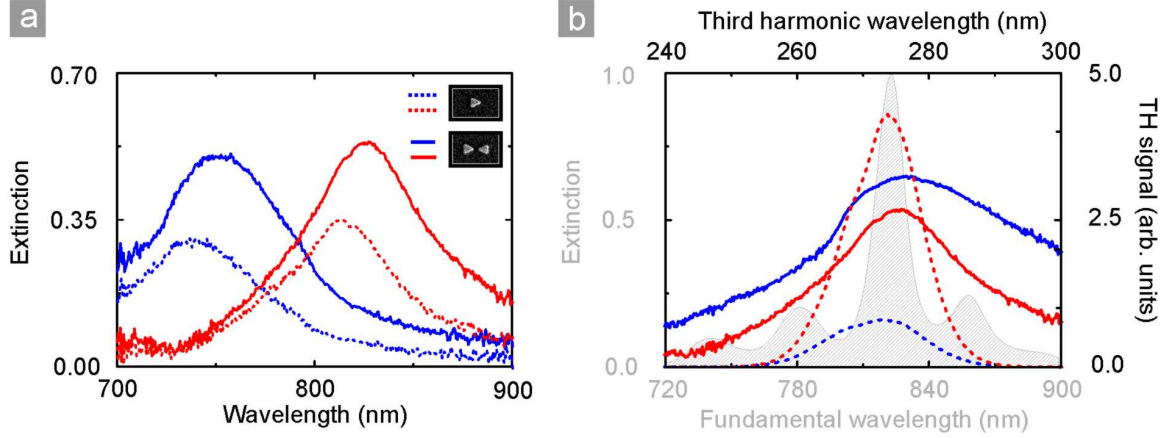


Figure 5.7.: (a) Linear extinction spectra of uncovered (solid) and SiO_2 covered (dotted) bowtie antenna arrays. The overcoating leads to a resonance red-shift as well as to a narrowing of the linewidth and thus an increase of the quality factor. (b) Linear (grey) and nonlinear (black) spectra of covered (dotted) and uncovered (solid) bowtie antenna arrays. In order for the structures to be resonant at about the same wavelength, the covered structures are smaller in size. Despite the larger linear spectral overlap of the uncovered antenna the we find that the TH signal from the covered antenna array is significantly stronger. The reason is the higher quality factor of the resonance.

antennas radiate a significantly stronger TH signal for similar spectral overlap. In order to unravel the reason for the different conversion efficiencies we examine the linear optical response of bowtie and glass covered bowtie antenna arrays in figure 5.7 as most of our findings so far could be explained by considering the linear optical properties of the structure.

Figure 5.7 (a) compares the linear extinction spectra for bowtie antenna arrays with and without a SiO_2 overcoating. The geometrical dimensions are identical (triangle size $(125 \times 150) \text{ nm}^2$, single triangle and 70 nm gap, respectively). The solid lines depict the spectra of the uncovered structures, the dotted ones the covered ones. Two distinct changes are apparent: Due to the higher effective refractive index of the environment the resonances undergo a spectral red-shift. Additionally, the linewidth of the resonances decreases and the amplitude increases. The amplitude increase upon decrease of the width is a direct consequence of the unchanged volume of the nanostructure. The resonance dipole strength, which is linked to the number of free electrons and thus to the volume, manifests itself as the area content of the extinction spectrum. A narrowing of the resonance hence necessarily leads to an increased amplitude. The decreased linewidth implies an increased dephasing time of the plasmonic resonance as the spectral width of a resonance is directly linked to the dephasing time of the collective electron oscillation. Plasmonic resonances are radiation damped systems, meaning that the main dephasing channel is caused by radiative losses, i.e., the re-emission of photons. Intrinsic

losses such as ohmic losses can be mostly neglected. The increased dephasing time of the resonance is most likely caused by so-called dielectric screening. The homogenous environment of the antenna will respond to the strong electric near-fields of the antenna with an induced electric polarization of opposite sign (yet much smaller than the antenna polarization). This will alter the far-field response as it effectively reduces the dipole moment of the resonance and thus prolongs the dephasing time due to reduced radiation efficiency. Hence, the glass covered bowtie antennas are expected to produce a stronger TH signal. The antennas are basically cavities which store energy and convert part of this energy in TH radiation. An increased dephasing time will increase the interaction time of the near-field with the structures and will thus boost the nonlinear signal strength. Therefore, on first sight, it would be beneficial to increase the quality factor of the resonance as strongly as possible. Yet, it is important to note that an external light field will not be able to efficiently couple energy into a high quality factor cavity. The in- and outcoupling efficiency of a cavity are linked to one another due to reciprocity.

In the above reported experiments it became apparent that the resonant excitation of an antenna is of crucial importance. Thus, we can not directly compare the TH response of the antenna arrays shown in figure 5.7 (a). The uncovered antenna arrays are blue-shifted with respect to the laser spectrum. Therefore a comparison is not meaningful. Figure 5.7 (b) depicts the linear and nonlinear spectra of an uncovered (solid) and a covered (dotted) bowtie antenna array with nearly identical resonance frequencies. In choosing different basic sizes of the triangles we can compensate the resonance red-shift due to the glass overcoating. The linear resonances show a very good overlap with the spectrum of the driving laser source. Again, very different linewidths of the resonances can be observed, partially caused by dielectric screening. Additionally, as the covered structures are smaller, the overall dipolemoment is smaller than for the uncovered, bigger one. Just considering the maximised spectral overlap argument one would expect the uncovered antenna to be the more efficient TH emitter. In contrast one observes a much stronger TH emission from the covered antenna. The reason for this behaviour is the significantly higher quality factor of the covered structure. The prolonged interaction time boosts the TH signal.

5.3. The Nonlinear Harmonic Oscillator Model

The above discussion is a qualitative one. A number of questions remain unanswered. In particular, we have still not convincingly determined the role of the nanoscale gap. The reported findings suggest that the TH signal actually originates from the antenna material itself rather than from the dielectric environment. This is the only explanation why the strongly enhanced near-fields inside the gap do not lead to an additional TH signal from the SiO_2 below or within the gap (in case of the overcoated structures). Indeed, recent reports point to the fact, that the nonlinearity of gold exceeds the one of

SiO_2 by about three orders of magnitude. [335] Therefore, the actual gap size and the strength of the enhanced field within this gap would be of minor influence. Only very small gaps below or close to the experimentally achievable structure sizes of ~ 20 nm would lead to noticeable TH from the SiO_2 or from an enhanced confinement of the field to the gold itself.

Another drawback of the linear spectral overlap model and the quality factor argumentation are their inability for any a priori predictions for, e.g., TH signal strengths.

In order to truly unravel different contributions one needs to be able to model one of these contributions and check for experiment-model deviations which would prove the existence of an additional signal contribution. In the following we will perform such a comparison on the basis of a simple harmonic oscillator model.

We now demonstrate that all observed features of the nonlinear response are a direct consequence of the linear response of the antenna. We model the plasmon resonance of the antenna as a harmonic oscillator, with resonance frequency ω_0 , mass m , intrinsic damping constant γ_0 , and charge e . To allow a nonlinear response, we add a cubic perturbation term b to the differential equation [327] of the extension x

$$\ddot{x} + \gamma_0 \dot{x} + \omega_0^2 x - bx^3 = -e/m \cdot E_0 e^{-i\omega t} \quad (5.1)$$

The oscillator is driven by an optical field (frequency ω , amplitude E_0). A medium consisting of such oscillators at a number density N can be described by a linear polarizability $\chi^{(1)}(\omega)$

$$\chi^{(1)}(\omega) = \frac{Ne^2}{\epsilon_0 m} \cdot \frac{1}{\omega_0^2 - \omega^2 - i\omega\gamma_0} = \frac{Ne^2}{\epsilon_0 m} \cdot \frac{1}{D(\omega)} \quad (5.2)$$

The linear extinction spectrum $\alpha(\omega)$ is given as

$$\alpha(\omega) = \omega/c \cdot \text{Im}(\chi^{(1)}(\omega)) \quad (5.3)$$

First, we note that despite the complex shape of the plasmonic nanoantenna, its linear extinction spectrum is well fitted using these relations (see green curves in the left column of figure 5.8). This finding indicates that the bowtie antenna behaves like a single harmonic oscillator despite the fact that the excited mode is a hybridized mode of two nanoparticles. The spectral position of this mode is tuned by the gap size. From the fit we extract the resonance frequency ω_0 , the damping constant γ_0 , and an overall amplitude describing the strength of the resonance.

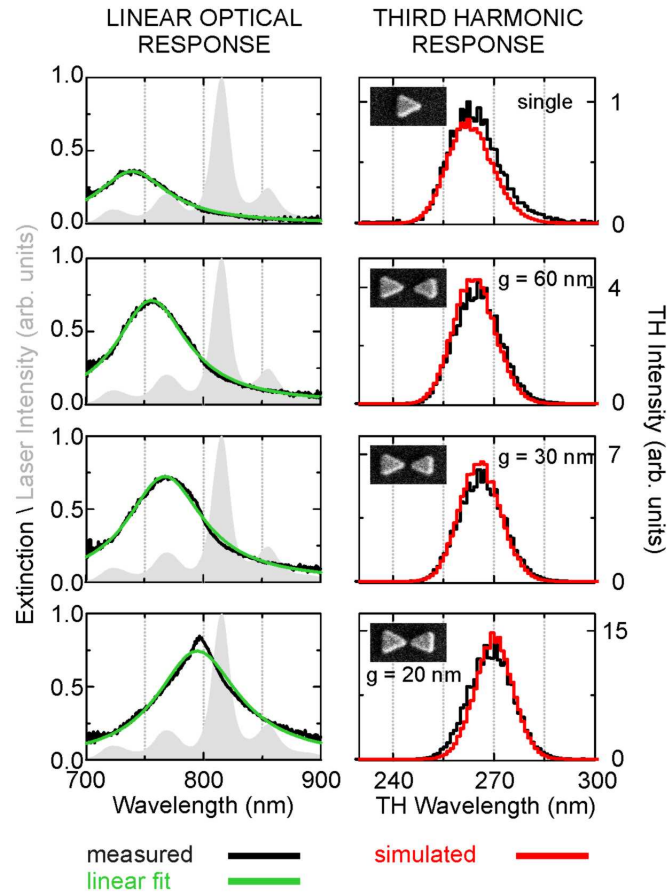


Figure 5.8.: Linear (left column) and nonlinear (right column) optical response of bowtie antenna patches of four different gap sizes but unchanged triangle size. The plasmonic resonance of the bowtie antenna arrays is gradually red-shifting into the regions of higher laser intensity (grey) with decreasing gap size. Simultaneously one observes an increase in TH signal strength and a spectral shift of its center wavelength. A damped nonlinear oscillator model catches all experimentally found features directly from the linear optical properties of the bowtie antennas, which enter the model via a fit to the extinction spectra (green).

In this model, [327] the third order polarizability is given as

$$\chi^{(3)}(\omega_i, \omega_j, \omega_k, \omega_{THG} = \omega_i + \omega_j + \omega_k) = \frac{Ne^4}{\epsilon_0 m^3} \cdot \frac{b}{D(\omega_i) \cdot D(\omega_j) \cdot D(\omega_k) \cdot D(\omega_{THG})} \quad (5.4)$$

Taking the broad coherent laser spectrum $E(\omega) = E_0(\omega) \cdot e^{i\omega t}$ into account, we calculate the TH emission spectrum as

$$I_{THG}(\omega_{THG} = \omega_i + \omega_j + \omega_k) \propto \omega_{THG}^2 \left| \int_{\omega_i} \int_{\omega_j} \int_{\omega_k} \chi^{(3)} E_0(\omega_i) E_0(\omega_j) E_0(\omega_k) d\omega_i d\omega_j d\omega_k \right| \quad (5.5)$$

The contribution of the substrate is modelled as spectrally constant $\chi_{Sub}^{(3)}$ and added coherently. The nonlinearity parameter b is adjusted such that one value describes all spectra simultaneously. We compare measured and simulated TH spectra for a series of equal bowtie triangle size but different gap sizes in figure 5.6. Overall we find excellent agreement between the measurement and the simulation showing that the model is able to predict the entire TH spectrum in position, shape, and relative amplitude solely from the linear optical properties.

Our nonlinear oscillator model summarizes all the details of the local field distribution in and around the nanoantenna and the corresponding values of the third order polarizability $\chi^{(3)}$ into the nonlinearity parameter b . In a microscopic picture, the plasmon resonance enhances the local field which leads to locally enhanced third-harmonic generation. In such a microscopic picture, one would then integrate coherently over all sources of THG, as done in previous work. [317] The excellent agreement of data and simulations in the right column of figure 5.6 demonstrates that already the much simpler macroscopic nonlinear oscillator model contains the essence. At the same time, we expect the model to fail when the local field distribution changes drastically.

In order to test the limits of the nonlinear oscillator model, we varied triangle size and gap size of the bowtie antennas, resulting in 99 different combinations (for the geometrical dimensions see Supporting Information). To modify the field distribution even further, we changed the index of refraction of the environment by covering an identical sample with 100 nm SiO_2 . Thirdly, we changed the shape of the antennas from a bowtie antenna (consisting of triangles) to a gap antenna (consisting of rectangles), again varying size of the rectangle and the gap between the rectangles. In total we thus examined 297 antenna fields.

To allow a direct comparison of experiment and simulation for all fields, figure 5.9 compares the integrated TH intensity for bowtie antennas (in black), gap antennas (in

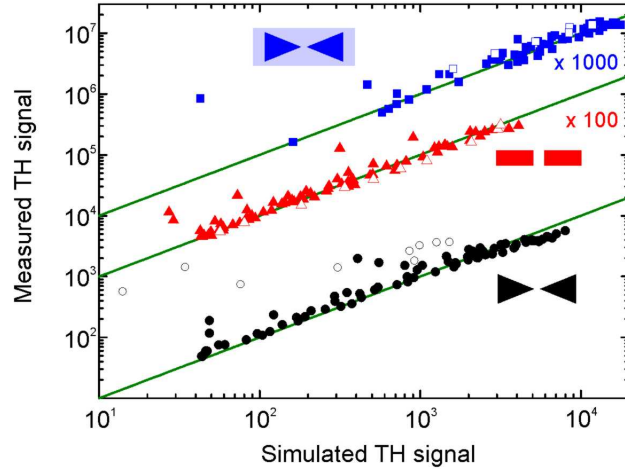


Figure 5.9.: Measured spectrally integrated TH signal versus simulated integrated TH signal based on a single nonlinear oscillator model. The data for the gap antennas (red) and the glass covered bowties (blue) are shifted vertically for clarity with respect to the bowties (black). The green lines represent a one-to-one ratio. The experimental data and the model show a very good overall agreement. The antennas behave like single nonlinear oscillators, independently of the antenna gap. Open symbols represent antennas with the smallest gap sizes (~ 20 nm). All those data points are not included for which the linear spectrum could not be fitted reliably, as the peak position is outside the spectral window of the laser source.

red), and glass-covered bowtie antennas (in blue). The data points for the gap antennas and the covered bowtie antennas are displaced vertically for clarity; the green lines each depict a one-to-one relation. Each of the three sets of antennas is described by one constant nonlinearity parameter b , which relate as $b_{\text{bowtie}}^2 : b_{\text{gapantenna}}^2 : b_{\text{coveredbowtie}}^2 = 1 : 2 : 3$. This reflects the variation in local field distribution between the three sets. Overall we find excellent quantitative agreement between the measurement and our model for all three different antenna varieties. Despite the fact that the antennas consist of two independent, yet strongly near-field coupled nanoparticles, they behave as a single oscillator whose nonlinear third harmonic response is excellently modelled by a constant cubic perturbation. We observe a maximum enhancement of the TH signal compared to the TH signal of the bare substrate of about 62 for the gap antennas, 115 for the bowtie antennas, and 311 for the covered bowtie antennas. In each case the antenna geometry that exhibits the maximum enhancement is the one that shows the best spectral overlap and hence highest excitation efficiency of the antenna. For the bowtie antennas this geometry is actually the biggest triangle size with the biggest gap.

If the TH from the hot spot dominated the TH from the antenna itself, then the nonlinear conversion efficiency of a dimer nanoantenna should drastically increase when the gap size decreases as the near-field localization is particularly strong for small gap sizes. In order to check this intuitive picture, the antennas with the smallest gap sizes are depicted with open symbols in figure 5.9. For the gap antennas and the glass-covered

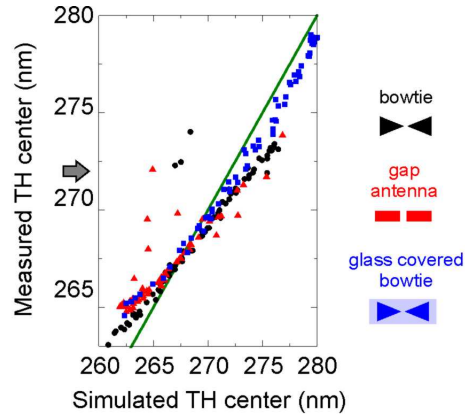


Figure 5.10.: Measured center TH wavelength versus the simulated TH center wavelength. The very good agreement demonstrates that the TH spectrum is not only defined by the laser spectrum but also by the plasmon. Without plasmon resonance, the TH center would be expected at one third of the laser spectral center, indicated by the grey arrow. Hence, within a certain wavelength regime, it is possible to shift the center of the TH spectrum by manipulating the plasmon alone. In this figure only patches are included that produce at least 3 times the background THG, as the latter is independent of the plasmon resonance wavelength.

bowtie antennas they are equally distributed among the data points, indicating that they do not form a sub-group of higher conversion efficiency. In contrast, for the bowtie antennas the data points are consistently above the one-to-one relation line. This finding is an indication that these antennas seem to deviate from the single nonlinear oscillator assumption, showing slightly higher conversion efficiency. SEM inspection of the structures seems to indicate that the gaps of these antennas are slightly smaller than the smallest ones of the covered bowties and the gap antennas. Here, the very small gap modified the local field distribution, leading to a deviation from the nonlinear oscillator model. Apparently only gap sizes below about 20 nm lead to hot spot THG that can dominate antenna THG. Overall we thus find that the nonlinear signal strength of a plasmonic nanoantenna depends on the oscillator strength of the plasmon and its efficient resonant excitation. The only free and designable properties for TH enhancement are the linear properties of the oscillator, which are quality factor (linewidth), resonance frequency, and amplitude. The magnitude of the nonlinearity parameter b can not be manipulated much by simple geometrical variations of the nanoantenna. Our experimentally achieved gaps are not small enough in order to cause an additional nonlinear contribution. Hence, for gaps ≥ 20 nm the gap merely acts as tuning element.

The integrated TH intensity contains only part of the information in our measured and simulated spectra. To go more into detail, we now turn our attention to the spectral center of mass of the nonlinear spectra. In a naïve picture this position should be solely determined by the laser spectrum, hence it should be identical for all antenna variations. Strikingly, we have seen already in figure 5.8 that the TH spectra undergo spectral shifts when changing the plasmon resonance wavelength. This indicates that the

linear plasmon spectrum plays a crucial role for the center of mass of the TH spectrum. We find that the nonlinear oscillator model catches the essence of the physics behind this spectral shift. This is demonstrated in figure 5.10, which compares the spectral center of mass of the simulated TH spectra to the measured data. The plasmon spectrum causes a shift of the TH center wavelength, as it determines together with the spectrum of the laser source the spectral position of highest interaction and hence the strongest TH signal. Yet, we still find small deviations from the expected 1:1 wavelength relation (shown as green line in figure 5.10). A spectral phase of the laser source, i.e., a temporal chirp between the different wavelength components of the broadband laser pulse, is the likely explanation for these deviations.

In conclusion, we have demonstrated that nonlinearities in plasmonic nanoantennas are governed by the linear response of the nanoantenna for a large range of geometries. The plasmon resonance energies and the oscillator strength are the key properties that determine the TH signal strength. Not only the spectral detuning between the center wavelength of the laser source and the plasmonic resonance needs to be minimized in order to drive the resonance most efficiently, but also the overall coupling strength of the plasmonic resonance to the external light field needs to be maximized. This coupling strength is characterized by the oscillator strength of the resonance which is fundamentally stemming from the number of electrons involved and hence the volume of the nanostructure. The crucial importance of the plasmonic resonance and the associated enhanced near-fields is underlined by shape and position variations of the TH spectrum. The TH center wavelength can to a large extent be predicted from the laser spectrum and the plasmon resonance.

An additional contribution by the strongly enhanced near-fields concentrated in the gap region is only found for gap sizes below 20 nm. For larger gap sizes the microscopic field distribution does not change any more. The gap size primarily manifests itself in the linear optical properties that influence the efficiency of the laser to drive the plasmon.

5.4. Nonlinear Plasmon Optics in Terms of Resonantly Enhanced Optical Nonlinearities

We have seen that the nonlinear optical properties of plasmonic structures are governed by their resonant behaviour. Hence, it is straightforward and intriguing to view this process in the framework of resonant nonlinearities. Nonlinear optical processes have become of the utmost importance in basic research as well as in industrial and commercial applications [339, 340]. Mostly, they rely on bulk materials exhibiting off-resonant nonlinearities which are weak and only deliver large signals when employing phase matching techniques [341–343]. Commonly used nonlinear optical materials, such as beta barium

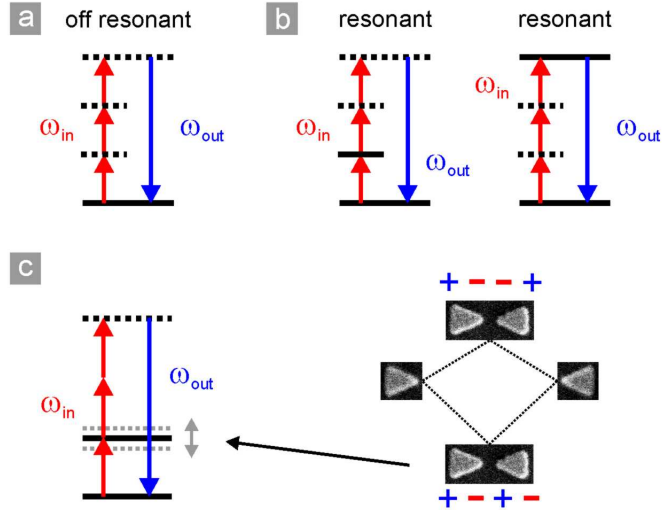


Figure 5.11.: (a) Energy level diagram for off-resonant third harmonic generation. (b) The resonant excitation of a resonant energy level, either an intermediate (left) or the final (right) state, leads to an increased excitation probability and hence to a resonantly enhanced third harmonic signal. (c) Plasmon hybridization scheme for a bowtie nanoantenna. Two collective modes are formed, namely a symmetric dipole-allowed one with a lower resonance energy and an antisymmetric dark mode with higher resonance energy. The dipole-allowed mode serves as the resonant energy level which can be tuned in resonance energy by the size of the triangles and the gap size.

borate (BBO) or lithium niobate ($LiNbO_3$), have no resonant optical transitions in their respective operational regime, hence being nearly perfectly transparent. In contrast, optical materials with a resonant transition can enhance nonlinear optical processes when the incident light is tuned to this resonance. Often, these transitions are narrow, weak, and fixed in wavelength as they depend on material parameters, e. g., for second harmonic generation in solids [344, 345] as well as sum-frequency generation and second harmonic generation in molecules [346–348].

The nonlinear optical polarization for third harmonic generation can be written as

$$P_i(3\omega) \propto \chi_{ijkl}^{(3)} E_j(\omega) E_k(\omega) E_l(\omega) \quad (5.6)$$

where $E_j(\omega)$ (with $i, j, k, l = x, y, z$) are the electric field components of the incident light field and $\chi_{ijkl}^{(3)}$ is the susceptibility tensor.

The absolute value of the susceptibility tensor components are determined by the linear optical properties of the system. In order for a third harmonic photon to be emitted three photons of the fundamental light field have to be absorbed simultaneously. This process

is sketched in figure 5.11 (a). The value of the tensor component is directly proportional to the sum over all transition matrix elements for the three photon absorption process. If there are no absorptive optical transitions in the material all sketched intermediate states are virtual or strongly off-resonant states. As a consequence the tensor component will take a small value, thus the process will be very inefficient. There is, however, a benefit afforded: As there are no resonant transitions involved the tensor component will be nearly independent of the energy of the incoming photons. The process is thus nearly equally inefficient for all energies. Therefore one has an inefficient yet spectrally flat process which is highly desirable for many applications. The conversion process can be made highly efficient by employing, e.g., phase matching techniques in bulk materials. This type of process is therefore termed off-resonant nonlinearity.

Figure 5.11 (b) sketches two possibilities for a resonant nonlinear optical process: If one of the intermediate or the final state is an absorptive material transition the corresponding term in the sum of the transition matrix elements will become resonant. As a consequence the susceptibility tensor component will take a large value. Intuitively, this process is straightforward to understand: If an absorptive transition is present a photon can be efficiently absorbed and the energy will be stored, thus increasing the probability of another photon being absorbed by the material during the lifetime of the excited state and thus increasing the overall conversion efficiency. The drawback, however, is obvious: the process is only efficient for a very limited energy range as it intrinsically relies on a resonance. In this context, we can view nonlinear plasmonics as an elegant and universal method to strongly enhance an otherwise nonresonant and flat spectral response of the bare gold material. Figure 5.11 (c) depicts a sketch of the working principle. In close proximity to one another the plasmonic resonances in the individual particles of the gap nanoantenna mix and hybridize giving rise to two new collective modes, as shown in the plasmon hybridization scheme depicted in figure 5.11 (c). For light polarized along the long axis of the antenna, the symmetric dipole allowed mode is decreased in resonance energy, whereas the antisymmetric mode is increased in energy. The latter mode cannot be excited for normal light incidence due to its antisymmetric mode pattern. Hence, the gap size as well as the size of the triangles will determine the spectral position of the dipole allowed mode, giving convenient parameters for shifting and tuning the resonant energy level depicted in the energy level diagram.

The proposed scheme of plasmon resonance enhanced nonlinearity offers a multitude of scaling opportunities and extensions. Designing a plasmonic system with simultaneous resonances at the fundamental as well as the harmonic wavelength will allow for resonant enhancement of both levels, rendering even higher conversion efficiencies possible. Additionally, it should be feasible to favour a certain nonlinear process, e.g. difference frequency generation or four wave mixing, over the dominant second and third order processes, respectively, by designing the resonant enhancement of the plasmonic system accordingly.

5.5. Nanoantenna Enhanced Second and Third Harmonic Generation

In the previous sections we have experimentally demonstrated that the nonlinear optical response of gold bowtie and gap antennas is governed by their linear optical properties. From this behavior we can undoubtedly deduce that the strongly enhanced near-fields within the nanoscale gaps play a minor role in the nonlinear conversion process as the actual strength of the near-fields is not encoded in the linear optical response. However, simulations as well as experiments show a significant enhancement of the field strength in the gap. The reason for this apparent contradiction: The gold of the antenna is the source of the nonlinear signal. Consequently, no enhanced third harmonic signal is to be expected unless the increasing field strength within the gap causes increased field strength within the adjacent gold as well. Our data convincingly shows that this process only starts to play a significant role for gap sizes in the order of 20 nm or below. However, a number of recent publications show a strong influence of the gap size of nanoantennas or rough surfaces on nonlinear processes. In these cases, the antenna itself is not the source of the signal but an optically active species is responsible for the signal and the antenna is "dark". This observation is in particular true for surface enhanced Raman scattering (SERS) [349–351] and experiments or surface enhanced infrared absorption spectroscopy (SEIRA) [30, 352]. If one indeed aims at mapping the near-fields one can make use of two-photon photoluminescence [329, 331], multi-photon absorption [353], or by direct techniques such as scattering and scanning type optical near-field microscopy [354–356]. In these experiments a strongly enhanced field strength within the gap has been found as well.

In order to benefit from these strongly enhanced fields we thus have to place a nonlinear optical medium inside of the nanoscale gap, or at least within the enhanced near-fields in the vicinity of the nanostructure. So far, in our own experiments, only glass is present next to the structures, which has a small χ^3 when compared to gold or silver [327, 335].

Even so this combination of field enhancement and nonlinear optics has already been proposed in the first publications on metamaterials [33], only a very limited number of publications reports conclusive and by data well supported experiments. In most experiments the role of the plasmonic structures is twofold in that it concentrates the incoming radiation and is the source of the harmonic radiation. In 2007 Chen and co-workers demonstrated plasmon-enhanced second harmonic generation from ionic self-assembled multilayer films [357]. The experiment is extremely convincing and, with all necessary control experiments done, does not leave a shred of doubt about its interpretation. To a surprise, the study appears not to be well known in the plasmonics community. The authors utilize silver triangles fabricated by colloidal lithography to enhance the SH emission from 3 bilayers of the ionic self-assembled film by about a factor of 1600. In 2008 Kim et al. reported high-harmonic generation in argon gas that was

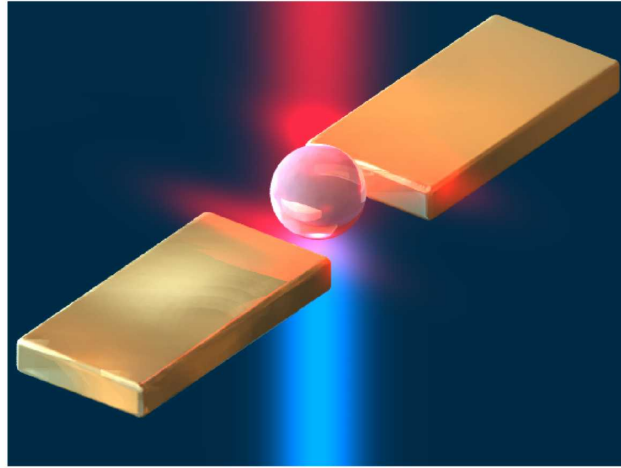


Figure 5.12.: Artists impression of a gold nanoantenna loaded with a nonlinear optical active material. The nanoantenna confines the incoming radiation, enhancing its field strength significantly in the process. The local fields then drive the conversion process in the nonlinear material. If the material intrinsically breaks inversion symmetry it can produce even numbered harmonics which can not be radiated by the antenna itself, at least as long as one only considers the electric dipole approximation.

blown on bowtie antenna arrays [194]. However, recent results reported by Sivis et al. suggest that the observed phenomenon might in fact rather be connected to enhanced atomic line emission, rather than higher harmonics generation [195]. Another again very convincing experiment has been performed by Niesler and co-workers in 2009 [314]. The authors fabricated split ring resonators on top of a crystalline gallium arsenide substrate and have demonstrated enhanced second harmonic emission caused by the interplay of the local near-fields of the split ring resonator and the substrate. As a last example, Utikal et al. buried Au gratings within a dielectric waveguide consisting of alumina, indium tin oxide, or tungsten trioxide, and studied the third harmonic spectra [317]. They found that the overall signal is generated not only by the gold itself, but, depending on the nonlinearity of the dielectric waveguide material itself, as well by the waveguide dielectric.

One obvious idea drawn from these earlier experiments it thus to use standard nonlinear materials such as beta-barium borat (BBO) or lithiumniobate ($LiNbO_3$) and selectively position them inside the gaps of nanoantennas, as shown in an artist's impression in figure 5.12. These materials can be fabricated as nanoparticles, either directly from a wet chemical process or by mechanical milling. In what follows wet chemically synthesized $LiNbO_3$ nanoparticles have been used. [358, 359]

Another benefit afforded by the nanocrystals/nanoantenna array approach is as follows: As the nanoantenna array is inversion symmetric, it will not exhibit a second harmonic response for a normal incident light field. The $LiNbO_3$ nanocrystals on the other hand

intrinsically break the inversion symmetry due to their crystal structure. The key idea of combining these two systems is thus to only boost the second harmonic response from the nanocrystals while the antenna array itself is "dark", meaning it does not radiate any second harmonic light.

Figure 5.13 (a) illustrates the basic steps in producing these samples. Gold nanoantennas as well as gold alignment marks are fabricated via standard electronbeam-lithography in PMMA resist. The sample is afterwards coated once again with PMMA. Using the alignment marks one forms openings in the resist exposing the gap regions of the antennas. After development and oxygen plasma cleaning the samples are immersed in the $LiNbO_3$ solution which consists of the nanocrystals diluted in water. The sample is repeatedly dipped into the solution and afterwards blown dry using nitrogen. The crystals are highly hydrophobic, as is the PMMA layer. However, the particles are strongly attracted to the bare glass surface. Therefore, they are agglomerating on the exposed glass surface. Additionally, there is strong attraction between the $LiNbO_3$ nanocrystals such that clusters of particles are forming and growing with every additional dipping step. As a final step the PMMA layer is removed in acetone. During this step the sample is resting upside down on additional pieces of glass in order to prevent the nanocrystals which previously lay on top of the PMMA layer from falling down onto the substrate. The small inset in figure 5.13 (a) depicts a tilted view SEM micrograph of a single gold bowtie nanoantenna. One can clearly see the nanocrystals which have agglomerated in the gap region.

In figure 5.13 (b) additional SEM micrographs of the fabricated structures are shown. In order to track the agglomeration using an optical microscope large crosses are defined in the resist layer. Within these openings the particles will as well accumulate. In contrast to the small openings the suggestive filling of these large crosses can be easily monitored. The SEM micrograph depicts such a cross after lift-off. The residual structures thus consist solely of $LiNbO_3$ nanocrystals. The next image shows a reference structure. No antenna structures have been defined, yet with the same periodicity same sized openings have been defined. After depositing the particles, one observes a perfect square lattice of $LiNbO_3$ nanocrystals. In particular, no defects or empty lattice sites can be found, indicating the extremely high efficiency of this surprisingly easy and straightforward process. The last image finally depicts an array of selectively filled bowtie antennas. Again, every single antenna is filled with $LiNbO_3$ nanocrystals. Most importantly, no particles are deposited in between the antennas.

In figure 5.14 we study the linear optical properties of bowtie nanoantennas which have been selectively filled with $LiNbO_3$ nanoparticles. The basic size of the triangles has been varied in order to shift the position of the linear resonance over the entire accessible wavelength range of the laser sources, while the gap size has been kept constant. The blue spectra depict the response of the empty bowtie antennas. For excitation along the antenna axis (left column) the strong dipolar resonance undergoes a significant red-shift with increasing size, additionally the scattering amplitude increases, as is expected due

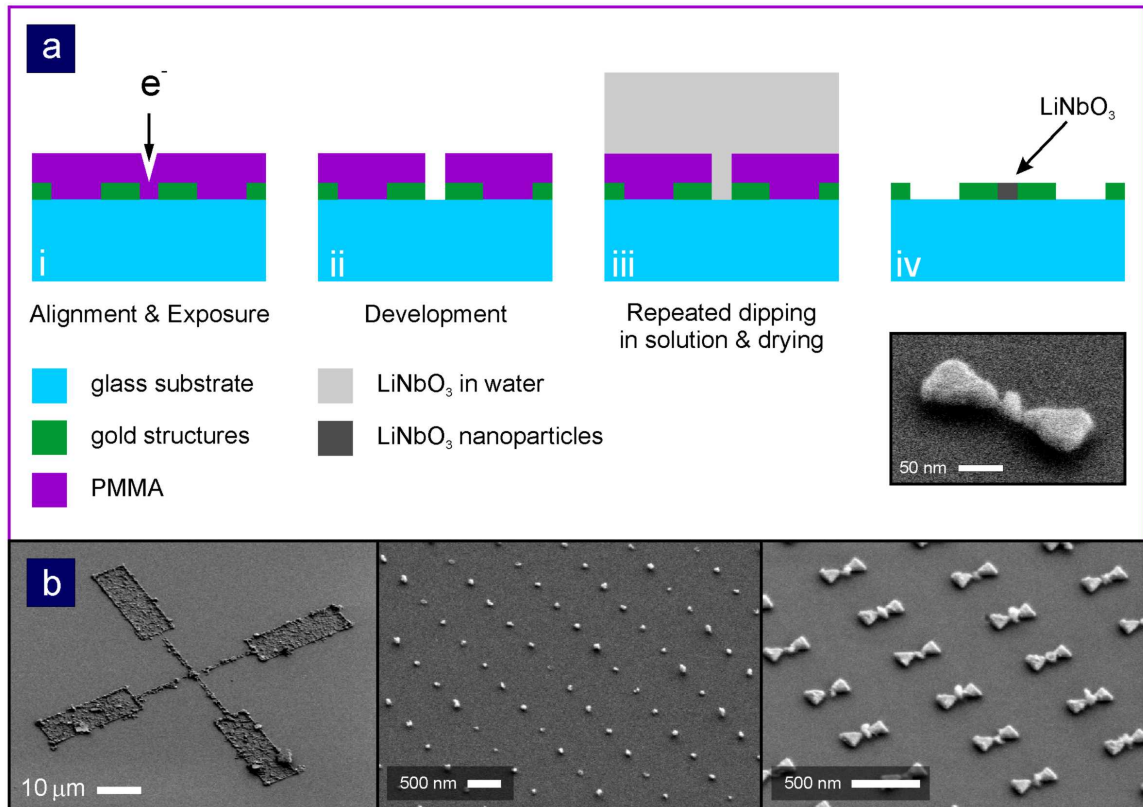


Figure 5.13.: (a) Production steps for the selective filling of gap nanoantennas with $LiNbO_3$ nanocrystals. i) In the first step a substrate with gold nanoantennas and alignment marks is covered with PMMA. After careful alignment openings are defined within the resist layer directly above the gap regions of the antennas. ii) The sample is developed and oxygen plasma cleaned. iii) The sample is dipped into a solution of $LiNbO_3$ nanocrystals and water and afterwards blown dry using nitrogen. This routine is repeated until additionally defined large openings appear to be filled up (optical microscope inspection), see first image in (b). iv) After lift-off only the $LiNbO_3$ nanocrystals deposited inside the antenna gaps remain, cf. close-up SEM of a single structure. (b) Overview SEM micrographs of fabricated structures (after lift-off). Left: Cross mark consisting of nanocrystals. Middle: Reference array of $LiNbO_3$ nanocrystals. Right: Selectively $LiNbO_3$ nanocrystals filled bowtie nanoantenna array.

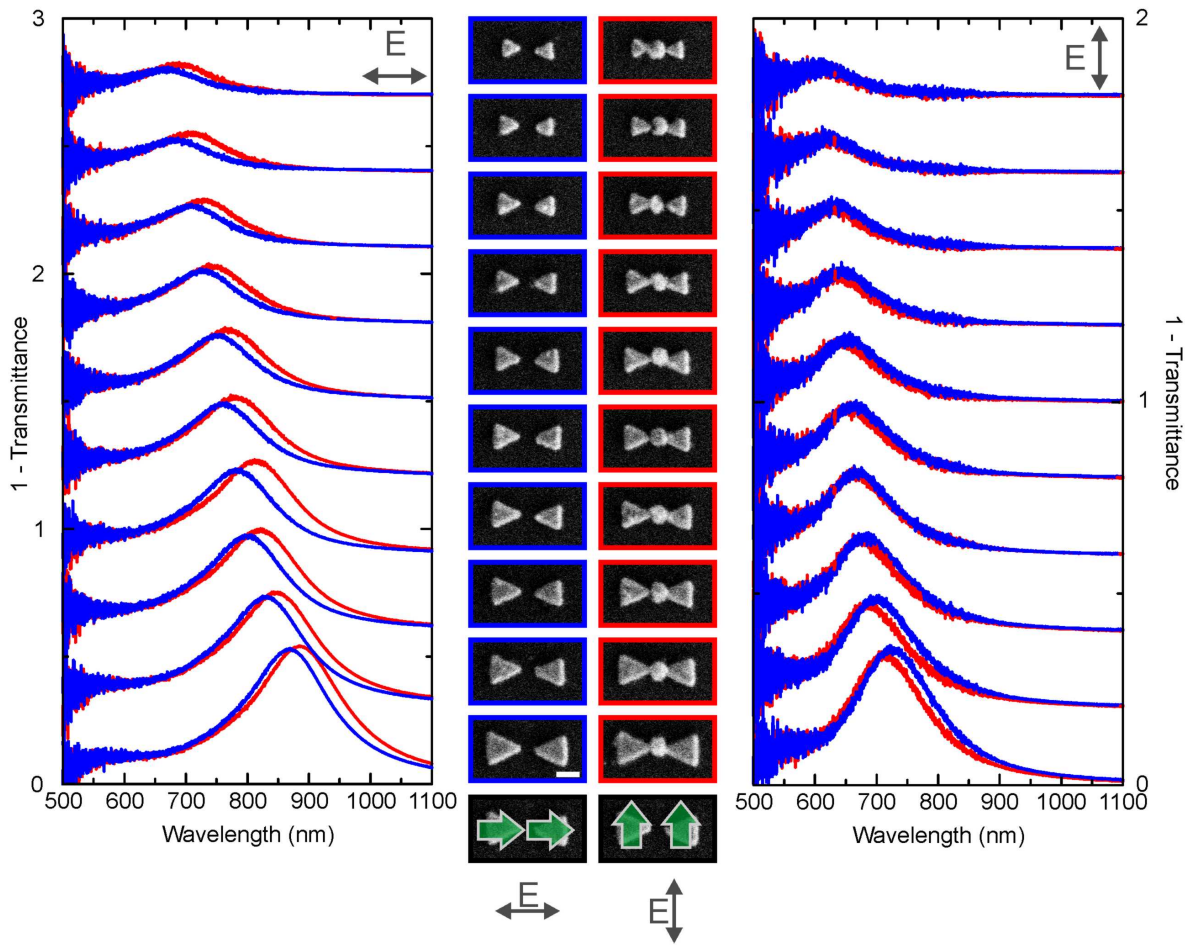


Figure 5.14.: Linear 1-Transmittance spectra for bowtie antenna arrays (blue) and selectively lithiumniobate filled bowtie antennas (red) for excitation polarized along the antenna axis (left column) and perpendicular to the antenna axis (right column). The antenna gap is fixed at ~ 50 nm, the basic size of the antennas is increased from top to bottom. The linear spectra for both polarization directions exhibit a red-shift of the plasmonic modes for increasing size, as expected. Inserting the lithiumniobate nanoparticles into the gap increases the coupling strength between the two antenna arms. Due to the different mode character, as sketched in the bottom of the figure, the modes exhibit a different spectral shift. For excitation along the antenna axis the attractive interaction between the particles is increased leading to a red-shift. For excitation perpendicular to the antenna axis the repulsive interaction between the dipoles causes a blue-shift. Overall, the spectra demonstrate the excellent filling rate of the antenna gaps, leading to a consistent behaviour between the different arrays.

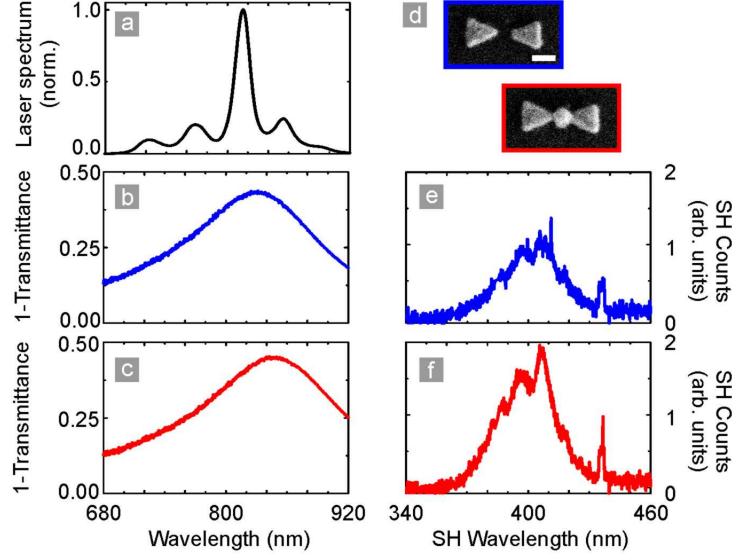


Figure 5.15.: Linear and nonlinear properties of a bowtie antenna array and a filled bowtie antenna array. (a) Spectrum of the driving 8 fs laser source. (b) and (c) Linear spectra of the two arrays as shown in (d). (e) and (f) second harmonic emission spectra of the two arrays. The increased signal strength observed for the filled antenna array is most likely caused by an increased spectral overlap between the antennas and the laser, rather than being due to the lithiumniobate nanoparticles.

to the increasing size and volume of the nanostructure. For excitation perpendicular to the antenna axis (right column) one as well observes a resonance, yet due to the smaller dimensions of the antennas in this direction, the resonance is significantly blue shifted.

The red spectra show the optical response of the $LiNbO_3$ filled antennas. For all geometries one observes spectral shifts in the position of the resonances, indicating that the antenna gaps have been filled with high efficiency. On closer inspection one observes a red-shift for excitation along the antenna axis and a blue-shift for excitation perpendicular to the antenna-axis. The reason for this behavior is the different character of the plasmonic modes. In both cases they are hybridized modes between the two dipolar modes of the individual triangles. Yet, for excitation along the antenna axis it is a head to tail configuration whereas for excitation perpendicular to the axis one observes a head to head configuration (see sketches in figure 5.14). Filling the antenna gap with a high refractive index material will lead to an increased coupling strength between the two triangles. For the head to tail configuration this results in a lowering of the resonance energy due to increased attractive interaction. For the head to head configuration the repulsive interaction will increase and therefore cause a blue shift of the mode. Overall, the spectra demonstrate the excellent filling rate manifesting itself in pronounced and reproducible spectral shifts in the linear response.

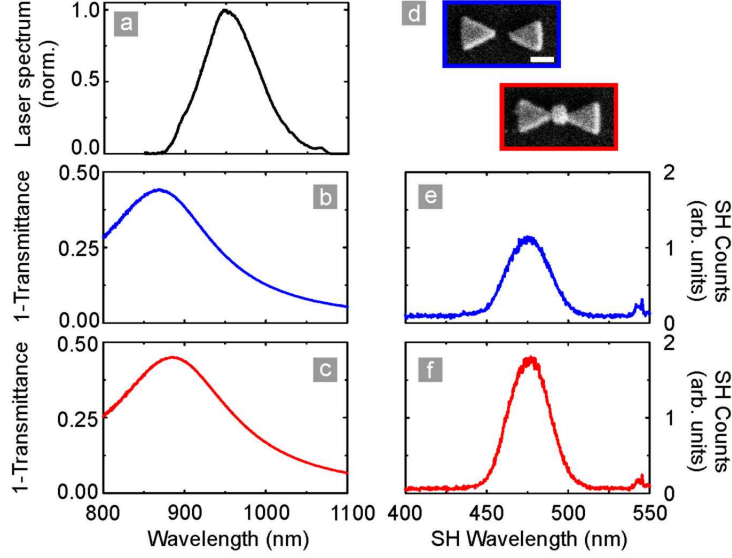


Figure 5.16.: Linear and nonlinear properties of a bowtie antenna array and a filled bowtie antenna array. (a) Spectrum of the driving laser source. (b) and (c) Linear spectra of the two arrays as shown in (d). (e) and (f) second harmonic emission spectra of the two arrays. As in the previous case one observes an increase in second harmonic signal, however, it is caused by the increased spectral overlap, rather than by the nonlinear material deposited in the gap region.

The nonlinear optical properties of the structures have been studied using two different laser sources. Figure 5.15 depicts the measurements of a filled and unfilled nanoantenna array using the setup described in the previous section. The laser spectrum is centred on 817 nm, as shown in figure 5.15 (a). Panels (b) and (c) depict the linear optical response of the antenna arrays, in blue for the unfilled and in red for the filled antennas (SEM micrographs shown in (d)). Panels (e) and (f) finally depict the second harmonic emission spectrum of the two arrays. On first sight one might be tempted to see an increased second harmonic signal for the $LiNbO_3$ filled antennas. However, one needs to be cautious about this conclusion. First of all, already the bowtie antenna array produces a second harmonic signal, which should be symmetry forbidden in electric dipole approximation. Second, we have not taken the changing linear optical properties into account. When examining the panels (b) and (c) we can clearly see that the linear extinction spectrum is shifting such that the overlap between the driving laser source and the extinction is increasing. Along the findings of the previous sections, we can thus deduce that it is very likely that the increased SH response is caused by this shift and not by an additional SH signal originating from the nanocrystals. The different peaks in the spectrum are caused by frequency mixing between the different spectral contributions of the fundamental laser spectrum.

The results shown in figure 5.16 confirm this interpretation even further. The results have

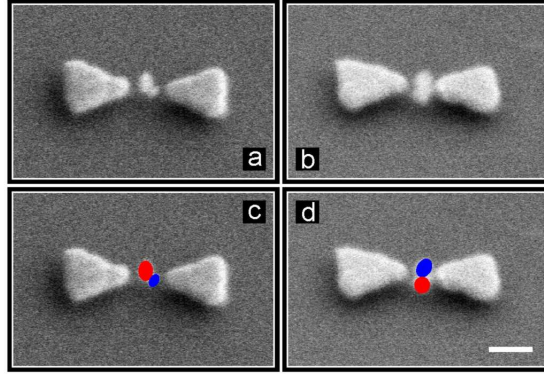


Figure 5.17.: Tilted view close-up SEM images of two exemplary selectively lithiumniobate filled bowtie antennas, panels (a) and (b). The antenna gaps contain several nanoparticles each, at least two, as indicated by the coloured dots in the lower panels (c) and (d). The Scale bar is 100 nm.

been obtained using a different laser source, [360,361] its spectrum is shown in panel (a), pulse duration approximately 30 fs. As in the previous figure panels (b) and (c) depict the linear optical response of the antenna arrays, in blue for the unfilled and in red for the filled antennas (SEM micrographs shown in (d)). Panels (e) and (f) finally depict the second harmonic emission spectrum of the two arrays. The bare antenna array again radiates second harmonic light, the filled nanoantenna array produces a significantly strong signal. However, very similar to the previous case the linear spectrum undergoes a spectral red-shift. This red-shift increases the overlap between the spectrum of the laser source and the linear extinction spectrum even stronger than in the case shown in figure 5.15. Again, the increased signal is thus rather caused by a change in the linear response than by the insertion of the nanocrystals.

These findings indicate that we do not observe second harmonic generation from the nanocrystals. What remains puzzling, however, is the fact that the arrays without the crystals already show a significant SH emission. In electric dipole approximation we do not expect second harmonic emission from an inversion symmetric structure illuminated under normal incidence.

There are two possible explanations for the observed behaviour:

- Lithiumniobate is a poor frequency converter. As already discussed earlier, it is an off-resonant conversion process, which is very inefficient and only becomes efficient for phase matched geometries in bulk crystals. The absolute values of the $\chi^{(2)}$ tensor components are small. As the particles have a size of about 50 nm they are extremely weak emitters. This conclusion is supported by the recent reports by Knabe et al., on the second harmonic emission from single lithiumniobate nanocrystals (these particles have been supplied to us and have been used), showing

small conversion efficiencies under excitation with tightly focused nanosecond-laser pulses [359].

- For the lithiumniobate crystals several $\chi^{(2)}$ tensor components are symmetry allowed. Therefore, it makes a huge difference how the particles are deposited inside the gap and how they are aligned relative to the antenna axis. On the one hand the absolute values of the components are very different, rendering the conversion efficiency strongly dependent on the orientation of the particles. On the other hand, the SH contributions from different components are emitted with different phases, causing destructive interference of the SH emission from an ensemble of particles. Figure 5.17 depicts tilted view close-up SEM images of filled bowtie antennas clearly showing more than one particle inside of the gaps. In the lower row the particles have been marked for clarity.
- Recent reports suggest that the nonlinearity of gold is very strong. Already the emission of thin layers boosted by the presence of a plasmon resonance yields strong signals. The earlier reported results for third harmonic generation from nanoantennas as well support this interpretation as the point to the gold being the sole source of the TH signal.

We intended to suppress the strong nonlinearity of gold itself by rendering the antenna array itself centrosymmetric. No SH should be observable. This finding seems to indicate a fundamental problem as it suggests that symmetry considerations do not hold for our structures. We will discuss this intriguing finding later in detail, showing that the symmetry rules might not be violated after all. However, a signal from the antennas themselves might not be suppressible. In order to increase a possible signal from the $LiNbO_3$ particles, which intrinsically break inversion symmetry, we have to align them with respect to the antenna axis. As the particles are ferroelectric such an alignment can be accomplished by so-called corona poling. [362] As a ferroelectric material the crystals show a spontaneous macroscopic electric polarization. When applying a strong external electric field the particles can be aligned with respect to the field and thus with respect to the antenna axis. However, as the particles already stick to the sample surface it might not be possible to align them in a post-processing step. If it is possible to accomplish the alignment while depositing the particle is not yet clear. Nevertheless, the results of this section suggested that the $\chi^{(2)}$ nonlinearity of lithiumniobate might be too small in order to observe a strong SH emission from the hybrid system. The particles are only about 50 nm in diameter, hence the small conversion volume needs to be compensated by a significantly enhanced fundamental field strength.

The absolute value of the enhanced near-fields is still highly debated and it is not yet fully understood what fundamentally limits the field strength. Finally, the extremely high electric field strength might be limited by either electron tunnelling processes between the extremely closely spaced metallic nanoparticles [260, 363, 364] or by a so-called nonlocal

effects where the dielectric function of the materials becomes wavevector and space depended [365]. Yet, it seems to be commonly accepted that the initially from theoretical and simulation studies proposed enhancements of several order of magnitude are not achievable in experiment. Moreover, the extremely high field strengths are only observed for incredibly small gaps, that is, for gaps below 1 nm. Fabrication plasmonic structures with such small gap sizes in a reliable and reproducible way is extremely challenging and only a very limited number of publications has so far demonstrated the ability to achieve this goal. In all these cases, the techniques are very demanding, such as high-resolution electron beam lithography [134, 366], self-assembled molecular monolayers [365], spacer layer engineering via atomic layer deposition [349], self-assembly of metallic nanoparticles with DNA and other molecular binding units [350, 367–369], or by self-alignment of chemically synthesised metal particles [370]. In any case, even if field enhancements of ~ 80 might be achievable in Angstrom scale gaps [363], the volume in which this field strength is present is extremely small, thus the volume of the active material will be small, too. If the extremely small amount of active material can be compensated by the high field strength is doubtful. So, in the end, what good will it do?

5.6. The Role of Symmetries in Nonlinear Optics

Symmetry is of crucial importance in every physical system. In 1823 Franz Ernst Neumann was the first to realize this close connection in studying double refraction [371]. He deduced the elastic constants which in turn determine the optical properties, by employing the assumption that the symmetry of the elastic behavior of a crystal was equal to that of its form. He thus assumed that the absolute values of the components of the electivity tensor in symmetric positions are equivalent. This assumption substantially reduced the number of independent constants and greatly simplified the elastic equations. This fundamental principle was explicitly formulated in 1885 by Woldemar Voigt and in 1887 by Bernhard Minnigerode [372], both students of Neumann, and became known as Neumann's Principle:

"The symmetry of a physical phenomenon is at least as high as the crystallographic symmetry."

Note that the symmetry of the phenomenon is related to the symmetry of the tensor that describes this phenomenon. As an example, let us consider the refractive index of an amorphous medium. The refractive index is in principle given as a tensor as it might depend on the direction of propagation as well as on the polarization state of light. In an amorphous medium, however, the tensor collapses to a scalar. The extremely high "symmetry" of the systems enforces that all tensor components are identical; the refractive index neither depends on the propagation direction nor on the polarization. (Please note that it is of course possible that the symmetry of a physical property is

higher than that of the underlying crystallographic structure due to degeneracy.)

Not only in theoretical, elementary particle, or solid state physics [373, 374] but also in plasmonics symmetry arguments have been used extensively. The symmetry imposes the nature of the modes that can be supported by a plasmonic nanostructure. This connection has been utilized in numerous studies to rigorously deduce the plasmonic modes from a purely geometrical standpoint [71, 121, 128, 137, 264, 375].

5.6.1. Maxwell's Equations and the Wave Equation

Optics is covered by Maxwell's equations, which read

$$\text{rot}\vec{H} = \vec{j} + \frac{\partial}{\partial t}\vec{D} = \sigma\vec{E} + \frac{\partial}{\partial t}(\epsilon_0\vec{E} + \vec{P} - \nabla\vec{Q}) \quad (5.7)$$

$$\text{rot}\vec{E} = -\frac{\partial}{\partial t}\vec{B} = \mu_0\frac{\partial}{\partial t}(\vec{H} + \vec{M}) \quad (5.8)$$

where \vec{E}, \vec{H} are the vacuum electric and magnetic fields, respectively, \vec{P} the electric polarization, and \vec{M} the magnetization in the medium. $\nabla\vec{Q}$ describes a higher order quadrupolar contribution to the electric polarization. Higher order contributions to polarization and magnetization, such as electric octupoles and magnetic quadrupoles are considered to be negligible.

If the field strength of the incoming radiation is high, the material fields might no longer be linear in the electric field. Considering the expansion till second order (third order terms read accordingly), the material fields read

$$\vec{P} = \vec{P}_L + \vec{P}_{NL} = \epsilon_0\chi^{(1),e}\vec{E} + \epsilon_0\chi^{(2),e}:\vec{E}\vec{E} \quad (5.9)$$

$$\vec{M} = \vec{M}_L + \vec{M}_{NL} = 0 + \epsilon_0\frac{C}{n(\omega)}\chi^{(2),m}:\vec{E}\vec{E} \quad (5.10)$$

$$\nabla\vec{Q} = \nabla\vec{Q}_L + \nabla\vec{Q}_{NL} = 0 + \frac{\epsilon_0 c}{i2\omega n(\omega)}\hat{e}_k\chi^{(2),q}:\vec{E}\vec{E} \quad (5.11)$$

with $\hat{e}_k = \vec{k}/|\vec{k}|$. Please note the tensorial character of the susceptibilities, accordingly : denotes a tensorial product. The superscripts (1) and (2) denote the order of the tensor and e, m , and q denote electric, magnetic, and quadruple, respectively.

We assume the material to be non-ferromagnetic. As for dia- and paramagnetic materials the susceptibilities are zero ($\chi_{Dia}, \chi_{Para} \approx 0$), the linear contribution to the magnetization is hence zero. Similarly, the linear contribution to the electric quadrupole contribution is negligible.

These relation lead to the wave equation

$$\left(\Delta - \frac{\epsilon}{c^2} \frac{\partial}{\partial t} \right) \vec{E} = \vec{S} \quad (5.12)$$

with

$$\vec{S} = \mu_0 \frac{\partial^2}{\partial t^2} \vec{P}_{NL} + \mu_0 \vec{\nabla} \times \frac{\partial}{\partial t} \vec{M}_{NL} - \mu_0 \frac{\partial^2}{\partial t^2} (\vec{\nabla} Q_{NL}) \quad (5.13)$$

with being the source of the nonlinear wave. Note that the source term has three distinct contributions: The electric dipole, the magnetic dipole, and the electric quadrupole.

In most text books on nonlinear optics only the first contribution is taken into account, which is referred to as the electric dipole approximation. Within this framework, second harmonic generation in inversion symmetric systems is symmetry forbidden. This can be easily seen when employing Neumann's principle. The nonlinear polarization in component notation is given as:

$$P_i \propto \chi_{ijk}^{(2),e} E_j(\omega) E_k(\omega) \quad (5.14)$$

Applying an inversion operation $\bar{1}$, keeping in mind that $\bar{E}_j(\omega) = -E_j(\omega)$ and $\bar{P}_i(2\omega) = -P_i(2\omega)$ hold, and additionally that the susceptibility tensor is inversion symmetric due to Neumann's principle, and thus $\bar{\chi}_{ijk}^{(2),e} = \chi_{ijk}^{(2),e}$ holds, one obtains

$$-P_i(2\omega) \propto \bar{\chi}_{ijk}^{(2),e} \bar{E}_j(\omega) \bar{E}_k(\omega) = \chi_{ijk}^{(2),e} E_j(\omega) E_k(\omega) \propto P_i(2\omega) \quad (5.15)$$

This relation can only be fulfilled if $P_i(2\omega) \equiv 0$ and hence $\chi_{ijk}^{(2),e} \equiv 0$. Therefore, in electric dipole approximation SH is symmetry forbidden in an inversion symmetric system. As a consequence, it is often stated in perplexing generality that inversion symmetric systems do not radiate second harmonic radiation at all. However, this is incorrect. The magnetic dipole and electric quadrupole contributions do not vanish in inversion symmetric systems. Thus, in particular for inversion symmetric systems they must not be neglected and allow for SHG. However, it should be noted that the magnetic dipole and electric quadrupole contributions are in general much smaller than the electric dipole contribution. In performing a strict mathematical deduction one finds that these

two terms are higher order corrections to the nonlinear source term suppressed by a factor of λ/a with λ the wavelength of the fundamental field and a the lattice constant of the crystal.

Which tensor components can be non-zero is again determined by symmetry. In performing a symmetry analysis one can thus find all components that can contribute to a nonlinear signal. Note, that some components, while symmetry allowed, might still vanish. A symmetry analysis cannot predict the magnitude of the components.

In a first step all symmetry operations of a system have to be found, that are, all mathematical operations that transfer the crystal into itself. We distinguish three classes of operations:

1. **Translations:** The system is translated by arbitrary multiples of the lattice constants.
2. **Parity operations:**
 - Space inversion $(x, y, z) \rightarrow (-x, -y, -z)$
 - Time inversion $t \rightarrow -t$
 - Charge inversion $q \rightarrow -q$

As we only study amagnetic and charge-free systems, we only have to take space inversion into account.

3. **Rotations:** In crystals only rotations by 60° , 90° , 120° , 180° , and 360° are possible, thus we can have 6-, 4-, 3-, 2-, and 1-fold rotations. It needs to be noted that in so-called quasi-crystalline systems odd-fold rotations are observed, however we will not consider this in this context.

The identification of non-zero tensor components now seems straightforward: Due to Neumann's principle every symmetry operation R of a crystal has leave the tensor invariant:

$$T'_{ij\dots n} = R_{ii'}R_{jj'}\dots R_{nn'}T_{i'j'\dots n'} \stackrel{!}{=} T_{ij\dots n} \quad (5.16)$$

From all the consisting relations obtained, the non-zero components can be deduced. Fortunately, there is a whole field of mathematics and physics dedicated to this, namely group theory. If we have determined the symmetry operations we know the crystals symmetry class and from that we can infer on the form of the tensors.

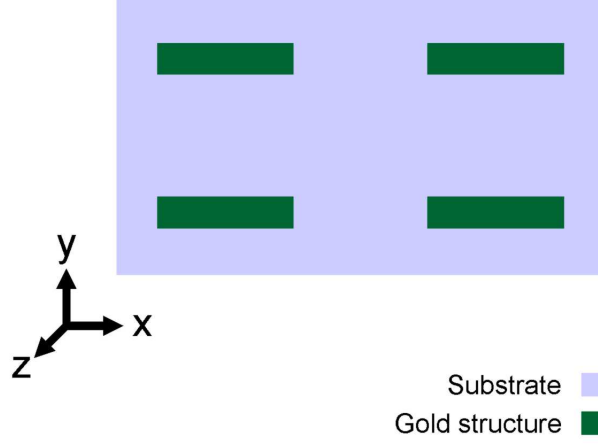


Figure 5.18.: Geometrical sketch of a nanoantenna array, in green the gold nanostructures, light blue indicates the substrate. Only three non-trivial symmetry operations exist: A 2-fold rotation around the z-axis, a 2-fold rotation with simultaneous space inversion around the x-axis, and a 2-fold rotation with simultaneous space inversion around the y-axis. Consequently, the depicted structure belongs to the symmetry class is $mm2$

As an example, let us consider an array of nanorods or nanoantennas, as sketched in figure 5.18. Taking the substrate into account, the only symmetry operations are: The identity, a 2-fold rotation around the z-axis, a 2-fold rotation with simultaneous space inversion around the x-axis, and a 2-fold rotation with simultaneous space inversion around the y-axis. The corresponding symmetry class is $mm2$. For the electric dipole contribution (polar tensor of rank 3) one obtains an E_3 tensor, for the magnetic dipole contribution (axial tensor of rank 3) an D_3 tensor, and for the electric quadrupole contribution (polar tensor of rank 4) an D_4 tensor [326].

Taking all symmetry allowed components into account, the electric dipole contribution to the nonlinear source term reads

$$\vec{P}_{NL}(2\omega) \propto \begin{pmatrix} 2\chi_{xxz}^e E_x E_z \\ 2\chi_{yyz}^e E_y E_z \\ \chi_{xxz}^e E_x^2 + \chi_{zyy}^e E_y^2 + \chi_{zzz}^e E_z^2 \end{pmatrix} \quad (5.17)$$

For the magnetic dipole contribution one obtains

$$\vec{M}^{NL}(2\omega) \propto \begin{pmatrix} 2\chi_{xyz}^m E_y E_z \\ 2\chi_{yxz}^m E_x E_z \\ \chi_{zxy}^m E_x E_y \end{pmatrix} \quad (5.18)$$

For its contribution to the source term

$$\vec{S}_{NL}^M \propto \nabla \times \vec{M}^{NL}(2\omega) \propto \begin{pmatrix} 2\chi_{zxy}^m E_x E_y - 2\chi_{yxz}^m E_x E_z \\ 2\chi_{xyz}^m E_y E_z - 2\chi_{zxy}^m E_x E_y \\ 2\chi_{yxz}^m E_x E_z - 2\chi_{xyz}^m E_y E_z \end{pmatrix} \quad (5.19)$$

holds.

For the electric quadrupole contribution one obtains

$$\vec{Q}^{NL}(2\omega) \propto \begin{pmatrix} \chi_{xxxx}^q e_x E_x^2 + \chi_{xxyy}^q e_x E_y^2 + 2\chi_{xyxy}^q e_y E_x E_y + \chi_{xxzz}^q e_x E_z^2 + 2\chi_{xzzx}^q e_z E_x E_z \\ \chi_{yyyy}^q e_y E_y^2 + \chi_{yyxx}^q e_y E_x^2 + 2\chi_{yxyx}^q e_x E_x E_y + \chi_{yyzz}^q e_y E_z^2 + 2\chi_{yzyz}^q e_z E_y E_z \\ \chi_{zzzz}^q e_z E_z^2 + \chi_{zzxx}^q e_z E_x^2 + 2\chi_{zyyx}^q e_x E_x E_y + \chi_{zzyy}^q e_z E_y^2 + 2\chi_{zyzy}^q e_y E_y E_z \end{pmatrix} \quad (5.20)$$

with $\hat{e} = (e_x, e_y, e_z)$.

When studying harmonic generation from the wire antenna array the polarization of the incident light field will be set along the long axis of the antennas in order to be resonant with the fundamental antenna mode. In literature it has thus been stated that quite a number of nonlinear contribution, as listed above, will vanish as $E_y = E_z = 0$ and $\hat{e} = (1, 0, 0)$ hold. Additionally, no z-polarized second harmonic light can be radiated. The nonlinear contributions thus collapse to

$$\vec{P}_{NL}(2\omega) \equiv 0 \quad (5.21)$$

$$\vec{S}_{NL}^M \propto \nabla \times \vec{M}^{NL}(2\omega) \equiv 0 \quad (5.22)$$

$$\vec{Q}^{NL}(2\omega) \propto \begin{pmatrix} \chi_{xxxx}^q e_x E_x^2 \\ 0 \\ 0 \end{pmatrix} \quad (5.23)$$

Intuitively, this behaviour is not surprising: The interface between air and substrate is responsible for breaking the inversion symmetry of the system, thus, in particular for the electric dipole contribution, allowing a second order process at all. For normal incidence this symmetry breaking will be of no immediate consequence, only for slanted incidence the interface will play a major role.

However, this simple ansatz might not be correct after all. Plasmonic structures confine external radiation into deep subwavelength volumes, thus massively increasing the local electric field strength. These local fields are the in turn ultimately responsible for the

generation of the nonlinear signals, not the incoming light field. Therefore, it is not sufficient to consider only the polarization components of the incoming light field, but one has to consider the local electric fields. It is well known that the local electric fields in the near-field regime of a plasmonic nano-object can point into different directions than the exciting light field. In general, even for an object as simple as a wire, in the near-field all electric field polarizations are present. Therefore, the electric dipole contribution does not vanish as all electric field components are non-zero. The same holds true for the higher order contributions.

In fact, this phenomenon has already been experimentally proven in an important, yet somehow overlooked, experiment: Niesler et al. have studied second harmonic generation from a composite system of gold split ring resonators and a crystalline gallium arsenide substrate [314]. The authors observe a second harmonic signal from a tensor component of the GaAs substrate which should not be accessible with the polarization and illumination setting applied. The signal is then explained by the presence of different polarisation directions of the electric field in the near-field of the split ring resonator which then in turn drives the second harmonic emission from the substrate.

This very important finding has not been considered in quite a number of publications. Canfield and co-workers for example studied second harmonic generation from L-shaped nanoparticles and found that the nonlinear response seemingly violates the symmetry rules as an explicitly forbidden tensor component produces a strong SH signal [294, 376]. The authors attribute this finding to defects and asymmetries in the fabricated structures. However, another potential explanation is given by the different electric field components in the near- and far-field regime. The authors observe a y polarized SH signal when exciting the structures along the y axis. They thus conclude that it must be generated by the χ_{yyy} tensor component, which is indeed symmetry forbidden for the studied structure. However, four tensor components are symmetry allowed and do as well radiate SH polarized along the y axis: $\chi_{yyx} = \chi_{yxy}$ and $\chi_{yyz} = \chi_{zyy}$. Taking the local electric fields polarized in z direction into account, these components might as well be responsible for the observed SH signal. It is noteworthy, however, that the authors recently reported that the symmetry forbidden signal indeed seems to vanish for higher quality samples [377]. leaving this intriguing question open for debate for the time being.

Another intriguing consequence of symmetry is shown in figure 5.19. In order for a dipole allowed second harmonic contribution inversion symmetry needs to be broken. However, this is not restricted to space inversion symmetry, it is also possible to break time inversion symmetry to obtain a dipole allowed second harmonic contribution. Let us consider a wire grating. A magnetization can be induced in direction perpendicular or parallel to the wires, for example by making them out of nickel or cobalt. If one does not want to sacrifice a strong plasmonic response (nickel and cobalt are "bad" plasmonic materials) one can utilize a layered structure of gold and a ferromagnet [378, 379]. If a magnetization is present in the wires, as indicated by the arrow, the structure is of $\underline{2mm}$

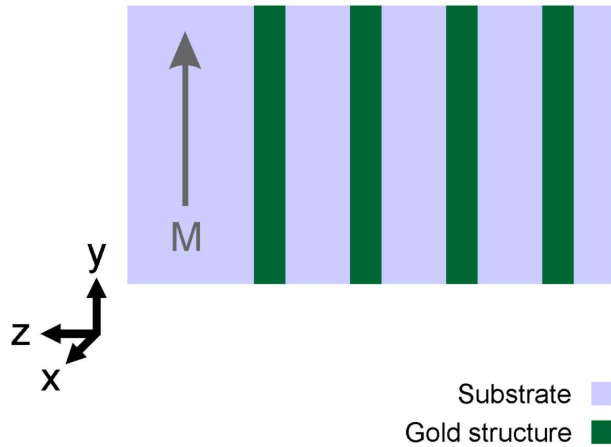


Figure 5.19.: Geometrical sketch of a wire grid, in green the gold wires, light blue indicates the substrate. In the presence of a magnetization, sketched by the gray arrow, the structure is of $2mm$ symmetry, breaking time inversion symmetry and thus exhibits a dipole allowed second harmonic contribution.

symmetry and breaks time inversion symmetry thus exhibiting dipole allowed contributions to the second harmonic response [326, 344, 345]. Importantly, if the magnetization vanishes, all tensor components associated with the magnetic ordering vanish as well. It would be most interesting to observe the strength of the second harmonic signal in dependence of the magnetization in the system. One would expect the signal to increase with increasing "degree" of magnetic order, that is, with increasing order parameter which scales with the magnetization [345].

5.7. Conclusions, Summary & Outlook

The field of nonlinear plasmon optics is still in the very beginning. Even so the first experiments have already been conducted in the early 1980s, quite a number of questions and problems remain unresolved. Surprisingly, this is often caused by the high complexity of the studied systems. The motivation behind the complex structures is multifold: Firstly, the structures allow for a nearly arbitrary manipulation of their linear optical properties. Secondly, the structural geometry of the systems can be manipulated which is believed to be particularly important due to the strong symmetry dependence of nonlinear optical processes. Thirdly, researchers are driven by the dream of disentangling linear and nonlinear optical properties, that is, strongly different nonlinear optical responses of two systems despite identical linear optical ones.

However, as we have demonstrated in this chapter, most of these properties are intimately connected and it is extremely difficult to disentangle the respective contribu-

tions. It is in particular important to realize the huge importance of the properties of the plasmonic resonances on the radiated nonlinear signals. We have shown that third harmonic generation from plasmonic dimer nanoantennas can be described by a simple nonlinear harmonic oscillator model. In this model the radiated third harmonic intensity is proportional to the fourth power of the amplitude of the resonance. The linewidth, representing the dephasing time and thus the time the energy is stored in the plasmonic cavity, enters. Hence, the nonlinear signal is extremely sensitive to seemingly minute changes in the linear optical properties of the plasmonic resonances. In fact, a number of experiments might actually be dominated entirely by the change in the linear optical properties rather than by the intended manipulation of, e.g., the symmetry of the system.

Thus far, we have not tailored the nonlinear optical properties of artificial structures beyond what nature already offers. As discussed in the section "Nonlinear Plasmon Optics in Terms of Resonantly enhanced optical nonlinearities" the nonlinear optical properties of crystals are fully determined by their crystallographic symmetry and by their linear optical response. The symmetry determines the non-zero tensor components and the linear response determines their absolute values. This very same behaviour has been observed for the dimer nanoantennas. From the linear spectrum the nonlinear response one could deduce (apart from a physically meaningless scaling factor).

The dream, however, would be to go beyond this restriction and gain additional tunability, that is to have similar or even identical linear optical responses, yet the nonlinear optical properties would be strongly different. Only a limited number of experiments could demonstrate that the linear and nonlinear optical properties of a plasmonic or plasmon-hybrid system can indeed decouple. In all these cases, the cause for this deviation is actually the contribution of a dielectric medium, e.g., a waveguide. Utikal and co-workers demonstrated that the nonlinear response of different plasmon waveguide hybrid systems can be different in spite of nearly identical linear optical properties [317]. In this case energy is transferred from the "bright" plasmonic resonance to the "dark" waveguide mode. The exact fraction of energy stored in the plasmon and waveguide modes is not encoded in the far-field spectra. Additionally, both systems have entirely different nonlinearities. Thus, the overall nonlinear response is determined by the relative near-field intensities and the relative strength of the nonlinearity in the two systems. Therefore, the nonlinear response cannot be predicted from the knowledge of the linear spectrum alone. Such behaviour has not been demonstrated in a purely plasmonic system, despite claims made. In contrast to the hybrid systems, energy can only be transferred from one plasmonic mode to another, for example between a bright dipolar mode of a rod and a dark quadrupolar mode in a wire pair, as utilized in a plasmonic analogue of electromagnetically induced transparency structure. These two modes both are supported by gold nanostructures, thus having identical nonlinearities. One commonly expects deviations from the predications of the linear optical response as well, as the quadrupolar mode is associated with a prolonged dephasing time due to reduced radiative losses, indicating higher near-field strength and thus strong nonlinear emis-

sion. The "reshuffling" of energy between the two modes should thus have significant influence. However, the prolonged dephasing time manifests itself in reduced resonances linewidth and is thus fully encoded in the linear response. On second sight one would thus not expect these systems to show responses deviating from the predications of the linear response alone.

However, one needs to note that different plasmonic modes have extremely different field distributions. Thus, the overlap of the near-fields with the gold itself as well as the surrounding dielectric will be different as well. Such an effect can actually be observed in the dimer nanoantenna experiment: The harmonic oscillator model is capable of correctly describing the TH emission down to gap sizes of 20 nm. After an initial calibration for a set of antennas it even predicts the absolute amplitude of the TH. However, for gaps below 20 nm one observes deviations from the predictions. The reason is linked to a change in the plasmonic mode. It appears that the mode profile and near-field intensity distribution is barely changing when decreasing the gap size down to about 20 nm. However, below this value, the mode is seemingly distorted and suffers significant spatial and intensity rearrangement of the near-field hot spots. As a consequence, the nonlinearity parameter of the mode is changed, causing a significantly increased signal for the same oscillator parameters. Most likely the increased signal is actually caused by the gold of the antenna itself. The substrate has not contributed any significant signal, despite the fact that already for larger gaps there is significant field enhancement within the gap. Therefore, the increased signal is a direct consequence of an increased nonlinearity parameter of the corresponding plasmonic mode. This actually seems to offer the possibility to manipulate the nonlinear response of a plasmonic system by mode-tailoring. However, in accordance with the discussion above, the expected effect will be small as the nonlinearity parameters are expected to be all of the same magnitude as they are all fundamentally stemming from the gold itself. Only if exchanging the material system, one can expect a high degree of tunability.

From the conclusions above it thus appears that the most promising route is the combination of plasmonically active components and dielectrics into hybrid structures, in particular if these dielectric subsystems are nonlinear-optically active. As in the case of the nonlinear waveguide the dielectric system does not manifest itself optically and thus does not allow for an accurate prediction of the nonlinear properties solely from the linear ones. The same holds for the nonlinear self-assembled monolayers on top of silver triangles, [357] where the monolayers are the source of the signal, rather than the silver triangles themselves. The main hurdle, however, is the in comparison to noble metals, such as gold or silver, weak nonlinearity of dielectrics. Nonlinear waveguides are thus a double clever choice as the waveguide mode is an extended one and thus the interaction volume is large. Coupling of extended photonic modes to localized plasmonic modes thus seems appealing.

However, a number of experiments can be envisioned which study the response or complex plasmonic structures in detail. Even if the relative strengths of the nonlinear signals

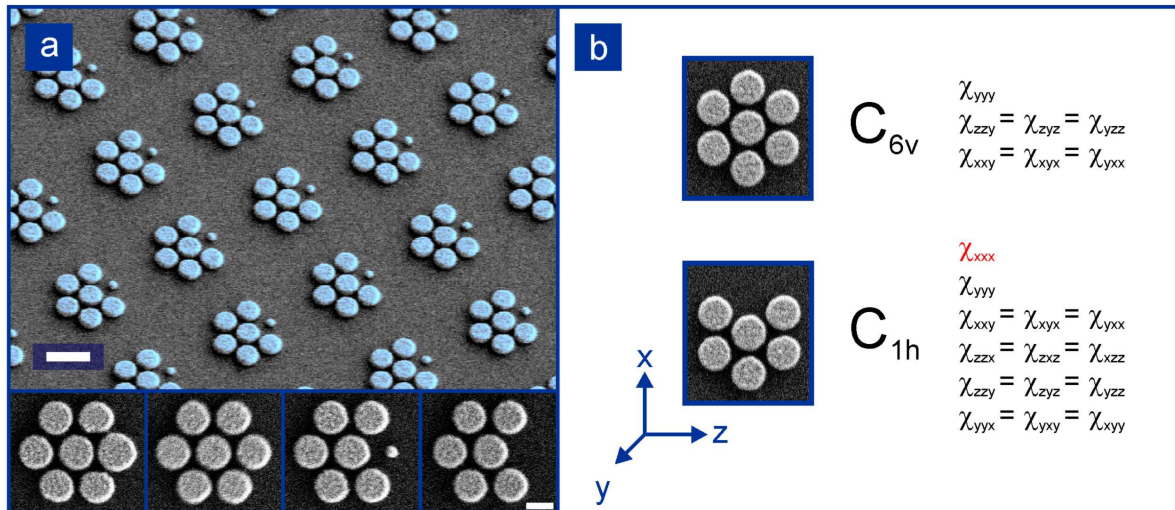


Figure 5.20.: (a) Tilted view image of an array of symmetry broken heptamers. The scale bar is 500 nm. Lower row: Close-ups of a series of heptamers with successively reduced size of the rightmost particle (note that for the leftmost cluster the particle is bigger than the other ring particles). The scale bar is 200 nm. b) In reducing the size of one ring particle the 6-fold rotational symmetry around the y-axis is lost and the symmetry class changes from C_{6v} to C_{1h} . For the symmetry broken structure new second harmonic tensor components become symmetry allowed. In studying the evolution of the absolute value of these components with the "degree of asymmetry", that is the size of the particle, one can investigate on the role of symmetry for nonlinear optical properties of such complex plasmonic nanostructures.

generated by the different modes are very similar it is still intriguing to decompose their relative spectral behaviour and the exact origin of the signal, in space as well as in mechanism. E.g., the harmonic oscillator model assumes a cubic nonlinearity, however the exact source of this nonlinearity remains unclear within the framework of the model. Conceptually, it could be a nonlinear oscillation of the plasmon itself or just a parameterization of the local electric fields interacting with a constant off-resonant molecular $\chi^{(3)}$ of the environment. Theoretical models have been developed for the first case, showing strong emission of odd harmonics from small (10^3 atoms) particle clusters [380–383]. However, these contributions vanish if the cluster exceeds a certain size as the electron oscillation will be less and less influenced by the presence of the surface leading to a nearly perfectly harmonic potential. Therefore, the exact origin of the nonlinearity remains unclear within our model and requires further investigation.

Another intriguing question concerns the role of symmetry in plasmon nonlinear optics. A number of experiments suggest that the symmetry rules are obeyed [311,315], yet others report deviations from these rules [376,377], either due to fabrication inhomogeneities or other influencing factors. In any case, the question arises whether or not these rules are applicable at all. The vast majority of all structures studied must not be considered an effective medium, they are rather arrangements of resonators of roughly wavelength

size. Therefore, can we expect symmetry considerations, as applied to crystals with crystal structures of deeply subwavelength dimensions, to hold for wavelength-scale objects? At least the plasmonic modes in these kind of systems can be deduced utilizing group theory [71].

Another fascinating aspect is connected to the higher order contribution to the nonlinear source term, the magnetic dipole and the electric quadrupole terms. It is found that these terms are generally suppressed by a factor λ/a , with λ the wavelength of the fundamental field and a the lattice constant of the crystal. In crystals this factor is much bigger than one. However, for our plasmonic systems this factor approaches unity, suggesting that the contributions might actually be of similar magnitude, assuming its validity. This would offer the fascinating possibility to further tune the nonlinear optical emission by three quasi-independent quantities.

All these questions are difficult to answer and would require the careful separation of structural changes and the resulting changes in the linear spectrum which might mask the symmetry effect. An example is given in figure 5.20 (a), depicting symmetry broken plasmonic heptamer structures. Successively removing one of the ring particles changes the linear optical properties only slightly, however, the symmetry is drastically reduced in losing the 6-fold rotational symmetry around the y-axis, thus the symmetry class changes from C_{6v} to C_{1h} [326]. In particular, for a C_{1h} structure an electric dipole term to the second harmonic source term is allowed for normal incidence. Conceptually intriguing, the symmetry is broken as soon as the particle is smaller by only a fraction of its total size. The optical properties, however, need to change smoothly with the "degree" of asymmetry towards the case of a completely missing particle. Thus, it should be possible to observe the dependence of the second harmonic response on the "degree of asymmetry". Breaking the inversion symmetry leads to a number of additional symmetry allowed tensor components, as listed in figure 5.20 (b). In particular, the symmetry broken structure allows for the component, with two incoming electric field components along the x-axis and the outgoing second harmonic as well polarized along the x-axis. One would study the evolution of this tensor component with increasing "symmetry breaking", in particular whether or not the absolute value of the component increases. Unfortunately, physics is more complex than suggested. The linear optical properties do change, even so the changes appear to be minute. Preliminary measurements suggest that the overall response is strongly determined by the changes in the linear response. It appears to be impossible to separate the influence of the changes in linear response and symmetry. However, the experiment points into the right direction: Identifying structures which display strictly forbidden and allowed contributions might answer the raised questions by targeting these components.

The field of nonlinear plasmon optics remains partially uncharted. With advances in sophisticated fabrication techniques for composite and hybrid structures as well as advances in the rapidly growing field of theoretical and simulation based descriptions of nonlinear plasmon optics, and one can expect quite a number of fascinating discoveries

in the next few years.

A. Appendix

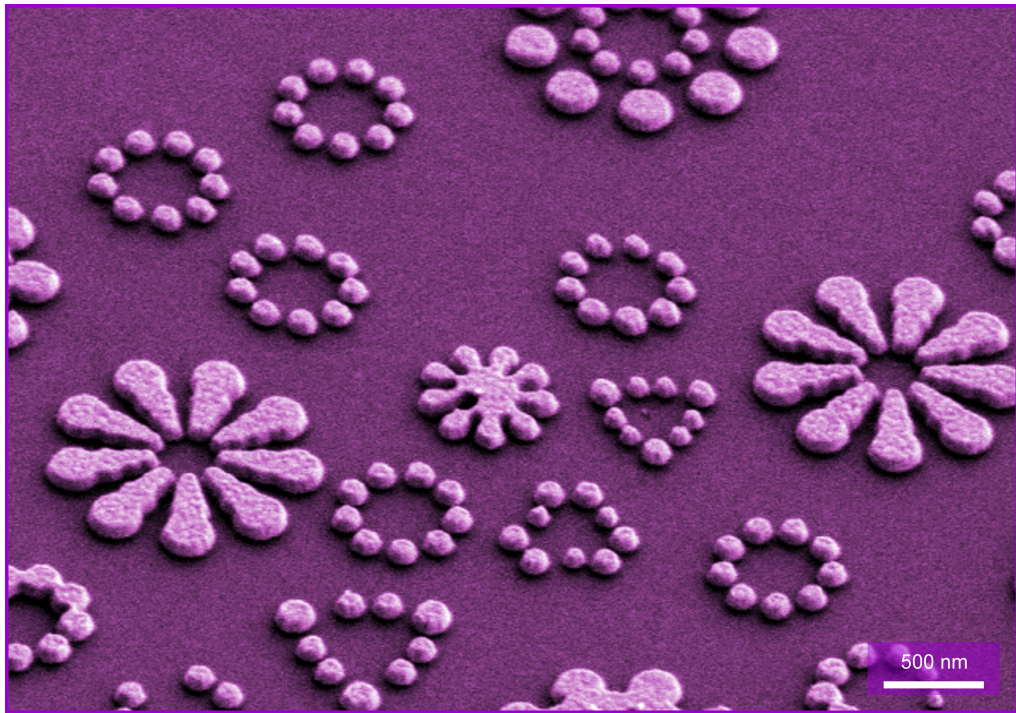


Figure A.1.: Plasmonic flower meadow [77, 78, 89].

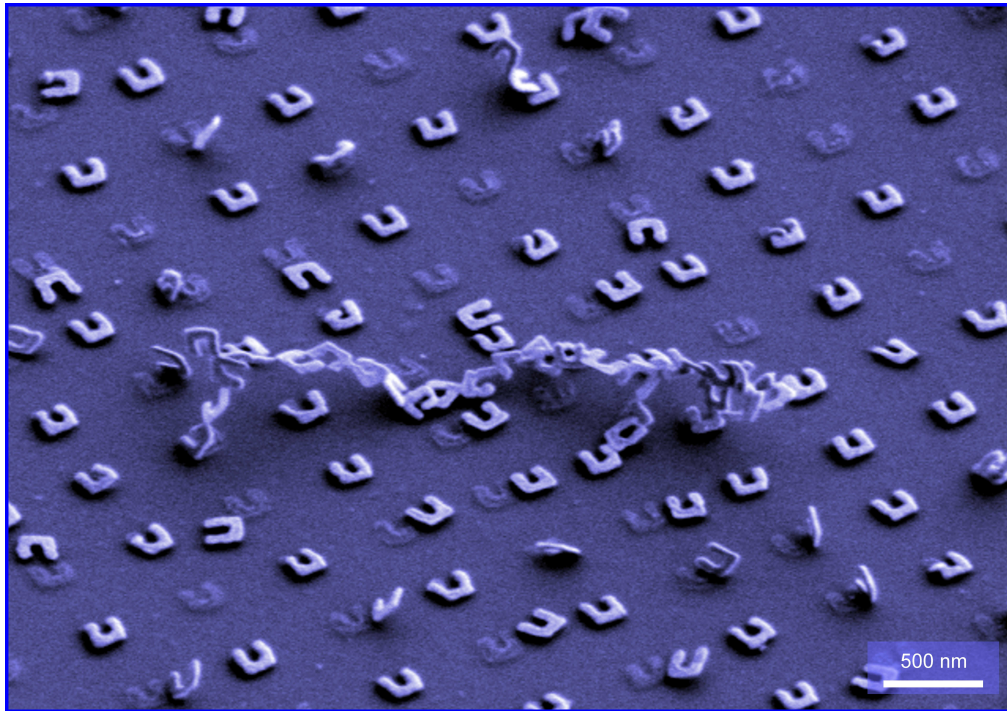


Figure A.2.: Split ring resonators which were separated from the surface due to laser irradiation [315]. The shadow on the substrate surface is the remaining chromium adhesion layer.

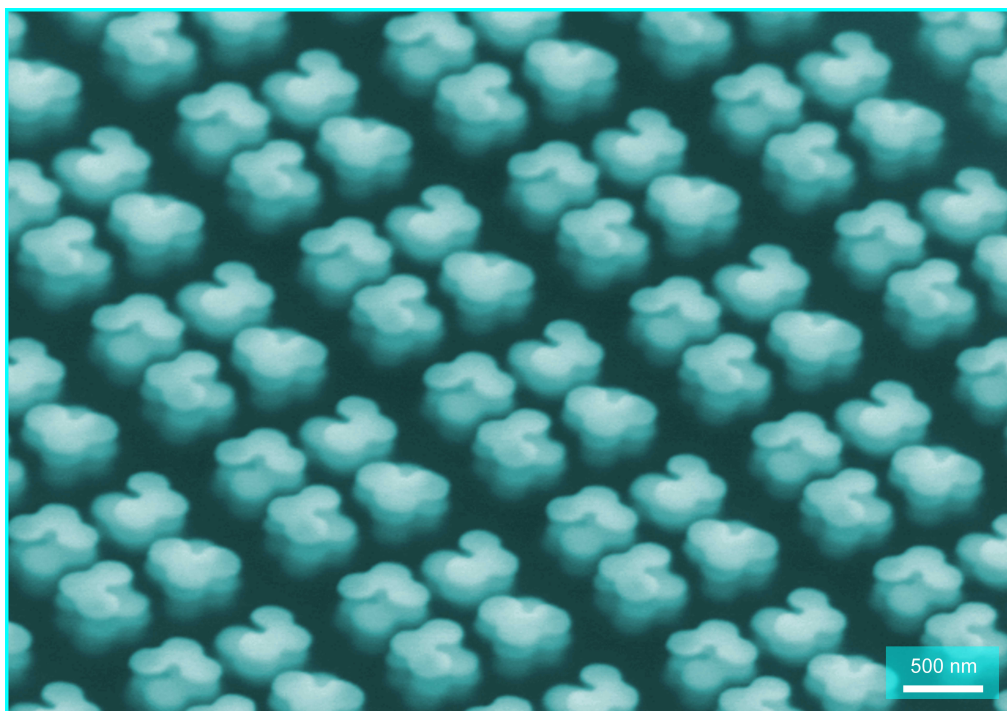


Figure A.3.: Chiral structure consisting of four individual layers.

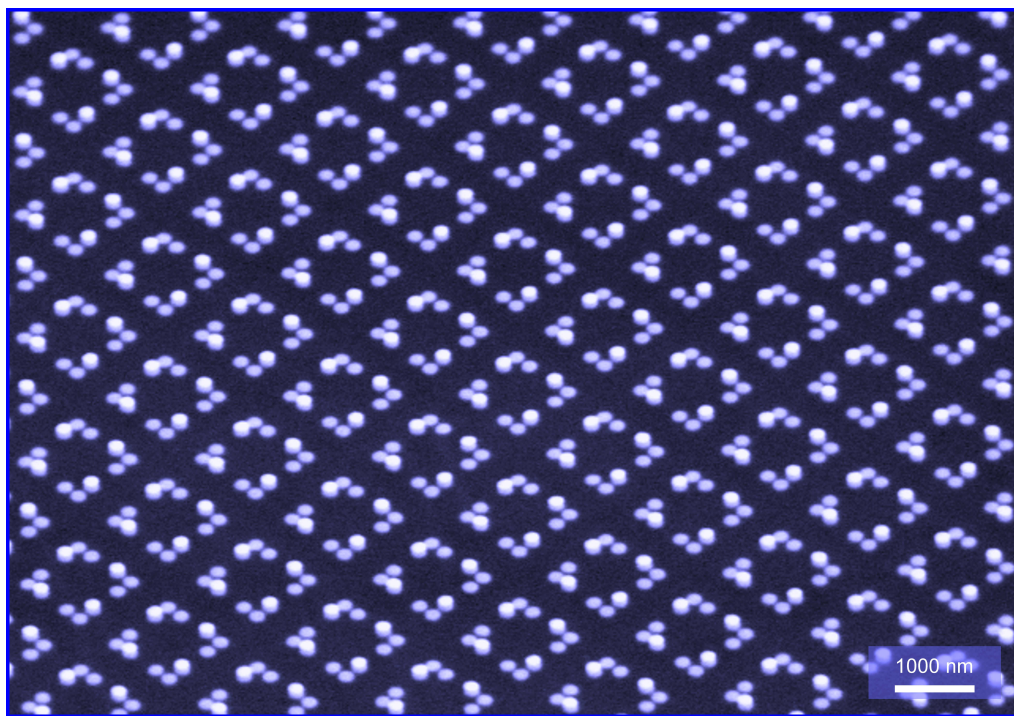


Figure A.4.: Stacked chiral structure [90].

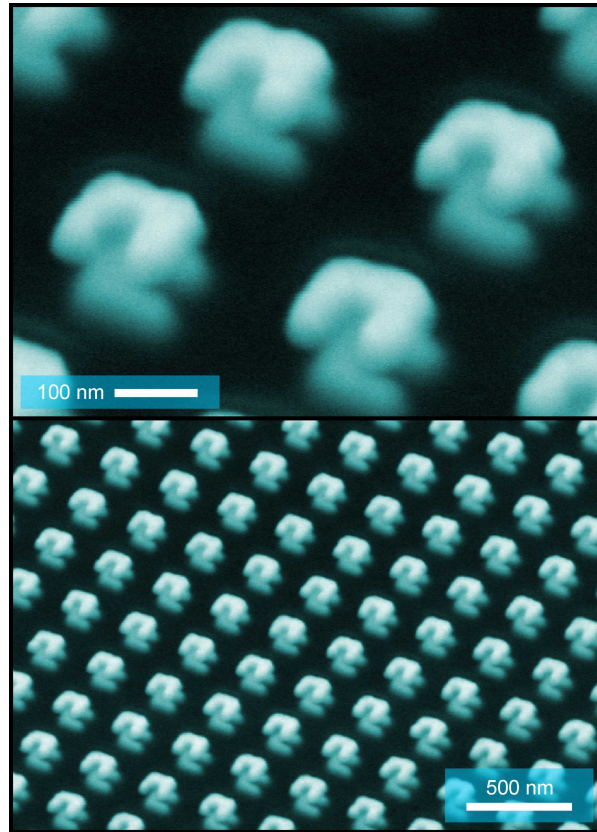


Figure A.5.: Twisted stacked split ring resonators, periodicity 300 nm.

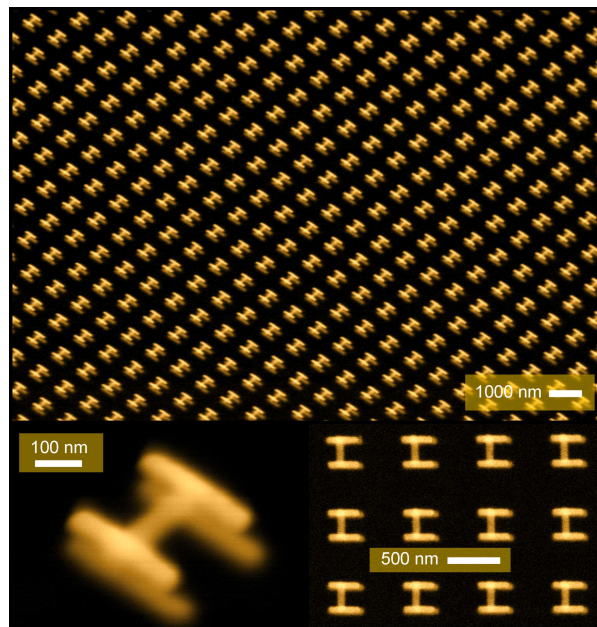


Figure A.6.: Three-layered structure exhibiting double electromagnetically induced transparency [92].

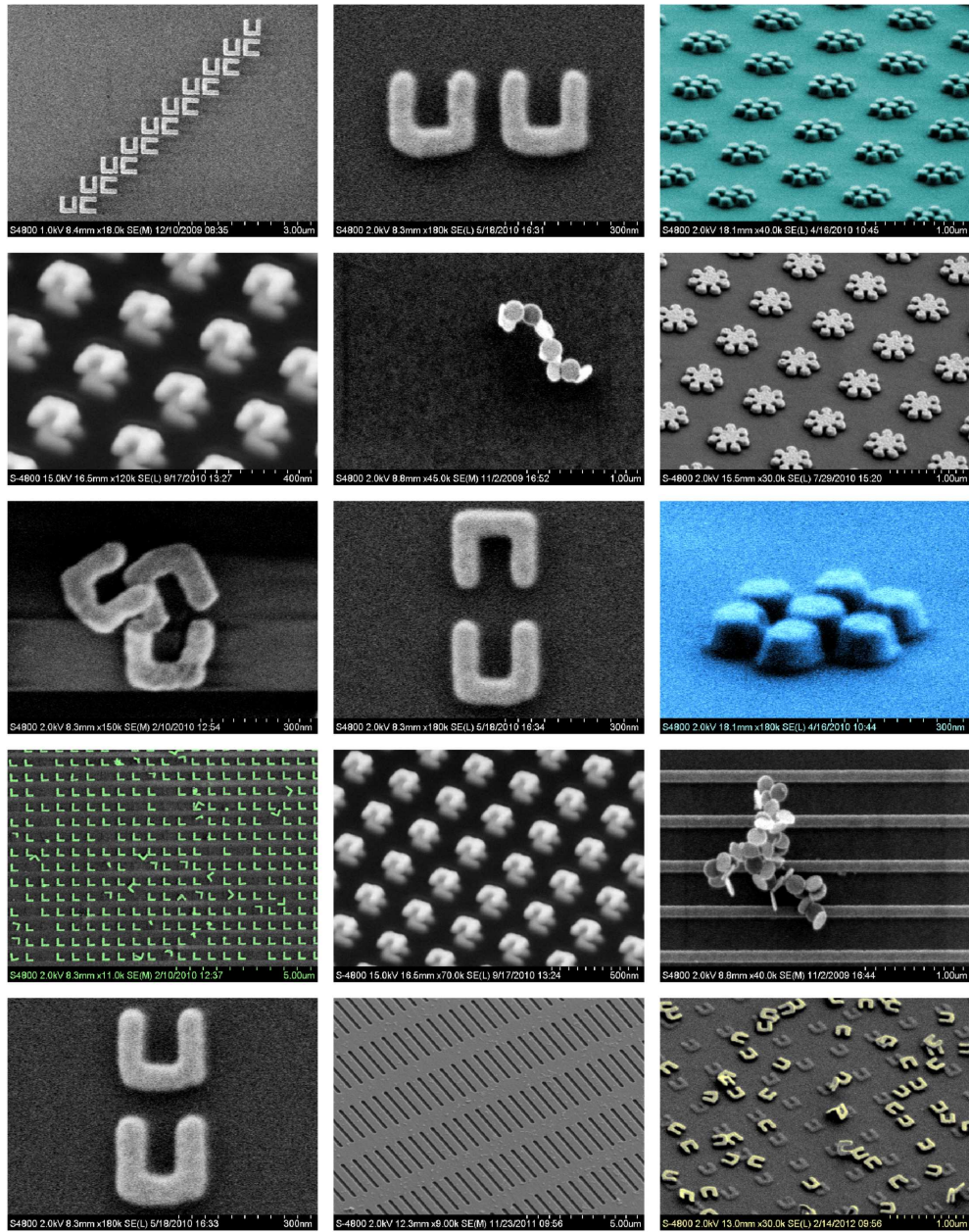


Figure A.7.: Various SEM and optical micrographs.

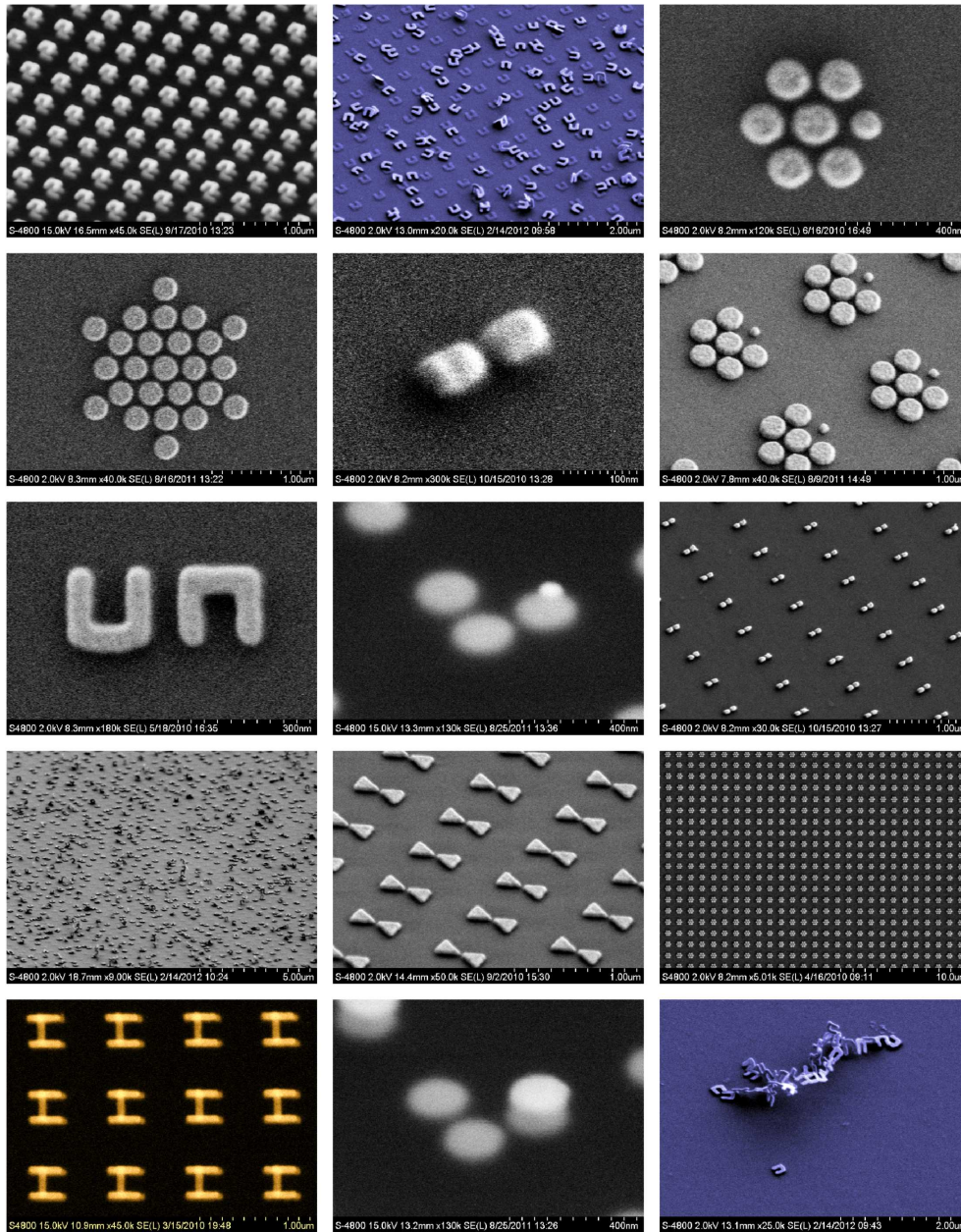


Figure A.8.: Various SEM and optical micrographs.

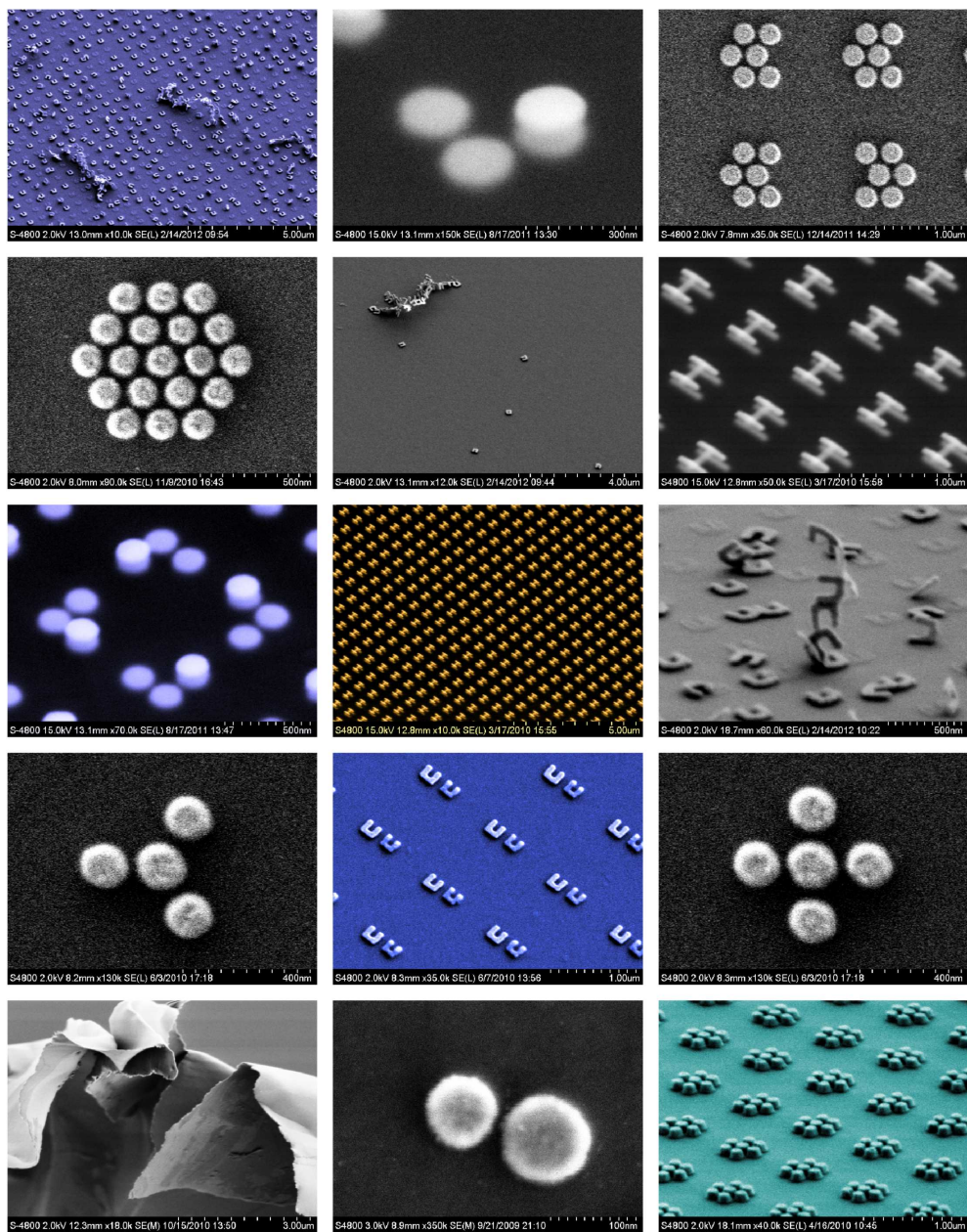


Figure A.9.: Various SEM and optical micrographs.

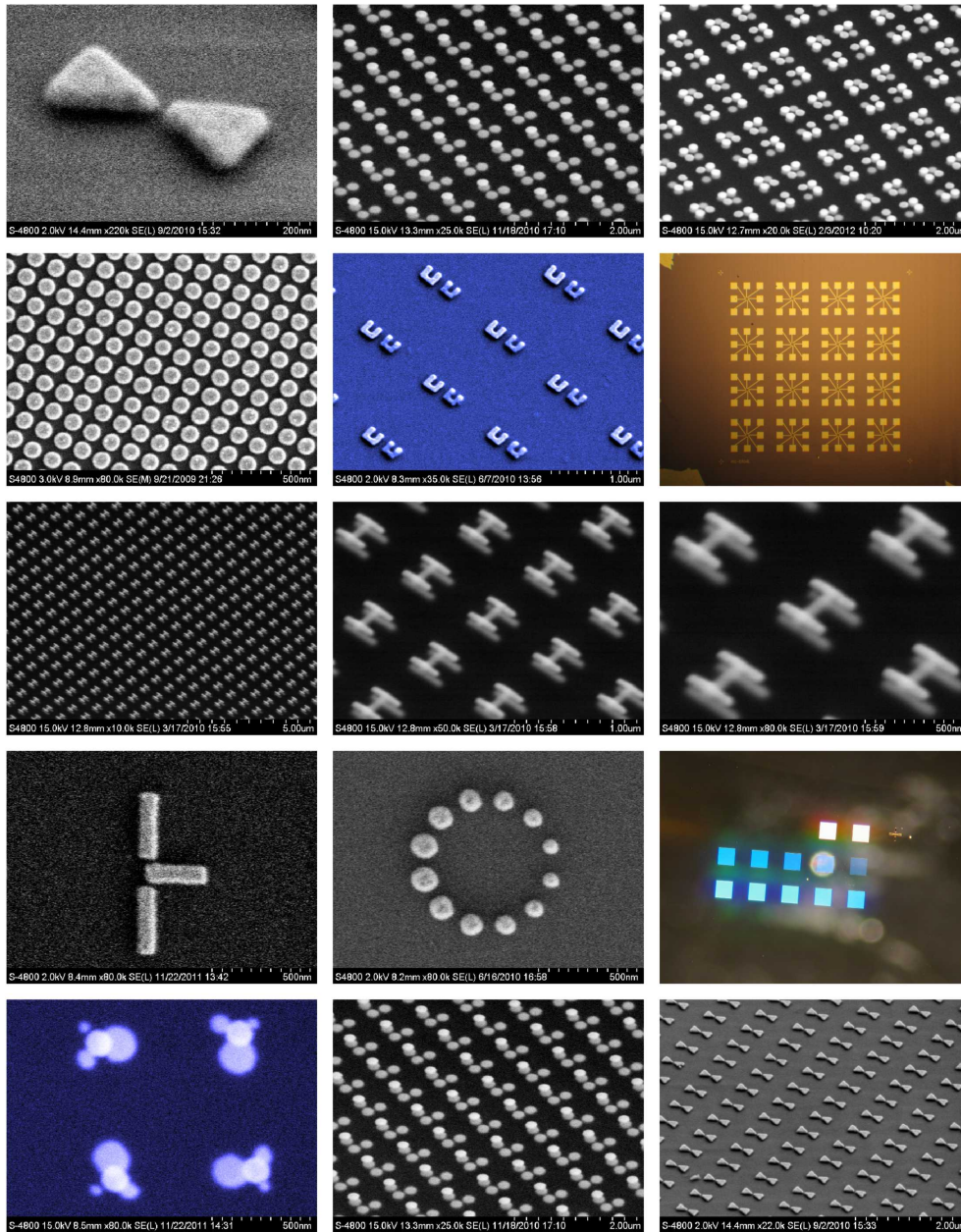


Figure A.10.: Various SEM and optical micrographs.

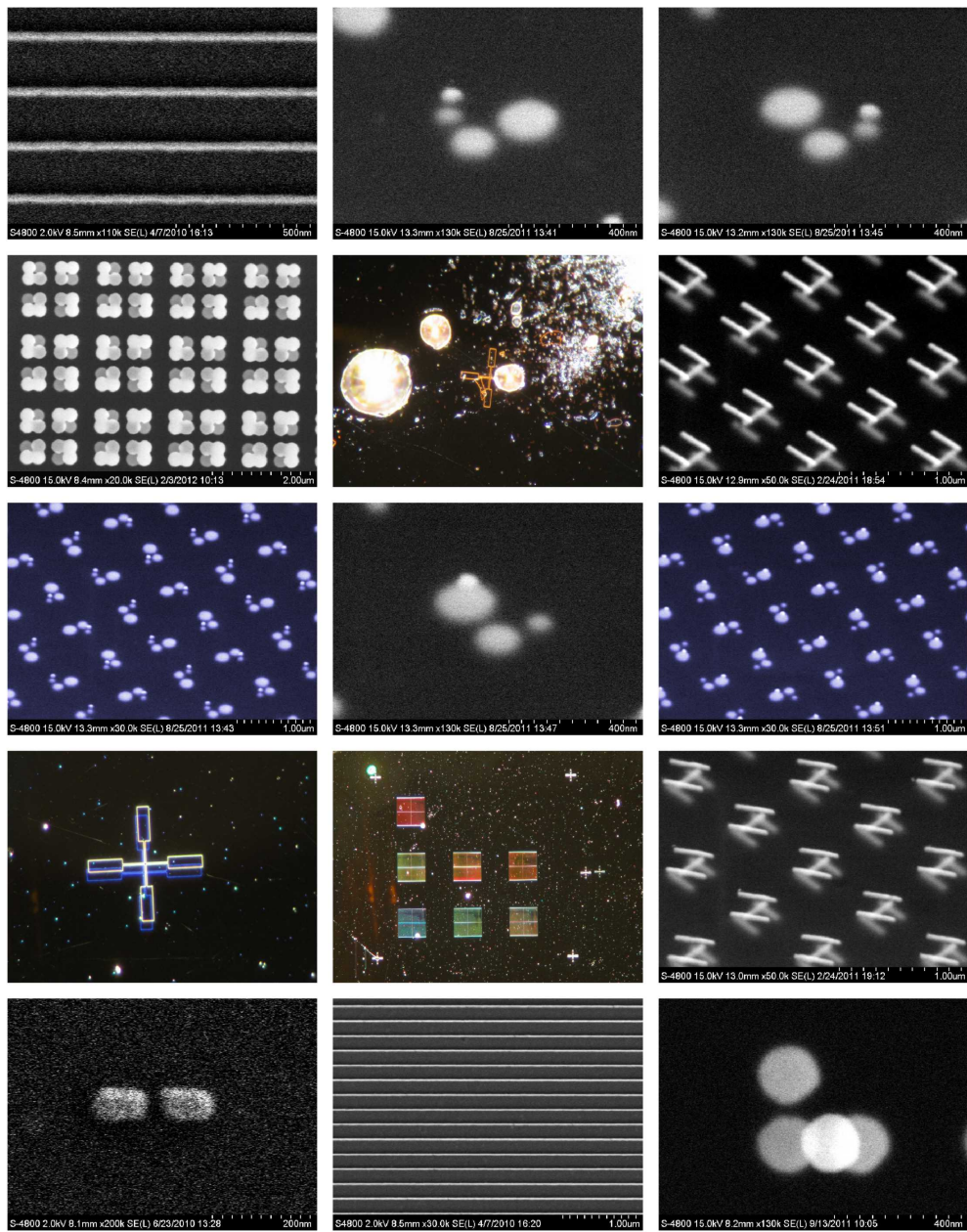


Figure A.11.: Various SEM and optical micrographs.

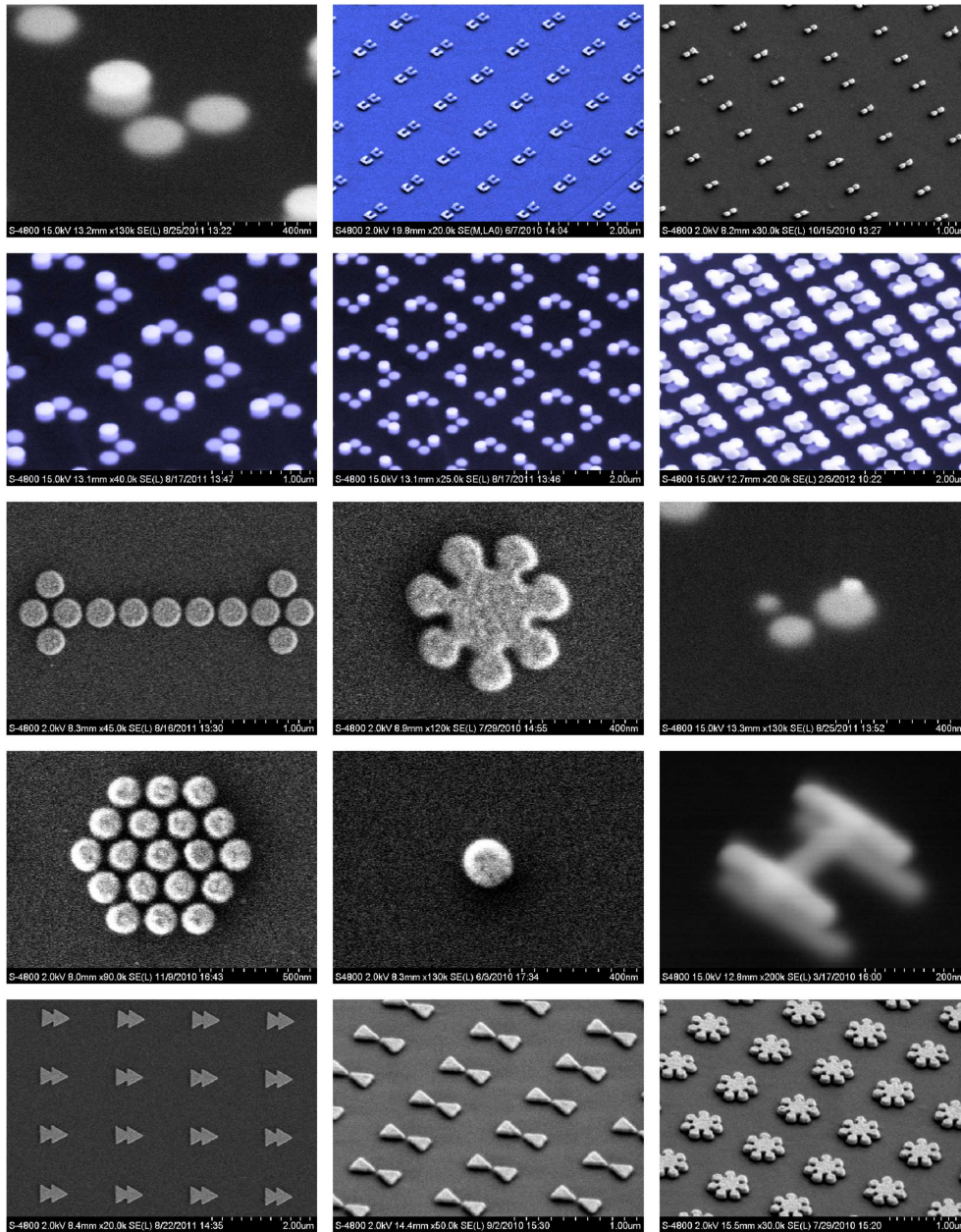


Figure A.12.: Various SEM and optical micrographs.

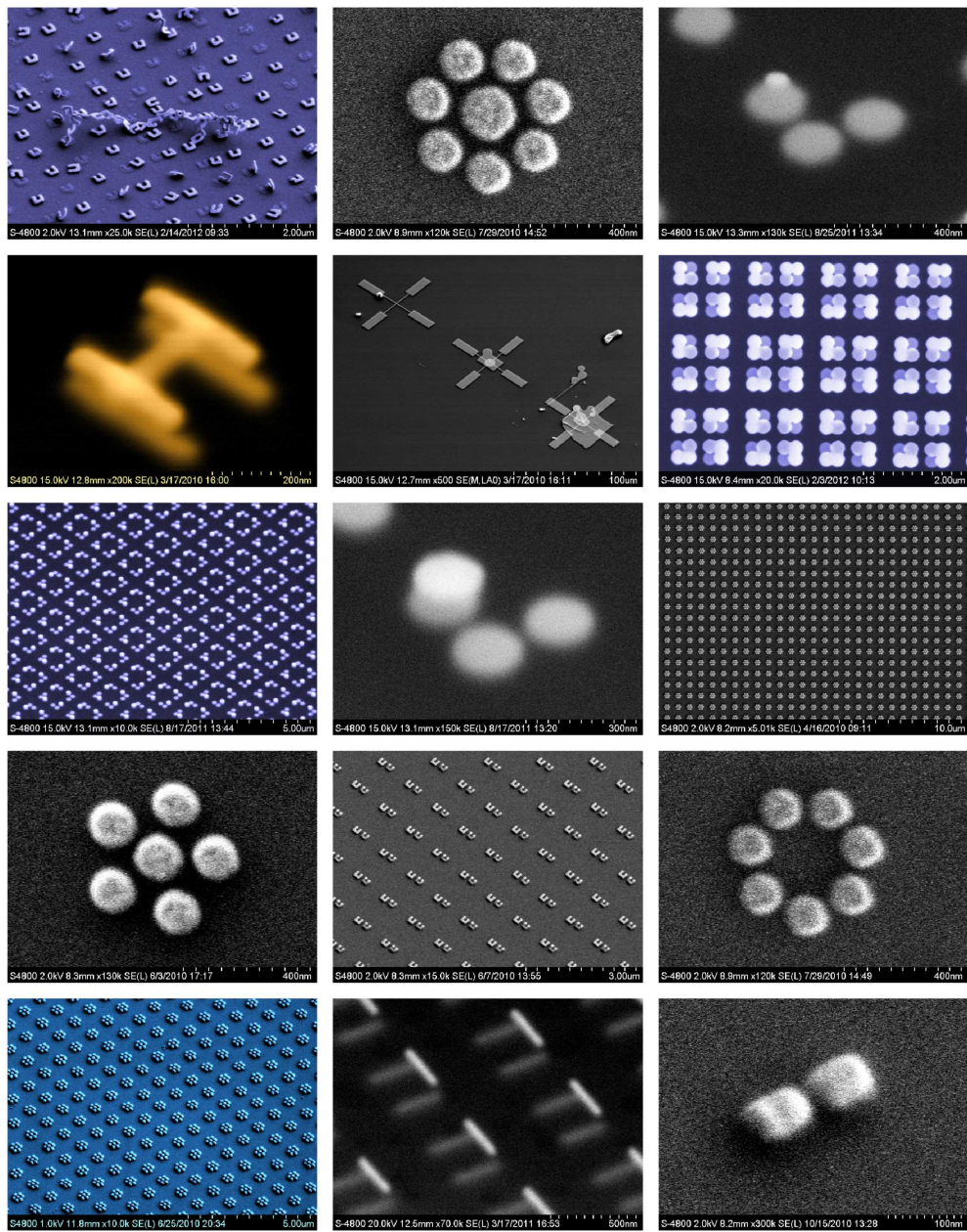


Figure A.13.: Various SEM and optical micrographs.

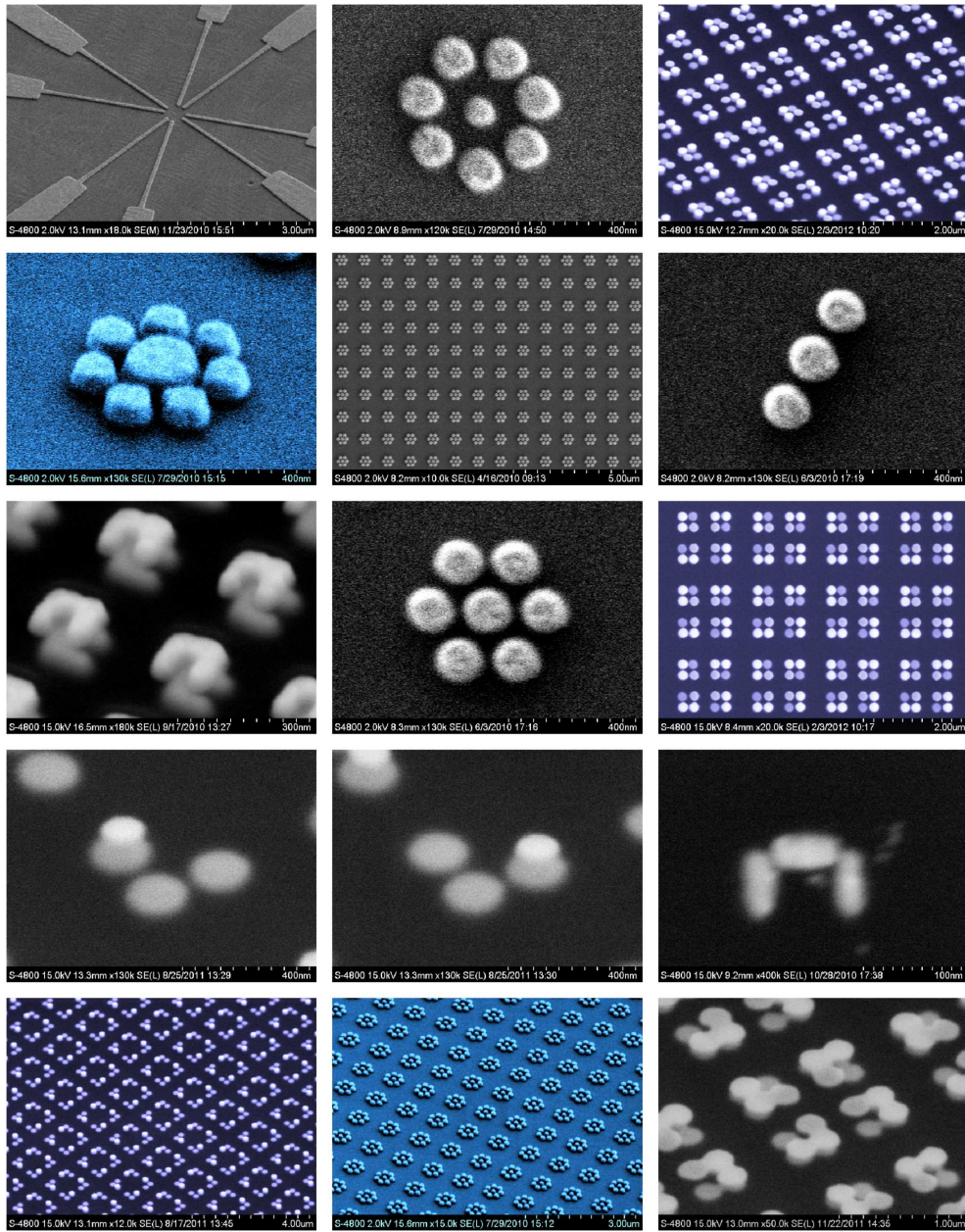


Figure A.14.: Various SEM and optical micrographs.

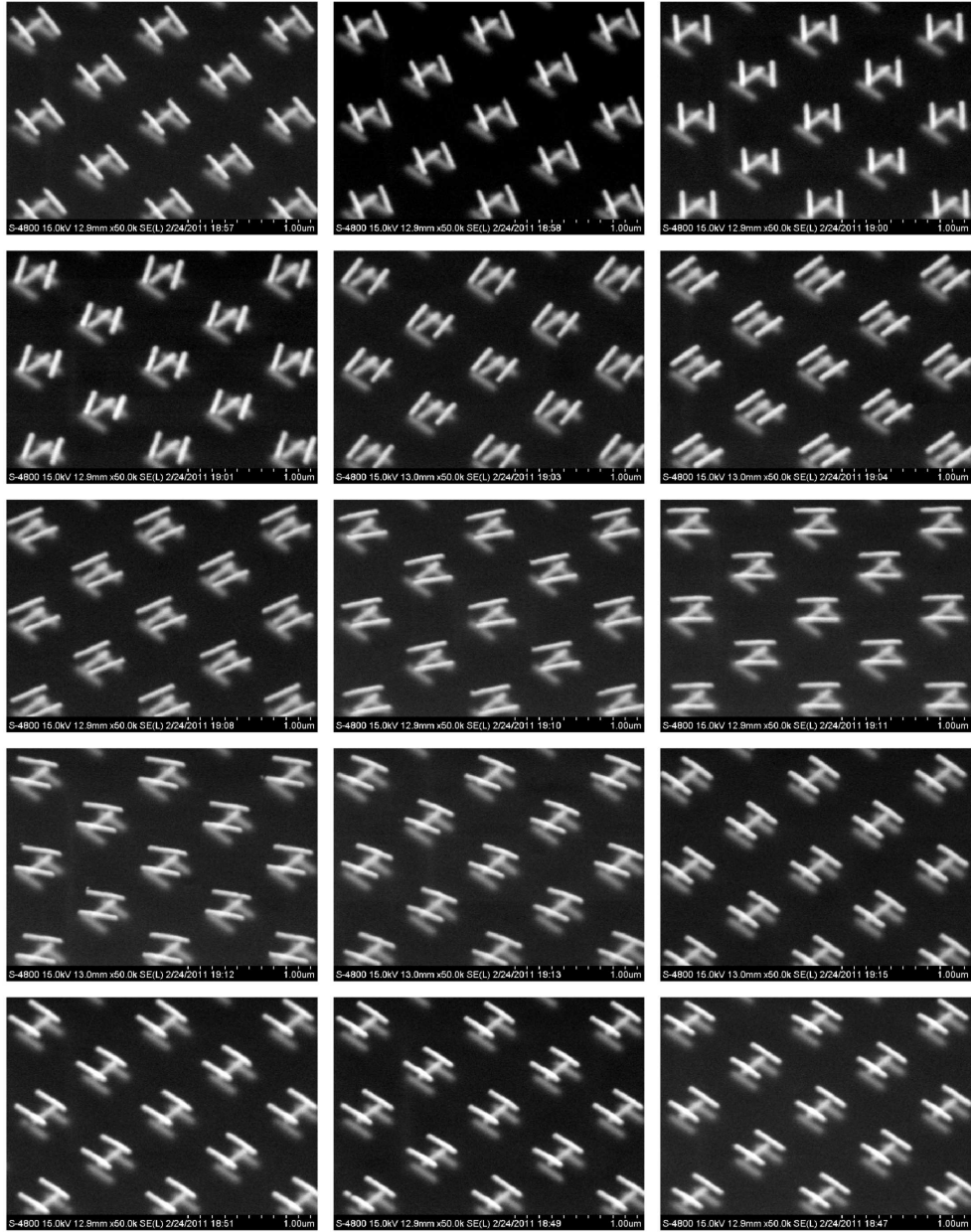


Figure A.15.: Various SEM and optical micrographs.

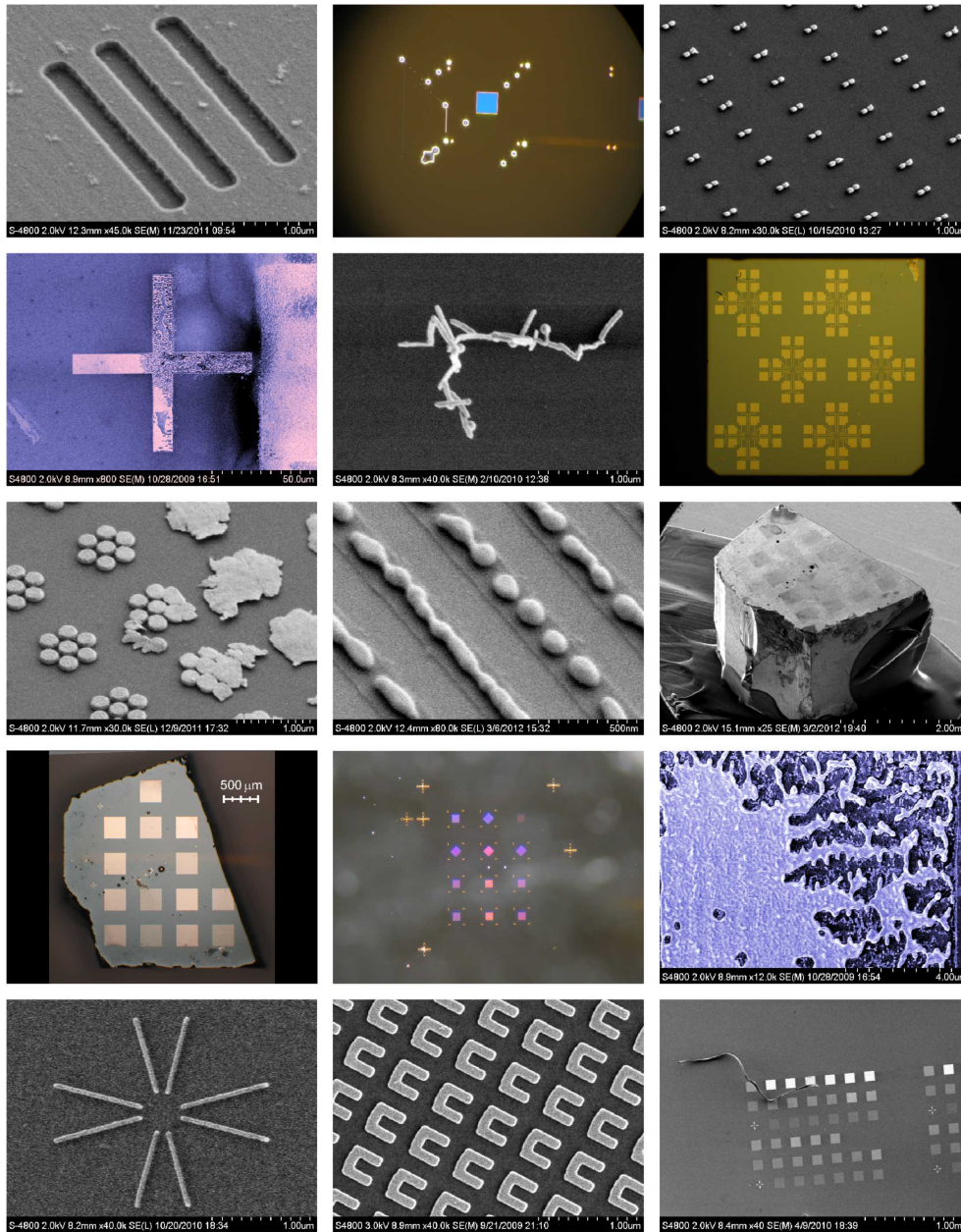


Figure A.16.: Various SEM and optical micrographs.

Bibliography

- [1] M. Faraday, “The Bakerian Lecture: Experimental Relations of Gold (and Other Metals) to Light,” *Philosophical Transactions of the Royal Society of London* **147**, 145–181 (1857).
- [2] R. W. Wood, “On a Remarkable Case of Uneven Distribution of Light in a Diffraction Grating Spectrum,” *Proceedings of the Physical Society* **18**, 269–275 (1902).
- [3] R. H. Ritchie, E. T. Arakawa, J. J. Cowan, and R. N. Hamm, “Surface-Plasmon Resonance Effect in Grating Diffraction,” *Physical Review Letters* **21**, 1530–1533 (1968).
- [4] J. C. Maxwell Garnett, “Colours in Metal Glasses and in Metallic Films,” *Philosophical Transactions of the Royal Society of London. Series A* **203**, 385–420 (1904).
- [5] G. Mie, “Beiträge zur Optik trüber Medien, speziell kolloidaler Metallösungen,” *Annalen der Physik* **4**, 377–445 (1908).
- [6] R. Gans, “Über die Form ultramikroskopischer Goldteilchen,” *Annalen der Physik* **342**, 881–900 (1912).
- [7] D. Pines, “Collective Energy Losses in Solids,” *Reviews of Modern Physics* **28**, 184–198 (1956).
- [8] R. H. Ritchie, “Plasma Losses by Fast Electrons in Thin Films,” *Physical Review* **106**, 874–881 (1957).
- [9] U. Kreibig and P. Zacharias, “Surface plasma resonances in small spherical silver and gold particles,” *Zeitschrift für Physik* **231**, 128–143 (1970).
- [10] A. Otto, “Excitation of Nonradiative Surface Plasma Waves in Silver by the Method of Frustrated Total Reflection,” *Zeitschrift für Physik* **216**, 398–410 (1968).

- [11] E. Kretschmann and H. Raether, “Radiative decay of non-radiative surface plasmons excited by light,” *Zeitschrift für Naturforschung* **23a**, 2135 (1968).
- [12] M. Fleischmann, “Raman spectra of pyridine absorbed at silver electrode,” *Chemical Physics Letters* **26**, 163–166 (1974).
- [13] W. L. Barnes, A. Dereux, and T. W. Ebbesen, “Surface plasmon subwavelength optics,” *Nature* **424**, 824–830 (2003).
- [14] J. A. Schuller, E. S. Barnard, W. Cai, Y. C. Jun, J. S. White, and M. L. Brongersma, “Plasmonics for extreme light concentration and manipulation.” *Nature Materials* **9**, 193–204 (2010).
- [15] K. M. Mayer and J. H. Hafner, “Localized surface plasmon resonance sensors.” *Chemical Reviews* **111**, 3828–3857 (2011).
- [16] K. A. Willets and R. P. Van Duyne, “Localized surface plasmon resonance spectroscopy and sensing.” *Annual Review of Physical Chemistry* **58**, 267–297 (2007).
- [17] K. L. Kelly, E. Coronado, L. L. Zhao, and G. C. Schatz, “The optical properties of metal nanoparticles: The influence of size, shape, and dielectric environment,” *Journal of Physical Chemistry B* **107**, 668–677 (2003).
- [18] A. J. Haes and R. P. Van Duyne, “A nanoscale optical biosensor: Sensitivity and selectivity of an approach based on the localized surface plasmon resonance spectroscopy of triangular silver nanoparticles.” *Journal of the American Chemical Society* **124**, 596–604 (2002).
- [19] A. J. Haes, S. Zou, G. C. Schatz, and R. P. Van Duyne, “A nanoscale optical biosensor: The long range distance dependence of the localized surface plasmon resonance of noble metal nanoparticles,” *The Journal of Physical Chemistry B* **108**, 109–116 (2004).
- [20] J. N. Anker, W. P. Hall, C. Nilam, J. Zhao, and P. Van, “Biosensing with plasmonic nanosensors,” *Nature Materials* **7**, 442–453 (2008).
- [21] H. Chen, X. Kou, Z. Yang, W. Ni, and J. Wang, “Shape- and size-dependent refractive index sensitivity of gold nanoparticles.” *Langmuir* **24**, 5233–5237 (2008).
- [22] J. Homola, S. S. Yee, and G. Gauglitz, “Surface plasmon resonance sensors: Review,” *Sensors and Actuators B: Chemical* **54**, 3–15 (1999).
- [23] L. Rodríguez-Lorenzo, R. de la Rica, R. A. Alvarez-Puebla, L. M. Liz-Marzán,

- and M. M. Stevens, “Plasmonic nanosensors with inverse sensitivity by means of enzyme-guided crystal growth.” *Nature Materials* **11**, 604–607 (2012).
- [24] E. M. Larsson, C. Langhammer, I. Zorić, and B. Kasemo, “Nanoplasmonic probes of catalytic reactions.” *Science* **326**, 1091–1094 (2009).
- [25] N. Verellen, P. Van Dorpe, C. Huang, K. Lodewijks, G. A. E. Vandenbosch, L. Lagae, and V. V. Moshchalkov, “Plasmon line shaping using nanocrosses for high sensitivity localized surface plasmon resonance sensing.” *Nano Letters* **11**, 391–397 (2011).
- [26] N. Liu, T. Weiss, M. Mesch, L. Langguth, U. Eigenthaler, M. Hirscher, C. Sönnichsen, and H. Giessen, “Planar metamaterial analogue of electromagnetically induced transparency for plasmonic sensing.” *Nano Letters* **10**, 1103–1107 (2010).
- [27] N. Liu, M. Mesch, T. Weiss, M. Hentschel, and H. Giessen, “Infrared perfect absorber and its application as plasmonic sensor.” *Nano Letters* **10**, 2342–2348 (2010).
- [28] A. A. Yanik, M. Huang, A. Artar, T.-Y. Chang, and H. Altug, “Integrated nanoplasmonic-nanofluidic biosensors with targeted delivery of analytes,” *Applied Physics Letters* **96**, 021101 (2010).
- [29] N. Liu, M. L. Tang, M. Hentschel, H. Giessen, and A. P. Alivisatos, “Nanoantenna-enhanced gas sensing in a single tailored nanofocus.” *Nature Materials* **10**, 631–636 (2011).
- [30] F. Neubrech, A. Pucci, T. Cornelius, S. Karim, A. García-Etxarri, and J. Aizpurua, “Resonant plasmonic and vibrational coupling in a tailored nanoantenna for infrared detection,” *Physical Review Letters* **101**, 157403 (2008).
- [31] C. Wu, A. B. Khanikaev, R. Adato, N. Arju, A. A. Yanik, H. Altug, and G. Shvets, “Fano-resonant asymmetric metamaterials for ultrasensitive spectroscopy and identification of molecular monolayers,” *Nature Materials* **10**, 69–75 (2011).
- [32] R. Adato, A. a. Yanik, J. J. Amsden, D. L. Kaplan, F. G. Omenetto, M. K. Hong, S. Erramilli, and H. Altug, “Ultra-sensitive vibrational spectroscopy of protein monolayers with plasmonic nanoantenna arrays.” *Proceedings of the National Academy of Sciences of the United States of America* **106**, 19227–19232 (2009).
- [33] J. Pendry, A. Holden, D. Robbins, and W. Stewart, “Magnetism from conductors and enhanced nonlinear phenomena,” *IEEE Transactions on Microwave Theory and Techniques* **47**, 2075–2084 (1999).

- [34] L. D. Landau, E. M. Lifshitz, and L. P. Pitaevskii, *Electrodynamics of Continuous Media* (Butterworth-Heinemann, 1984), 2nd edn.
- [35] V. G. Veselago, “Electrodynamics of substances with simultaneously negative values of sigma and mu,” *Soviet Physics Uspekhi - USSR* **10**, 509 (1968).
- [36] J. Pendry, “Negative refraction makes a perfect lens,” *Physical Review Letters* **85**, 3966–3969 (2000).
- [37] R. A. Shelby, D. R. Smith, and S. Schultz, “Experimental verification of a negative index of refraction.” *Science* **292**, 77–79 (2001).
- [38] N. Fang, H. Lee, C. Sun, and X. Zhang, “Sub-diffraction-limited optical imaging with a silver superlens,” *Science* **1783**, 534–537 (2005).
- [39] V. M. Shalaev, “Optical negative-index metamaterials,” *Nature Photonics* **1**, 41–48 (2007).
- [40] D. R. Smith, J. B. Pendry, and M. C. K. Wiltshire, “Metamaterials and negative refractive index.” *Science* **305**, 788–792 (2004).
- [41] V. M. Shalaev, W. Cai, U. K. Chettiar, H.-K. Yuan, A. K. Sarychev, V. P. Drachev, and A. V. Kildishev, “Negative index of refraction in optical metamaterials.” *Optics Letters* **30**, 3356–3358 (2005).
- [42] S. Linden, C. Enkrich, M. Wegener, J. Zhou, T. Koschny, and C. M. Soukoulis, “Magnetic response of metamaterials at 100 terahertz.” *Science* **306**, 1351–1353 (2004).
- [43] J. Valentine, S. Zhang, T. Zentgraf, E. Ulin-Avila, D. A. Genov, G. Bartal, and X. Zhang, “Three-dimensional optical metamaterial with a negative refractive index.” *Nature* **455**, 376–9 (2008).
- [44] A. Houck, J. Brock, and I. Chuang, “Experimental Observations of a Left-Handed Material That Obeys Snell’s Law,” *Physical Review Letters* **90**, 137401 (2003).
- [45] C. M. Soukoulis, S. Linden, and Wegener, “Negative Refractive Index at Optical Wavelength,” *Science* **315**, 47–50 (2007).
- [46] U. Leonhardt, “Optical conformal mapping.” *Science* **312**, 1777–1780 (2006).
- [47] J. B. Pendry, D. Schurig, and D. R. Smith, “Controlling electromagnetic fields.” *Science* **312**, 1780–1782 (2006).

- [48] J. B. Pendry, A. Aubry, D. R. Smith, and S. A. Maier, “Transformation Optics and Subwavelength Control of Light,” *Science* **337**, 549–552 (2012).
- [49] T. Zentgraf, Y. Liu, M. H. Mikkelsen, J. Valentine, and X. Zhang, “Plasmonic Luneburg and Eaton lenses.” *Nature Nanotechnology* **6**, 151–155 (2011).
- [50] U. Leonhardt, “Notes on conformal invisibility devices,” *New Journal of Physics* **8**, 118–118 (2006).
- [51] U. Leonhardt and T. G. Philbin, “General relativity in electrical engineering,” *New Journal of Physics* **8**, 247–247 (2006).
- [52] D. Schurig, J. J. Mock, B. J. Justice, S. A. Cummer, J. B. Pendry, A. F. Starr, and D. R. Smith, “Metamaterial electromagnetic cloak at microwave frequencies.” *Science* **314**, 977–980 (2006).
- [53] W. Cai, U. K. Chettiar, A. V. Kildishev, and V. M. Shalaev, “Optical cloaking with metamaterials,” *Nature Photonics* **1**, 224–227 (2007).
- [54] V. M. Shalaev, “Transforming Light,” *Science* **322**, 384–386 (2008).
- [55] J. Li and J. B. Pendry, “Hiding under the Carpet: A New Strategy for Cloaking,” *Physical Review Letters* **101**, 203 901 (2008).
- [56] U. Leonhardt and T. Tyc, “Broadband Invisibility by Non-Euclidean Cloaking,” *Science* **323**, 110–112 (2009).
- [57] R. Liu, C. Ji, J. J. Mock, J. Y. Chin, T. J. Cui, and D. R. Smith, “Broadband ground-plane cloak.” *Science* **323**, 366–369 (2009).
- [58] J. Valentine, J. Li, T. Zentgraf, G. Bartal, and X. Zhang, “An optical cloak made of dielectrics.” *Nature Materials* **8**, 568–571 (2009).
- [59] L. H. Gabrielli, J. Cardenas, C. B. Poitras, and M. Lipson, “Silicon nanostructure cloak operating at optical frequencies,” *Nature Photonics* **3**, 461–463 (2009).
- [60] J. H. Lee, J. Blair, V. A. Tamma, Q. Wu, S. J. Rhee, C. J. Summers, and W. Park, “Direct visualization of optical frequency invisibility cloak based on silicon nanorod array,” *Optics Express* **17**, 12 922–12 928 (2009).
- [61] I. Smolyaninov, V. Smolyaninova, A. Kildishev, and V. Shalaev, “Anisotropic metamaterials emulated by tapered waveguides: Application to optical cloaking,” *Physical Review Letters* **102**, 213 901 (2009).

- [62] A. Alu and N. Engheta, “Achieving transparency with plasmonic and metamaterial coatings,” *Physical Review E* **72**, 016 623 (2005).
- [63] T. Ergin, N. Stenger, P. Brenner, J. B. Pendry, and M. Wegener, “Three-dimensional invisibility cloak at optical wavelengths.” *Science* **328**, 337–339 (2010).
- [64] H. Haken and H. C. Wolf, *Molecular physics and elements of quantum chemistry* (Springer, Berlin, 2003).
- [65] E. Prodan, C. Radloff, N. J. Halas, and P. Nordlander, “A hybridization model for the plasmon response of complex nanostructures.” *Science* **302**, 419–422 (2003).
- [66] P. Nordlander, C. Oubre, E. Prodan, K. Li, and M. I. Stockman, “Plasmon Hybridization in Nanoparticle Dimers,” *Nano Letters* **4**, 899–903 (2004).
- [67] D.-S. Kim, J. Heo, S.-H. Ahn, S. W. Han, W. S. Yun, and Z. H. Kim, “Real-space mapping of the strongly coupled plasmons of nanoparticle dimers.” *Nano Letters* **9**, 3619–25 (2009).
- [68] W. Rechberger, A. Hohenau, A. Leitner, J. R. Krenn, B. Lamprecht, and A. F. R., “Optical properties of two interacting gold nanoparticles,” *Optics Communications* **220**, 137–141 (2003).
- [69] A. Alù and N. Engheta, “Hertzian plasmonic nanodimer as an efficient optical nanoantenna,” *Physical Review B* **78**, 195 111 (2008).
- [70] T. Davis, K. Vernon, and D. Gómez, “Designing plasmonic systems using optical coupling between nanoparticles,” *Physical Review B* **79**, 155 423 (2009).
- [71] D. W. Brandl, N. A. Mirin, and P. Nordlander, “Plasmon modes of nanosphere trimers and quadrumers.” *The journal of physical chemistry B* **110**, 12 302–12 010 (2006).
- [72] Y. A. Urzhumov, G. Shvets, J. Fan, F. Capasso, D. Brandl, and P. Nordlander, “Plasmonic nanoclusters : A path towards negative-index metafluids,” *Optics Express* **15**, 14 129–14 145 (2007).
- [73] J. Alegret, T. Rindzevicius, T. Pakizeh, Y. Alaverdyan, L. Gunnarsson, and M. Käll, “Plasmonic properties of silver trimers with trigonal symmetry fabricated by electron-beam lithography,” *Journal of Physical Chemistry C* **112**, 14 313–14 317 (2008).
- [74] J. A. Fan, C. Wu, K. Bao, J. Bao, R. Bardhan, N. J. Halas, V. N. Manoharan,

- P. Nordlander, G. Shvets, and F. Capasso, "Self-assembled plasmonic nanoparticle clusters," *Science* **328**, 1135–1138 (2010).
- [75] J. A. Fan, K. Bao, C. Wu, J. Bao, R. Bardhan, N. J. Halas, V. N. Manoharan, G. Shvets, P. Nordlander, and F. Capasso, "Fano-like interference in self-assembled plasmonic quadrumer clusters," *Nano Letters* **10**, 4680–4685 (2010).
- [76] J. B. Lassiter, H. Sobhani, J. A. Fan, J. Kundu, F. Capasso, P. Nordlander, and N. J. Halas, "Fano resonances in plasmonic nanoclusters: Geometrical and chemical tunability," *Nano Letters* **10**, 3184–3189 (2010).
- [77] M. Hentschel, M. Saliba, R. Vogelgesang, H. Giessen, A. P. Alivisatos, and N. Liu, "Transition from isolated to collective modes in plasmonic oligomers." *Nano Letters* **10**, 2721–2726 (2010).
- [78] D. Dregely, M. Hentschel, and H. Giessen, "Excitation and Tuning of Higher-Order Fano Resonances in Plasmonic Oligomer Clusters." *ACS Nano* **5**, 8202–8211 (2011).
- [79] B. Luk'yanchuk, N. I. Zheludev, S. A. Maier, N. J. Halas, P. Nordlander, H. Giessen, and C. T. Chong, "The Fano resonance in plasmonic nanostructures and metamaterials," *Nature Materials* **9**, 707–715 (2010).
- [80] N. J. Halas, S. Lal, W.-S. Chang, S. Link, and P. Nordlander, "Plasmons in strongly coupled metallic nanostructures." *Chemical Reviews* **111**, 3913–3961 (2011).
- [81] Y. Sonnefraud, N. Verellen, H. Sobhani, G. a. E. Vandenbosch, V. V. Moshchalkov, P. Van Dorpe, P. Nordlander, and S. A. Maier, "Experimental realization of sub-radiant, superradiant, and fano resonances in ring/disk plasmonic nanocavities." *ACS Nano* **4**, 1664–70 (2010).
- [82] N. Verellen, Y. Sonnefraud, H. Sobhani, F. Hao, V. V. Moshchalkov, P. Van Dorpe, P. Nordlander, and S. A. Maier, "Fano resonances in individual coherent plasmonic nanocavities," *Nano Letters* **9**, 1663–1667 (2009).
- [83] A. Artar, A. A. Yanik, and H. Altug, "Multispectral plasmon induced transparency in coupled meta-atoms." *Nano Letters* **11**, 1685–1689 (2011).
- [84] L. S. Slaughter, B. A. Willingham, W.-S. Chang, M. H. Chester, N. Ogden, and S. Link, "Toward Plasmonic Polymers." *Nano Letters* **12**, 3967–3972 (2012).
- [85] H. U. I. Wang, D. W. Brandl, P. Nordlander, and N. J. Halas, "Plasmonic Nanostructures : Artificial Molecules," *Accounts of Chemical Research* **40**, 53–62 (2007).

- [86] M. Rahmani, B. Lukiyanchuk, B. Ng, K. G. A. Tavakkoli, Y. F. Liew, and M. H. Hong, "Generation of pronounced Fano resonances and tuning of subwavelength spatial light distribution in plasmonic pentamers." *Optics Express* **19**, 4949–56 (2011).
- [87] H. W. Lee, M. a. Schmidt, and P. S. J. Russell, "Excitation of a nanowire "molecule" in gold-filled photonic crystal fiber." *Optics Letters* **37**, 2946–2948 (2012).
- [88] M. Hentschel, T. Utikal, H. Giessen, and M. Lippitz, "Quantitative Modeling of the Third Harmonic Emission Spectrum of Plasmonic Nanoantennas." *Nano Letters* **12**, 3778–3782 (2012).
- [89] M. Hentschel, D. Dregely, R. Vogelgesang, H. Giessen, and N. Liu, "Plasmonic oligomers: The role of individual particles in collective behavior." *ACS Nano* **5**, 2042–2050 (2011).
- [90] M. Hentschel, M. Schäferling, T. Weiss, N. Liu, and H. Giessen, "Three-dimensional chiral plasmonic oligomers." *Nano Letters* **12**, 2542–2547 (2012).
- [91] M. Hentschel, L. Wu, M. Schäferling, P. Bai, E. P. Li, and H. Giessen, "Optical properties of chiral three-dimensional plasmonic oligomers at the onset of charge-transfer plasmons." *ACS Nano* **6**, 10355–10365 (2012).
- [92] N. Liu, M. Hentschel, T. Weiss, A. P. Alivisatos, and H. Giessen, "Three-dimensional plasmon rulers." *Science* **332**, 1407–1410 (2011).
- [93] C. Sönnichsen, T. Franzl, T. Wilk, G. von Plessen, and J. Feldmann, "Drastic reduction of plasmon damping in gold nanorods," *Physical Review Letters* **88**, 077402 (2002).
- [94] L. V. Brown, H. Sobhani, J. B. Lassiter, P. Nordlander, and N. J. Halas, "Heterodimers: plasmonic properties of mismatched nanoparticle pairs." *ACS Nano* **4**, 819–32 (2010).
- [95] S.-C. Yang, H. Kobori, C.-L. He, M.-H. Lin, H.-Y. Chen, C. Li, M. Kanehara, T. Teranishi, and S. Gwo, "Plasmon hybridization in individual gold nanocrystal dimers: Direct observation of bright and dark modes," *Nano Letters* **10**, 632–637 (2010).
- [96] N. Liu and H. Giessen, "Coupling effects in optical metamaterials." *Angewandte Chemie International Edition* **49**, 9838–9852 (2010).
- [97] S. J. Barrow, A. M. Funston, D. E. Gómez, T. J. Davis, and P. Mulvaney, "Surface

- plasmon resonances in strongly coupled gold nanosphere chains from monomer to hexamer.” *Nano Letters* **11**, 4180–4187 (2011).
- [98] A. J. Pasquale, B. M. Reinhard, and L. Dal Negro, “Engineering photonic-plasmonic coupling in metal nanoparticle necklaces.” *ACS Nano* **5**, 6578–6585 (2011).
- [99] M. Lieb and A. J. Meixner, “A high numerical aperture parabolic mirror as imaging device for confocal microscopy.” *Optics Express* **8**, 458–474 (2001).
- [100] L. Novotny and B. Hecht, *Principles of Nano Optics* (Cambridge University Press, 2006).
- [101] K. Youngworth and T. Brown, “Focusing of high numerical aperture cylindrical-vector beams.” *Optics Express* **7**, 77–87 (2000).
- [102] R. Dorn, S. Quabis, and G. Leuchs, “Sharper focus for a radially polarized light beam,” *Physical Review Letters* **91**, 233 901 (2003).
- [103] M. Stalder and M. Schadt, “Linearly polarized light with axial symmetry generated by liquid-crystal polarization converters.” *Optics Letters* **21**, 1948–1950 (1996).
- [104] P. Banzer, U. Peschel, S. Quabis, and G. Leuchs, “On the experimental investigation of the electric and magnetic response of a single nano-structure,” *Optics Express* **18**, 273–276 (2010).
- [105] G. M. Lerman, M. Grajower, A. Yanai, and U. Levy, “Light transmission through a circular metallic grating under broadband radial and azimuthal polarization illumination.” *Optics Letters* **36**, 3972–4 (2011).
- [106] S. W. Hell, “Far-field optical nanoscopy.” *Science* **316**, 1153–1158 (2007).
- [107] S. Sheikholeslami, Y.-W. Jun, P. K. Jain, and A. P. Alivisatos, “Coupling of optical resonances in a compositionally asymmetric plasmonic nanoparticle dimer.” *Nano Letters* **10**, 2655–2660 (2010).
- [108] H. Fredriksson, Y. Alaverdyan, a. Dmitriev, C. Langhammer, D. Sutherland, M. Zäch, and B. Kasemo, “Hole Mask Colloidal Lithography,” *Advanced Materials* **19**, 4297–4302 (2007).
- [109] T. Shegai, B. Brian, V. D. Miljković, and M. Käll, “Angular distribution of surface-enhanced Raman scattering from individual au nanoparticle aggregates.” *ACS Nano* **5**, 2036–41 (2011).

- [110] N. Liu, S. Kaiser, and H. Giessen, “Magnetoinductive and Electroinductive Coupling in Plasmonic Metamaterial Molecules,” *Advanced Materials* **20**, 4521–4525 (2008).
- [111] N. Feth, M. König, M. Husnik, K. Stannigel, J. Niegemann, K. Busch, M. Wegener, and S. Linden, “Electromagnetic interaction of split-ring resonators : The role of separation and relative orientation,” *Optics Express* **18**, 215–217 (2010).
- [112] B. T. Draine and P. J. Flatau, “Discrete-dipole approximation for scattering calculations,” *Journal of the Optical Society of America A* **11**, 1491–1499 (1994).
- [113] I. Sersic, A. Tuambilangana, T. Kampfrath, and K. A. F., “Magneto-electric point scattering theory for metamaterial scatterers,” *Physical Review B* **83**, 245 102 (2011).
- [114] L. Langguth and H. Giessen, “Coupling strength of complex plasmonic structures in the multiple dipole approximation,” *Optics Express* **19**, 157–162 (2011).
- [115] C. Hafner, “Boundary methods for optical nano structures,” *Physica Status Solidi (B)* **244**, 3435–3447 (2007).
- [116] P. Alonso-Gonzalez, M. Schnell, P. Sarriugarte, H. Sobhani, C. Wu, N. Arju, A. Khanikaev, F. Golmar, P. Albella, L. Arzubiaga, F. Casanova, L. E. Hueso, P. Nordlander, G. Shvets, and R. Hillenbrand, “Real-space mapping of Fano interference in plasmonic metamolecules.” *Nano Letters* **11**, 3922–3926 (2011).
- [117] M. I. Stockman, “Nanoscience: Dark-hot resonances,” *Nature* **467**, 541–542 (2010).
- [118] Y. Jian, F. Wen, H. Sobhani, B. Lassiter, P. Van Dorpe, P. Nordlander, and N. J. Halas, “Plasmonic nanoclusters: Near field properties of the Fano resonance interrogated with Surface Enhanced Raman Scattering,” *Nano Letters* **12**, 1660–1667 (2012).
- [119] F. Wen, J. Ye, N. Liu, P. Van Dorpe, P. Nordlander, and N. J. Halas, “Plasmon transmutation: Inducing new modes in nanoclusters by adding dielectric nanoparticles.” *Nano Letters* **12**, 5020–5026 (2012).
- [120] N. A. Mirin, K. Bao, and P. Nordlander, “Fano resonances in plasmonic nanoparticle aggregates.” *The Journal of Physical Chemistry. A* **113**, 4028–4034 (2009).
- [121] M. Frimmer, T. Coenen, and A. F. Koenderink, “Signature of a Fano Resonance in a Plasmonic Metamolecule’s Local Density of Optical States,” *Physical Review Letters* **108**, 077 404 (2012).

- [122] M. Rahmani, D. Y. Lei, V. Giannini, B. Lukiyanchuk, M. Ranjbar, T. Y. F. Liew, M. Hong, and S. A. Maier, “Subgroup decomposition of plasmonic resonances in hybrid oligomers: Modeling the resonance lineshape.” *Nano Letters* **12**, 2101–2106 (2012).
- [123] J. B. Lassiter, H. Sobhani, M. W. Knight, W. S. Mielczarek, P. Nordlander, and N. J. Halas, “Designing and deconstructing the Fano lineshape in plasmonic nanoclusters.” *Nano Letters* **12**, 1058–62 (2012).
- [124] P. B. Johnson and C. R. W., “Optical Constants of the Noble Metals,” *Physical Review B* **6**, 4370–4379 (1972).
- [125] M. Rahmani, T. Tahmasebi, Y. Lin, B. Lukiyanchuk, T. Y. F. Liew, and M. H. Hong, “Influence of plasmon destructive interferences on optical properties of gold planar quadrumers.” *Nanotechnology* **22**, 245 204 (2011).
- [126] M. Rahmani, B. Lukiyanchuk, T. Tahmasebi, Y. Lin, T. Y. F. Liew, and M. H. Hong, “Polarization-controlled spatial localization of near-field energy in planar symmetric coupled oligomers,” *Applied Physics A* (2011).
- [127] M. Rahmani, B. Lukiyanchuk, T. T. V. Nguyen, T. Tahmasebi, Y. Lin, T. Y. F. Liew, and M. H. Hong, “Influence of symmetry breaking in pentamers on Fano resonance and near-field energy localization,” *Optical Materials Express* **1**, 1409–1415 (2011).
- [128] N. Talebi, W. Sigle, R. Vogelgesang, C. T. Koch, C. Fernández-López, L. M. Liz-Marzán, B. Ögüt, M. Rohm, and P. a. van Aken, “Breaking the mode degeneracy of surface plasmon resonances in a triangular system.” *Langmuir* **28**, 8867–8873 (2012).
- [129] I. Romero, J. Aizpurua, G. W. Bryant, and F. J. García De Abajo, “Plasmons in nearly touching metallic nanoparticles: Singular response in the limit of touching dimers.” *Optics Express* **14**, 9988–9999 (2006).
- [130] J. B. Lassiter, J. Aizpurua, L. I. Hernandez, D. W. Brandl, I. Romero, S. Lal, J. H. Hafner, P. Nordlander, and N. J. Halas, “Close Encounters between Two Nanoshells,” *Nano Letters* **8**, 1212–1218 (2008).
- [131] O. Pérez-González, N. Zabala, A. G. Borisov, N. J. Halas, P. Nordlander, and J. Aizpurua, “Optical spectroscopy of conductive junctions in plasmonic cavities.” *Nano Letters* **10**, 3090–3095 (2010).
- [132] O. Pérez-González, N. Zabala, and J. Aizpurua, “Optical characterization of charge

transfer and bonding dimer plasmons in linked interparticle gaps,” *New Journal of Physics* **13**, 083 013 (2011).

- [133] J.-S. Huang, V. Callegari, P. Geisler, C. Brüning, J. Kern, J. C. Prangma, X. Wu, T. Feichtner, J. Ziegler, P. Weinmann, M. Kamp, A. Forchel, P. Biagioni, U. Sennhauser, and B. Hecht, “Atomically flat single-crystalline gold nanostructures for plasmonic nanocircuitry,” *Nature Communications* **1**, 150 (2010).
- [134] H. Duan, H. Hu, K. Kumar, Z. Shen, and J. K. W. Yang, “Direct and reliable patterning of plasmonic nanostructures with sub-10-nm gaps.” *ACS Nano* **5**, 7593–7600 (2011).
- [135] A. Artar, A. A. Yanik, and H. Altug, “Directional double Fano resonances in plasmonic hetero-oligomers.” *Nano Letters* **11**, 3694–700 (2011).
- [136] Y. H. Fu, J. B. Zhang, Y. F. Yu, and B. Luk’yanchuk, “Generating and manipulating higher order Fano resonances in dual-disk ring plasmonic nanostructures.” *ACS Nano* **6**, 5130–5137 (2012).
- [137] K. Bao, N. A. Mirin, and P. Nordlander, “Fano resonances in planar silver nanosphere clusters,” *Applied Physics A* **100**, 333–339 (2010).
- [138] N. Liu, S. Mukherjee, K. Bao, L. V. Brown, J. Dorfmueller, P. Nordlander, and N. J. Halas, “Magnetic plasmon formation and propagation in artificial aromatic molecules.” *Nano Letters* **12**, 364–369 (2012).
- [139] N. Liu, S. Mukherjee, K. Bao, Y. Li, L. V. Brown, P. Nordlander, and N. J. Halas, “Manipulating magnetic plasmon propagation in metallic nanocluster networks.” *ACS Nano* **6**, 5482–5488 (2012).
- [140] S. Zhang, D. A. Genov, Y. Wang, M. Liu, and X. Zhang, “Plasmon-induced transparency in metamaterials,” *Physical Review Letters* **101**, 047 401 (2008).
- [141] N. Liu, L. Langguth, T. Weiss, J. Kästel, M. Fleischhauer, T. Pfau, and H. Giessen, “Plasmonic analogue of electromagnetically induced transparency at the Drude damping limit,” *Nature Materials* **8**, 758–762 (2009).
- [142] S. E. Harris, J. E. Field, and A. Imamoglu, “Nonlinear optical processes using electromagnetically induced transparency,” *Physical Review Letters* **64**, 1107–1110 (1990).
- [143] A. Litvak and M. Tokman, “Electromagnetically induced transparency in ensembles of classical oscillators,” *Physical Review Letters* **88**, 095 003 (2002).

- [144] C. L. Garrido Alzar, M. a. G. Martinez, and P. Nussenzeveig, “Classical analog of electromagnetically induced transparency,” *American Journal of Physics* **70**, 37 (2002).
- [145] S. E. Harris, “Electromagnetically induced transparency in an ideal plasma,” *Physical Review Letters* **77**, 5357–5360 (1996).
- [146] K. Totsuka, N. Kobayashi, and M. Tomita, “Slow light in coupled-resonator-induced transparency,” *Physical Review Letters* **98**, 213 904 (2007).
- [147] Q. Xu, S. Sandhu, M. Porinelli, J. Shakya, S. Fan, and M. Lipson, “Experimental realization of an on-chip all-optical analogue to electromagnetically induced transparency,” *Physical Review Letters* **96**, 123 901 (2006).
- [148] M. F. Yanik, W. Suh, Z. Wang, and S. Fan, “Stopping light in a waveguide with an all-optical analog of electromagnetically induced transparency,” *Physical Review Letters* **93**, 233 903 (2004).
- [149] D. Smith, H. Chang, K. A. Fuller, R. T. Rosenberger, and R. W. Boyd, “Coupled-resonator-induced transparency,” *Physical Review A* **69**, 063 804 (2004).
- [150] C. Wu, A. B. Khanikaev, and S. G., “Broadband slow light metamaterial based on a double-continuum Fano resonance,” *Physical Review Letters* **106**, 107 403 (2011).
- [151] P. Tassin, L. Zhang, T. Koschny, E. Economou, and C. Soukoulis, “Low-loss metamaterials based on classical electromagnetically induced transparency,” *Physical Review Letters* **102**, 053 901 (2009).
- [152] N. Papasimakis, V. Fedotov, N. Zheludev, and S. Prosvirnin, “Metamaterial analog of electromagnetically induced transparency,” *Physical Review Letters* **101**, 253 903 (2008).
- [153] R. Kekatpure, E. S. Barnard, W. Cai, and B. M. L., “Phase-coupled plasmon-induced transparency,” *Physical Review Letters* **104**, 243 902 (2010).
- [154] S. N. Sheikholeslami, A. García-Etxarri, and J. A. Dionne, “Controlling the interplay of electric and magnetic modes via Fano-like plasmon resonances,” *Nano Letters* **11**, 3927–34 (2011).
- [155] M. Fleischhauer, A. Imamoglu, and J. Marangos, “Electromagnetically induced transparency: Optics in coherent media,” *Reviews of Modern Physics* **77**, 633–673 (2005).

- [156] L. Maleki, A. B. Matsko, A. A. Savchenkov, and V. S. Ilchenko, “Tunable delay line with interacting whispering-gallery-mode resonators,” *Optics Letters* **29**, 626–628 (2004).
- [157] A. Christ, S. Tikhodeev, N. Gippius, J. Kuhl, and H. Giessen, “Waveguide-Plasmon Polaritons: Strong Coupling of Photonic and Electronic Resonances in a Metallic Photonic Crystal Slab,” *Physical Review Letters* **91**, 183 901 (2003).
- [158] A. Christ, T. Zentgraf, J. Kuhl, S. Tikhodeev, N. Gippius, and H. Giessen, “Optical properties of planar metallic photonic crystal structures: Experiment and theory,” *Physical Review B* **2004**, 125 113 (70).
- [159] A. Christ, T. Zentgraf, S. Tikhodeev, N. Gippius, J. Kuhl, and H. Giessen, “Controlling the interaction between localized and delocalized surface plasmon modes: Experiment and numerical calculations,” *Physical Review B* **74**, 155 435 (2006).
- [160] T. Zentgraf, A. Christ, J. Kuhl, N. Gippius, S. Tikhodeev, D. Nau, and H. Giessen, “Metallodielectric photonic crystal superlattices: Influence of periodic defects on transmission properties,” *Physical Review B* **73**, 115 103 (2006).
- [161] C. Sönnichsen, B. M. Reinhard, J. Liphardt, and A. P. Alivisatos, “A molecular ruler based on plasmon coupling of single gold and silver nanoparticles,” *Nature Biotechnology* **23**, 741–745 (2005).
- [162] G. L. Liu, Y. Yin, S. Kunchakarra, B. Mukherjee, D. Gerion, S. D. Jett, D. G. Bear, J. W. Gray, A. P. Alivisatos, L. P. Lee, and F. F. Chen, “A nanoplasmonic molecular ruler for measuring nuclease activity and DNA footprinting.” *Nature Nanotechnology* **1**, 47–52 (2006).
- [163] Y.-W. Jun, S. Sheikholeslami, D. R. Hostetter, C. Tajon, C. S. Craik, and A. P. Alivisatos, “Continuous imaging of plasmon rulers in live cells reveals early-stage caspase-3 activation at the single-molecule level.” *Proceedings of the National Academy of Sciences of the United States of America* **106**, 17 735–40 (2009).
- [164] X. Su and X. Liu, “The Plasmonic Ruler Goes 3D!” *ChemPhysChem* **12**, 2707–2708 (2011).
- [165] L. Stryer, “Fluorescence energy transfer as a spectroscopic ruler.” *Annual review of biochemistry* **47**, 819–46 (1978).
- [166] C. Sönnichsen and A. P. Alivisatos, “Gold nanorods as novel nonbleaching plasmon-based orientation sensors for polarized single-particle microscopy.” *Nano Letters* **5**, 301–044 (2005).

- [167] C. Mao, W. Sun, and N. C. Seeman, “Assembly of Borromean rings from DNA,” *Nature* **379**, 126–126 (1997).
- [168] E. Winfree, F. Liu, L. A. Wenzler, and N. C. Seeman, “Design and self-assembly of two-dimensional DNA crystals.” *Nature* **394**, 539–44 (1998).
- [169] J. Zheng, J. J. Birktoft, Y. Chen, T. Wang, R. Sha, P. E. Constantinou, S. L. Ginell, C. Mao, and N. C. Seeman, “From molecular to macroscopic via the rational design of a self-assembled 3D DNA crystal.” *Nature* **461**, 74–7 (2009).
- [170] S. J. Tan, M. J. Campolongo, D. Luo, and W. Cheng, “Building plasmonic nanostructures with DNA.” *Nature Nanotechnology* **6**, 268–276 (2011).
- [171] A. J. Mastroianni, S. A. Claridge, and A. P. Alivisatos, “Pyramidal and chiral groupings of gold nanocrystals assembled using DNA scaffolds,” *Journal of the American Chemical Society* **131**, 8455–8459 (2009).
- [172] J. Sharma, R. Chhabra, A. Cheng, J. Brownell, Y. Liu, and H. Yan, “Control of self-assembly of DNA tubes through integration of gold nanoparticles,” *Science* **323**, 112–116 (2009).
- [173] P. Cigler, A. K. R. Lytton-Jean, D. G. Anderson, M. G. Finn, and S. Y. Park, “DNA-controlled assembly of a NaI lattice structure from gold nanoparticles and protein nanoparticles.” *Nature Materials* **9**, 918–922 (2010).
- [174] M. R. Jones, R. J. Macfarlane, B. Lee, J. Zhang, K. L. Young, A. J. Senesi, and C. A. Mirkin, “DNA-nanoparticle superlattices formed from anisotropic building blocks.” *Nature Materials* **9**, 913–917 (2010).
- [175] J. Zheng, P. E. Constantinou, C. Micheel, A. P. Alivisatos, R. A. Kiehl, and N. C. Seeman, “Two-dimensional nanoparticle arrays show the organizational power of robust DNA motifs.” *Nano Letters* **6**, 1502–1504 (2006).
- [176] D. Han, S. Pal, J. Nangreave, Z. Deng, Y. Liu, and H. Yan, “DNA origami with complex curvatures in three-dimensional space.” *Science* **332**, 342–6 (2011).
- [177] A. M. Akulshin, S. Barreiro, and A. Lezama, “Electromagnetically induced absorption and transparency due to resonant two-field excitation of quasidegenerate levels in Rb vapor,” *Physical Review A* **57**, 2996–3002 (1998).
- [178] A. Lezama, S. Barreiro, and A. M. Akulshin, “Electromagnetically induced absorption,” *Physical Review A* **59**, 4732–4735 (1999).
- [179] A. Lipsich, S. Barreiro, A. M. Akulshin, and A. Lezama, “Absorption spectra

- of driven degenerate two-level atomic systems,” *Physical Review A* **61**, 053803 (2000).
- [180] T. Shegai, S. Chen, V. D. Miljković, G. Zengin, P. Johansson, and M. Käll, “A bimetallic nanoantenna for directional colour routing.” *Nature Communications* **2**, 481 (2011).
- [181] D. Dregely, R. Taubert, J. Dorfmüller, R. Vogelgesang, K. Kern, and H. Giessen, “3D optical Yagi Uda nanoantenna array,” *Nature Communications* **2**, 267 (2011).
- [182] T. Pakizeh and M. Käll, “Unidirectional Ultracompact Optical Nanoantennas,” *Nano Letters* **9**, 2343–2349 (2009).
- [183] M. Rahmani, B. Luk’yanchuk, and M. Hong, “Fano resonance in novel plasmonic nanostructures,” *Laser & Photonics Reviews* **21**, DOI: 10.1002/lpor.201200021 (2012).
- [184] P. Tassin, L. Zhang, R. Zhao, A. Jain, T. Koschny, and C. Soukoulis, “Electromagnetically induced transparency and absorption in metamaterials: The radiating two-oscillator model and its experimental confirmation,” *Physical Review Letters* **109**, 187401 (2012).
- [185] B. Lamprecht, A. Leitner, and F. R. Aussenegg, “SHG studies of plasmon dephasing in nanoparticles,” *Applied Physics B* **423**, 419–423 (1999).
- [186] M. Klein, T. Tritzschler, M. Wegener, and S. Linden, “Lineshape of harmonic generation by metallic nanoparticles and metallic photonic crystal slabs,” *Physical Review B* **72**, 115113 (2005).
- [187] M. Liu, M. Pelton, and P. Guyot-Sionnest, “Reduced damping of surface plasmons at low temperatures,” *Physical Review B* **79**, 035418 (2009).
- [188] J.-S. G. Bouillard, W. Dickson, D. P. O’Connor, G. Wurtz, and A. V. Zayats, “Low-temperature plasmonics of metallic nanostructures,” *Nano Letters* **12**, 1561–1565 (2012).
- [189] S. Link and M. A. El-Sayed, “Size and temperature dependence of the plasmon absorption of colloidal gold nanoparticles,” *Journal of Physical Chemistry B* **103**, 4212–4217 (1999).
- [190] R. Taubert, M. Hentschel, J. Kästel, and H. Giessen, “Classical Analog of Electromagnetically Induced Absorption in Plasmonics.” *Nano Letters* **12**, 1367–1371 (2012).

- [191] J. A. Fan, Y. He, K. Bao, C. Wu, J. Bao, N. B. Schade, V. N. Manoharan, G. Shvets, P. Nordlander, D. R. Liu, and F. Capasso, "DNA-enabled self-assembly of plasmonic nanoclusters." *Nano Letters* pp. 3–8 (2011).
- [192] J. A. Fan, K. Bao, L. Sun, J. Bao, V. N. Manoharan, P. Nordlander, and F. Capasso, "Plasmonic mode engineering with templated self-assembled nanoclusters." *Nano Letters* **12**, 5318 (2012).
- [193] S. Lal, S. Link, and N. J. Halas, "Nano-optics from sensing to waveguiding," *Nature Photonics* **1**, 641–648 (2007).
- [194] S. Kim, J. Jin, Y.-J. Kim, I.-Y. Park, Y. Kim, and S.-W. Kim, "High-harmonic generation by resonant plasmon field enhancement," *Nature* **453**, 757–60 (2008).
- [195] M. Sivi, M. Duwe, B. Abel, and C. Ropers, "Nanostructure-enhanced atomic line emission." *Nature* **485**, E1–E3 (2012).
- [196] N. Engheta, "Circuits with light at Nnanoscales: Optical nanocircuits inspired by metamaterials," *Science* **317**, 1698–1702 (2008).
- [197] N. Engheta, S. A, and A. Alu, "Circuit elements at optical frequencies: Nanoinductors, nanocapacitors, and nanoresitors," *Physical Review Letters* **95**, 095504 (2005).
- [198] L. D. Barron, *Molecular light scattering and optical activity* (Cambridge Univ. Press, 2004), 2nd edn.
- [199] P. Y. Bruice, *Organic Chemistry* (Pearson Prentice Hall, 2004), 4th edn.
- [200] B. Norden, "The asymmetry of life," *Journal of Molecular Evolution* **1**, 313–332 (1978).
- [201] A. G. Griesbeck and U. J. Meierhenrich, "Asymmetric photochemistry and photochirogenesis," *Angewandte Chemie International Edition* **41**, 3147–3154 (2002).
- [202] U. J. Meierhenrich, *Amino Acids and the Asymmetry of Life* (Springer, Berlin, 2008).
- [203] W. A. Bonner, "The origin and amplification of biomolecular chirality," *Origins of Life and Evolution of the Biosphere* **21**, 59–111 (1991).
- [204] P. L. Luisi, *The Emergence of Life - From Chemical Origins to Synthetic Biology* (Cambridge University Press, 2006).

- [205] P. Scott and R. Rines, “Naming the Loch Ness monster,” *Nature* **258**, 466–468 (1975).
- [206] J. K. Gansel, M. Thiel, M. S. Rill, M. Decker, K. Bade, V. Saile, G. von Freymann, S. Linden, and M. Wegener, “Gold helix photonic metamaterial as broadband circular polarizer,” *Science* **325**, 1513–1515 (2009).
- [207] J. K. Gansel, M. Latzel, A. Fröhlich, J. Kaschke, M. Thiel, and M. Wegener, “Tapered gold-helix metamaterials as improved circular polarizers,” *Applied Physics Letters* **100**, 101 109 (2012).
- [208] A. Radke, T. Gissibl, T. Klotzbücher, P. V. Braun, and H. Giessen, “Three-dimensional bichiral plasmonic crystals fabricated by direct laser writing and electroless silver plating,” *Advanced Materials* **23**, 3018–3021 (2011).
- [209] N. Liu, H. Liu, S. Zhu, and H. Giessen, “Stereometamaterials,” *Nature Photonics* **3**, 157–162 (2009).
- [210] M. Decker, M. Ruther, C. E. Kriegler, J. Zhou, C. M. Soukoulis, S. Linden, and M. Wegener, “Strong optical activity from twisted-cross photonic metamaterials,” *Optics Letters* **34**, 2501–2503 (2009).
- [211] C. Helgert, E. Pshenay-Severin, M. Falkner, C. Menzel, C. Rockstuhl, E.-B. Kley, A. Tünnermann, F. Lederer, and T. Pertsch, “Chiral metamaterial composed of three-dimensional plasmonic nanostructures.” *Nano Letters* **11**, 4400–4 (2011).
- [212] C. Menzel, C. Helgert, C. Rockstuhl, E.-B. Kley, A. Tünnermann, T. Pertsch, and F. Lederer, “Asymmetric transmission of linearly polarized light at optical metamaterials,” *Physical Review Letters* **104**, 253 902 (2010).
- [213] Z. Zhu, W. Liu, Z. Li, B. Han, Y. Zhou, Y. Gao, and Z. Tang, “Manipulation of collective optical activity in one dimensional plasmonic assembly.” *ACS Nano* **6**, 2326–2332 (2012).
- [214] A. Guerrero-Martínez, J. L. Alonso-Gómez, B. Auguié, M. M. Cid, and L. M. Liz-Marzán, “From individual to collective chirality in metal nanoparticles,” *Nano Today* **6**, 381–400 (2011).
- [215] A. Guerrero-Martínez, B. Auguié, J. L. Alonso-Gómez, Z. Džolić, S. Gómez-Graña, M. Žinić, M. M. Cid, and L. M. Liz-Marzán, “Intense optical activity from three-dimensional chiral ordering of plasmonic nanoantennas.” *Angewandte Chemie* **50**, 5499–5503 (2011).

- [216] Y. Zhao, M. Belkin, and A. Alù, “Twisted optical metamaterials for planarized ultrathin broadband circular polarizers,” *Nature Communications* **3**, 870 (2012).
- [217] A. Christofi, N. Stefanou, G. Gantzounis, and N. Papanikolaou, “Giant Optical Activity of Helical Architectures of Plasmonic Nanorods,” *The Journal of Physical Chemistry C* **116**, 16 674–16 679 (2012).
- [218] Z. Fan and A. O. Govorov, “Chiral nanocrystals: Plasmonic spectra and circular dichroism.” *Nano Letters* **12**, 3283–3289 (2012).
- [219] C. Menzel, C. Rockstuhl, T. Paul, and F. Lederer, “Retrieving effective parameters for quasiplanar chiral metamaterials,” *Applied Physics Letters* **93**, 233 106 (2008).
- [220] A. Papakostas, A. Potts, D. Bagnall, S. Prosvirnin, H. Coles, and N. Zheludev, “Optical manifestations of planar chirality,” *Physical Review Letters* **90**, 107 404 (2003).
- [221] E. Plum, X.-X. Liu, V. Fedotov, Y. Chen, D. Tsai, and N. Zheludev, “Metamaterials: Optical activity without chirality,” *Physical Review Letters* **102**, 113 902 (2009).
- [222] E. Plum, V. a. Fedotov, and N. I. Zheludev, “Extrinsic electromagnetic chirality in metamaterials,” *Journal of Optics A: Pure and Applied Optics* **11**, 074 009 (2009).
- [223] B. K. Canfield, S. Kujala, M. Kauranen, K. Jefimovs, T. Vallius, and J. Turunen, “Remarkable polarization sensitivity of gold nanoparticle arrays,” *Applied Physics Letters* **86**, 183 109 (2005).
- [224] F. Eftekhari and T. Davis, “Strong chiral optical response from planar arrays of subwavelength metallic structures supporting surface plasmon resonances,” *Physical Review B* **86**, 075 428 (2012).
- [225] M. Decker, M. W. Klein, M. Wegener, and S. Linden, “Circular dichroism of planar chiral magnetic metamaterials,” *Optics Letters* **32**, 856–858 (2007).
- [226] B. Gallinet and O. J. F. Martin, “Influence of Electromagnetic Interactions on the Line Shape of Plasmonic Fano Resonances,” *ACS Nano* **5**, 8999–9008 (2011).
- [227] I. Ament, J. Prasad, A. Henkel, S. Schmachtel, and C. Sönnichsen, “Single unlabeled protein detection on individual plasmonic nanoparticles.” *Nano Letters* **12**, 1092–1095 (2012).
- [228] P. Zijlstra, P. M. R. Paulo, and M. Orrit, “Optical detection of single non-absorbing

- molecules using the surface plasmon resonance of a gold nanorod.” *Nature Nanotechnology* **7**, 379–382 (2012).
- [229] Y. Tang and A. E. Cohen, “Enhanced enantioselectivity in excitation of chiral molecules by superchiral light,” *Science* **332**, 333–336 (2011).
- [230] K. Bliokh and F. Nori, “Characterizing optical chirality,” *Physical Review A* **83**, 021 803(R) (2011).
- [231] Y. Tang and A. E. Cohen, “Optical Chirality and Its Interaction with Matter,” *Physical Review Letters* **104**, 163 901 (2010).
- [232] M. Schäferling, D. Dregely, M. Hentschel, and H. Giessen, “Tailoring enhanced optical chirality: Design principles for chiral plasmonic nanostructures,” *Physical Review X* **2**, 031 010 (2012).
- [233] M. Schäferling, X. Yin, and H. Giessen, “Formation of chiral fields in a symmetric environment,” *Optics Express* **20**, 856–858 (2012).
- [234] E. Hendry, T. Carpy, J. Johnston, M. Popland, R. V. Mikhaylovskiy, A. J. Laphorn, S. M. Kelly, L. D. Barron, N. Gadegaard, and M. Kadodwala, “Ultra-sensitive detection and characterization of biomolecules using superchiral fields,” *Nature Nanotechnology* **5**, 783–787 (2010).
- [235] A. O. Govorov, Z. Fan, P. Hernandez, J. M. Slocik, and R. R. Naik, “Theory of circular dichroism of nanomaterials comprising chiral molecules and nanocrystals: plasmon enhancement, dipole interactions, and dielectric effects.” *Nano Letters* **10**, 1374–1382 (2010).
- [236] A. O. Govorov, “Plasmon-Induced Circular Dichroism of a Chiral Molecule in the Vicinity of Metal Nanocrystals. Application to Various Geometries,” *The Journal of Physical Chemistry C* **115**, 7914–7923 (2011).
- [237] I. Agranat, H. Caner, and J. Caldwell, “Putting chirality to work: The strategy of chiral switches,” *Nature Reviews Drug Discovery* **1**, 753–768 (2002).
- [238] M. Eichelbaum and A. S. Gross, “Stereochemical aspects of drug action and disposition,” *Advances in Drug Research* **28**, 1–64 (1996).
- [239] W. Zhu, D. Wang, and K. Crozier, “Direct observation of beamed Raman scattering.” *Nano Letters* **12**, 6235–6243 (2012).
- [240] M. A. Olson, A. Coskun, R. Klajn, L. Fang, S. K. Dey, K. P. Browne, B. A. Grzybowski, and J. F. Stoddart, “Assembly of polygonal nanoparticle clusters

- directed by reversible noncovalent bonding interactions.” *Nano Letters* **9**, 3185–90 (2009).
- [241] D. Zerrouki, J. Baudry, D. Pine, P. Chaikin, and J. Bibette, “Chiral colloidal clusters,” *Nature* **455**, 380–382 (2008).
- [242] G. Shemer, O. Krichevski, G. Markovich, T. Molotsky, I. Lubitz, and A. B. Kotlyar, “Chirality of silver nanoparticles synthesized on DNA,” *Journal of the American Chemical Society* **128**, 11 006–11 007 (2006).
- [243] W. Chen, A. Bian, A. Agarwal, L. Liu, H. Shen, L. Wang, C. Xu, and N. A. Kotov, “Nanoparticle superstructures made by polymerase chain reaction: Collective interactions of nanoparticles and a new principle for chiral materials,” *Nano Letters* **9**, 2153–2159 (2009).
- [244] C.-L. Chen, P. Zhang, and N. L. Rosi, “A new peptide-based method for the design and synthesis of nanoparticle superstructures: Construction of highly ordered gold nanoparticle double helices,” *Journal of the American Chemical Society* **130**, 13 555–13 557 (2008).
- [245] X. Shen, C. Song, J. Wang, D. Shi, Z. Wang, N. Liu, and B. Ding, “Rolling up gold nanoparticle-dressed DNA origami into three-dimensional plasmonic chiral nanostructures.” *Journal of the American Chemical Society* **134**, 146–149 (2012).
- [246] K. E. van Holde, W. C. Johnson, and P. S. Ho, *Principles of Physical Biochemistry* (Prentice Hall, Upper Saddle River, New Jersey, 1998).
- [247] A. O. Govorov, Y. K. Gun’ko, J. M. Slocik, V. A. Gérard, Z. Fan, and R. R. Naik, “Chiral nanoparticle assemblies: circular dichroism, plasmonic interactions, and exciton effects,” *Journal of Materials Chemistry* **8**, 16 806–16 818 (2011).
- [248] Z. Fan and A. O. Govorov, “Plasmonic circular dichroism of chiral metal nanoparticle assemblies.” *Nano Letters* **10**, 2580–2587 (2010).
- [249] Z. Fan and A. O. Govorov, “Helical metal nanoparticle assemblies with defects: Plasmonic chirality and circular dichroism,” *Journal of Physical Chemistry* **115**, 13 254–13 261 (2011).
- [250] N. Liu, H. Guo, L. Fu, S. Kaiser, H. Schweizer, and H. Giessen, “Three-dimensional photonic metamaterials at optical frequencies,” *Nature Materials* **7**, 31–37 (2008).
- [251] M. Decker, R. Zhao, C. M. Soukoulis, S. Linden, and M. Wegener, “Twisted split-ring-resonator photonic metamaterial with huge optical activity,” *Optics Letters* **35**, 1593–1595 (2010).

- [252] R. Kuroda, T. Harada, and Y. Shindo, “A solid-state dedicated circular dichroism spectrophotometer: Development and application,” *Review of Scientific Instruments* **72**, 3802–3810 (2001).
- [253] H. G. Kuball, “CD and ACD Spectroscopy on Anisotropic Samples - Chirality of Oriented Molecules in Anisotropic Phases,” *Enantiomer* **7**, 197–205 (2002).
- [254] H. G. Kuball and T. Höfer, “Encyclopedia of Spectroscopy and Spectrometry,” (Academic Press, London, 1999), chap. Chiroptica, pp. 267–281.
- [255] T. J. Davis, M. Hentschel, N. Liu, and H. Giessen, “Analytical model of the three-dimensional plasmonic ruler.” *ACS Nano* **6**, 1291–1298 (2012).
- [256] A. Kuzyk, R. Schreiber, Z. Fan, G. Pardatscher, E.-M. Roller, A. Högele, F. C. Simmel, A. O. Govorov, and T. Liedl, “DNA-based self-assembly of chiral plasmonic nanostructures with tailored optical response,” *Nature* **483**, 311–314 (2012).
- [257] M. Castro-Lopez, D. Brinks, R. Sapienza, and N. F. van Hulst, “Aluminum for nonlinear plasmonics: Resonance-driven polarized luminescence of Al, Ag, and Au nanoantennas.” *Nano Letters* **11**, 4674–4678 (2011).
- [258] A. Jakab, C. Rosman, Y. Khalavka, J. Becker, A. Trügler, U. Hohenester, and C. Sönnichsen, “Highly sensitive plasmonic silver nanorods.” *ACS Nano* **5**, 6880–6885 (2011).
- [259] L. S. Slaughter, Y. Wu, B. A. Willingham, P. Nordlander, and S. Link, “Effects of symmetry breaking and conductive contact on the plasmon coupling in gold nanorod dimers.” *ACS Nano* **4**, 4657–4666 (2010).
- [260] R. Esteban, A. G. Borisov, P. Nordlander, and J. Aizpurua, “Bridging quantum and classical plasmonics with a quantum-corrected model.” *Nature Communications* **3**, 825 (2012).
- [261] E. D. Palik, *Handbook of Optical Constants of Solids* (Academic, 1998).
- [262] H. Husu, J. Mäkitalo, J. Laukkanen, M. Kuittinen, and M. Kauranen, “Particle plasmon resonances in L-shaped gold nanoparticles.” *Optics Express* **18**, 16 601–16 606 (2010).
- [263] A. Lukach, K. Liu, H. Thérien-Aubin, and E. Kumacheva, “Controlling the degree of polymerization, bond lengths and bond angles of plasmonic polymers.” *Journal of the American Chemical Society* **134**, 18 853–18 859 (2012).
- [264] D. E. Gómez, K. C. Vernon, and T. J. Davis, “Symmetry effects on the optical

- coupling between plasmonic nanoparticles with applications to hierarchical structures,” *Physical Review B* **81**, 1–10 (2010).
- [265] N. Liu, L. Langguth, T. Weiss, J. Kästel, M. Fleischhauer, T. Pfau, and H. Giessen, “Plasmonic analogue of electromagnetically induced transparency at the Drude damping limit.” *Nature Materials* **8**, 758–62 (2009).
- [266] M. A. Fox and J. K. Whitesell, *Organic Chemistry* (Jones & Bartlett Publishers, 2004), 3rd edn.
- [267] W. Yan, L. Xu, C. Xu, W. Ma, H. Kuang, L. Wang, and N. A. Kotov, “Self-assembly of chiral nanoparticle pyramids with strong R/S optical activity.” *Journal of the American Chemical Society* **134**, 15 114–15 121 (2012).
- [268] C. Rockstuhl, C. Menzel, T. Paul, and F. Lederer, “Optical activity in chiral media composed of three-dimensional metallic meta-atoms,” *Physical Review B* **79**, 035 321 (2009).
- [269] B. Auguie, J. L. Alonso-Gomez, A. Guerrero-Martinez, and L. M. Liz-Marzan, “Fingers crossed : Optical activity of a chiral dimer of plasmonic nanorods,” *The Journal of Physical Chemistry Letters* **2**, 846–851 (2011).
- [270] M. Kuwata-Gonokami, N. Saito, Y. Ino, M. Kauranen, K. Jefimovs, T. Vallius, J. Turunen, and Y. Svirko, “Giant optical activity in quasi-two-dimensional planar nanostructures,” *Physical Review Letters* **95**, 227 401 (2005).
- [271] E. Hendry, R. V. Mikhaylovskiy, L. D. Barron, M. Kadodwala, and T. J. Davis, “Chiral electromagnetic fields generated by arrays of nanoslits.” *Nano Letters* **12**, 3640–3644 (2012).
- [272] M. R. Jones, K. D. Osberg, R. J. Macfarlane, M. R. Langille, and C. A. Mirkin, “Templated techniques for the synthesis and assembly of plasmonic nanostructures,” *Chemical Reviews* **111**, 3736–3827 (2011).
- [273] N. C. Seeman, “Nucleic acid junctions and lattices,” *Journal of Theoretical Biology* **99**, 237–247 (1982).
- [274] R. J. Macfarlane, B. Lee, M. R. Jones, N. Harris, G. C. Schatz, and C. A. Mirkin, “Nanoparticle superlattice engineering with DNA,” *Science* **334**, 204–208 (2011).
- [275] C. A. Mirkin, R. L. Letsinger, R. C. Mucic, and J. J. Storhoff, “A DNA-based method for rationally assembling nanoparticles into macroscopic materials,” *Nature* **382**, 607–609 (1996).

- [276] A. P. Alivisatos, K. P. Johnsson, X. Peng, T. E. Wilson, C. J. Loweth, M. P. Bruchez, and P. G. Schultz, "Organization of 'nanocrystal molecules' using DNA," *Nature* **382**, 609–611 (1996).
- [277] N. A. Abdulrahman, Z. Fan, T. Tonooka, S. M. Kelly, N. Gadegaard, E. Hendry, A. O. Govorov, and M. Kadodwala, "Induced chirality through electromagnetic coupling between chiral molecular layers and plasmonic nanostructures." *Nano Letters* **12**, 977–983 (2012).
- [278] A. A. Yanik, A. E. Cetin, M. Huang, A. Artar, S. H. Mousavi, A. Khanikaev, J. H. Connor, G. Shvets, and H. Altug, "Seeing protein monolayers with naked eye through plasmonic Fano resonances." *Proceedings of the National Academy of Sciences of the United States of America* **108**, 11 784–11 789 (2011).
- [279] B. N. Feltis, B. A. Sexton, F. L. Glenn, M. J. Best, M. Wilkins, and T. J. Davis, "A hand-held surface plasmon resonance biosensor for the detection of ricin and other biological agents." *Biosensors & Bioelectronics* **23**, 1131–1136 (2008).
- [280] A. Wokaun, J. Bergman, A. Heritage, A. Glass, P. Liao, and D. Olson, "Surface second-harmonic generation from metal island films and microlithographic structures," *Physical Review B* **24**, 849–856 (1981).
- [281] D. Ricard, P. Roussignol, and C. Flytzanis, "Surface-mediated enhancement of optical phase conjugation in metal colloids." *Optics Letters* **10**, 511–513 (1985).
- [282] C. K. Chen, T. F. Heinz, D. Ricard, and Y. R. Shen, "Surface-enhanced second-harmonic generation and Raman scattering," *Physical Review B* **27**, 1965–1979 (1983).
- [283] G. Boyd, T. Rasing, J. Leite, and Y. Shen, "Local-field enhancement on rough surfaces of metals, semimetals, and semiconductors with the use of optical second-harmonic generation," *Physical Review B* **30**, 519–526 (1984).
- [284] M. Moskovits, "Surface roughness and the enhanced intensity of Raman scattering by molecules adsorbed on metals," *The Journal of Chemical Physics* **69**, 4159–4161 (1978).
- [285] S. McCall, P. Platzman, and P. Wolff, "Surface enhanced Raman scattering," *Physics Letters A* **77**, 381–383 (1980).
- [286] J. Gersten and A. Nitzan, "Electromagnetic theory of enhanced Raman scattering by molecules adsorbed on rough surfaces," *The Journal of Chemical Physics* **73**, 3023 (1980).

- [287] J. E. Sipe and R. W. Boyd, “Nonlinear susceptibility of composite optical materials in the Maxwell Garnett model,” *Physical Review A* **46**, 1614–1629 (1992).
- [288] V. M. Shalaev, “Electromagnetic properties of small-particle composites,” *Physics Reports* **272**, 61–137 (1996).
- [289] V. Shalaev, E. Poliakov, and V. Markel, “Small-particle composites. II. Nonlinear optical properties.” *Physical Review B: Condensed matter* **53**, 2437–2449 (1996).
- [290] A. V. Butenko, P. A. Chubakov, Y. E. Danilova, S. V. Karpov, A. K. Popov, S. G. Rautian, V. P. Safonov, V. V. Slabko, V. M. Shalaev, and M. I. Stockman, “Nonlinear optics of metal fractal clusters,” *Z. Phys. D - Atoms, Molecules and Clusters* **17**, 283–289 (1990).
- [291] M. Lippitz, M. A. van Dijk, and M. Orrit, “Third-harmonic generation from single gold nanoparticles,” *Nano Letters* **5**, 799–802 (2005).
- [292] M. W. Klein, C. Enkrich, M. Wegener, and S. Linden, “Second-harmonic generation from magnetic metamaterials,” *Science* **313**, 502–4 (2006).
- [293] T. Zentgraf, A. Christ, J. Kuhl, and H. Giessen, “Tailoring the ultrafast dephasing of quasiparticles in metallic photonic crystals,” *Physical Review Letters* **93**, 243 901 (2004).
- [294] B. K. Canfield, S. Kujala, K. Jefimovs, Y. Svirko, J. Turunen, and M. Kauranen, “A macroscopic formalism to describe the second-order nonlinear optical response of nanostructures,” *Journal of Optics A: Pure and Applied Optics* **8**, S278–S284 (2006).
- [295] B. K. Canfield, H. Husu, J. Laukkanen, B. Bai, M. Kuittinen, J. Turunen, and M. Kauranen, “Local field asymmetry drives second-harmonic generation in non-centrosymmetric nanodimers,” *Nano Letters* **7**, 1251–1255 (2007).
- [296] M. J. Huttunen, G. Bautista, M. Decker, S. Linden, M. Wegener, and M. Kauranen, “Nonlinear chiral imaging of subwavelength-sized twisted-cross gold nanodimers,” *Optical Materials Express* **1**, 2501–2503 (2011).
- [297] V. K. Valev, A. V. Silhanek, N. Verellen, W. Gillijns, P. Van Dorpe, O. a. Akt-sipetrov, G. A. E. Vandenbosch, V. V. Moshchalkov, and T. Verbiest, “Asymmetric optical second-harmonic generation from chiral G-shaped gold nanostructures,” *Physical Review Letters* **104**, 127 401 (2010).
- [298] V. K. Valev, X. Zheng, C. G. Biris, A. V. Silhanek, V. Volskiy, B. D. Clercq, O. A. Aktsipetrov, M. Ameloot, N. C. Panoiu, G. A. E. Vandenbosch, and V. V.

Moshchalkov, “The origin of second harmonic generation hotspots in chiral optical metamaterials,” *Optical Materials Express* **1**, 6233–6241 (2011).

- [299] V. K. Valev, A. V. Silhanek, W. Gillijns, Y. Jeyaram, H. Paddubrouskaya, A. Volodin, C. G. Biris, N. C. Panoiu, B. De Clercq, M. Ameloot, O. A. Akt-sipetrov, V. V. Moshchalkov, and T. Verbiest, “Plasmons reveal the direction of magnetization in nickel nanostructures.” *ACS Nano* **5**, 91–96 (2011).
- [300] Y. Zhang, N. K. Grady, C. Ayala-Orozco, and N. J. Halas, “Three-Dimensional Nanostructures as Highly Efficient Generators of Second Harmonic Light.” *Nano Letters* **11**, 5519–5523 (2011).
- [301] T. Xu, X. Jiao, G. P. Zhang, and S. Blair, “Second-harmonic emission from sub-wavelength apertures : Effects of aperture symmetry and lattice arrangement,” *Optics Express* **15**, 13 894–13 906 (2007).
- [302] A. Lesuffleur, L. K. S. Kumar, and R. Gordon, “Enhanced second harmonic generation from nanoscale double-hole arrays in a gold film,” *Applied Physics Letters* **88**, 261 104 (2006).
- [303] A. M. Moran, J. Sung, E. M. Hicks, R. P. Van Duyne, and K. G. Spears, “Second harmonic excitation spectroscopy of silver nanoparticle arrays.” *The Journal of Physical Chemistry B* **109**, 4501–4506 (2005).
- [304] T. Hanke, G. Krauss, D. Träutlein, B. Wild, R. Bratschitsch, and A. Leitenstorfer, “Efficient nonlinear light emission of single gold optical antennas driven by few-cycle near-infrared pulses,” *Physical Review Letters* **103**, 257 404 (2009).
- [305] T. Hanke, J. Cesar, V. Knittel, A. Trügler, U. Hohenester, A. Leitenstorfer, and R. Bratschitsch, “Tailoring spatiotemporal light confinement in single plasmonic nanoantennas.” *Nano Letters* **12**, 992–996 (2012).
- [306] K. D. Ko, A. Kumar, K. H. Fung, R. Ambekar, G. L. Liu, N. X. Fang, and K. C. Toussaint, “Nonlinear optical response from arrays of Au bowtie nanoantennas,” *Nano Letters* **11**, 61–65 (2011).
- [307] B. Lamprecht, J. R. Krenn, A. Leitner, and F. R. Aussenegg, “Resonant and off-resonant light-driven plasmons in metal nanoparticles studied by femtosecond-resolution third-harmonic generation,” *Physical Review Letters* **83**, 4421–4424 (1999).
- [308] M. Danckwerts and L. Novotny, “Optical frequency mixing at coupled gold nanoparticles,” *Physical Review Letters* **98**, 026 104 (2007).

- [309] S. Palomba, M. Danckwerts, and L. Novotny, “Nonlinear plasmonics with gold nanoparticle antennas,” *Journal of Optics A: Pure and Applied Optics* **11**, 114 030 (2009).
- [310] M. W. Klein, M. Wegener, N. Feth, and S. Linden, “Experiments on second- and third-harmonic generation from magnetic metamaterials,” *Optics Express* **15**, 5238–47 (2007).
- [311] S. Linden, F. Niesler, J. Förstner, Y. Grynko, T. Meier, and M. Wegener, “Collective effects in second-harmonic generation from split-ring-resonator arrays,” *Physical Review Letters* **109**, 015 502 (2012).
- [312] N. Feth, S. Linden, M. W. Klein, M. Decker, F. B. P. Niesler, Y. Zeng, W. Hoyer, J. Liu, S. W. Koch, J. V. Moloney, and M. Wegener, “Second-harmonic generation from complementary split-ring resonators.” *Optics Letters* **33**, 1975–1977 (2008).
- [313] A. Podlipensky, J. Lange, G. Seifert, H. Graener, and I. Cravetchi, “Second-harmonic generation from ellipsoidal silver nanoparticles embedded in silica glass.” *Optics Letters* **28**, 716–718 (2003).
- [314] F. B. P. Niesler, N. Feth, S. Linden, J. Niegemann, J. Gieseler, K. Busch, and M. Wegener, “Second-harmonic generation from split-ring resonators on a GaAs substrate.” *Optics Letters* **34**, 1997–9 (2009).
- [315] M. Gentile, M. Hentschel, R. Taubert, H. Guo, H. Giessen, and M. Fiebig, “Investigation of the nonlinear optical properties of metamaterials by second harmonic generation.” *Applied Physics B* **105**, 149–162 (2011).
- [316] T. Utikal, M. I. Stockman, A. P. Heberle, M. Lippitz, and H. Giessen, “All-optical control of the ultrafast dynamics of a hybrid plasmonic system,” *Physical Review Letters* **104**, 113 903 (2010).
- [317] T. Utikal, T. Zentgraf, T. Paul, C. Rockstuhl, F. Lederer, M. Lippitz, and H. Giessen, “Towards the origin of the nonlinear response in hybrid plasmonic systems,” *Physical Review Letters* **106**, 133 901 (2011).
- [318] T. Utikal, M. Hentschel, and H. Giessen, “Nonlinear photonics with metallic nanostructures on top of dielectrics and waveguides.” *Applied Physics B* **105**, 51–65 (2011).
- [319] I.-y. Park, S. Kim, J. Choi, D.-h. Lee, Y.-j. Kim, M. F. Kling, M. I. Stockman, and S.-w. Kim, “Plasmonic generation of ultrashort extreme-ultraviolet light pulses,” *Nature Photonics* **5**, 677–681 (2011).

- [320] Y. Pu, R. Grange, C.-L. Hsieh, and D. Psaltis, “Nonlinear optical properties of core-shell nanocavities for enhanced second-harmonic generation,” *Physical Review Letters* **104**, 207 402 (2010).
- [321] P.-Y. Chen and A. Alù, “Optical nanoantenna arrays loaded with nonlinear materials,” *Physical Review B* **82**, 235 405 (2010).
- [322] P.-Y. Chen, C. Argyropoulos, and A. Alu, “Enhanced nonlinearities using plasmonic nanoantennas,” *Nanophotonics* **1**, 221–233 (2012).
- [323] K. Thyagarajan, S. Rivier, A. Lovera, and O. J. Martin, “Enhanced second-harmonic generation from double resonant plasmonic antennae,” *Optics Express* **20**, 12 860 (2012).
- [324] H. Harutyunyan, G. Volpe, R. Quidant, and L. Novotny, “Enhancing the nonlinear optical response using multifrequency gold-nanowire antennas,” *Physical Review Letters* **108**, 217 403 (2012).
- [325] H. Aouani, M. Navarro-Cia, M. Rahmani, T. Sidiropoulos, M. Hong, R. Oulton, and S. a. Maier, “Multiresonant broadband optical antennas as efficient tunable nanosources of second harmonic light.” *Nano letters* **12**, 4997–5002 (2012).
- [326] R. R. Birss, *Symmetry and Magnetism* (North-Holland Publishing Company, 1966).
- [327] R. W. Boyd, *Nonlinear Optics* (Elsevier, 2008), 3rd edn.
- [328] Y. R. Shen, *The Principles of Nonlinear Optics* (Wiley-Interscience, 2002).
- [329] P. Mühlischlegel, H.-J. Eisler, O. J. F. Martin, B. Hecht, and D. W. Pohl, “Resonant optical antennas,” *Science* **308**, 1607–1609 (2005).
- [330] L. Novotny and N. van Hulst, “Antennas for light,” *Nature Photonics* **5**, 83–90 (2011).
- [331] P. J. Schuck, D. P. Fromm, A. Sundaramurthy, G. S. Kino, and W. E. Moerner, “Improving the mismatch between light and nanoscale objects with gold bowtie nanoantennas,” *Physical Review Letters* **94**, 017 402 (2005).
- [332] P. Biagioni, J.-S. Huang, and B. Hecht, “Nanoantennas for visible and infrared radiation,” *Reports on Progress in Physics* **75**, 024 402 (2012).
- [333] H. Fischer and O. J. F. Martin, “Engineering the optical response of plasmonic nanoantennas,” *Optics Express* **16**, 9144–9154 (2008).

- [334] J. Renger, R. Quidant, N. van Hulst, and L. Novotny, “Surface-enhanced nonlinear four-wave mixing,” *Physical Review Letters* **104**, 046 803 (2010).
- [335] J. Renger, R. Quidant, and L. Novotny, “Enhanced nonlinear response from metal surfaces,” *Optics Express* **19**, 1777–1785 (2011).
- [336] D. K. Polyushkin, E. Hendry, E. K. Stone, and W. L. Barnes, “THz generation from plasmonic nanoparticle arrays.” *Nano Letters* **11**, 4718–4724 (2011).
- [337] H. Husu, R. Siikanen, J. Mäkitalo, J. Lehtolahti, J. Laukkanen, M. Kuittinen, and M. Kauranen, “Metamaterials with tailored nonlinear optical response.” *Nano Letters* **12**, 673–677 (2012).
- [338] J. Zuloaga, E. Prodan, and P. Nordlander, “Quantum Description of the Plasmon Resonances of a Nanoparticle Dimer,” *Nano Letters* **9**, 887–891 (2009).
- [339] Y. S. Kivshar, “Nonlinear optics: The next decade,” *Optics Express* **16**, 22 126–8 (2008).
- [340] M. Kauranen and A. V. Zayats, “Nonlinear plasmonics,” *Nature Photonics* **6**, 737–748 (2012).
- [341] T. Sasaki, Y. Mori, M. Yoshimura, Y. K. Yap, and T. Kamimura, “Recent development of nonlinear optical borate crystals: Key materials for generation of visible and UV light,” *Materials Science and Engineering: R: Reports* **30**, 1–54 (2000).
- [342] R. S. Weis and T. K. Gaylord, “Lithium Niobate: Summary of Physical Properties and Crystal Structure,” *Applied Physics A* **37**, 191–203 (1985).
- [343] M. Fejer, G. Magel, D. Jundt, and R. Byer, “Quasi-phase-matched second harmonic generation: Tuning and tolerances,” *IEEE Journal of Quantum Electronics* **28**, 2631–2654 (1992).
- [344] M. Fiebig, D. Fröhlich, T. Lottermoser, V. Pavlov, R. Pisarev, and H.-J. Weber, “Second harmonic generation in the centrosymmetric antiferromagnet NiO,” *Physical Review Letters* **87**, 137 202 (2001).
- [345] M. Fiebig, V. V. Pavlov, and R. V. Pisarev, “Second-harmonic generation for studying electronic and magnetic structures of crystals : Review,” *Journal of the Optical Society of America B* **22**, 96–118 (2005).
- [346] T. F. Heinz, C. K. Chen, D. Ricard, and Y. R. Shen, “Spectroscopy of Molecular Monolayers by Resonant Second-Harmonic Generation,” *Physical Review Letters* **48**, 478–481 (1982).

- [347] D. A. Higgins, M. B. Abrams, S. K. Byerly, and R. M. Corn, “Resonant second harmonic generation studies of p-nitrophenol adsorption at condensed-phase interfaces,” *Langmuir* **8**, 1994–2000 (1992).
- [348] M. Belkin, S. Han, X. Wei, and Y. Shen, “Sum-Frequency Generation in Chiral Liquids near Electronic Resonance,” *Physical Review Letters* **87**, 1–4 (2001).
- [349] H. Im, K. C. Bantz, N. C. Lindquist, C. L. Haynes, and S.-H. Oh, “Vertically oriented sub-10-nm plasmonic nanogap arrays.” *Nano Letters* **10**, 2231–2236 (2010).
- [350] D.-K. Lim, K.-S. Jeon, H. M. Kim, J.-M. Nam, and Y. D. Suh, “Nanogap-engineerable Raman-active nanodumbbells for single-molecule detection,” *Nature Materials* **9**, 60–67 (2010).
- [351] J. F. Li, Y. F. Huang, Y. Ding, Z. L. Yang, S. B. Li, X. S. Zhou, F. R. Fan, W. Zhang, Z. Y. Zhou, D. Y. Wu, B. Ren, Z. L. Wang, and Z. Q. Tian, “Shell-isolated nanoparticle-enhanced Raman spectroscopy.” *Nature* **464**, 392–395 (2010).
- [352] A. Pucci, F. Neubrech, D. Weber, S. Hong, T. Toury, and M. L. de la Chapelle, “Surface enhanced infrared spectroscopy using gold nanoantennas,” *Physica Status Solidi (B)* **247**, 2071–2074 (2010).
- [353] G. Volpe, M. Noack, S. S. Aćimović, C. Reinhardt, and R. Quidant, “Near-Field Mapping of Plasmonic Antennas by Multiphoton Absorption in Poly(methyl methacrylate).” *Nano Letters* **12**, 4864–4868 (2012).
- [354] P. Alonso-González, P. Albella, M. Schnell, J. Chen, F. Huth, A. García-Etxarri, F. Casanova, F. Golmar, L. Arzubiaga, L. Hueso, J. Aizpurua, and R. Hillenbrand, “Resolving the electromagnetic mechanism of surface-enhanced light scattering at single hot spots,” *Nature Communications* **3**, 684 (2012).
- [355] M. Schnell, A. Garcia-Etxarri, J. Alkorta, J. Aizpurua, and R. Hillenbrand, “Phase-resolved mapping of the near-field vector and polarization state in nanoscale antenna gaps,” *Nano Letters* **10**, 3524–3528 (2010).
- [356] L. Arzubiaga, F. Casanova, L. E. Hueso, A. Chuvilin, M. Schnell, and R. Hillenbrand, “Nanofocusing of mid-infrared energy with tapered transmission lines,” *Nature Photonics* **5**, 283–287 (2011).
- [357] K. Chen, C. Durak, J. R. Heflin, and H. D. Robinson, “Plasmon-enhanced second-harmonic generation from ionic self-assembled multilayer films.” *Nano Letters* **7**, 254–258 (2007).

- [358] B. Knabe, D. Schu, T. Jungk, M. Svete, and W. Assenmacher, "Synthesis and characterization of Fe-doped LiNbO₃ nanocrystals from a triple-alkoxide method," *physica status solidi (a)* **862**, 857–862 (2011).
- [359] B. Knabe, K. Buse, W. Assenmacher, and W. Mader, "Spontaneous polarization in ultrasmall lithium niobate nanocrystals revealed by second harmonic generation," *Physical Review B* **86**, 195 428 (2012).
- [360] B. Metzger, A. Steinmann, and H. Giessen, "High-power widely tunable sub-20 fs Gaussian laser pulses for ultrafast nonlinear spectroscopy." *Optics Express* **19**, 24 354–24 360 (2011).
- [361] B. Metzger, M. Hentschel, M. Lippitz, and H. Giessen, "Third-harmonic spectroscopy and modeling of the nonlinear response of plasmonic nanoantennas," *Optics Letters* **37**, 4741–4743 (2012).
- [362] D. Schütze, B. Knabe, M. Ackermann, and K. Buse, "Orientation of colloiddally suspended LiNbO₃ nanocrystals in externally applied electric fields," *Applied Physics Letters* **97**, 242 908 (2010).
- [363] D. C. Marinica, A. K. Kazansky, P. Nordlander, J. Aizpurua, and A. G. Borisov, "Quantum Plasmonics: Nonlinear Effects in the Field Enhancement of a Plasmonic Nanoparticle Dimer." *Nano Letters* **12**, 1333–1339 (2012).
- [364] L. Wu, H. Duan, P. Bai, M. Bosman, J. K. W. Yang, and E. P. Li, "Fowler-Nordheim Tunneling Induced Charge Transfer Plasmons between Nearly-Touching Nanoparticles." *ACS Nano* p. 10.1021/nn304970v (2012).
- [365] C. Ciraci, R. T. Hill, J. J. Mock, Y. Urzhumov, A. I. Fernandez-Dominguez, S. A. Maier, J. B. Pendry, A. Chilkoti, and D. R. Smith, "Probing the Ultimate Limits of Plasmonic Enhancement," *Science* **337**, 1072–1074 (2012).
- [366] H. Duan, A. I. Fernández-Domínguez, M. Bosman, S. A. Maier, and J. K. W. Yang, "Nanoplasmonics: Classical down to the Nanometer Scale." *Nano Letters* **12**, 1683–1689 (2012).
- [367] R. W. Taylor, T.-C. Lee, O. A. Scherman, R. Esteban, J. Aizpurua, F. M. Huang, J. J. Baumberg, and S. Mahajan, "Precise subnanometer plasmonic junctions for SERS within gold nanoparticle assemblies using cucurbit[n]uril "glue"." *ACS Nano* **5**, 3878–3887 (2011).
- [368] Y. Chen and W. Cheng, "DNA-based plasmonic nanoarchitectures: from structural design to emerging applications." *Wiley interdisciplinary reviews. Nanomedicine and nanobiotechnology* **4**, 587–604 (2012).

- [369] B. Pelaz, S. Jaber, D. J. de Aberasturi, V. Wulf, T. Aida, J. M. de la Fuente, J. Feldmann, H. E. Gaub, L. Josephson, C. R. Kagan, N. A. Kotov, L. M. Liz-Marzán, H. Mattoussi, P. Mulvaney, C. B. Murray, A. L. Rogach, P. S. Weiss, I. Willner, and W. J. Parak, “The state of nanoparticle-based nanoscience and biotechnology: Progress, promises, and challenges.” *ACS Nano* **6**, 8468–83 (2012).
- [370] J. Kern, S. Grossmann, N. V. Tarakina, T. Häckel, M. Emmerling, M. Kamp, J.-S. Huang, P. Biagioni, J. Prangma, and B. Hecht, “Atomic-scale confinement of resonant optical fields.” *Nano Letters* **12**, 5504–5509 (2012).
- [371] F. E. Neumann, *Beiträge zur Krystallonomie* (Ernst Siegfried Mittler, Berlin, 1823).
- [372] Bernhard Minnigerode, “No Title,” *Neues Jahrb. Mineral Geol. Paleontol.* **5**, 145 (1887).
- [373] E. Wigner, *Symmetries and Reflections* (Indiana Univ. Press., 1967).
- [374] T. Debs and M. Redhead, *Objectivity, Invariance, and Convention: Symmetry in Physical Science* (Harvard Univ. Press., 2007).
- [375] A. M. Funston, C. Novo, T. J. Davis, and P. Mulvaney, “Plasmon coupling of gold nanorods at short distances and in different geometries.” *Nano Letters* **9**, 1651–8 (2009).
- [376] B. K. Canfield, S. Kujala, K. Jefimovs, and M. Kauranen, “Linear and nonlinear optical responses influenced by broken symmetry in an array of gold nanoparticles,” *Optics Express* **12**, 419–423 (2004).
- [377] R. Czaplicki, M. Zdanowicz, K. Koskinen, J. Laukkanen, M. Kuittinen, and M. Kauranen, “Dipole limit in second-harmonic generation from arrays of gold nanoparticles.” *Optics Express* **19**, 26 866–71 (2011).
- [378] V. V. Temnov, G. Armelles, U. Woggon, D. Guzatov, A. Cebollada, A. Garcia-Martin, J.-M. Garcia-Martin, T. Thomay, A. Leitenstorfer, and R. Bratschitsch, “Active magneto-plasmonics in hybrid metal–ferromagnet structures,” *Nature Photonics* **4**, 107–111 (2010).
- [379] V. V. Temnov, “Ultrafast acousto-magneto-plasmonics,” *Nature Photonics* **6**, 728–736 (2012).
- [380] S. V. Fomichev, S. V. Popruzhenko, D. F. Zaretsky, and W. Becker, “Laser-induced nonlinear excitation of collective electron motion in a cluster,” *Journal of Physics B: Atomic, Molecular and Optical Physics* **4075**, 3817–3834 (2003).

- [381] S. Fomichev, S. Popruzhenko, D. Zaretsky, and W. Becker, “Nonlinear excitation of the Mie resonance in a laser-irradiated cluster.” *Optics Express* **11**, 2433–2439 (2003).
- [382] S. Fomichev, D. Zaretsky, D. Bauer, and W. Becker, “Classical molecular-dynamics simulations of laser-irradiated clusters: Nonlinear electron dynamics and resonance-enhanced low-order harmonic generation,” *Physical Review A* **71**, 1–13 (2005).
- [383] S. V. Fomichev, D. F. Zaretsky, and W. Becker, “Classical modelling of the nonlinear properties of clusters in strong low-frequency laser fields,” *Journal of Physics B: Atomic, Molecular and Optical Physics* **37**, L175–L182 (2004).

Curriculum Vitae

Personal Data:

Last name Hentschel
First name Mario
Date of birth 03.12.1982
Place of birth Attendorn
Residence Brühlstraße 1, 70563 Stuttgart
Phone 0711-68565108
Mail m.hentschel@physik.uni-stuttgart.de

Education:

06.2002 Ev. Gymnasium Meinerzhagen, Abitur
(German university entrance qualification)
2003 - 2008 Studies of Physics at the Rheinische Friedrich-Wilhelms-Universität
Bonn, Germany.
Specialized courses in Crystal Optics, Laserphysics and
Quantumoptics, Applied Optics, Laser Cooling and Spectroscopy, and
Condensed Matter Physics.
Subsidiary subjects include Astronomy,
Nuclear Medicine, and Geophysics.
2007 - 2008 Diploma thesis
"Non-linear Optical Spectroscopy of Metamaterials"
in the group of Prof. Manfred Fiebig
12.2008 Diploma in Physics
12.2008 - 02.2009 Research Assistant in the group of Prof. Fiebig
Since 03.2009 Ph.D. student in the group of Prof. Harald Giessen,
University of Stuttgart, and Max Planck Institute for
Solid State Research, Stuttgart
Since 2012 Peer review for ACS Nano, Nano Letters,
Applied Physics Letters, and Optics Express

Teaching:

Winter term 06/07 Tutor for the Physics Basic Studies Lecture on
"Electromagnetism"
Summer term 07 Tutor for the Beginners Lab Course for Physics Students
01.2008 - 12.2008 Physics Lab Course for medical students
Since 05.2009 Advanced Lab Course "Gamma Radiation and Matter"

Acknowledgments

The last few years have been an amazing time. For all the science, projects, and papers but also for everything beyond all that I am deeply grateful to so many people.

To Prof. Harald Giessen for accepting me as a PhD student and for giving me the possibility to work in his group. For the countless discussions, for all the ideas, for his advice, insight, support, and encouragement which have been essential for all projects.

To my examination committee Prof. Christian Holm, Prof. Peter Michler, and Prof. Stefan Linden for their support.

To Prof. Markus Lippitz for helpful advice, council, and discussions, as well as for his ideas and support with the antenna third harmonic project.

To Na Liu for sharing so many ideas and projects with me, for her support and encouragement as well as her insight and advice.

To Jürgen Weis for giving me the possibility to work in the clean room at the Max Planck Institute for Solid State Research as well as to Ulrike Waizmann and Thomas Reindl for all their support in processing and structuring.

To Monika Ubl for all her processing support in the Mikrostrukturlabor.

To Christine von Rekowski for her support in all administrative matters and her sympathetic ear for the smaller and bigger daily problems.

To Daniel Dregely and Richard Taubert for great and insightful discussions and the excellent team work on the common projects and papers.

To Bernd Metzger for giving me the opportunity to contribute to his nonlinear projects and for numerous highly insightful and vivid discussions.

To my office and lab mates Tobias Utikal and Jessie Chin for all the fun we had.

To Marius Vieweg and Daniel Dregely for our weekly sports appointment and the accompanying discussions as well as for all your advice and of course the fun we had - I will really miss it.

To all my colleagues from the 4th Physics Institute and the Max Planck Institute for Solid State Research for the awesome working environment and - besides work - all

the fun we had in the coffee corner, on the Fluchtbalkon, outside of university, etc., in particular Ralf Ameling, Jessie Chin, Christian Dicken, Daniel Dregely, Timo Gissibl, Klas Lindfors, Martin Mesch, Bernd Metzger, Thorsten Schumacher, Richard Taubert, Daniela Ulrich, Tobias Utikal, Marius Vieweg, and Christian Wolpert.

To my family for always being there for me and for their constant support for over 30 years now.